

**New interpretations of
pyrrhotite and pentlandite
surface electronic structures: A
route to the identification of
minority species**

By

Zoe Elizabeth Pettifer

*Thesis
Submitted to Flinders University
for the degree of*

Doctor of Philosophy
College of Science and Engineering
17th November 2020

TABLE OF CONTENTS

TABLE OF CONTENTS.....	I
ABSTRACT.....	V
DECLARATION.....	VII
ACKNOWLEDGEMENTS.....	VIII
PUBLICATIONS.....	X
Journal Articles.....	x
Oral Presentations.....	x
Poster Presentations.....	x
LIST OF FIGURES.....	XI
LIST OF TABLES.....	XVII
1 INTRODUCTION.....	1
1.1 Thesis structure and aims.....	2
1.2 References.....	4
2 LITERATURE REVIEW: LOOKING BEYOND THE EARTH'S CRUST TO SEE THE CRYSTAL STRUCTURES WITHIN.....	6
2.1 Transition metal chalcogenides.....	6
2.2 Pyrrhotite.....	7
2.3 Pentlandite.....	9
2.4 Electronic structure, bonding, and transitions in materials.....	11
2.5 Photoelectron spectroscopy of transition metal sulfides.....	12
2.5.1 Identification of surface states.....	13
2.5.2 Interpretation of bulk XPS line shapes.....	14
2.5.3 X-ray absorption spectroscopy and resonant valence band studies.....	15
2.6 Oxidation of sulfide surfaces.....	16
2.7 Overcoming limitations of techniques.....	17
2.8 Summary and objectives.....	18
2.9 References.....	18
3 MATERIALS AND METHODS.....	25
3.1 Minerals.....	25
3.1.1 Pentlandite synthesis.....	25
3.1.2 Mineral characterisation.....	25
3.1.3 Surface preparation.....	26
3.2 X-ray photoelectron spectroscopy.....	28
3.2.1 The photoelectron excitation process.....	29
3.2.2 Surface sensitivity.....	31
3.2.3 Data collection.....	33

3.2.4	Data processing	33
3.3	X-ray absorption spectroscopy	34
3.3.1	Data collection and processing	35
3.4	Resonant valence band photoemission spectroscopy	35
3.4.1	Data collection and analysis.....	36
3.5	Photoemission Electron Microscopy.....	36
3.5.1	Data collection and processing	37
3.6	Scanning transmission X-ray microscopy	38
3.6.1	Data collection	40
3.7	References	40
4	PRISTINE FRACTURE SURFACES OF MONOCLINIC PYRRHOTITE	43
4.1	Methods	44
4.2	Analysis of sulfur states	45
4.2.1	Identifying the sulfur states on pyrrhotite fracture surfaces	46
4.2.2	Fitting pyrrhotite S 2 <i>p</i> photoelectron spectra.....	49
4.2.3	Assignment of S 2 <i>p</i> peaks.....	52
4.2.4	Pyrrhotite bulk sulfide peak shape	54
4.3	Analysis of iron states	57
4.3.1	Fe 2 <i>p</i> X-ray photoelectron spectra.....	57
4.3.2	Fe states in the pyrrhotite valence band.....	59
4.3.3	Resonant valence band spectra over the Fe 2 <i>p</i> absorption threshold.....	60
4.4	Conclusions	65
4.5	References	67
5	OXIDISED SURFACES OF MONOCLINIC PYRRHOTITE.....	70
5.1	Methods.....	71
5.2	Monoclinic pyrrhotite.....	72
5.2.1	Polished monoclinic pyrrhotite surfaces	73
5.2.2	Surface of monoclinic pyrrhotite in pH 1 H ₂ SO ₄	78
5.2.3	NEXAFS spectra and PEEM images of pyrrhotite immersed in pH 1 H ₂ SO ₄ for 1 hour 82	
5.3	Conclusion.....	84
5.4	References	86
6	PRISTINE FRACTURE SURFACES OF PENTLANDITE.....	88
6.1	Introduction	88
6.1.1	Methods.....	89
6.2	Photoelectron spectra of the “Pn1” fractured surface	89
6.2.1	Pn1 Fe & Ni 2 <i>p</i> SXPS.....	90
6.2.2	Pn1 Sulfur 2 <i>p</i> spectra	92
6.2.3	Pn1 valence band	95

6.2.4	Assignment of sulfur peaks.....	97
6.2.5	Surface monosulfide species.....	97
6.2.6	Surface and bulk contributions to peak B.....	98
6.2.7	Pentlandite's sulfur high binding energy tail.....	99
6.3	Consistency of vacuum fracture method: Comparison to "Pn2".....	104
6.3.1	Pn2 Fe & Ni 2 <i>p</i> spectra.....	106
6.3.2	Sulfur 2 <i>p</i> spectra.....	108
6.3.3	Additional surface components.....	109
6.3.4	Pn2 valence band.....	112
6.4	Conclusions.....	114
6.5	References.....	115
7	ELECTRONIC STRUCTURE OF PRISTINE PENTLANDITE SURFACES	117
7.1	Introduction.....	117
7.2	Resonant valence band study of pentlandite electronic structure.....	117
7.2.1	Methods.....	118
7.2.2	Observation of Fe, Ni and S L edge NEXAFS spectra.....	122
7.2.3	Description of valence band for pentlandite.....	126
7.2.4	Resonant valence band spectra at the Fe 2 <i>p</i> absorption threshold.....	127
7.2.5	Resonant valence band spectra at the Ni 2 <i>p</i> absorption threshold.....	130
7.2.6	Conclusions from resonant valence band photoemission spectroscopy.....	132
7.3	Effect of stoichiometry on the valence band of pentlandite.....	133
7.3.1	Introduction.....	133
7.3.2	Methods.....	134
7.3.3	Comparison of survey and core level photoelectron spectra.....	136
7.3.4	Comparison of Fe _{4.2} Ni _{4.4} S _{8.3} and Fe _{3.6} Ni _{5.3} S _{8.1}	143
1.1.1	Comparison of Fe _{3.6} Ni _{5.3} S _{8.1} and Fe _{4.8} Ni _{3.9} S _{8.3} and Fe _{4.0} Ni _{4.9} S _{8.1}	147
7.4	Conclusion.....	151
7.5	References.....	153
8	PENTLANDITE SURFACES EXPOSED TO ENVIRONMENTAL CONDITIONS	157
8.1	Controlled oxidation of a stoichiometric pentlandite surface – 420 Langmuir H ₂ O vapour 157	
8.1.1	Methods.....	158
8.1.2	Survey spectrum for pentlandite dosed with H ₂ O vapour.....	159
8.1.3	Fe and Ni core-level spectra.....	160
8.1.4	S 2 <i>p</i> core-level spectrum.....	162
8.1.5	Valence band photoelectron spectra.....	166
8.1.6	Discussion.....	170
8.2	Polished pentlandite surfaces.....	171
8.2.1	Survey spectrum for polished pentlandite.....	171

8.2.2	S 2 <i>p</i> photoelectron spectrum for polished pentlandite.....	172
8.3	Surfaces of pentlandite exposed to pH 1 H ₂ SO ₄ for 1 hour	174
8.3.1	Survey spectrum for pentlandite in pH 1 H ₂ SO ₄	175
8.3.2	S 2 <i>p</i> photoelectron spectrum for pentlandite exposed to pH 1 H ₂ SO ₄ for 1 hour.....	176
8.3.3	Fe and Ni core-level spectra.....	178
8.4	Discussion and comparison of oxidised pentlandite samples	182
8.5	Conclusion.....	185
8.6	References	186
9	STXM – A NEW METHOD OF MINERALS ANALYSIS.....	188
9.1	Methods.....	190
9.2	Advantages and challenges of using STXM for minerals.....	191
9.2.1	Simple analysis reveals spatial distribution of species	192
9.2.2	Hydrated samples allow a degree of spatial freedom: the particles float.....	194
9.3	Effect of sample environment	196
9.3.1	Dry sample	196
9.3.2	Hydrated sample	199
9.4	Identification of minority species.....	202
9.4.1	Discussion of minority species	206
9.5	In situ capabilities.....	207
9.5.1	Quantification of mapped species	209
9.6	Conclusion.....	211
9.7	References	212
10	CONCLUSION.....	216
10.1	Future work	220

ABSTRACT

Transition metal sulfides have complex electronic structures which make them potentially useful as catalysts or for use in electronic devices. While photoemission spectroscopy is the best method to study these materials, accurate interpretation can be difficult for materials with complex electronic structures. With increasing interest in the applications of sulfides as catalysts, there is a growing need for clear and accurate interpretation of photoemission spectra. Improvements in sample preparation, resolution of spectroscopy techniques and recent developments of new spectromicroscopy techniques mean that the tools required to analyse surface electronic structure of minerals are more readily available. Increasing availability of these techniques is driving the necessity for improved understanding of the electronic structure and more accurate interpretations of spectra.

The original contribution to knowledge presented in this thesis is the advanced interpretation of photoemission spectra for pyrrhotite and pentlandite by the examination of electronic structure, and the subsequent enhanced ability to detect minority species on sulfide surfaces using photoemission spectroscopy and microscopy techniques. Empirical line shapes were defined for core level sulfur spectra for pyrrhotite (Fe_7S_8) and pentlandite ($[\text{Fe},\text{Ni}]_9\text{S}_8$), which allows additional surface species to be detected and quantified on reacted surfaces of these minerals. In addition to ultra-high vacuum spectroscopy techniques, scanning transmission X-ray microscopy is presented as a new method for sulfide analysis, which allows for the mapping of chemical species and detection of minority species on sulfide surfaces in oxidising conditions.

Photoemission spectroscopy was used with varied analysis depths to distinguish surface and bulk states on vacuum fracture surfaces of pyrrhotite and pentlandite. Pyrrhotite fracture surfaces were observed to form an undercoordinated surface monosulfide in addition to a disulfide and polysulfide species. Pentlandite fracture surfaces are interpreted to have two undercoordinated surface monosulfide species, which arise from the loss of at least one bonding partner as a result of fracture. Pentlandite's surface monosulfide species were seen to overlap with the bulk monosulfide species which has previously made the interpretation of pentlandite sulfur spectra difficult; however as a result of this study the correct interpretation is now provided. The difference in surface species reflect the polar and non-polar surfaces which are exposed on fracture surfaces of pyrrhotite and pentlandite, respectively.

By distinguishing the bulk line shapes of the core level spectra from the surface species, asymmetric line shapes were observed. Broadening on the high binding energy side of the sulfur spectra for both pyrrhotite and pentlandite were determined to originate from ligand to metal charge transfer final

states. These asymmetric line shapes were fitted with an empirical set of peaks, which subsequently enables the identification of minority surface species. These line shapes were vital for identifying and quantifying the surface species which result from oxidation of the samples.

The identification of minority species was further enhanced with the implementation of Scanning Transmission X-ray Microscopy (STXM). STXM is a novel spectromicroscopy technique, for investigating the changes to a mineral's surface species *in situ*, thus negating the requirement for UHV which may result in altered chemical states due to a change in environmental conditions. It was shown that the spatial resolution and chemical mapping ability of STXM was able to identify minority species on the mineral's surface which could not previously be distinguished from the bulk spectral contributions. This technique also provided the extended ability for *in situ* analysis of the electrochemical reduction of a mineral particle.

DECLARATION

I certify that this thesis does not incorporate without acknowledgment any material previously submitted for a degree or diploma in any university; and that to the best of my knowledge and belief it does not contain any material previously published or written by another person except where due reference is made in the text.

Signed.....

Date.....

ACKNOWLEDGEMENTS

My first and foremost thanks go to my primary supervisor Professor Sarah Hamer for her excellent guidance and support throughout this project. Since beginning research with her, she has provided excellent opportunities for data collection, knowledge development and personal and scientific growth. It has been a great pleasure to discuss ideas together and learn how to make strong scientific arguments. I am grateful for the opportunities this project has offered me, and the freedom Sarah has provided me to follow my curiosity and find satisfaction in problem solving. I would also like to acknowledge and thank my co-supervisor Professor Jamie Quinton for his continued support and feedback throughout my PhD. I am particularly thankful for his hard work and helpful comments on my writing during the drafting process. The knowledge and experience of both my supervisors has been invaluable to me; they make an excellent team. Their continual belief in my work and my ability has been a great motivator, especially as I approach completion.

I am deeply indebted to Professor Adam Hitchcock who has made significant contributions to my understanding of STXM analysis. On a number of occasions Adam has donated his time to assisting me and the research group with our analysis using Axis2000. I would like to acknowledge the time and resources provided by Professor Allan Pring and Dr Jing Zhao, notably for providing the equipment and training required to synthesise pentlandite samples, and for providing natural mineral samples along the way. Thanks to Allan also for the scientific and personal wisdom which he shared along the way. I gratefully acknowledge the assistance of Dr Benjamin Wade at Adelaide Microscopy for setting up microprobe analysis for the sulfides in this thesis and assisting with sample preparation.

The experiments in this thesis would not have been possible without the beamline staff who provided technical training, assistance, and guidance. I would like to acknowledge Dr Bruce Cowie, Dr Lars Thomsen and Dr Anton Tadich at the Australian Synchrotron soft X-ray beamline, Jian Wang at the Soft X-ray Spectromicroscopy beamline at the CLS, Lucia Zuin and Xiaoyu Cui at the VLS-PGM beamline also at the CLS, Canada, and Dr Der-Hsin Wei at the PEEM beamline at the NSRRC, Taiwan. I would especially like to thank the PEEM beamline staff and students who often stayed at the beamline during unsociable hours to assist with our analysis and made sure we had everything we needed. Special thanks to Canis and Tina who did their best to care for us when I was very unwell during experiments. A special thanks also to Dr Ben Watts at the PolLux beamline at SLS, Switzerland, for making the extra effort to make us feel welcome and well supported, and for sharing a few laughs with us while we were there.

I am grateful for the opportunity to start my PhD journey with the HERCULES synchrotron school in July 2015 at NSRRC, Taiwan. The lectures, tutorials and practical sessions were a wonderful formal introduction to synchrotron radiation science and were highly valuable to me as I considered my experiments and analysis during my project. I highly recommend any similar training program to future students or early career researchers. The lecturers, staff and particularly the fellow participants of HERCULES in Taiwan were one of the many highlights of the program. To all the friends I made at this school; you are very dear to me, and I hope to see you all again someday. 🐼

My completion of this thesis would not have been possible without the support and contributions from past and present members of the Harmer research group. I mention in particular Belinda Bleeze and Connor Retallick who I have had the great pleasure of sharing this journey with from the beginning of Honours. I would like to acknowledge their work with me collecting data at beamlines. There have been many flights and sleepless nights, and I thank you for your individual contributions to this work.

My deepest gratitude to Tom, who didn't choose the PhD, but has had to endure it regardless. Thank you for your love and patience and for supporting me through the best and the worst of it all. There are many personal friends and family who have contributed, sometimes in seemingly small ways, but I am grateful for you all. Thank you for your continued friendship, comfort and support; I truly could not have completed this without you

I acknowledge the contribution of the Australian Government Research Training Program Scholarship. This project was supported by the Australian Research Council funding (FT110100099). Travel to international synchrotrons was supported through the Australian Synchrotron International Synchrotron Access Plan (ISAP), specifically ISAP4141/8084, ISP9551, ISP12193 and 20-6273.

PUBLICATIONS

Journal Articles

Z.E. Pettifer, J.S. Quinton, W.M. Skinner, S.L. Harmer, New interpretation and approach to curve fitting synchrotron X-ray photoelectron spectra of (Fe,Ni)₉S₈ fracture surfaces, *Applied Surface Science*, 504 (2020) 144458.

Oral Presentations

Z.E. Pettifer, S.L. Harmer, *Developments in micro and spectromicroscopy techniques for studying mineral processing systems*, RACI Physical Chemistry Symposium, Flinders University City Campus, Adelaide, 8th December 2015.

Z.E. Pettifer, S.L. Harmer, *Using Scanning Transmission X-ray Microscopy (STXM) to detect fine changes in chalcocite surface chemical species*, RACI Physical Chemical Symposium, University of Adelaide, Adelaide, 24th November 2017.

Z.E. Pettifer, S.L. Harmer, *Surface speciation of pentlandite (Fe,Ni)₉S₈ by XPS*, Flinders University Institute for Nanoscale Science & Technology 9th Annual Conference, 18th June 2019.

Poster Presentations

Z.E. Pettifer, S.L. Harmer, *Photoemission electron microscopy (PEEM) for heterogeneous minerals*, Asia-Pacific Edition of HERCULES in Taiwan poster session, NSRRC, Hsinchu, Taiwan, 10th July 2015.

Z.E. Pettifer, S.L. Harmer, *Photoemission Electron Microscopy (PEEM) for Nanoscale Imaging of Heterogeneous Minerals*, International Conference on Nanoscience and Nanotechnology (ICONN), National Convention Centre, Canberra, 7th – 11th February 2016.

Z.E. Pettifer, S.L. Harmer, *Characterisation of chalcocite (Cu₂S) surface oxidation products using Scanning Transmission X-ray Microscopy*, Soft X-ray Microscopy Masterclass, Australian Synchrotron, Clayton, Victoria, 20th – 21st September 2018.

LIST OF FIGURES

Figure 2.1: Monoclinic structure of pyrrhotite. Blue: Fe atoms, grey: sulfur atoms. Iron vacancies occur in alternating planes parallel to the c-axis. The topmost iron layer in the shown structure is a lacunar plane.	8
Figure 2.2: Crystal structure of pentlandite M_9S_8 . Blue: cation sites, grey: sulfur sites.....	10
Figure 2.3: crystal field splitting of d orbitals in tetrahedral and octahedral coordination. In the example in the text, the green atom is iron, and the grey atoms are sulfur.....	11
Figure 3.1: Example of survey spectrum for oxidised pentlandite, including peak assignments, obtained with $h\nu = 1487$ eV.....	29
Figure 3.2: Schematic of photoelectron (e_p^-) and Auger decay (e_A^-) processes [4].....	30
Figure 3.3: Schematic diagram of the photoemission electron microscopy (PEEM) optics, from [http://efd.nsrcc.org.tw/EFD.php?num=242].	37
Figure 3.4: Schematic of key optical components of a STXM endstation.	38
Figure 4.1: Survey spectrum for pristine vacuum fractured monoclinic pyrrhotite which shows no evidence of carbon or oxygen contamination at the surface. $h\nu = 1487$ eV.	44
Figure 4.2: Vacuum fractured monoclinic pyrrhotite S $2p$ photoelectron spectra collected with $h\nu = 260$ eV, 846 eV, and 1487 eV.....	45
Figure 4.3: Difference spectrum calculated by subtracting S $2p$ 846 eV spectrum from 260 eV spectrum. The difference spectrum shows evidence of three doublet features labelled A, B and C.	47
Figure 4.4: Bulk peak shape obtained by subtracting the difference spectrum (Figure 4.3) from the 846 eV spectrum.	48
Figure 4.5: Sulfur $2p$ spectra for vacuum fractured monoclinic pyrrhotite, collected with $h\nu =$ (a) 260 eV, (b) 846 eV, and (c) 1487 eV, each fitted with asymmetric bulk peaks in addition to symmetric surface peaks as identified in Figure 4.3.....	49
Figure 4.6: (a) Bulk peak shape obtained by subtracting the difference spectrum (Figure 4.3) from the 846 eV spectrum, and sulfur $2p$ photoelectron spectra collected with a photon energy of (b) 1487 eV, (c) 846 eV, and (d) 260 eV, each fitted with additional peaks to account for the high binding energy tail and surface components where necessary.....	51
Figure 4.7: Sulfur $L_{2,3}$ NEXAFS spectrum for vacuum fractured monoclinic pyrrhotite showing a spin-orbit splitting of 1.3 eV.....	56
Figure 4.8: Fe $2p$ photoelectron spectrum for vacuum fractured pyrrhotite shows a broad Fe $2p_{3/2}$ peak at 707.7 eV. $h\nu = 846$ eV (blue, dotted), and 1487 eV (black, dashed).....	57
Figure 4.9: Fe $L_{2,3}$ NEXAFS spectrum for vacuum fractured pyrrhotite showing the L_3 peak at 706.8 eV with pre-edge peak at 705.1 eV.....	59
Figure 4.10: Pyrrhotite off-resonance ($h\nu = 695.5$ eV) valence band spectrum, showing Fe $3d$ states in the upper valence band, and S $3p$ and $3s$ states in the lower valence band. Key features are indicated by blue dotted lines at 0.25, 2.5, 3.8 and 6.0 eV.....	60
Figure 4.11: Pyrrhotite valence band spectra collected with photon energies across the Fe $2p$ absorption spectrum. A strong increase in seen in the lower valence band region at the absorption peak photon energy.	61
Figure 4.12: Resonant valence band spectra each with the off-resonance spectrum ($h\nu = 695.5$ eV) subtracted to show the constant LMM Auger feature moving through the spectra. The 705.1 – 713.5 eV spectra have been vertically offset for clarity.	63

Figure 4.13: Resonant valence band spectra collected with $h\nu = 695.5$ eV (black), 705.1 eV (red) and 706.8 eV (blue). The binding energy of highlighted features is shown above the spectra. The $h\nu = 695.5$ eV spectrum has been scaled $\times 10$. The features at 4.7 eV and 3.0 eV binding energy have been highlighted.	65
Figure 5.1: Survey spectra of polished monoclinic pyrrhotite and monoclinic pyrrhotite exposed to pH 1 H_2SO_4 for 1 hour, each obtained with $h\nu = 1487$ eV.	72
Figure 5.2: S 2 <i>p</i> photoelectron spectra for polished pyrrhotite and pyrrhotite in pH 1 H_2SO_4 collected with (a) $h\nu = 1487$ eV, and (b) $h\nu = 260$ eV. The S 2 <i>p</i> spectra from the fractured pyrrhotite sample of Chapter 4 have been included for comparison.	73
Figure 5.3: Fitted S 2 <i>p</i> spectra of polished monoclinic pyrrhotite collected with (a) $h\nu = 1487$ eV, and (b) $h\nu = 260$ eV fitted with a Shirley background [9], (c) fitted with a Tougaard background [10], and (d) fitted with a linear background.	75
Figure 5.4: Fe 2 <i>p</i> spectra for pyrrhotite exposed to pH 1 H_2SO_4 for 1 hour (black) and vacuum fractured (blue) monoclinic pyrrhotite from Chapter 4.	79
Figure 5.5: Fitted S 2 <i>p</i> spectra of monoclinic pyrrhotite exposed to pH 1 H_2SO_4 for 1 hour, collected with $h\nu =$ (a) 1487 eV and (b) 260 eV.	80
Figure 5.6: (a) Fe $L_{2,3}$ edge NEXAFS spectra for vacuum fractured pyrrhotite and pyrrhotite in pH 1 H_2SO_4 , (b) Oxygen K edge NEXAFS for pyrrhotite in pH 1 H_2SO_4	83
Figure 5.7: Images of monoclinic pyrrhotite surface after 1 hour in pH 1 H_2SO_4 , collected (a) below the iron absorption edge, (b) at the iron absorption edge (background removed) and (c) at the oxygen absorption edge (background removed). Field of view = 450 μm	84
Figure 6.1: Survey spectrum for vacuum fractured Pn1 sample, showing no apparent contribution from carbon or oxygen species, $h\nu = 1400$ eV.	90
Figure 6.2: (a) Fe 2 <i>p</i> XPS spectra of pristine pentlandite collected with $h\nu = 846$ eV, 1110 eV, and 1400 eV, (b) Ni 2 <i>p</i> XPS spectra collected with $h\nu = 1110$ eV, and 1400 eV.	91
Figure 6.3: S 2 <i>p</i> synchrotron X-ray photoelectron spectra collected from <i>in situ</i> fractured pentlandite ($Fe_{4.4}Ni_{4.6}S_8$) obtained with $h\nu =$ (a) 260 eV, (b) 400 eV, (c) 600 eV, (d) 846 eV, and (e) 1400 eV, each fitted with three symmetric doublets.	94
Figure 6.4: Residual signal from the Pn1 S 2 <i>p</i> spectra taken at each incident photon energy, after subtraction of the fitted spectra with three symmetric spin-orbit-split doublets.	95
Figure 6.5: (a) X-ray valence band spectra of <i>in-situ</i> fractured Pn1 collected at photon varied photon energies. (b) photoionization cross sections of selected atomic subshells, from [15]	96
Figure 6.6: (a) Pentlandite crystal structure terminated at the (110) fracture plane, (b) $h\nu = 260$ eV S 2 <i>p</i> spectrum fitted with three monosulfide components, and an asymmetric bulk tail, described in section 6.2.7.	99
Figure 6.7: Sulfur 2 <i>p</i> spectrum of pentlandite obtained with 1400 eV incident photon energy, fitted with three distinct features and the asymmetric tail shape described in Table 6.3.	101
Figure 6.8: Stack plot of S 2 <i>p</i> residual signal after subtracting the three tail peaks and fitted monosulfide species from each spectrum.	102
Figure 6.9: Difference between $h\nu = 260$ eV spectrum and $h\nu = 1400$ eV spectrum and $h\nu = 846$ eV spectrum respectively. All spectra are normalised to the bulk peak.	103
Figure 6.10: Survey spectrum of vacuum fractured “Pn2” obtained with $h\nu = 1600$ eV, indicating some small contribution from carbon and oxygen species.	104
Figure 6.11: Photoionization cross section of atomic subshells [15] used for approximate quantification of the XPS survey spectrum.	105

Figure 6.12: (a) Fe 3 <i>p</i> photoelectron spectra obtained with $h\nu = 850$ eV (red), 1050 eV (blue) and 1530 eV (black), and (b) Ni 2 <i>p</i> photoelectron spectra obtained with $h\nu = 1050$ eV (red), 1400 eV (blue), and 1600 eV (black).	107
Figure 6.13: (a) Fe L _{2,3} NEXAFS spectrum, (b) Ni L _{2,3} NEXAFS spectrum of Pn2.	108
Figure 6.14: Fitted sulfur 2 <i>p</i> spectra collected with $h\nu =$ (a) 260 eV, (b) 400 eV, (c) 600 eV, (d) 850 eV, and (e) 1050 eV.	109
Figure 6.15: Residual signal from subtracting fitted components from the S 2 <i>p</i> spectra in Figure 6.14.	110
Figure 6.16: Pn2 S 2 <i>p</i> spectra fitted with polymerised surface components in addition to the observed surface and bulk components.	111
Figure 6.17: X-ray valence band spectra of in situ fractured Pentlandite 2 obtained with $h\nu = 260, 400, 600, 1050$ and 1400 eV. Inset: Valence band spectra normalised to the upper valence band peak.	113
Figure 7.1: Binding energy calibration from Au 4 <i>f</i> _{7/2} reference spectra.	119
Figure 7.2: Survey spectrum of vacuum fractured pentlandite, $h\nu = 1487$ eV.	120
Figure 7.3: (a) Fe 2 <i>p</i> and (b) Ni 2 <i>p</i> spectra from three vacuum fractured pentlandite samples show the iron sites on the pentlandite surface are partly oxidised.	121
Figure 7.4: S 2 <i>p</i> spectrum for vacuum fractured pentlandite showing no evidence of polymerised sulfur, $h\nu = 1475$ eV.	122
Figure 7.5: Fe L _{2,3} absorption spectrum for vacuum fractured pentlandite shows evidence of both Fe ^{II} and Fe ^{III} components.	123
Figure 7.6: Ni L _{2,3} absorption spectrum for vacuum fractured pentlandite shows a broad contribution due to multiplet structure arising from Ni-S covalency.	124
Figure 7.7: S L _{2,3} absorption spectrum for vacuum fractured pentlandite.	125
Figure 7.8: Pentlandite valence band photoelectron spectrum, $h\nu = 695.6$ eV.	126
Figure 7.9: Photoelectron spectra collected with photon energies across the Fe 2 <i>p</i> absorption spectrum show an increase in intensity of the lower valence band at photon energies at and above the L ₃ absorption peak.	127
Figure 7.10: Photoelectron spectra collected with $h\nu = 695.6$ eV (off-resonance), 705.2 eV (pre-edge) and 706.8 eV (peak energy). The binding energies of specific features are labelled above the graph in eV.	128
Figure 7.11: Resonant valence band spectra each with the off-resonance spectrum ($h\nu = 695.6$ eV) subtracted to show the constant kinetic energy Auger feature moving through the spectra. The 705.2 – 708.2 eV spectra have been vertically offset for clarity.	129
Figure 7.12: Photoelectron spectra collected with photon energies across the Ni 2 <i>p</i> absorption spectrum show a strong increase in intensity for photon energies at and above the L ₃ absorption edge.	130
Figure 7.13: Photoelectron spectra collected with $h\nu = 845.9$ eV (off-resonance), 851.8 eV (pre-edge) and 853.0 eV (peak energy). The binding energies of specific features are labelled above the graph in eV.	131
Figure 7.14: Resonant valence band spectra collected with photon energies over the Ni absorption edge each with the off-resonance spectrum ($h\nu = 845.9$ eV) subtracted to show the constant kinetic energy Auger feature moving through the spectra.	132
Figure 7.15: Ternary plot showing the stoichiometry of pentlandite samples used in this chapter as a proportion of sulfur, iron and nickel.	135

Figure 7.16: Photoionization cross section of valence level atomic subshells [40].....	136
Figure 7.17: Survey spectra for the four pentlandite samples: (i) $\text{Fe}_{4.2}\text{Ni}_{4.4}\text{S}_{8.3}$, (ii) $\text{Fe}_{3.6}\text{Ni}_{5.3}\text{S}_{8.1}$, (iii) $\text{Fe}_{4.8}\text{Ni}_{3.9}\text{S}_{8.3}$, (iv) $\text{Fe}_{4.0}\text{Ni}_{4.9}\text{S}_{8.1}$. Si contamination is only observed in (i). For each spectrum, $h\nu = 240$ eV.	137
Figure 7.18: (a) Fe/Ni 3 <i>p</i> spectra with background removed for $h\nu = 150$ eV and 240 eV, showing changes to Fe and Ni species at the surface. (b) Fitted S 2 <i>p</i> spectra showing sulfur species present at the surface. (i) $\text{Fe}_{4.2}\text{Ni}_{4.4}\text{S}_{8.3}$, (ii) $\text{Fe}_{3.6}\text{Ni}_{5.3}\text{S}_{8.1}$, (iii) $\text{Fe}_{4.8}\text{Ni}_{3.9}\text{S}_{8.3}$, (iv) $\text{Fe}_{4.0}\text{Ni}_{4.9}\text{S}_{8.1}$	139
Figure 7.19: Photoemission spectra in the valence band region for (a) $\text{Fe}_{4.2}\text{Ni}_{4.4}\text{S}_{8.3}$ normalised to constant flux and (b) normalised to the main peak, and (c) $\text{Fe}_{3.6}\text{Ni}_{5.3}\text{S}_{8.1}$ normalised to constant flux and (d) normalised to the main peak.	144
Figure 7.20: Photoelectron spectra of the valence band region of (a) Pn1 and (b) Pn2, normalised to the main peak at 1.1 eV. The change in the relative intensities of the lower valence band between the two samples is attributed to polymerised sulfur.....	145
Figure 7.21: Photoemission spectra in the valence band region for (a) $\text{Fe}_{4.2}\text{Ni}_{4.4}\text{S}_{8.3}$ and (b) $\text{Fe}_{3.6}\text{Ni}_{5.3}\text{S}_{8.1}$ collected with $h\nu = 30, 35, 40,$ and 50 eV. The background in the $\text{Fe}_{4.2}\text{Ni}_{4.4}\text{S}_{8.3}$ valence band spectra is attributed to Si contamination.	147
Figure 7.22: Pentlandite photoemission spectra in the valence band region for (a) $\text{Fe}_{3.6}\text{Ni}_{5.3}\text{S}_{8.1}$ normalised to constant flux and (b) normalised to the main peak, (c) $\text{Fe}_{4.8}\text{Ni}_{3.9}\text{S}_{8.3}$ normalised to constant flux and (d) normalised to the main peak, and (e) $\text{Fe}_{4.0}\text{Ni}_{4.9}\text{S}_{8.1}$ normalised to constant flux and (f) normalised to the main peak.....	148
Figure 7.23: Photoemission spectra in the valence band region of (a) $\text{Fe}_{3.6}\text{Ni}_{5.3}\text{S}_{8.1}$, (b) $\text{Fe}_{4.8}\text{Ni}_{3.9}\text{S}_{8.3}$ and (c) $\text{Fe}_{4.0}\text{Ni}_{4.9}\text{S}_{8.1}$ collected with $h\nu = 30, 35, 40,$ and 50 eV show a striking difference between the $\text{Fe}_{4.0}\text{Ni}_{4.9}\text{S}_{8.1}$ valence band spectrum, which is largely attributed to sulfate species, and the $\text{Fe}_{3.6}\text{Ni}_{5.3}\text{S}_{8.1}$ and $\text{Fe}_{4.8}\text{Ni}_{3.9}\text{S}_{8.3}$ valence band spectra.	151
Figure 8.1: Photoionization cross sections of valence level atomic subshells [15].	159
Figure 8.2: Survey spectrum for synthetic stoichiometric pentlandite after fracture in nitrogen filled glove bag (fresh) and after 420 Langmuir controlled dosing with H_2O vapour (dosed). $h\nu = 240$ eV.	160
Figure 8.3: Fe/Ni 3 <i>p</i> spectra with background removed for $h\nu = 150$ eV (black) and $h\nu = 240$ eV (blue) from (a) fresh pentlandite ($\text{Fe}_{4.2}\text{Ni}_{4.4}\text{S}_{8.3}$) (reproduced from Chapter 7) and (b) dosed pentlandite, showing a significant difference in both Fe and Ni structure at the surface in comparison to the bulk species.	162
Figure 8.4: S 2 <i>p</i> photoelectron spectrum for pentlandite dosed with 420 Langmuir of H_2O vapour. $h\nu = 240$ eV. “Fresh” pentlandite refers to the $\text{Fe}_{4.2}\text{Ni}_{4.4}\text{S}_{8.3}$ sample prior to dosing, repeated from Chapter 7.....	163
Figure 8.5: Difference spectrum calculated by subtracting the S 2 <i>p</i> spectrum of the fresh pentlandite sample from the S 2 <i>p</i> spectrum collected for the dosed sample. The negative peaks indicate a decrease in 4-coordinate monosulfide species, while the positive peaks show an increase in sulfur-oxy species.	166
Figure 8.6: Photoelectron spectra in the valence band region for (a) $\text{Fe}_{4.2}\text{Ni}_{4.4}\text{S}_{8.3}$ fractured in a nitrogen glove bag, (b) the same sample after 420 Langmuir H_2O vapour dosing, and (c) $\text{Fe}_{4.8}\text{Ni}_{3.9}\text{S}_{8.3}$. The $\text{Fe}_{4.2}\text{Ni}_{4.4}\text{S}_{8.3}$ and $\text{Fe}_{4.8}\text{Ni}_{3.9}\text{S}_{8.3}$ samples were discussed in the previous chapter and are included here for comparison. $h\nu = 240$ eV (blue) and 150 eV (red).	167
Figure 8.7: Photoelectron spectra in the valence band region collected with $h\nu = 30 - 50$ eV for (a) Stoichiometric pentlandite ($\text{Fe}_{4.2}\text{Ni}_{4.4}\text{S}_{8.3}$) fractured in a nitrogen glove bag, (b) the same sample after 420 Langmuir H_2O vapour dosing, and (c) $\text{Fe}_{4.0}\text{Ni}_{4.9}\text{S}_{8.1}$. The $\text{Fe}_{4.2}\text{Ni}_{4.4}\text{S}_{8.3}$ and $\text{Fe}_{4.0}\text{Ni}_{4.9}\text{S}_{8.1}$ samples were discussed in section 7.3 and are included here for comparison.	169

Figure 8.8: Survey spectrum for synthetic pentlandite surfaces, $h\nu = 1487$ eV.	172
Figure 8.9: S 2 <i>p</i> photoelectron spectra collected from polished pentlandite sample, with $h\nu =$ (a) 1487 eV, and (b) 260 eV.	173
Figure 8.10: Survey spectrum for synthetic pentlandite surfaces, $h\nu = 1487$ eV.	176
Figure 8.11: S 2 <i>p</i> photoelectron spectra collected from the sample of pentlandite in pH 1 H ₂ SO ₄ for 1 hour, with $h\nu =$ (a) 1487 eV, and (b) 260 eV.	177
Figure 8.12: (a) Fe 2 <i>p</i> spectrum and (b) Ni 2 <i>p</i> spectrum for pentlandite exposed to pH 1 H ₂ SO ₄ for 1 hour, compared to "Pn1" and "Pn2" from Chapter 6.	179
Figure 8.13: (a) Fe L _{2,3} absorption spectrum, (b) Ni L _{2,3} absorption spectrum for pentlandite in pH 1 H ₂ SO ₄ solution for 1 hour.	180
Figure 8.14: PEEM images collected at photon energies corresponding to (a) Fe L ₃ peak (706.8 eV), (b) Fe L ₃ shoulder (708.2 eV) (c) Ni L ₃ peak (853.2 eV).	181
Figure 9.1: (a) Transmission image of chalcocite particle collected at 926.5 eV, just below the Cu L ₃ absorption edge. (b) Optical density image of chalcocite particle. (c) Cu L _{2,3} absorption spectrum averaged over the blue line indicated in (b); inset spectrum is the external I ₀ signal used to convert the spectrum to OD.	193
Figure 9.2: Image of chalcocite particles converted to optical density, collected with a photon energy of (a) 931.3 eV, (b) 932.4 eV, (c) 935.2 eV, and (d) RGB overlay of (a), (b), and (c) respectively. Scale = 1 μm.	193
Figure 9.3: Schematic of sample holder for hydrated samples.	194
Figure 9.4: OD images of chalcocite particle in solution, in temporal order, showing the particle floating off the field of view.	195
Figure 9.5: (a) Average stack image of chalcocite particle exposed to H ₂ SO ₄ . (b) regions from which spectra are collected. (c) Cu L edge spectra collected from the regions of interest in (b).	196
Figure 9.6: (a): internal spectra mapped to the stack, (b) mapped regions of (i) Cu ^I – chalcocite species (ii) Cu ^{II} species (iii) saturated region, (c) overlaid RGB image of the mapped regions in (b).	197
Figure 9.7: (a) image from residual stack showing intensity of poorly fit region near 932.2 eV, (b) mask generated from image in (a), used to isolate the average spectrum from those regions in the stack, (c) spectrum generated from the regions indicated in the mask in (b), plotted against the spectra from Figure 9.6.	197
Figure 9.8: (a) Mapped regions of (i) Cu ^I – chalcocite, (ii) Cu ^{II} , and (iii) regions poorly fit due to changes in pre-edge peak height. (b) RGB overlaid image of the three regions shown in (a).	198
Figure 9.9: (a) broad scan image of chalcocite particle in solution, (b) C K edge and Cu L edge spectra collected from the line indicated in (a), (c) location of the spectra along the line scans.	199
Figure 9.10: (a) average image from Cu L edge stack, (b) internal spectra used for fitting. Blue spectrum show saturated signal due to sample thickness.	200
Figure 9.11: (a) mapped regions of (i) Cu ^I - chalcocite, (ii) Cu ^{II} , (iii) saturated Cu species, (b) RGB overlaid image of the mapped regions shown in (a).	201
Figure 9.12: Large scale low resolution images in transmission mode of a liquid cell. Grey regions indicate greater absorption associated with the likely presence of solution.	203
Figure 9.13: (a) Transmission image of particles used for the analysis, (b) average spectrum over the stack.	204
Figure 9.14: (a) Cu L edge spectra mapped to the stack, (b) mapped regions of (i) Cu ^I similar to chalcocite, (ii) Cu ^{II} , (iii) mixed Cu ^I and Cu ^{II} signal, (c) RGB overlay of the images from (b).	205

Figure 9.15: Spectrum of high residual region (solid, black), plotted against the Cu^I signal (dotted, red), showing difference in relative peak heights.206

Figure 9.16: (a) WE = working electrode, RE = reference electrode, CE = counter electrode, (b) internal signals collected from the stack, (c) RGB overlay of mapped internal signals.208

Figure 9.17: (a) three spectra collected from the stack representing Cu^{II}, Cu^I chalcocite, and Cu⁰, (b) mapped regions of (i) Cu^I, (ii) Cu^{II}, and (iii) Cu⁰, (c) RGB overlay of three mapped signals.....209

Figure 9.18: (a) calculated X-ray parameters for Cu metal, CuO, and Cu₂S, with the volume densities assumed for each material. (b) OD1 spectra normalised to the calculated intensity for 1 nm material.210

Figure 9.19: RGB overlaid image of quantitative mapped CuO, Cu₂S, and Cu metal species, showing approximate thicknesses of the areas indicated.211

LIST OF TABLES

Table 3.1: Estimated proportion and percentage of the signal which originates from the first monolayer (<i>Rs</i>) of pyrrhotite and pentlandite surfaces, respectively, calculated for each photoelectron spectrum.....	32
Table 4.1: Peak contributions to sulfur 2 <i>p</i> spectra of pristine pyrrhotite, fitted with asymmetric bulk peaks.....	50
Table 4.2: Peak parameters for symmetric peaks fitting the high binding energy tail of bulk pyrrhotite, relative to the bulk 2 <i>p</i> _{3/2} peak.....	51
Table 4.3: Peak contributions to the pyrrhotite sulfur 2 <i>p</i> spectra fitted with empirical tail shapes. The “% contribution from asymmetric fit” data is taken from	52
Table 5.1: Atomic % elements for the samples of polished pyrrhotite and pyrrhotite in pH 1 H ₂ SO ₄ for 1 hour.....	72
Table 5.2: Fitted components of the polished monoclinic S 2 <i>p</i> spectrum, including the binding energy (BE), peak width (FWHM), % contribution represents the contribution of that species to each spectrum, with Tougaard background removal(T), and linear background removal (L), and overall atomic % contribution calculated from the <i>hν</i> = 1487 eV spectrum.....	77
Table 5.3: Fitted components of the S 2 <i>p</i> spectra of monoclinic pyrrhotite in pH 1 H ₂ SO ₄ for 1 hour. The binding energy (BE), peak width (FWHM), % contribution to the fit for both <i>hν</i> = 1487 eV and 260 eV spectra, and overall atomic % contribution to the sample calculated from the <i>hν</i> = 1487 eV spectrum.	82
Table 6.1: Approximate quantification from the <i>hν</i> = 1400 eV survey spectrum for Pn1.....	90
Table 6.2: Contribution of each component to the fitted S 2 <i>p</i> spectra, and estimated contribution from the first monolayer for each spectrum.....	93
Table 6.3: Parameters used for the three peaks used to fit the tail region. Values are relative to the bulk peak at 162.2 eV.	100
Table 6.4: Quantification of the percentage contribution of each feature to the fit, with the 5-coordinate bulk peak fitted with the empirically-derived asymmetric tails described in Table 6.3.	104
Table 6.5: Approximate atomic % contribution of species for the <i>hν</i> = 1600 eV survey spectrum.	105
Table 6.6: Contribution from each of the features to the fitted spectra shown in Figure 6.14. The tail components are included in the bulk 5-coordinate contribution.....	109
Table 6.7: Contribution from each of the features to the fitted spectra shown in Figure 6.16. The tail components are included in the bulk 5-coordinate contribution.....	111
Table 7.1: Au 4 <i>f</i> _{7/2} reference for energy calibration.	119
Table 7.2: Atomic % contribution from species to survey spectrum shown in Figure 7.2.....	120
Table 7.3: Quantification of % contribution of each feature to the fitted S 2 <i>p</i> spectrum.	122
Table 7.4: Binding energy and % contribution to fitted S 2 <i>p</i> spectrum for each sample.	141
Table 7.5: Overview of observations of survey and core level spectra for pentlandite samples.	142
Table 8.1: Quantification of sulfur species fitted to S 2 <i>p</i> spectrum in Figure 8.4, including the quantification of sulfur species for Fe _{4.2} Ni _{4.4} S _{8.3} before dosing. “%” represents the contribution to the fit.	165
Table 8.2: Quantification of species observed in the survey spectrum for the polished synthetic pentlandite surface shown in Figure 8.8.	172

Table 8.3: Binding energy, peak width, and % contribution from each species fitted to the $h\nu = 1487$ eV and 260 eV S $2p$ spectra shown in Figure 8.9. Binding energy and peak width (FWHM) are reported in units of eV.	174
Table 8.4: Quantification of species observed in survey spectrum for the surface of synthetic pentlandite in pH 1 H_2SO_4 shown in Figure 8.10. The quantification from the polished sample is included for comparison. These values are taken from Table 8.2.	176
Table 8.5: Binding energy, peak width, and % contribution from each species fitted to the $h\nu = 1487$ eV and 260 eV S $2p$ spectra shown in Figure 8.11. Binding energy and peak width (FWHM) are reported in units of eV.	178

1 INTRODUCTION

Transition metal sulfides have typically been valued for their economic and environmental impact, as a large proportion of economically important metals are bound up in the earth's crust as sulfide ores. This is of particular interest for Australia which has large mineral deposits, and where mining export in 2018 amounted to over \$200 billion and 8.4% of the gross domestic product [1]. Separating the valuable minerals from the gangue is an important step in the metal refinement process and requires a good understanding of the surface structures of mineral phases. Sulfide minerals are also highly reactive and are subsequently large contributors to acid mine drainage. As the sulfidic rock is exposed during the mining process, oxygen and water oxidises the sulfide minerals to produce sulfuric acid which contains high concentrations of heavy metals and other toxic elements [2]. In addition to the economic and environmental impacts of mining sulfide ores, many sulfide minerals have interesting crystal structures and electronic properties, and most are considered small band gap semiconductors. With an ever increasing demand for cheap and clean energy production, attention is turning to metal sulfide structures as a viable alternative for catalysts and photocatalysts [3, 4], specifically for harvesting solar energy for water splitting [4-6]. To effectively utilise these mineral structures in such devices, and to efficiently separate natural mineral phases from mined ore bodies, a detailed understanding is required of the surface structures and electronic structures of these materials, and the reactions that take place on their surfaces.

X-ray spectroscopies such as X-ray photoelectron spectroscopy and X-ray absorption spectroscopy are advantageous for investigating changes to electronic structure. Since the shape and intensity of these spectra depend on the band structure of the mineral, they are highly sensitive to changes in oxidation state, ligand binding, and local coordination. X-ray photoelectron spectroscopy is considered a near surface technique and is therefore the best available technique to investigate changes to the electronic structure, and oxidation species on the surfaces of minerals. However, correct interpretation of transition metal sulfide spectra is non-trivial and is often overlooked in studies seeking to use photoelectron spectroscopy as a simple characterisation tool. This is particularly pressing for the primary nickel bearing sulfide pentlandite ($[\text{Fe,Ni}]_9\text{S}_8$), which has received recent interest for its use as a catalyst for the hydrogen evolution reaction [7-13]. Continuing confusion regarding the interpretation of pentlandite photoelectron spectra in particular is driving the need for studies devoted to accurate and detailed interpretation of spectra and identification of surface species.

Chapter 1: Introduction

Detailed interpretation of X-ray spectra of transition metal chalcogenides has historically been difficult for a number of reasons. Sample preparation techniques have been limited for the highly reactive sulfides, as some surface oxidation prior to analysis has been unavoidable. Consequently, there is an unknown amount of oxidised surface species contributing to the spectra, which masks the bulk contribution. The limited spectral resolution available to many prior studies has also obscured the bulk signal, as the contributions from multiple surface states overlap with each other and the bulk component, contributing to the difficulty in correctly interpreting core level spectra. Bulk components of photoelectron spectra of transition metal chalcogenides are also seen to have unusual line shapes and additional features which arise from final state effects caused by electron correlation between the core hole and the valence electrons. These effects are difficult to predict with electronic structure calculations and therefore require detailed analysis of the valence band to justify and explain the origin thereof. The ability to prepare samples by fracturing within ultra-high vacuum and transfer them directly to an analysis chamber ensures the samples are as pristine as possible. Also, recent developments in analysis techniques, notably with the addition of a synchrotron radiation photon source and improved analysers, provides greater spectral resolution to existing spectroscopy techniques. These notable improvements make a more detailed interpretation of core level spectra possible.

While pristine mineral surfaces are highly advantageous for detailed investigations into electronic structures, these are not characteristic of the mineral surfaces found in nature or in applications such as catalysts. Therefore, it is also necessary to study mineral surfaces in environmental conditions such as exposed to air, or solutions, to understand how the surfaces change in conditions relevant to mineral separation or catalytic applications. Comparing photoelectron spectra of oxidised minerals to spectra of pristine minerals is a good method for investigating changes to surfaces and has been used extensively for this purpose. However, these analyses must be completed in ultra-high vacuum, and assume that there is minimal change to the surface between removing the mineral from the oxidative conditions and analysing it. The other major limitation of surface spectroscopy techniques is that the results are averaged over an area which contains multiple species, and therefore the spatial distribution of the detected species is not known, and minority species are potentially not detected. There is a need for new techniques which are able to resolve the spatial distribution of chemical species, which thereby enable detection of minority species.

1.1 Thesis structure and aims

The aim for this thesis is to develop the interpretation of X-ray photoemission spectra and X-ray absorption spectra for the transition metal sulfide minerals pyrrhotite (Fe_7S_8) and pentlandite

Chapter 1: Introduction

([Fe,Ni]₉S₈), which are often closely intergrown in nature. Chapter 2 of this thesis provides a literature review into previous interpretations of X-ray photoelectron spectroscopy (XPS) and X-ray absorption spectroscopy of transition metal chalcogenides. It discusses the methods used to improve interpretations and examples of how these techniques have been used to develop our understanding of mineral surfaces under environmental conditions. Chapter 3 details the methods used in the experimental sections of this thesis, including a brief description of each of the techniques, sample preparation, and instrumental details for each technique.

The experimental chapters begin at Chapter 4, with a detailed investigation of a pristine vacuum fractured surface of monoclinic pyrrhotite (Fe₇S₈). X-ray photoelectron spectroscopy (XPS) is used primarily to identify the surface species on pristine fracture surfaces and distinguish the bulk line shape from the surface components. Resonance valence band spectroscopy is used to investigate the electronic structure of the sample to provide an explanation for the bulk line shapes identified in the photoelectron spectra. This chapter gives the first detailed explanation for the asymmetric bulk line shape observed for pyrrhotite core level spectra, and clearly distinguishes the bulk sulfide line shape from surface species.

Chapter 5 makes use of the interpretation developed in Chapter 4 when surfaces of oxidised pyrrhotite sample are investigated using photoelectron spectroscopy. This chapter reveals the surface structure of pyrrhotite after oxidation in air, and exposure to acidic conditions and discusses the development of the surface structure, and the effect on the photoelectron spectra.

Chapter 6 investigates the surfaces of two pristine pentlandite vacuum fractured surfaces and reveals the surface species formed upon fracture. This is significant for the interpretation of pentlandite photoelectron spectra and resolves the contentious assignment of sulfur species which has been discussed in previous literature. Part of this chapter has been published in Applied Surface Science (Z.E. Pettifer, J.S. Quinton, W.M. Skinner, S.L. Harmer, New interpretation and approach to curve fitting synchrotron X-ray photoelectron spectra of (Fe,Ni)₉S₈ fracture surfaces, Applied Surface Science, 504 (2020) 144458).

The valence band of pristine pentlandite is investigated experimentally for the first time in Chapter 7. These experiments aim to identify the origin of the broad asymmetric line shape of the core level photoelectron spectra, and also investigate changes seen in the pentlandite valence band as a result of changes to the mineral's stoichiometry. This is necessary to develop an understanding of the

Chapter 1: Introduction

electronic structure of this mineral phase and justify the bulk line shapes applied in Chapter 6, which will aid future applications of pentlandite as a catalyst.

Chapter 8 investigates the interaction of water vapour with the surface of pentlandite to understand how surface oxidation reactions occur for this mineral phase. This chapter then examines more extensive oxidation by exposure of pentlandite to air and acidic solution. The newly developed interpretation of core level and valence band photoelectron spectra highlights how these environmental conditions affect the pentlandite surfaces and how these changes are observed in photoelectron spectra. This has significant implications for future studies where oxidised pentlandite surfaces are used as catalysts and will aid in understanding how the surfaces change in similar conditions.

Chapter 9 extends the current analytical methods to include a new and emerging microspectroscopy technique, which until this thesis, has not been used for sulfide minerals. Therefore, Chapter 9 presents a new chemical mapping method for sulfide minerals, with a discussion about the challenges faced when applying this method to minerals, with suggestions of how to overcome such challenges, and examples of the possibilities available for similar studies. This is a significant development for sulfide analysis, since the analytical techniques used in Chapters 4 – 8 require ultra-high vacuum, and the effect of this vacuum on the surface components is not distinctly known. Therefore, the purpose of Chapter 9 is to provide an additional technique to evaluate the effect of the chamber environment on the observed surface species. Chapter 9 concludes with an example of the future of this technique, to analyse the electrochemical reduction of a mineral particle *in situ*, thereby showing the flexibility of this new technique.

1.2 References

- [1] A. Senior, A. Britt, D. Summerfield, A. Hughes, A. Hitchman, A. Cross, D. Champion, D. Huston, E. Bastrakov, M. Sexton, J. Moloney, J. Pheeney, A. Schofield, Australia's Identified Mineral Resources 2019, Geoscience Australia, Canberra, (2020).
- [2] A. Akcil, S. Koldas, Acid Mine Drainage (AMD): causes, treatment and case studies, *Journal of Cleaner Production*, 14 (2006) 1139-1145.
- [3] K. Zhang, L. Guo, Metal sulphide semiconductors for photocatalytic hydrogen production, *Catalysis Science & Technology*, 3 (2013) 1672-1690.
- [4] P. Yadav, P.K. Dwivedi, S. Tonda, R. Boukherroub, M.V. Shelke, Metal and Non-metal Doped Metal Oxides and Sulfides, in: M. Naushad, S. Rajendran, E. Lichtfouse (Eds.) *Green Photocatalysts*, Springer International Publishing, Cham, 2020, pp. 89-132.
- [5] T.-T. Zhuang, Y. Liu, Y. Li, Y. Zhao, L. Wu, J. Jiang, S.-H. Yu, Integration of Semiconducting Sulfides for Full-Spectrum Solar Energy Absorption and Efficient Charge Separation, *Angewandte Chemie International Edition*, 55 (2016) 6396-6400.

- [6] A.B. Laursen, S. Kegnæs, S. Dahl, I. Chorkendorff, Molybdenum sulfides—efficient and viable materials for electro - and photoelectrocatalytic hydrogen evolution, *Energy & Environmental Science*, 5 (2012) 5577-5591.
- [7] Y.X. Zhou, H.B. Yao, Y. Wang, H.L. Liu, M.R. Gao, P.K. Shen, S.H. Yu, Hierarchical Hollow Co₉S₈ Microspheres: Solvothermal Synthesis, Magnetic, Electrochemical, and Electrocatalytic Properties, *Chemistry – A European Journal*, 16 (2010) 12000-12007.
- [8] M. Al-Mamun, Y. Wang, P. Liu, Y.L. Zhong, H. Yin, X. Su, H. Zhang, H. Yang, D. Wang, Z. Tang, H. Zhao, One-step solid phase synthesis of a highly efficient and robust cobalt pentlandite electrocatalyst for the oxygen evolution reaction, *Journal of Materials Chemistry A*, 4 (2016) 18314-18321.
- [9] B. Konkena, K.J. Puring, I. Sinev, S. Piontek, O. Khavryuchenko, J.P. Dürholt, R. Schmid, H. Tüysüz, M. Muhler, W. Schuhmann, U.-P. Apfel, Pentlandite rocks as sustainable and stable efficient electrocatalysts for hydrogen generation, *Nature Communications*, 7 (2016) 12269.
- [10] I. Zegkinoglou, A. Zendegani, I. Sinev, S. Kunze, H. Mistry, H.S. Jeon, J. Zhao, M.Y. Hu, E.E. Alp, S. Piontek, M. Smialkowski, U.-P. Apfel, F. Körmann, J. Neugebauer, T. Hickel, B. Roldan Cuenya, Operando Phonon Studies of the Protonation Mechanism in Highly Active Hydrogen Evolution Reaction Pentlandite Catalysts, *Journal of the American Chemical Society*, 139 (2017) 14360-14363.
- [11] S. Piontek, C. Andronesco, A. Zaichenko, B. Konkena, K.j. Puring, B. Marler, H. Antoni, I. Sinev, M. Muhler, D. Mollenhauer, B.R. Cuenya, W. Schuhmann, U.-P. Apfel, Influence of the Fe:Ni Ratio and Reaction Temperature on the Efficiency of (Fe_xNi_{1-x})₉S₈ Electrocatalysts Applied in the Hydrogen Evolution Reaction, *ACS Catalysis*, 8 (2018) 987-996.
- [12] Y. Tang, H. Yang, J. Sun, M. Xia, W. Guo, L. Yu, J. Yan, J. Zheng, L. Chang, F. Gao, Phase-pure pentlandite Ni_{4.3}Co_{4.7}S₈ binary sulfide as an efficient bifunctional electrocatalyst for oxygen evolution and hydrogen evolution, *Nanoscale*, 10 (2018) 10459-10466.
- [13] Q. Hu, G. Li, X. Liu, B. Zhu, G. Li, L. Fan, X. Chai, Q. Zhang, J. Liu, C. He, Coupling pentlandite nanoparticles and dual-doped carbon networks to yield efficient and stable electrocatalysts for acid water oxidation, *Journal of Materials Chemistry A*, 7 (2019) 461-468.

2 LITERATURE REVIEW: LOOKING BEYOND THE EARTH'S CRUST TO SEE THE CRYSTAL STRUCTURES WITHIN

2.1 Transition metal chalcogenides

Transition metal chalcogenides form a large group of substances containing transition metal ions bonded to group VI elements, known as the chalcogenides: most commonly oxides and sulfides. Transition metal oxides and sulfides constitute a large proportion of mineral deposits in the Earth's crust and are a major source of transition metals. The valuable mineral phases are often intergrown with other less valuable phases, and their effective separation is a critical step in extracting the valuable metals from the ores. In addition to their value as natural resources, transition metal chalcogenides are of increasing significance due to their interesting crystal structures, electronic properties, and potential for application in novel electronic devices. Transition metal chalcogenides, and sulfides in particular, due to their stability and semiconducting nature have recently been highlighted as potential catalysts for reactions such as the hydrogen evolution or oxygen evolution reactions [1-3].

Understanding and accurately characterising the surface electronic structure of these materials is of critical importance for their application as catalysts, and implications for the efficient separation and beneficiation of these naturally occurring minerals. Photoelectron spectroscopy is commonly used to characterise surface chemistry of metal sulfides for mineral separation studies (ref [4], and references within), and is increasingly being applied to transition metal sulfides synthesised for catalyst studies [5]. Unfortunately, too often the interpretation of photoelectron spectra is oversimplified or misinterpreted, and consequently either critical information is overlooked [6-9], or the misinterpretation of spectra produces erroneous results [9, 10]. An accurate and detailed interpretation of photoelectron spectra requires a good understanding and careful consideration of the crystal structure and the electronic structure of the material, as small changes to the structure can result in perplexing features in the spectra.

Pentlandite is the major naturally occurring nickel bearing sulfide ore, and is often closely intergrown with pyrrhotite, amongst other phases. As the global demand for nickel steadily increases, the need to refine low grade nickel bearing sulfide deposits becomes more pressing [11]. Froth flotation is the method used to separate pyrrhotite from pentlandite and relies on the difference in surface hydrophobicity between the mineral phases to effectively separate them [12, 13]. Formation of hydrophobic polysulfide species, or hydrophilic species such as oxyhydroxide species and the distribution of these species across the surface plays a key role in the flotability of the mineral phase.

Therefore, understanding the surfaces of these minerals, and the reactions they undergo is important for their separation for metal extraction, and for their application as catalysts.

2.2 Pyrrhotite

Pyrrhotites are the second most common iron sulfides found in nature, second only to pyrite (FeS_2). It is not considered to be an economically important mineral, except in the need to separate it from other valuable mineral phases. Pyrrhotite is commonly found intergrown with other minerals and is considered to be an unfavourable phase in sulfide ores. It is the most sulfur-containing phase, and its removal is critical for minimising SO_2 production, and reducing the potential for sulfuric acid production within mining waste [14].

The pyrrhotite crystal structure is based on the NiAs structure, which varies with iron deficiencies in the lattice. The Fe rich endmember of the pyrrhotite series is troilite (FeS) which is found primarily in meteorites due to the high temperatures of formation [15]. Troilite has a stoichiometric hexagonal structure, based on close packed layers of alternating iron and sulfur atoms, sometimes with other transition metals such as Ni or Co in place of Fe in the structure. In general, pyrrhotite has a variable structure, which arises from ordered vacancies of iron in the lattice, resulting in super cell structures. The general formula for pyrrhotite is Fe_{1-x}S , where x may range from 0 to 0.125 [16]. Pyrrhotite with a higher iron content will have a hexagonal structure, whereas more iron deficient pyrrhotite such as Fe_7S_8 has a monoclinic structure [17], as seen in Figure 2.1. While iron-rich pyrrhotite structures display little or no magnetic response, the iron-deficient monoclinic structure of Figure 2.1 has a measured magnetic moment of $53.18 \mu_B$ [18], however the origin of this magnetism is debated [19].

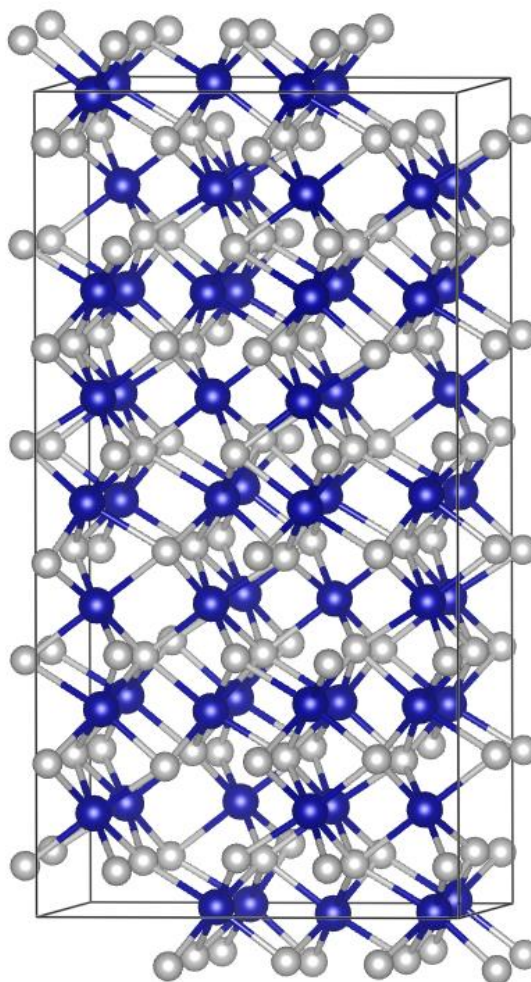


Figure 2.1: Monoclinic structure of pyrrhotite. Blue: Fe atoms, grey: sulfur atoms. Iron vacancies occur in alternating planes parallel to the c-axis. The topmost iron layer in the shown structure is a lacunar plane.

The most commonly studied pyrrhotite structure is the 4C monoclinic pyrrhotite with Fe_7S_8 stoichiometry, which is found most commonly intergrown with pentlandite [20]. The iron vacancies in this structure are confined to alternating iron layers parallel to the c axis [21]. The Fe atoms exist in octahedral coordination with either 5 or 6 sulfur atoms, which are only mildly distorted due to Fe vacancies. The mean distances between the Fe atoms along the c axis are relatively short, which may indicate some delocalisation of valence electrons. The measured magnetic moment for monoclinic pyrrhotite indicates the number of unpaired electrons per atom is equal to 4.27, and that iron is therefore in high-spin configuration [22]. The simplistic view of pyrrhotite dominated by high-spin Fe^{II} introduces a problem with balancing the charge of the Fe and S valencies. Therefore, pyrrhotite necessarily has some amount of Fe^{3+} in the structure to account for the Fe deficiency in the lattice [23].



In Eq. (1), L denotes an iron vacancy. The ordering of Fe^{III} in the lattice is less clear. Mössbauer spectroscopy was not able to identify the presence of Fe^{III} cations in the lattice, indicating they were itinerant and were not localised on the time scale of the technique ($10^{-7} - 10^{-8}$ s) [21]. The presence of Fe^{III} was definitively shown using X-ray photoelectron spectroscopy, which was able to distinguish the Fe^{III} signal from the Fe^{II} signal using high resolution $2p$ spectra [24]. An explanation has been provided for why Mössbauer spectroscopy was not able to detect Fe^{III} . It is suggested that there is a critical separation for cations in a lattice, below which the d -electrons are shared, and above which the cations can be considered localised. For Fe^{II} cations, this critical distance is 3.0 \AA [25], whereas the Fe-Fe distances are more than 3.1 \AA , except in the filled Fe layer, where the distances are 2.944 \AA . This is further indication that there is some delocalization of d -electrons, which may account for the effective movement of Fe^{III} in the lattice [21].

2.3 Pentlandite

As described in reference [26], pentlandite is formed by exsolution from the Fe-Ni-S monosulfide solid solution (mss). As the mss cools, a nickeliferous phase is exsolved, commonly along fractures in the mss to form 'rims' of fine bladed particles, lamellae, and coarse granular pentlandite [27]. Previous studies have observed grains of pentlandite and pyrrhotite with preferential orientation in slowly cooled solid solutions, but rapidly cooled solid solutions have only randomly oriented blebs of pentlandite [28]. Pentlandite has face centred cubic crystal structure with $Fm\bar{3}m$ symmetry and a chemical formula of M_9S_8 , where the metal sites are most commonly occupied by iron and nickel atoms in a ratio close to 1:1 [29]. Pentlandite has been known to contain small amounts of other transition metals, especially cobalt, up to approximately 1% [16], and may contain some other elements such as silver in argentian pentlandite ($[\text{Fe},\text{Ni}]_8\text{AgS}_8$) [30]. The pentlandite structure, shown in Figure 2.2 consists of approximately close-packed alternating layers of metal and sulfur atoms. The cation sites are distributed across 32 tetrahedral sites and 8 octahedral sites. The tetrahedral sites are each bonded to 4 sulfur anions and arranged in a cube cluster. The tetrahedral cation sites of neighbouring cube clusters have short interatomic distances, indicating some delocalisation of valence electrons, which may account for the metallic properties observed for pentlandite [31]. The 32 sulfur anions are distributed across 24 5-coordinate sites, which cap the faces of the cube clusters, and eight 4-coordinate sites which link the cube clusters [32].

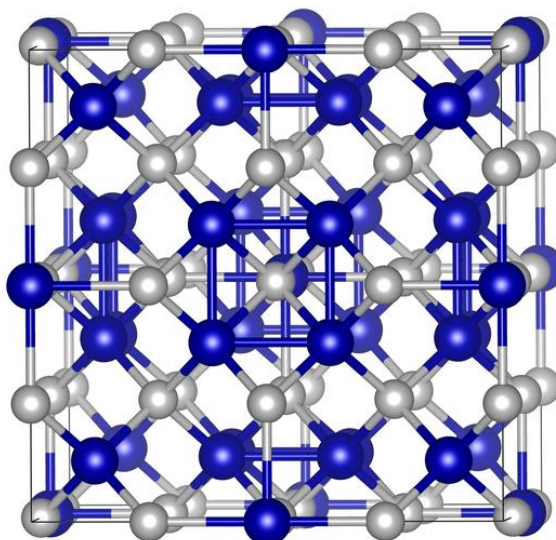


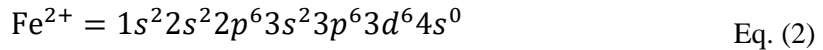
Figure 2.2: Crystal structure of pentlandite M_9S_8 . Blue: cation sites, grey: sulfur sites.

It was originally thought that the thermal expansion of the pentlandite unit cell was irreversible. It was postulated that the migration of Fe from the octahedral to tetrahedral sites results in an almost random distribution of metal atoms in the octahedral site [33]. A subsequent study which investigated a natural pentlandite sample which was heated and subsequently cooled showed that the unit cell decreased in size during cooling, but did not return to the original cell dimensions [34]. It is postulated that the overall increase in unit cell dimension is due to the randomized distribution of Fe and Ni atoms in the octahedral site [35]. A comparison of the unit cell dimensions of synthetic and natural samples showed that over long annealing times, the unit cell parameters of synthetic samples decrease to values similar to those found in natural samples, suggesting the reordering of Fe atoms into the octahedral sites [36, 37], and highlighting the high mobility of metal atoms within the lattice.

The size of the pentlandite unit cell causes difficulty in calculating the electronic structure of such a material, which is further complicated by the uncertainty in the ordering of cations in the lattice. There have been a number of studies attempting to calculate electronic structures of structures similar to pentlandite [38-43], however each of these studies is limited by the absence of high quality experimental data with which to compare the calculations. An understanding of the electronic structure is critical for accurate interpretation of photoelectron spectra, as is seen for other transition metal chalcogenides. The complex structures have significant effects on the line shapes and features observed in the core level spectra, and an understanding of these structures affects the interpretation of the core-level spectra.

2.4 Electronic structure, bonding, and transitions in materials.

The strength and orientation of bonds in the crystal lattice play a critical role in determining the electronic structure of a material, as it dictates the type of molecular orbitals which are formed between neighbouring atoms. The molecular orbitals, or band structure which forms, and the occupancy of valence electrons is what gives these materials their electronic properties. As an example, consider a ferrous ion (Fe^{2+}) in the ground state; it has six valence electrons in the $3d$ orbitals:



There are five d orbitals; d_{z^2} and $d_{x^2-y^2}$ are on-axis, that is, in the direction of the x , y and z axes, and d_{xy} , d_{xz} and d_{yz} are off-axis, meaning their direction is between the axes. In a free ion, these d orbitals are degenerate and have the same energy, but when the ion is bonded to a ligand such as sulfur in iron sulfides, the $3d$ orbitals become non-degenerate due to their mixing with the valence orbitals of the ligand. As shown in Figure 2.3, when the cation (green) is in octahedral coordination, the ligands (grey) are on-axis, while in tetrahedral coordination, the ligands are between the axes. This results in an energy splitting of the d electrons, with the orbitals oriented towards the ligands at a higher energy; that is, closer to the Fermi level. For a cation in octahedral coordination, the on-axis orbitals referred to as the e_g states, are a higher energy, while for a tetrahedrally coordinated cation, the off-axis orbitals, referred to as the t_{2g} states, are a higher energy.

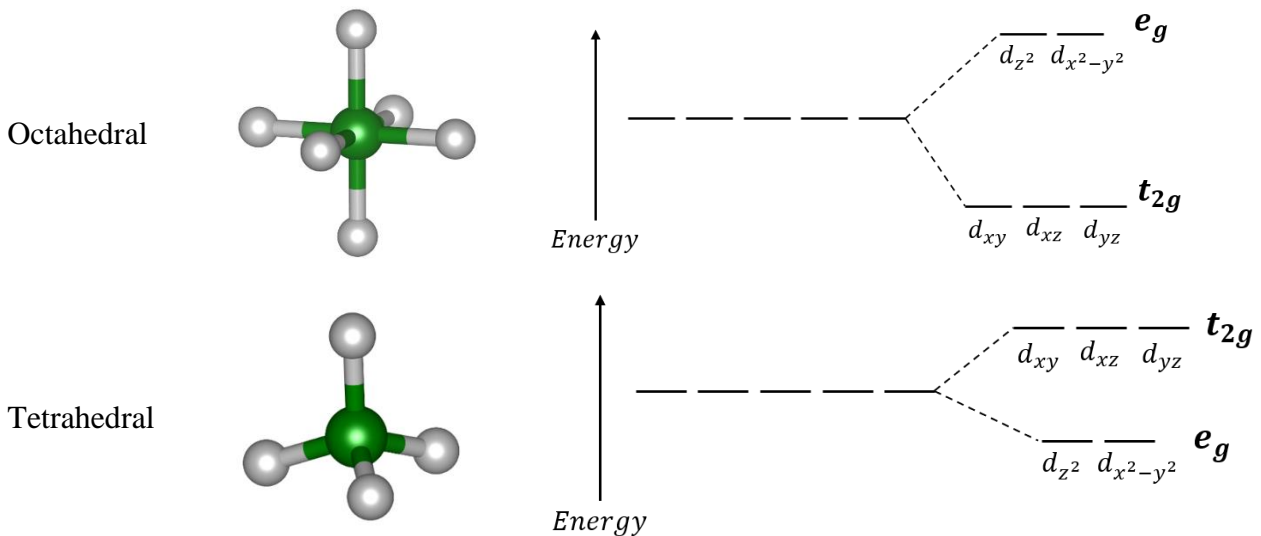


Figure 2.3: crystal field splitting of d orbitals in tetrahedral and octahedral coordination. In the example in the text, the green atom is iron, and the grey atoms are sulfur.

Electrons fill the orbitals from lowest to highest energy. However, for a ferrous ion with six d electrons there are two possibilities, based on the crystal field splitting; that is, the energy difference between the t_{2g} and e_g states, and the spin pairing energy, which is the energy difference between the spin up (majority spin) and spin down (minority spin) electrons. If the crystal field splitting is less than the spin pairing energy, the electrons will occupy the higher energy levels before pairing in opposite spin states. The result is the atom is in the “high spin” state, as the number of unpaired electrons is maximised. This is more common for a ferrous ion in tetrahedral coordination, rather than octahedral coordination, as the crystal field splitting energy is smaller and is therefore more likely to be smaller than the pairing energy. Tetrahedral high spin Fe^{2+} would consist of a “spin up” or “majority spin” electron in each orbital, with one of the lower energy e_g orbitals occupied by a second “spin down” or “minority spin” electron. If the spin pairing energy is less than the crystal field splitting, the electrons will pair in opposite spin states in the same orbital before the higher energy orbitals are occupied. This is known as a “low spin” configuration, as the number of unpaired electrons is minimised. The shape of the cation core level photoelectron peak is affected by the number of unpaired electrons in the valence band, due to the coupling between the remaining unpaired core electron and the unpaired valence electrons which results in a splitting of the main cation $2p$ photoelectron peak, known as multiplet splitting.

Multiplet splitting of the transition metal core level $2p$ lines results in an asymmetric line shape which consists of a series of multiplet states. Attempts have been made to calculate the shape of these multiplet features for the first row transition metals in different valence states [44, 45], and to empirically fit the asymmetric line shapes [46-48]. However, the multiplet structure is dependent on the ligand and the local coordination which is sensitive to any changes to bonding. Therefore, any line shape defined for one molecule does not take into account structural variations from that model and is consequently not applicable to materials beyond those from which the line shapes were defined. A more rigorous method of analysing spectra involves distinguishing the surface states from the bulk line shapes and justifying the observed line shapes with analyses of the electronic structure of the material.

2.5 Photoelectron spectroscopy of transition metal sulfides

X-ray photoelectron spectroscopy (XPS) is an important tool for understanding the electronic structure of transition metal chalcogenides. For the first row transition metal sulfides, there is a strong interaction between the $2p$ core level and the $3d$ valence band, thus photoelectron spectroscopy of the $2p$ core level is highly sensitive to changes which occur within these structures. Consequently, XPS has been a key tool for understanding the surface changes which occur due to fracture [49-52],

Chapter 2: Literature review: Looking beyond the earth's crust to see the crystal structures within oxidation [53-59], and the interaction with flotation reagents [60-65]. To be an effective tool for studying mineral surfaces, oxidation and reactions with other molecules, requires a strong basis in the accurate interpretation of unaltered core-level spectra. This is most successfully achieved on pristine fracture surfaces, as these surfaces have the least opportunity for alteration prior to analysis.

2.5.1 Identification of surface states

As a near-surface analysis technique, XPS has a strong history in identifying surface states resulting from the fracture surfaces of minerals. The species which exist on a mineral's surface are likely on the top one or two monolayers of the sample, and while they do contribute to the photoelectron spectra, their signal is often minimal in conventional XPS, and can be difficult to distinguish from the bulk components. A synchrotron radiation photon source provides an advantage in this space, as the photon energy of the X-rays can be tuned to enhance the surface sensitivity of the technique [66]. This method involves altering the energy of the incident photons, which consequently alters the kinetic energy of the photoelectrons. The surface sensitivity of the technique is governed by the inelastic mean free path of the photoelectrons, which is defined as the average distance an electron will travel between inelastic collisions [67]. Photoelectrons with a lower kinetic energy will generally have a smaller inelastic mean free path (IMFP), with the smallest IMFP at kinetic energies around 100 eV. At kinetic energies below this, the IMFP rises sharply [67-69].

Using this method of altering the incident photon energy, the surface states can be distinguished from the bulk in the core level spectra. Binding energy shifts in core level spectra are used to identify changes to the electronic structure of the surface states in comparison to the bulk. Bulk and surface atoms in III-V and II-IV semiconductors are generally found to have different binding energies of their core levels. For example, the (110) surface of GaAs (with zinc blende structure) shows a shift in binding energy with respect to the bulk binding energy core levels for both Ga and As states. This is observed as a positive shift in binding energy for the Ga (cation) sites, and a negative shift in binding energy for the As (anion) sites. The binding energy shift is due to a ground state charge transfer in the bonds at the surface, resulting in an increase in electron density around the ligands as a result of the loss of a bonding partner [70].

Similar binding energy shifts are observed for transition metal sulfide surfaces. The sulfur spectrum of vacuum fractured pyrite surfaces has been shown to include a contribution from a surface monosulfide species, and a contribution from the surface disulfide atom [71, 72]. The iron sites of pyrite are shown to include a narrow bulk contribution from low-spin Fe^{II} and surface contributions from Fe^{II} species which have undergone changes to local coordination, resulting in multiplet splitting

Chapter 2: Literature review: Looking beyond the earth's crust to see the crystal structures within

of the main peak, in addition to a contribution from Fe^{3+} , which results from auto-oxidation of the surfaces [49, 72-74]. Using the described method of identifying surface components in the spectra, this auto-oxidation process was found to be common among a number of other minerals, and also necessary to stabilise the surfaces of loellengite (FeAs_2) and marcasite (FeS_2) [74]. Fracture surfaces of millerite (NiS) [75], bornite (Cu_5FeS_4) [51], chalcopyrite (CuFeS_2) [50], and troilite [76] have also been studied, identifying both relaxations and reconstructions on fracture surfaces, in addition to analysing the bulk contributions to the spectrum. Surface species on pyrrhotite fracture surfaces were also investigated [76], but the interpretation of these spectra was obstructed by the asymmetric line shape of the bulk peak and the overlapping energies of surface states. Attempts have been made to also identify the components in the pentlandite sulfur core level spectrum [77, 78], yet none of these are synchrotron XPS (SXPS) studies. The accurate interpretation of these spectra has also been difficult due to overlapping energies of distinct states, broad asymmetric line shapes, and the difficulty in producing unaltered and reproducible surfaces, as pentlandite has no natural cleavage and a propensity to fracture along pre-oxidised grains [79].

2.5.2 Interpretation of bulk XPS line shapes

Both pyrrhotite and pentlandite sulfur $2p$ core level spectra have been seen to have high binding energy asymmetric line shapes [76-78, 80], and this has been justified due to their small band gaps and presumed metal-metal bonding in the crystal lattices [21, 32]. Such high binding energy bulk line shapes have previously been observed for other materials. Citrin [81] observed a high binding energy tail in the X-ray photoemission spectrum of sodium metal and concluded that the tail is due to “excitation of the conduction electrons by the sudden creation of the core hole”. This is a final state effect commonly seen for metals which results in a skewed line shape for the core level spectra, with broad high binding energy tails. The skew line shape is comprised of a series of states arising from the readjustment of the metallic conduction electrons, due to the creation of the core hole [82]. It has been argued for both pyrrhotite and pentlandite that the asymmetric bulk line shapes arise due to the interatomic distances between neighbouring cations which are smaller than the threshold proposed for metallic bonding [25]. However, monoclinic pyrrhotite has a calculated band gap of 0.8 eV [83], indicating it is not a true conductor. Conversely, the pentlandite electronic structure is not well understood, despite the numerous calculations attempting to resolve the structure [38-41]. Calculations have indicated that pentlandite's stability arises from a pseudo-gap in the band structure at the Fermi level [40]. Furthermore, many first row transition metal chalcogenides have been found to be charge-transfer compounds. They are characterised by the ligand-to-metal charge-transfer energy, which is the energy difference between the $3d^n$ and $3d^{n+1}\underline{L}$ (charge transfer) state and is less than the $d-d$ Coulomb repulsion energy [84]. Periodic trends are observed for the charge transfer

Chapter 2: Literature review: Looking beyond the earth's crust to see the crystal structures within energy and the *d-d* Coulomb energy, related to the electronegativity of the cation and the ligands. Generally, as the cation atomic number increases, the charge transfer energy decreases, due to the increase in electronegativity and subsequent lowering in energy of the cation *d* orbitals. Concurrently, the *d-d* Coulomb repulsion energy increases due to the decrease in radial extent of the *3d* orbitals [84, 85]. However, the physical properties of materials such as their metallic or insulating nature and the size of their band gap are observed to not be smooth functions of these variables [85], and thus the electronic band structures of the transition metal sulfides require detailed investigation to understand the origin of features in the photoemission spectra.

2.5.3 X-ray absorption spectroscopy and resonant valence band studies

X-ray absorption spectroscopy can give additional insight into the valence band structure of a material. For first row transition metal sulfides, the structure around the *2p* absorption line is particularly sensitive to changes to electronic structure, which can be induced by change in bonding partner, or local symmetry [86]. Analysis of the *2p* absorption, or L edge, is sometimes referred to as Near Edge X-ray Absorption Fine Structure (NEXAFS) and is particularly sensitive for first row transition metal sulfides as the transitions from the *2p* core level to the unoccupied states in the *3d* band are particularly strong. Consequently, *2p* NEXAFS has been shown to be particularly useful for mineralogical and geochemical research [87].

NEXAFS has been essential for determining the oxidation state of copper in various minerals. Determining the oxidation state of cations in complex mineral systems is not trivial, and the sensitivity of L edge NEXAFS spectroscopy to the oxidation state of copper in particular has been instrumental for this purpose. In particular, for covellite (CuS), which has been claimed to be primarily Cu^{II}, but shown by NEXAFS to be primarily Cu^I [88, 89]. The copper in chalcopyrite was also shown to be monovalent [89], despite claims of divalent copper in the unaltered chalcopyrite structure [90]. The assignment of Cu^{II} by Todd, Sherman and Purton [90] was inaccurate due to the misunderstanding that Cu^I would not produce a L edge absorption spectrum, due to the full *3d* band, but the absorption features occur due to the *3d* character of the Cu *4s* band. This highlights the necessity for a clear understanding of the fundamental processes to ensure accurate interpretation of spectra.

A particularly powerful method of investigating the electronic structure of a material is by resonant photoemission spectroscopy. The valence band photoemission spectra are collected with photon energies corresponding to features in the soft X-ray absorption spectra. This method highlights features in the valence band which correspond to orbitals from elements in the material, and may

Chapter 2: Literature review: Looking beyond the earth's crust to see the crystal structures within highlight localised $3d$ states, arising from the strong interaction between the $2p$ and $3d$ electrons in materials with significant electron correlation [91]. Fujisawa, Suga, Mizokawa, Fujimori and Sato [92] used resonant valence band photoemission spectroscopy to investigate the electronic band structure of chalcopyrite (CuFeS_2) and were able to show that chalcopyrite has a ligand-to-metal charge transfer between the $\text{S } 3p \rightarrow \text{Fe } 3d$ states, and that the broad tails in both the Fe and S $2p$ core level photoelectron spectra are caused by the charge transfer final state [92]. Resonant photoemission has also been used to study pyrite-type minerals; namely FeS_2 (pyrite), CoS_2 and NiS_2 , observing the trends as the cation $3d$ band is progressively filled with the increase in atomic number of the cation [93]. As the number of electrons in the cation valence band increases, the width of the peak in the valence band spectrum attributed to $3d$ states increases, with the addition of a small shoulder near the Fermi energy, attributed to the e_g band, which is empty in FeS_2 , but progressively filled in CoS_2 and NiS_2 . Resonant enhancement was observed in the valence band for each of these materials, indicating that electron correlation plays an important role in the electronic structure of each. Notably for NiS_2 , this resonant valence band photoemission study showed that the higher binding energy satellite feature was due to a d^7 final state, and the main band of the spectrum is therefore attributable to the charge transfer $d^8\bar{L}$ final state, and that NiS_2 is therefore a charge-transfer type insulator [93].

2.6 Oxidation of sulfide surfaces

With a clear interpretation of spectra for pristine surface, and a strong fundamental understanding of the origin of the observed feature, X-ray spectroscopies can be a powerful tool for observing fine changes to the mineral surfaces due to oxidation. Even without the strong foundation of the fracture surfaces, photoelectron spectroscopy in particular has been used to study the oxidation of surfaces upon initial exposure to oxygen [59, 94, 95], or air [49], or the evolution of the surface species due to the extended exposure of the mineral to atmosphere, humidity or water [53, 55, 56, 75, 96-98], exposure to flotation related conditions [58, 62, 65, 99, 100], or acidic conditions common to leaching [96, 97, 101-103]. Only a few of these mentioned studies investigate the surface species specifically [49, 59, 94], while most observe the changes in the spectra of samples under the different conditions [53, 55, 56, 96, 102]. The latter technique is a valid method of observing the changes to a sample's surface, but small details have not been easily detected, partly due to highly variable sample preparation methods combined with the potential variability of natural samples and the limited resolution available in older studies.

Pyrrhotite oxidation studies have shown that after oxidation in air, the pyrrhotite surface forms an overlayer of Fe-oxyhydroxide species, which has a sulfur-rich underlayer, the stoichiometry of which gradually changes back to Fe_7S_8 in the bulk [24, 97]. However, the studies which show this compare

Chapter 2: Literature review: Looking beyond the earth's crust to see the crystal structures within

the spectra of oxidised pyrrhotite samples with the spectra of more pristine samples, rather than fitting the components of high resolution spectra. Pentlandite oxidised surfaces have been even more difficult to investigate, as it was shown in early studies that pentlandite surfaces naturally fracture along pre-oxidised surfaces such as in cracks or grain boundaries in the sample [79]. As a result, subsequent studies used abrading techniques to create reproducible pentlandite surfaces, which has masked the interpretation of the high resolution spectra and made the assignment of surface states difficult [77, 78]. A more rigorous method of analysis is to firstly have a well-studied fracture surface and well-defined bulk features, then comparing the well characterised bulk feature with the oxidised spectra to identify the surface species which result from the oxidising conditions.

2.7 Overcoming limitations of techniques

The next step to take in critically analysing transition metal sulfide surfaces is to develop an *in situ* analysis method. Characterising fracture surfaces is important, as is analysing oxidised surfaces, however the techniques discussed up to this point are limited by the analysis environment. This limitation is especially important for the oxidised samples, as the sample must be removed from its oxidising environment and placed in ultra-high vacuum (UHV) to carry out the analysis, and the changes which occur between exposing the surfaces to oxidising conditions and analysing them in vacuum are ambiguous. Scanning transmission X-ray microscopy (STXM) is an emerging technique which is able to illuminate this aspect, as the technique allows for analysis of hydrated samples. The use of soft X-rays has rendered this technique favourable for organic, polymer and biological samples due to the water window; that is, the ability for soft X-rays to penetrate water, and due to the low radiation dose delivered by the design of the instrument [104]. While STXM has been shown to be highly useful for the analysis of soft matter, it has also been used to map Al-containing minerals in multiphase mixtures [105], metal species in biofilms [106-109], and mapping ratios of ferrous and ferric iron in silicate samples [110].

The main advantage of applying this technique to sulfide samples is that samples can be analysed *in situ* without having to change the sample's environment such as solution pH, Eh, ion concentration, or pressure. This removes the assumptions made in the studies previously discussed, that the changes to the samples as a result of analysing them in UHV are minimal. Recent developments in this technique have seen novel designs of sample holders for studies of samples in specialised environments. An example was shown of an *in situ* analysis of an iron-based catalyst using a specially designed sample holder including a nanoreactor with gas inlets and electrical connections [111]. STXM has been used to study the electrochemical reduction of Cu^{II} to deposit metallic copper on a Au electrode using a specially designed wet cell with printed electrodes [112]. This sample holder

Chapter 2: Literature review: Looking beyond the earth's crust to see the crystal structures within

design has recently been further developed to enable similar investigations, but with continuous flow of electrolytes [113, 114]. The combination of chemical sensitivity, appropriateness for soft matter and transition metals, and the adaptability of the sample holder makes STXM a great candidate for sulfide mineral analysis.

2.8 Summary and objectives

This literature review has highlighted the need for careful characterisation of surface species and detailed understanding of the electronic structures of the transition metal sulfides pyrrhotite and pentlandite. X-ray photoelectron spectroscopy has been identified as a highly useful technique for investigating these aspects of transition metal chalcogenides. The original contribution to knowledge provided in this thesis is the investigation of the surface structure of pristine vacuum fractured pyrrhotite and pentlandite using tunable synchrotron radiation sources, and a detailed investigation into the electronic structures of these materials, thereby justifying the observed bulk line shapes. With carefully characterised pristine surfaces, the oxidised surfaces of these minerals are then investigated to identify the oxidation processes which occur on the surfaces of pyrrhotite and pentlandite, and their corresponding features in the photoelectron spectra. This is a significant contribution, especially with the increasing interest in pentlandite and related structures, as an accurate interpretation of spectra of these surfaces oxidised in air and in solution will help interpret the photoelectron spectra observed in literature more focussed on the application of these surfaces as catalysts. Finally, this literature review highlights that common photoemission spectra require the sample to be in UHV, which poses a significant limitation, especially for oxidised samples, which must be removed from their oxidising environments prior to analysis. An emerging microscopy technique has been highlighted as a possibility for overcoming this limitation. Hence, this thesis includes the first known application of STXM for analysis of transition metal sulfide minerals, to highlight its suitability for sulfide systems.

2.9 References

- [1] T. Heine, Transition Metal Chalcogenides: Ultrathin Inorganic Materials with Tunable Electronic Properties, *Accounts of Chemical Research*, 48 (2015) 65-72.
- [2] C.-H. Lai, M.-Y. Lu, L.-J. Chen, Metal sulfide nanostructures: synthesis, properties and applications in energy conversion and storage, *J. Mater. Chem.*, 22 (2012) 19-30.
- [3] P. Roy, S.K. Srivastava, Nanostructured copper sulfides: synthesis, properties and applications, *CrystEngComm*, 17 (2015) 7801-7815.
- [4] R.S.C. Smart, J. Amarantidis, W.M. Skinner, C.A. Prestidge, L. La Vanier, S.R. Grano, Surface Analytical Studies of Oxidation and Collector Adsorption in Sulfide Mineral Flotation, in: K. Wandelt, S. Thurgate (Eds.) *Solid—Liquid Interfaces: Macroscopic Phenomena — Microscopic Understanding*, Springer Berlin Heidelberg, Berlin, Heidelberg, 2003, pp. 3-62.
- [5] J. Hou, Y. Lei, F. Wang, X. Ma, S. Min, Z. Jin, J. Xu, In-situ photochemical fabrication of transition metal-promoted amorphous molybdenum sulfide catalysts for enhanced photosensitized hydrogen evolution, *International Journal of Hydrogen Energy*, 42 (2017) 11118-11129.

- [6] S.-H. Chang, M.-D. Lu, Y.-L. Tung, H.-Y. Tuan, Gram-Scale Synthesis of Catalytic Co_9S_8 Nanocrystal Ink as a Cathode Material for Spray-Deposited, Large-Area Dye-Sensitized Solar Cells, *ACS Nano*, 7 (2013) 9443-9451.
- [7] M. Al-Mamun, Y. Wang, P. Liu, Y.L. Zhong, H. Yin, X. Su, H. Zhang, H. Yang, D. Wang, Z. Tang, H. Zhao, One-step solid phase synthesis of a highly efficient and robust cobalt pentlandite electrocatalyst for the oxygen evolution reaction, *Journal of Materials Chemistry A*, 4 (2016) 18314-18321.
- [8] Y. Zhu, H. Liu, T. Chen, B. Xu, P. Li, Kinetics and thermodynamics of Eu(III) adsorption onto synthetic monoclinic pyrrhotite, *Journal of Molecular Liquids*, 218 (2016) 565-570.
- [9] H. Liu, Y. Zhu, B. Xu, P. Li, Y. Sun, T. Chen, Mechanical investigation of U(VI) on pyrrhotite by batch, EXAFS and modeling techniques, *Journal of Hazardous Materials*, 322 (2017) 488-498.
- [10] B. Konkena, K.J. Puring, I. Sinev, S. Piontek, O. Khavryuchenko, J.P. Dürholt, R. Schmid, H. Tüysüz, M. Muhler, W. Schuhmann, U.-P. Apfel, Pentlandite rocks as sustainable and stable efficient electrocatalysts for hydrogen generation, *Nature Communications*, 7 (2016) 12269.
- [11] W. Bacon, A. Dalvi, B. Rochon, M. Selby, Nickel outlook - 2000 to 2010, *CIM Bulletin*, 95 (2002) 47-52.
- [12] B.A. Wills, J.A. Finch, Chapter 12 - Froth Flotation, in: B.A. Wills, J.A. Finch (Eds.) *Wills' Mineral Processing Technology* (Eighth Edition), Butterworth-Heinemann, Boston, 2016, pp. 265-380.
- [13] M.C. Fuerstenau, G.J. Jameson, R.-H. Yoon, *Froth flotation: a century of innovation*, Society for Mining, Metallurgy, and Exploration, 2007.
- [14] G.E. Agar, Flotation of chalcopyrite, pentlandite, pyrrhotite ores, *International Journal of Mineral Processing*, 33 (1991) 1-19.
- [15] H.T. Evans, Lunar troilite: crystallography, *Science*, 167 (1970) 621-623.
- [16] B. Mason, L.G. Berry, *Elements of Mineralogy*, W.H. Freeman, San Francisco, 1968.
- [17] M. Fleet, The crystal structure of a pyrrhotite (Fe_7S_8), *Acta Crystallographica*, 27 (1971) 1864-1867.
- [18] M. Spender, J. Coey, A. Morrish, The magnetic properties and Mössbauer spectra of synthetic samples of Fe_3S_4 , *Canadian Journal of Physics*, 50 (1972) 2313-2326.
- [19] H. Miyauchi, T. Koide, T. Shidara, N. Nakajima, H. Kawabe, H. Fukutani, K. Shimada, A. Fujimori, K. Iio, T. Kamimura, Core-level magnetic circular dichroism in Fe_7S_8 and Fe_7Se_8 , *Journal of Electron Spectroscopy and Related Phenomena*, 78 (1996) 259-262.
- [20] S.M. Bulatovic, 18 - Flotation of Platinum Group Metal Ores, in: S.M. Bulatovic (Ed.) *Handbook of Flotation Reagents: Chemistry, Theory and Practice*, Elsevier, Amsterdam, 2010, pp. 19-45.
- [21] M. Tokonami, K. Nishiguchi, N. Morimoto, Crystal structure of a monoclinic pyrrhotite (Fe_7S_8), *American Mineralogist*, 57 (1972) 1066-1080.
- [22] L.J. Pauwels, Energy Level Diagrams of the "NiAs"-, "Pyrite"- and "Spinel"-Type Sulfides of Fe, Co and Ni, *Bulletin des Sociétés Chimiques Belges*, 79 (1970) 549-566.
- [23] E. Bertaut, Contribution à l'étude des structures lacunaires: la pyrrhotine, *Acta Crystallographica*, 6 (1953) 557-561.
- [24] A.R. Pratt, I.J. Muir, H.W. Nesbitt, X-ray photoelectron and Auger electron spectroscopic studies of pyrrhotite and mechanism of air oxidation, *Geochimica et Cosmochimica Acta*, 58 (1994) 827-841.
- [25] J.B. Goodenough, Cation-Cation Three-Membered Ring Formation, *Journal of Applied Physics*, 33 (1962) 1197-1199.
- [26] Z.E. Pettifer, J.S. Quinton, W.M. Skinner, S.L. Harmer, New interpretation and approach to curve fitting synchrotron X-ray photoelectron spectra of $(\text{Fe},\text{Ni})_9\text{S}_8$ fracture surfaces, *Applied Surface Science*, 504 (2020) 144458.
- [27] D. Kelly, D. Vaughan, Pyrrhotine-pentlandite ore textures: a mechanistic approach, *Mineralogical Magazine*, 47 (1983) 453-463.
- [28] C. Francis, M. Fleet, K. Misra, J. Craig, Orientation of exsolved pentlandite in natural and synthetic nickeliferous pyrrhotite, *American Mineralogist*, 61 (1976) 913-920.

- [29] A.D. Pearson, M.J. Buerger, Confirmation of the crystal structure of pentlandite, *American Mineralogist*, 41 (1956) 804-805.
- [30] S. Hall, J. Stewart, The crystal structure of argentian pentlandite $(\text{Fe, Ni})_8\text{AgS}_8$, compared with the refined structure of pentlandite $(\text{Fe, Ni})_9\text{S}_8$, *The Canadian Mineralogist*, 12 (1973) 169-177.
- [31] D.J. Vaughan, J.R. Craig, *Mineral Chemistry of Metal Sulfides*, Cambridge University Press, Cambridge, 1978.
- [32] V. Rajamani, C.T. Prewitt, Crystal chemistry of natural pentlandites, *The Canadian Mineralogist*, 12 (1973) 178-187.
- [33] O. Knop, C.-H. Huang, F.W.D. Woodhams, Chalcogenides of the transition elements. VII. A mössbauer study of pentlandite, *American Mineralogist*, 55 (1970) 1115-1130.
- [34] K. Tsukimura, Fe/Ni distribution in pentlandite at high temperature and the estimated pressure-temperature dependence of the distribution, *Mineralogical Journal*, 14 (1989) 323-337.
- [35] V. Rajamani, C. Prewitt, Thermal Expansion of the Pentlandite Structure, *American Mineralogist*, 60 (1975) 39-48.
- [36] B. Etschmann, A. Pring, A. Putnis, B.A. Grguric, A. Studer, A kinetic study of the exsolution of pentlandite $(\text{Ni,Fe})_9\text{S}_8$ from the monosulfide solid solution $(\text{Fe,Ni})\text{S}$, *American Mineralogist*, 89 (2004) 39-50.
- [37] F. Xia, J. Zhou, J. Brugger, Y. Ngothai, B. O'Neill, G. Chen, A. Pring, Novel Route To Synthesize Complex Metal Sulfides: Hydrothermal Coupled Dissolution–Reprecipitation Replacement Reactions, *Chemistry of Materials*, 20 (2008) 2809-2817.
- [38] J.K. Burdett, G.J. Miller, Polyhedral clusters in solids. The electronic structure of pentlandite, *Journal of the American Chemical Society*, 109 (1987) 4081-4091.
- [39] G.G. Hoffman, J.K. Bashkin, M. Karplus, Electronic structure of icosahedral cobalt-sulfur clusters, *Journal of the American Chemical Society*, 112 (1990) 8705-8714.
- [40] H.R. Chauke, D. Nguyen-Manh, P.E. Ngoepe, D.G. Pettifor, S.G. Fries, Electronic structure and stability of the pentlandites Co_9S_8 and $(\text{Fe,Ni})_9\text{S}_8$, *Physical Review B*, 66 (2002) 155105.
- [41] P.P. Mkhonto, H.R. Chauke, P.E. Ngoepe, Ab initio Studies of O_2 Adsorption on (110) Nickel-Rich Pentlandite $(\text{Fe}_4\text{Ni}_5\text{S}_8)$ Mineral Surface, *Minerals*, 5 (2015) 665-678.
- [42] C.N. Waterson, J.O. Sindt, J. Cheng, P.A. Tasker, C.A. Morrison, First-principles study on ligand binding and positional disorder in pentlandite, *The Journal of Physical Chemistry C*, 119 (2015) 25457-25468.
- [43] M. Fronzi, S.A. Tawfik, C. Stampfl, M.J. Ford, Magnetic properties of stoichiometric and defective Co_9S_8 , *Physical Chemistry Chemical Physics*, 20 (2018) 2356-2362.
- [44] R.P. Gupta, S.K. Sen, Calculation of multiplet structure of core p -vacancy levels, *Physical Review B*, 10 (1974) 71-77.
- [45] P.S. Bagus, R. Broer, W.A. de Jong, W.C. Nieuwpoort, F. Parmigiani, L. Sangaletti, Atomic Many-Body Effects for the p -Shell Photoelectron Spectra of Transition Metals, *Physical Review Letters*, 84 (2000) 2259-2262.
- [46] A.P. Grosvenor, B.A. Kobe, M.C. Biesinger, N.S. McIntyre, Investigation of multiplet splitting of Fe 2p XPS spectra and bonding in iron compounds, *Surface and Interface Analysis*, 36 (2004) 1564-1574.
- [47] M.C. Biesinger, L.W.M. Lau, A.R. Gerson, R.S.C. Smart, Resolving surface chemical states in XPS analysis of first row transition metals, oxides and hydroxides: Sc, Ti, V, Cu and Zn, *Applied Surface Science*, 257 (2010) 887-898.
- [48] M.C. Biesinger, B.P. Payne, A.P. Grosvenor, L.W.M. Lau, A.R. Gerson, R.S.C. Smart, Resolving surface chemical states in XPS analysis of first row transition metals, oxides and hydroxides: Cr, Mn, Fe, Co and Ni, *Applied Surface Science*, 257 (2011) 2717-2730.
- [49] A.G. Schaufuß, H.W. Nesbitt, I. Kartio, K. Laajalehto, G.M. Bancroft, R. Szargan, Incipient oxidation of fractured pyrite surfaces in air, *Journal of Electron Spectroscopy and Related Phenomena*, 96 (1998) 69-82.
- [50] S.L. Harmer, A.R. Pratt, W.H. Nesbitt, M.E. Fleet, Sulfur species at chalcopyrite (CuFeS_2) fracture surfaces, *American Mineralogist*, 89 (2004) 1026-1032.

- [51] S.L. Harmer, A.R. Pratt, H.W. Nesbitt, M.E. Fleet, Reconstruction of fracture surfaces on bornite, *The Canadian Mineralogist*, 43 (2005) 1619-1630.
- [52] S.L. Harmer, W.M. Skinner, A.N. Buckley, L.-J. Fan, Species formed at cuprite fracture surfaces; observation of O 1s surface core level shift, *Surface Science*, 603 (2009) 537-545.
- [53] A.N. Buckley, R. Woods, An x-ray photoelectron spectroscopic study of the oxidation of galena, *Applications of Surface Science*, 17 (1984) 401-414.
- [54] A.N. Buckley, R. Woods, An X-ray photoelectron spectroscopic study of the oxidation of chalcopyrite, *Australian Journal of Chemistry*, 37 (1984) 2403-2413.
- [55] A. Buckley, R. Woods, X-ray photoelectron spectroscopy of oxidized pyrrhotite surfaces: I. Exposure to air, *Applications of Surface Science*, 22/23 (1985) 280-287.
- [56] A.N. Buckley, R. Woods, The surface oxidation of pyrite, *Applied Surface Science*, 27 (1987) 437-452.
- [57] A.P. Grosvenor, B.A. Kobe, N.S. McIntyre, Studies of the oxidation of iron by water vapour using X-ray photoelectron spectroscopy and QUASES™, *Surface Science*, 572 (2004) 217-227.
- [58] D. Legrand, G. Bancroft, H. Nesbitt, Oxidation/alteration of pentlandite and pyrrhotite surfaces at pH 9.3: Part 1. Assignment of XPS spectra and chemical trends, *American Mineralogist*, 90 (2005) 1042-1054.
- [59] A.G. Berlich, H.W. Nesbitt, G.M. Bancroft, R. Szargan, Binding of oxygen on vacuum fractured pyrite surfaces: Reactivity of iron and sulfur surface sites, *Surface Science*, 611 (2013) 60-66.
- [60] E.W. Giesekke, A review of spectroscopic techniques applied to the study of interactions between minerals and reagents in flotation systems, *International Journal of Mineral Processing*, 11 (1983) 19-56.
- [61] J. Mielczarski, XPS study of ethyl xanthate adsorption on oxidized surface of cuprous sulfide, *Journal of Colloid and Interface Science*, 120 (1987) 201-209.
- [62] K. Laajalehto, P. Nowak, E. Suoninen, On the XPS and IR identification of the products of xanthate sorption at the surface of galena, *International Journal of Mineral Processing*, 37 (1993) 123-147.
- [63] D.L. Legrand, G.M. Bancroft, H.W. Nesbitt, Oxidation of pentlandite and pyrrhotite surfaces at pH 9.3: Part 2. Effect of xanthates and dissolved oxygen, *American Mineralogist*, 90 (2005) 1055-1061.
- [64] S.W. Goh, A.N. Buckley, B. Gong, R. Woods, R.N. Lamb, L.-J. Fan, Y.-w. Yang, Thiolate layers on metal sulfides characterised by XPS, ToF-SIMS and NEXAFS spectroscopy, *Minerals Engineering*, 21 (2008) 1026-1037.
- [65] Y. Kalegowda, Y.-L. Chan, D.-H. Wei, S.L. Harmer, X-PEEM, XPS and ToF-SIMS characterisation of xanthate induced chalcopyrite flotation: Effect of pulp potential, *Surface Science*, 635 (2015) 70-77.
- [66] K. Laajalehto, I. Kartio, E. Suoninen, XPS and SR-XPS techniques applied to sulphide mineral surfaces, *International Journal of Mineral Processing*, 51 (1997) 163-170.
- [67] C.J. Powell, The quest for universal curves to describe the surface sensitivity of electron spectroscopies, *Journal of Electron Spectroscopy and Related Phenomena*, 47 (1988) 197-214.
- [68] M.P. Seah, W. Dench, Quantitative electron spectroscopy of surfaces: a standard data base for electron inelastic mean free paths in solids, *Surface and Interface Analysis*, 1 (1979) 2-11.
- [69] S. Hüfner, *Photoelectron Spectroscopy*, 2nd ed., Springer-Verlag, Berlin, 1996.
- [70] W. Mönch, *Semiconductor Surfaces and Interfaces*, Springer-Verlag, Berlin, 1993.
- [71] M. Bronold, Y. Tomm, W. Jaegermann, Surface states on cubic *d*-band semiconductor pyrite (FeS₂), *Surface Science*, 314 (1994) 931-936.
- [72] H.W. Nesbitt, G.M. Bancroft, A.R. Pratt, M.J. Scaini, Sulfur and iron surface states on fractured pyrite surfaces, *American Mineralogist*, 83 (1998) 1067-1076.
- [73] I. Uhlig, R. Szargan, H.W. Nesbitt, K. Laajalehto, Surface states and reactivity of pyrite and marcasite, *Applied Surface Science*, 179 (2001) 222-229.

- [74] S.L. Harmer, H.W. Nesbitt, Stabilization of pyrite (FeS_2), marcasite (FeS_2), arsenopyrite (FeAsS) and loellingite (FeAs_2) surfaces by polymerization and auto-redox reactions, *Surface Science*, 564 (2004) 38-52.
- [75] D.L. Legrand, H.W. Nesbitt, G.M. Bancroft, X-ray photoelectron spectroscopic study of a pristine millerite (NiS) surface and the effect of air and water oxidation, *American Mineralogist*, 83 (1998) 1256-1265.
- [76] H.W. Nesbitt, A.G. Schaufuss, M. Scaini, G.M. Bancroft, R. Szargan, XPS measurement of fivefold and sixfold coordinated sulfur in pyrrhotites and evidence for millerite and pyrrhotite surface species, *American Mineralogist*, 86 (2001) 318-326.
- [77] D.L. Legrand, G.M. Bancroft, H.W. Nesbitt, Surface characterization of pentlandite, $(\text{Fe,Ni})_9\text{S}_8$, by X-ray photoelectron spectroscopy, *International Journal of Mineral Processing*, 51 (1997) 217-228.
- [78] S.W. Goh, A.N. Buckley, R.N. Lamb, L.-J. Fan, L.-Y. Jang, Y.-w. Yang, Pentlandite sulfur core electron binding energies, *Phys Chem Minerals*, 33 (2006) 445-456.
- [79] A.N. Buckley, R. Woods, Surface composition of pentlandite under flotation-related conditions, *Surface and Interface Analysis*, 17 (1991) 675-680.
- [80] W.M. Skinner, H.W. Nesbitt, A.R. Pratt, XPS identification of bulk hole defects and itinerant Fe 3d electrons in natural troilite (FeS), *Geochimica et Cosmochimica Acta*, 68 (2004) 2259-2263.
- [81] P. Citrin, High-resolution X-ray photoemission from sodium metal and its hydroxide, *Physical Review B*, 8 (1973) 5545-5556.
- [82] S. Doniach, M. Sunjic, Many-electron singularity in X-ray photoemission and X-ray line spectra from metals, *Journal of Physics C: Solid State Physics*, 3 (1970) 285-291.
- [83] S. Sakkopoulos, E. Vitoratos, T. Argyreas, Energy-band diagram for pyrrhotite, *Journal of Physics and Chemistry of Solids*, 45 (1984) 923-928.
- [84] A.E. Bocquet, T. Mizokawa, T. Saitoh, H. Namatame, A. Fujimori, Electronic structure of 3d-transition-metal compounds by analysis of the 2p core-level photoemission spectra, *Physical Review B*, 46 (1992) 3771-3784.
- [85] A. Fujimori, A.E. Bocquet, T. Saitoh, T. Mizokawa, Electronic structure of 3d transition metal compounds: systematic chemical trends and multiplet effects, *Journal of Electron Spectroscopy and Related Phenomena*, 62 (1993) 141-152.
- [86] J. Stöhr, *NEXAFS Spectroscopy*, Springer-Verlag, Berlin, 1992.
- [87] G. Cressey, C.M.B. Henderson, G. van der Laan, Use of L-edge X-ray absorption spectroscopy to characterize multiple valence states of 3d transition metals; a new probe for mineralogical and geochemical research, *Phys Chem Minerals*, 20 (1993) 111-119.
- [88] S.W. Goh, A.N. Buckley, R.N. Lamb, Copper(II) sulfide?, *Minerals Engineering*, 19 (2006) 204-208.
- [89] S.W. Goh, A.N. Buckley, R.N. Lamb, R.A. Rosenberg, D. Moran, The oxidation states of copper and iron in mineral sulfides, and the oxides formed on initial exposure of chalcopyrite and bornite to air, *Geochimica et Cosmochimica Acta*, 70 (2006) 2210-2228.
- [90] E. Todd, D. Sherman, J. Purton, Surface oxidation of chalcopyrite (CuFeS_2) under ambient atmospheric and aqueous (pH 2-10) conditions: Cu, Fe L- and O K-edge X-ray spectroscopy, *Geochimica et Cosmochimica Acta*, 67 (2003) 2137-2146.
- [91] J.F.W. Mosselmans, R.A.D. Patrick, G. Van Der Laan, J.M. Charnock, D.J. Vaughan, C.M.B. Henderson, C.D. Garner, X-ray absorption near-edge spectra of transition metal disulfides FeS_2 (pyrite and marcasite), CoS_2 , NiS_2 and CuS_2 , and their isomorphs FeAsS and CoAsS , *Phys Chem Minerals*, 22 (1995) 311-317.
- [92] M. Fujisawa, S. Suga, T. Mizokawa, A. Fujimori, K. Sato, Electronic structures of CuFeS_2 and $\text{CuAl}_{0.9}\text{Fe}_{0.1}\text{S}_2$ studied by electron and optical spectroscopies, *Physical Review B*, 49 (1994) 7155-7164.
- [93] A. Fujimori, K. Mamiya, T. Mizokawa, T. Miyadai, T. Sekiguchi, H. Takahashi, N. Mori, S. Suga, Resonant photoemission study of pyrite-type NiS_2 , CoS_2 and FeS_2 , *Physical Review B*, 54 (1996) 16329.

- [94] S. Mattila, J.A. Leiro, M. Heinonen, XPS study of the oxidized pyrite surface, *Surface Science*, 566-568 (2004) 1097-1101.
- [95] C.T. Campbell, An XPS study of molecularly chemisorbed oxygen on Ag(111), *Surface Science Letters*, 173 (1986) 641-646.
- [96] A. Buckley, R. Woods, Electrochemical and XPS studies of the surface oxidation of synthetic heazlewoodite (Ni_3S_2), *Journal of Applied Electrochemistry*, 21 (1991) 575-582.
- [97] C.F. Jones, S. LeCount, R.S.C. Smart, T.J. White, Compositional and structural alteration of pyrrhotite surfaces in solution: XPS and XRD studies, *Applied Surface Science*, 55 (1992) 65-85.
- [98] M.L. Farquhar, P.L. Wincott, R.A. Wogelius, D.J. Vaughan, Electrochemical oxidation of the chalcopyrite surface: an XPS and AFM study in solution at pH 4, *Applied Surface Science*, 218 (2003) 34-43.
- [99] R.G. Acres, S.L. Harmer, D.A. Beattie, Synchrotron XPS studies of solution exposed chalcopyrite, bornite, and heterogeneous chalcopyrite with bornite, *International Journal of Mineral Processing*, 94 (2010) 43-51.
- [100] M.C. Biesinger, B.R. Hart, R. Polack, B.A. Kobe, R.S.C. Smart, Analysis of mineral surface chemistry in flotation separation using imaging XPS, *Minerals Engineering*, 20 (2007) 152-162.
- [101] R.G. Acres, S.L. Harmer, D.A. Beattie, Synchrotron XPS, NEXAFS, and ToF-SIMS studies of solution exposed chalcopyrite and heterogeneous chalcopyrite with pyrite, *Minerals Engineering*, 23 (2010) 928-936.
- [102] A.N. Buckley, H.J. Wouterlood, R. Woods, The surface composition of natural sphalerites under oxidative leaching conditions, *Hydrometallurgy*, 22 (1989) 39-56.
- [103] J.E. Thomas, C.F. Jones, W.M. Skinner, R.S.C. Smart, The role of surface sulfur species in the inhibition of pyrrhotite dissolution in acid conditions, *Geochimica et Cosmochimica Acta*, 62 (1998) 1555-1565.
- [104] A.P. Hitchcock, C. Morin, T. Tylliszczak, I.N. Koprinarov, H. Ikeura-Sekiguchi, J.R. Lawrence, G.G. Leppard, SOFT X-RAY MICROSCOPY OF SOFT MATTER — HARD INFORMATION FROM TWO SOFTS, *Surface Review and Letters*, 09 (2002) 193-201.
- [105] T.H. Yoon, S.B. Johnson, K. Benzerara, C.S. Doyle, T. Tylliszczak, D.K. Shuh, G.E. Brown, In Situ Characterization of Aluminum-Containing Mineral-Microorganism Aqueous Suspensions Using Scanning Transmission X-ray Microscopy, *Langmuir*, 20 (2004) 10361-10366.
- [106] J.J. Dynes, T. Tylliszczak, T. Araki, J.R. Lawrence, G.D.W. Swerhone, G.G. Leppard, A.P. Hitchcock, Speciation and Quantitative Mapping of Metal Species in Microbial Biofilms Using Scanning Transmission X-ray Microscopy, *Environmental Science & Technology*, 40 (2006) 1556-1565.
- [107] A.P. Hitchcock, J.J. Dynes, J.R. Lawrence, M. Obst, G.D.W. Swerhone, D.R. Korber, G.G. Leppard, Soft X-ray spectromicroscopy of nickel sorption in a natural river biofilm, *Geobiology*, 7 (2009) 432-453.
- [108] K.P. Lam, A.P. Hitchcock, M. Obst, J.R. Lawrence, G.D.W. Swerhone, G.G. Leppard, T. Tylliszczak, C. Karunakaran, J. Wang, K. Kaznatcheev, D.A. Bazylinski, U. Lins, Characterizing magnetism of individual magnetosomes by X-ray magnetic circular dichroism in a scanning transmission X-ray microscope, *Chemical Geology*, 270 (2010) 110-116.
- [109] R.C. Hunter, A.P. Hitchcock, J.J. Dynes, M. Obst, T.J. Beveridge, Mapping the Speciation of Iron in *Pseudomonas aeruginosa* Biofilms Using Scanning Transmission X-ray Microscopy, *Environmental Science & Technology*, 42 (2008) 8766-8772.
- [110] F. Bourdelle, K. Benzerara, O. Beyssac, J. Cosmidis, D.R. Neuville, G.E. Brown, E. Paineau, Quantification of the ferric/ferrous iron ratio in silicates by scanning transmission X-ray microscopy at the Fe $L_{2,3}$ edges, *Contributions to Mineralogy*, 166 (2013) 423-434.
- [111] E. de Smit, I. Swart, J.F. Creemer, G.H. Hoveling, M.K. Gilles, T. Tylliszczak, P.J. Kooyman, H.W. Zandbergen, C. Morin, B.M. Weckhuysen, Nanoscale chemical imaging of a working catalyst by scanning transmission X-ray microscopy, *Nature*, 456 (2008) 222-225.

Chapter 2: Literature review: Looking beyond the earth's crust to see the crystal structures within

[112] A.P. Hitchcock, Z. Qin, S.M. Rosendahl, V. Lee, M. Reynolds, H. Hosseinkhannazer, Electrodeposition of Cu studied with in situ electrochemical scanning transmission x-ray microscopy, AIP Conference Proceedings, 1696 (2016) 020003.

[113] Flow Through Electrochemical cell for STXM Collaborative Project (2015):, A. Hitchcock, M. Obst, S.L. Harmer, H. Hooman, International consortium flow through electrochemical cell.

[114] V. Prabu, M. Obst, H. Hosseinkhannazer, M. Reynolds, S. Rosendahl, J. Wang, A.P. Hitchcock, Instrumentation for in situ flow electrochemical Scanning Transmission X-ray Microscopy (STXM), Review of Scientific Instruments, 89 (2018) 063702.

3 MATERIALS AND METHODS

3.1 Minerals

A combination of natural and synthetic mineral samples has been used for the research carried out in this thesis. All the single phase pentlandite samples were synthetic samples produced using high purity elements as starting materials.

3.1.1 Pentlandite synthesis

Pristine samples of natural pentlandite are difficult to obtain, since they often contain other mineral phases, namely pyrrhotite and violarite, and occasionally other phases such as millerite, pyrite and chalcopyrite, closely intergrown. Samples of pure pentlandite used in this thesis have been synthesised using an evacuated silica tube method, previously described by Xia, Zhou, Brugger, Ngothai, O'Neill, Chen and Pring [1]. Quantities of elemental iron (1 mm diameter wire, 99.99+%, Aldrich), elemental nickel (0.5 mm diameter wire, 99.99+%, Aldrich), and sulfur (flakes, 99.99+%, Aldrich) were weighed and placed inside silica tubing, which were sealed under a vacuum of at least 10^{-2} Torr. The stoichiometry of the final pentlandite samples was controlled approximately by selecting appropriate starting quantities of elemental materials. Samples were heated steadily to a temperature of 455°C, over 7 hours, and kept at that temperature for 3 hours before being heated at the same rate to the maximum temperature of 1150°C. Samples were held at this temperature for 10 hours, at which point the blast furnace was turned off and samples were allowed to gradually cool to room temperature overnight. This gradual heating process prevents the sealed silica tubes from exploding due to rapid vaporization of sulfur and allows for the sulfur to react with the iron and nickel. The resulting samples are composed of pure pentlandite, with a thin layer of millerite on the outside edge of the bullet [1, 2]. This thin millerite layer is removed using 1200 grit silicon-carbide sandpaper before analysing the sample's crystal structure and mineral purity.

3.1.2 Mineral characterisation

Each mineral sample was characterised using X-ray diffraction to show the crystal structure, and electron microprobe analysis to determine the average stoichiometry across the sample.

3.1.2.1 X-ray diffraction

The crystal structures of the minerals used in this thesis were determined by X-ray diffraction (XRD) using a Huber Guinier Image Plat G670 X-ray Diffractometer with Co $K\alpha$ radiation ($\lambda = 1.78892 \text{ \AA}$). Representative portions of each sample were finely ground in acetone and transferred to a silicon

crystal sample holder, and a diffraction pattern was obtained from across $2\theta = 10 - 90^\circ$. The peaks in each diffraction pattern were compared with mineral database files to confirm the crystal structure of the mineral, and the presence of any impurity phases. For the synthetic pentlandite samples, both ends of each bullet were analysed to examine homogeneity, and the samples selected for the work all showed good homogeneity across the whole sample.

3.1.2.2 *Electron microprobe analysis*

The stoichiometry of each sample was determined using quantitative electron microprobe analysis. A Cameca SXFive electron microprobe was used, operated at 20 kV, with a specimen current of 20 nA. A few small pieces of each sample were selected from regions throughout the pellet and set in a non-conductive resin, which was polished with a Struers TegraPol Automatic Polishing System, using a 9 μm cloth, followed by a 3 μm cloth, and finally with 0.04 μm colloidal silica, rinsing between each step. Once the samples were polished to a fine shine, they were coated with a fine carbon layer to prevent charging during analysis. During microprobe analysis, the distribution through the samples of different atomic species could be qualitatively observed by imaging using backscattered electron mode, which highlights differences in atomic mass with image contrast. At least 10 data points were collected for each phase in each sample to provide good statistics. Synthetic pentlandite samples that showed non-homogeneous distribution of iron and nickel atoms were rejected for this study.

3.1.3 Surface preparation

The specific surface preparation techniques used for each experiment are noted in the methods section of each chapter. An overview and description of each method is presented below.

3.1.3.1 *Pristine surfaces*

Two methods of creating clean mineral surfaces for analysis were used in the proceeding chapters: fracture in high vacuum, and fracture in nitrogen glove bag. For both these methods, prior to fracture, notches were made on the side of the minerals to create weak points along which the minerals would fracture. This served two purposes; firstly, to control the resulting shape of the mineral, and secondly to encourage the mineral to fracture through grains, rather than along grain boundaries, to expose a pristine surface, rather than a pre-oxidised surface.

The pristine mineral surfaces which were analysed at the Australian Synchrotron by XPS and NEXAFS were prepared by fracturing in high vacuum directly prior to analysis. Samples were prepared by shaping into approximately $5 \times 5 \times 10$ mm dimensions and mounting in a specially

designed, electrically conducting sample holder such that the long edge was protruding from the sample holder. The sample was then transferred into the preparation chamber of the endstation and evacuated to a pressure of at least 10^{-8} Torr. While under vacuum, a pair of opposing knife blade cleavers were used to apply a gradually increasing force to the edge of the sample until the sample fractured, revealing a pristine, unoxidized surface. The sample was then moved to the analysis chamber and the cleanliness of the sample assessed with an XPS broad survey scan, monitoring the carbon and oxygen signals to determine if the fractured sample was pristine.

The pentlandite samples presented in section 7.3 were analysed at the Canadian Light Source, where no fracture chamber was available on the endstation. Alternatively, the samples were fractured in an inert nitrogen atmosphere to achieve the most pristine surface possible. To achieve this, pentlandite samples which had already been notched were inserted into a glove bag which was temporarily fixed to the entrance of the introduction chamber of the endstation and was continuously flushed with nitrogen. The pentlandite samples were cleaved using hand-held steel end-cut wire cutters. Each sample was mounted on a molybdenum sample holder using carbon tape, with the pristine surface facing upwards. The samples were then transferred to the introduction chamber, and the door to the introduction chamber was sealed and beginning to evacuate before the glove bag was removed.

3.1.3.2 Dosed samples (controlled oxidation)

One of the pristine pentlandite samples from the Canadian Light Source was dosed with a controlled amount of H₂O vapour and is presented in Chapter 8. This was achieved in a preparation chamber which was maintained at a vacuum of at least 1×10^{-8} Torr. Demineralised water was held in a glass tube which was mounted on a valved inlet to the preparation chamber. The tube was surrounded by a liquid nitrogen filled vessel to freeze the water. The valve to the preparation chamber was opened to allow the vapour from the subliming water to enter the chamber where the pentlandite sample was held. The pressure in the chamber was closely monitored until the desired exposure was reached, at which point the valve to the subliming water was shut off and the vacuum allowed to recover. The pentlandite sample was then moved to the analysis chamber for measurements to be made.

3.1.3.3 Polished samples

The polished samples, and the samples exposed to acidic solution shown in Chapters 5 and 8 were polished using an incremental manual polishing procedure. Samples were separated from the ore where necessary by breaking off sections with hand-held end-cut wire cutters. Care was taken to avoid sections of obvious impurities sometimes present in natural samples, such as quartz. Samples

were shaped approximately using coarse grit (either 80 or 180 grit) wet-dry silicon-carbide sandpaper. The analysis face was then polished using increasing grit sandpaper (400, 600, 800, then 1200 grit), working the sample in figure-eight patterns to ensure even polishing of the surface and to remove scratches and pitting. The samples were then cleaned using ultrapure (MilliQ) water in an ultrasonic bath to remove residual silicon carbide, while preventing unnecessary crumbling of softer samples. To achieve a fine polish with a mirror shine, the samples were then polished using 1 μm diamond paste on a TriDent synthetic woven polishing cloth, working the sample in a figure-eight pattern. To remove the residual diamond paste, the samples were then cleaned once more in ultrapure water in an ultrasonic bath.

3.2 X-ray photoelectron spectroscopy

X-ray photoelectron spectroscopy (XPS) is a chemically sensitive spectroscopic technique which measures the energy of electrons which are ejected from the surface of a sample as a result of the interaction between incident photons (X-rays) and the sample matter. In a simple model, the energy of the photon is known ($h\nu$), the kinetic energy (E_k) of the ejected electron is measured, and the binding energy of that electron (E_b) is calculated by Eq. (3) [3].

$$h\nu = E_b + E_k + \phi \quad \text{Eq. (3)}$$

In Eq. (3), ϕ is the work function, or the minimum energy required to remove an electron from the sample. In practice, the work function includes the work function of the sample, and the work function of the spectrometer, and is constant across all measurements taken on the same instrument.

The binding energy of an ejected electron is characteristic of the atom and the subshell from which it originates and depends on the electrostatic attraction between the electron and the nucleus of the atom. Electrons in deeper subshells (closer to the nucleus) will have a binding energy greater than the valence electrons, due to the increased electrostatic attraction. An example of this can be seen in the survey spectrum for a slightly oxidised pentlandite sample, shown in Figure 3.1.

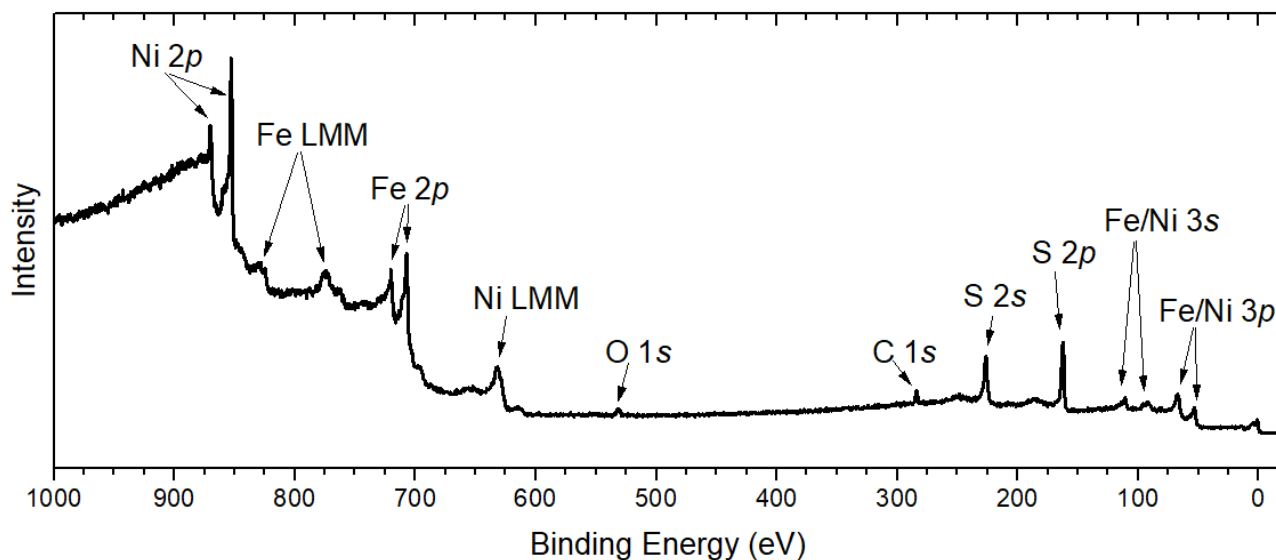


Figure 3.1: Example of survey spectrum for oxidised pentlandite, including peak assignments, obtained with $h\nu = 1487$ eV.

3.2.1 The photoelectron excitation process

A diagram of the photoelectron excitation process is shown in Figure 3.2. If the energy of the incident photons is sufficient; that is, if it exceeds the sum of the work function and the binding energy of the core electron, then the core electron will be ejected from the material as a photoelectron (e_p^-) with a kinetic energy determined by the difference between the energy of the incident photon and the binding energy of the electrons, given by Eq. (3). The photoelectron process leaves the atom in an excited state with a core hole, which results in a relaxation process to fill the core hole and leave the atom in its lowest energy state. One of the available relaxations processes is the Auger decay process, also shown in Figure 3.2. In this process, an electron from a higher shell fills the core hole. Due to the conservation of energy requirement, some energy must be released, and this may be done so by providing the energy to another electron which is emitted into the continuum. This electron is known as an Auger electron (e_A^-). In the example given in Figure 3.2, the core hole is in the K ($n = 1$) shell, an electron fills the core hole from the L_1 ($n = 2, l = 0$) shell and the Auger electron originates from the $L_{2,3}$ ($n = 2, l = 1$) sub shell. The Auger electron is then referred to as the KLL Auger electron, and its kinetic energy is determined by the difference between the K and L_1 energy levels, minus the energy of the $L_{2,3}$ level.

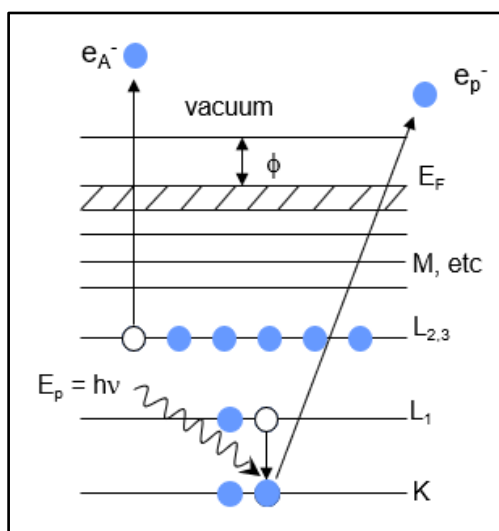


Figure 3.2: Schematic of photoelectron (e_p^-) and Auger decay (e_A^-) processes [4].

The binding energy of photoelectron peaks, and the kinetic energy of Auger electron peaks are characteristic of the atoms and the energy levels from which they originate. Therefore, XPS is a useful tool for identifying the chemical species in a sample. High resolution spectroscopy of core levels provides more detailed information about the bonding environments of the atoms in the sample, as small binding energy shifts in the peaks of a few eV can be observed. The fine changes to core level binding energy are caused by changes to the Coulomb potential, which is affected by the electron density around the atom. Changes to electron density around an atom are caused by the change in number of bonds or type of bonding partners, and can be affected by other factors such as bond length and strength [5]. Therefore, high resolution core level spectroscopy can give detailed bonding information about the sample.

There are additional features which can be observed in photoelectron spectra which arise from processes which have not yet been described herein. Extrinsic processes are caused by the interaction of the ejected photoelectron with the sample as it passes through to the surface and causes the secondary electrons to be liberated. This results in the loss of kinetic energy of the original photoelectron and presents in the photoelectron spectrum as a continuous background [6, 7]. Intrinsic processes occur simultaneously with the ejection of the original photoelectron and include features such as multiplet splitting and charge transfer satellites.

Multiplet splitting arises when there are unpaired electrons in the valence band. The unpaired core electron that remains due to photoionization couples with the unpaired valence electron(s) thus creating multiple possible final states. These multiple final states result in asymmetry of the core level photoelectron peak and can be a significant part of the spectrum. Multiplet peaks are particularly

prominent in many of the transition metal core level photoelectron peaks [8, 9]. The shape and intensity of the multiplet structure depends highly on the band structure of the material and therefore accurate and meaningful fitting of the multiplet structure is difficult [10].

When a core hole is created the system will create the lowest energy configuration available. Screening satellites are evidence of this outcome being achieved by a valence electron moving closer to the core hole and screening the coulomb potential of that core hole. Charge transfer satellites, such as those seen for first row transition metal fluoride compounds [11] are screening satellites which occur due to the creation of the core hole and are named as such since the valence electron is being transferred either from the metal to the ligand, or the ligand to the metal. These satellite peaks are observed at a higher binding energy than the core level peak and are generally seen with increasing intensity with increasing atomic number [12].

3.2.2 Surface sensitivity

XPS is considered to be a near surface sensitive technique, rather than a bulk analysis technique, due to the relatively short mean free path of electrons through a solid. However, the mean free path of electrons varies with their kinetic energy, and therefore the surface sensitivity can be ‘tuned’ by changing the energy of the initial photons, and therefore varying the kinetic energy of the photoelectrons. The sampling depth of an experiment is defined as 3λ , where λ is the inelastic mean free path of the photoelectrons. An approximation of the surface sensitivity can be calculated as described by Mönch [13].

$$R_s = 1 - e^{-d_{hkl}/\Lambda} \quad \text{Eq. (4)}$$

Eq. (4) calculates the proportion of the signal which originates from the first surface monolayer of a crystal, where d_{hkl} is the distance between $\{hkl\}$ lattice planes parallel to the surface, and Λ is the escape depth of the photoelectrons. The escape depth has been calculated [14] using the inelastic mean free path (IMFP) data published in literature [15]. Table 3.1 shows the surface sensitivity, including the inelastic mean free path of photoelectrons, and the proportion of the signal originating from the first surface layer. The average value of d_{ave} for pyrrhotite was calculated to be 2.2 Å, based on cell parameter values of $a = 11.9$ Å, $b = 6.85$ Å, and $c = 22.79$ Å [16], with a band gap of 0 eV and a density of 4.6 g/cm³ [17]. For pentlandite, the value of d_{110} was calculated to be 1.8 Å, based on a cell parameter value of $a_0 = 10.1$ Å [18], with a band gap of 0 eV and a density of 4.8 g/cm³ [19].

Table 3.1: Estimated proportion and percentage of the signal which originates from the first monolayer (R_s) of pyrrhotite and pentlandite surfaces, respectively, calculated for each photoelectron spectrum.

Pyrrhotite				
	hν (eV)	IMFP (\AA)	R_s	% Surface signal
Fe 2p	846	5.66	0.322	32.2
	1487	16.49	0.125	12.5
S 2p	260	5.12	0.349	34.9
	846	15.11	0.135	13.5
	1487	24.77	0.0850	8.5
Valence Band	700	15.27	0.134	13.4
	730	15.74	0.130	13.0
Pentlandite				
	hν (eV)	IMFP (\AA)	R_s	% Surface signal
Fe 2p	846	5.79	0.267	26.7%
	1110	10.42	0.159	15.9%
	1400	15.14	0.112	11.2%
	2000	24.13	0.072	7.2%
Ni 2p	1110	7.84	0.205	20.5%
	1400	12.74	0.132	13.2%
	2000	21.95	0.079	7.9%
S 2p	260	5.22	0.292	29.2%
	400	7.50	0.213	21.3%
	600	10.93	0.152	15.2%
	846	14.98	0.113	11.3%
	1110	18.98	0.090	9.0%
	1400	23.26	0.074	7.4%
	1475	24.34	0.0071	7.1%
Valence Band	260	7.84	0.205	20.5%
	400	10.25	0.161	16.1%
	600	13.55	0.124	12.4%
	846	17.40	0.098	9.8%

3.2.3 Data collection

The XPS data presented in this thesis were obtained at either the Australian Synchrotron or the Canadian Light Source, utilising the bright and tunable photons generated by these synchrotron facilities as a source of incident photons.

The Australian Synchrotron soft X-ray beamline is equipped with an elliptically polarised undulator, with a 1200 line/mm monochromator grating and 20 μm monochromator exit slit. This achieves an optimal energy range of 90 – 2000 eV, with a resolution of better than 0.01 eV at photon energies below 800 eV and a resolution of about 0.2 eV at higher energies around 1100 eV. The endstation is equipped with a SPECS Phoibos 150 hemispherical analyser and the samples were placed at 90° to the detector [20]. Survey scans were collected with a pass energy of 50 eV, resulting in a resolution of a little less than 1 eV. Fe and Ni $2p$ spectra, and O and C $1s$ spectra were each collected with a pass energy of 10 eV, providing an energy resolution of 0.2 eV, while the S $2p$ spectra were collected with a pass energy of 5 eV, giving an energy resolution of 0.1 eV [21].

The spectra presented in sections 7.3 and 8.1 were collected at the Canadian Light Source Variable Line Spacing Plane Grating Monochromator (VLS-PGM) (11ID-2) beamline with the Photoemission endstation fitted with a Scienta100 electron analyser. The beamline is equipped with a planar undulator source which provides photons of 5.5 – 260 eV energy [22]. The pass energy was set to 10 eV for each spectrum, and the entrance and exit slits were adjusted for each sample at each energy to maximise the signal while not overloading the detector. The spot size of the beamline is up to $500 \times 500 \mu\text{m}$, with an energy resolution of approximately 0.01 eV, and a spectral resolution of less than 0.2 eV [23].

3.2.4 Data processing

All photoelectron spectra were analysed with CasaXPS software [24]. The specific binding energy calibration used for spectra is noted in the methods section of each chapter and is either referenced to the Au $4f$ peak at 84.00 eV [25], or to adventitious carbon at 284.8 eV [7]. High resolution core level spectra were normalised to the bulk signal, and valence band spectra were normalised to constant flux at a binding energy below the onset of the spectrum.

Spectra were fitted by first fitting the leading edge of each spectrum with a symmetric peak shape, and then adding subsequent peaks at higher binding energies with similar peak widths, using the least number of peaks necessary, unless otherwise justified, until each spectrum is well fit. A Voigt function was chosen for the peak shape with a ratio of Gaussian and Lorentzian line shape of 50:50.

GL(50) is considered a reasonable choice for the synchrotron data, since the Gaussian broadening due to the analyser is expected to be around 0.1 eV, and the Lorentzian broadening due to the lifetime of a core hole is expected to also be approximately 0.1 eV [11].

The sulfur $2p$ spectra were fitted with two peaks for each feature attributable to the $2p_{3/2}$ and the $2p_{1/2}$ components of each feature. The $2p_{3/2}$ peak is fitted to the spectrum as it is the peak with the lowest binding energy, while the $2p_{1/2}$ peak is set to have the same peak width and half the area of the $2p_{3/2}$ peak, and fixed at a binding energy 1.19 eV higher. Each subsequent doublet feature is expected to have a similar peak width to the bulk peak, with the exception of sulfur-oxy species, and the polysulfide peak, which can be attributed to varying length polysulfide chains, and thus represent a range of sulfur binding energies [26].

3.3 X-ray absorption spectroscopy

X-ray absorption spectroscopy (XAS) is a complementary technique to XPS, since while XPS provides information about the core level electrons in a sample, XAS provides information about the unoccupied valence levels. X-ray absorption spectra represent the absorption of photons by a sample as the photon energy is varied across an absorption edge and is therefore able to measure the excitation of core electrons to unoccupied bound and continuum states. Spectra are collected with a variable energy photon source. The energy of the photon source is varied from below to above an absorption edge, and a measurement is made of the absorption function. Below the absorption edge, the incident photons do not have sufficient energy to excite the electron from its core shell. Just below the main absorption edge there is often some fine structure which is attributed to core electrons excited to previously unoccupied bound (valence) states, and the absorption energy of these features is equal to the difference between the initial (core) and final (bound states). When the photon energy equals that of the binding energy of the core level electron there is a dramatic increase in the absorption intensity, as the core electron is excited to the continuum. This region may show some structure due transitions to higher level bound states. The analysis of the region from just below to just above the absorption edge is known as X-ray Absorption Near Edge Spectroscopy (XANES), or sometimes especially for absorption edges in the soft X-ray region, it is known as Near Edge X-ray Absorption Fine Structure (NEXAFS) spectroscopy. Since the fine structure of the absorption edge reflects the transition to bound valence states, this technique is highly sensitive to bonding environment and electronic structure.

3.3.1 Data collection and processing

The drain current is the simplest method for detection of a NEXAFS spectrum. As electrons are excited from the ground state, they are replaced by the electrical connection to the sample. A measurement of the current from the sample is directly proportional to the absorption spectrum [27]. The surface sensitivity of total electron yield (TEY) detection is slightly larger than that for XPS of a similar core level [28, 29]. NEXAFS spectra in this thesis were collected at the Australian Synchrotron soft X-ray beamline, which measures the incident photon flux by a gold mesh. The flux was accounted for in the measured spectra by dividing the measured signal by the incident photon signal. Where possible, the spectra from internal Fe and Ni metal standards were measured simultaneously with the experimental spectra to calibrate the photon energy of the beamline. The main line of the Fe metal standard was calibrated to 706.8 eV [30, 31] and the main line of the Ni metal standard was calibrated to 852.7 eV [32]. A linear background from below the absorption edge was subtracted from each spectrum.

3.4 Resonant valence band photoemission spectroscopy

The spectra presented in sections 4.3 and 7.2 combine both photoemission and X-ray absorption techniques and the technique is referred to in this thesis as resonant valence band spectroscopy. The technique involves measuring the photoemission spectra of the valence band of the respective sample using selected photon energies of the transitions in the X-ray absorption L edge spectra. This technique allows for the identification of certain photoemission channels by their resonant enhancement at select photon energies. The technique employed in this thesis uses energies from below and above the $2p$ absorption threshold which promotes $2p$ core level electrons into the $3d$ states, while simultaneously measuring the $3d$ valence photoelectrons.

To understand this technique, it is helpful to consider it in two stages, although these stages happen simultaneously. The first stage is the absorption process, which promotes a core electron to the conduction band. The second step is the Auger decay process, in which a higher core electron decays into the deep core hole as another electron is ejected as an Auger electron, and a shallow core hole remains. Since the final state of this two-step process is the same as for the valence band photoemission process, it is possible for these two channels to interact [11]. This interaction can either cause resonance or antiresonance behaviour for sufficiently localized and therefore coherent final states, and is referred to as Fano resonance [33]. If the intermediate states are delocalized and therefore not coherent, the intensity of the spectra will simply be a superposition of the photoemission and Auger decay channels [34].

3.4.1 Data collection and analysis

Spectra for the resonant valence band studies were collected from pristine mineral surfaces at the Australian Synchrotron soft X-ray beamline. X-ray absorption spectra were obtained over the L_{2,3} edges of iron and nickel. Energies of interest were identified in these spectra at peaks and inflections, and these photon energies were used, in addition to photon energies below and above the L edges, to obtain the valence band spectra. The beamline photon energy was calibrated by energy correcting the internally collected absorption spectra of Fe metal to 706.8 eV [30, 31] and Ni metal to 852.7 eV [35]. Careful calibration of the electron analyser was achieved by recording the Au 4*f* photoelectron spectrum at some of the photon energies used throughout the experiments. The calibration of the binding energy of the Au 4*f*_{7/2} peak at 84.00 eV [25] at each photon energy was used to create a calibration curve by which each of the valence band spectra were calibrated. These calibration curves are shown in the respective results chapters. The valence band spectra were normalised to constant flux at an energy 5 eV below the onset of the valence band photoemission spectrum.

3.5 Photoemission Electron Microscopy

Photoemission electron microscopy (PEEM) is a technique which combines photoelectron spectroscopy with small scale imaging to produce images of the surface which show both topography and spatial distribution of chemical states. This spectromicroscopy technique utilises soft X-ray absorption spectra to distinguish chemical states. As the photons interact with the sample, electrons are emitted and are accelerated through a series of electrostatic lenses, to focus onto a fluorescent screen. The image produced on the screen is captured by a CCD detector to produce an image, in which the intensity of each pixel is dependent of the intensity of the emitted electrons. A schematic of a PEEM endstation is shown in Figure 3.3.

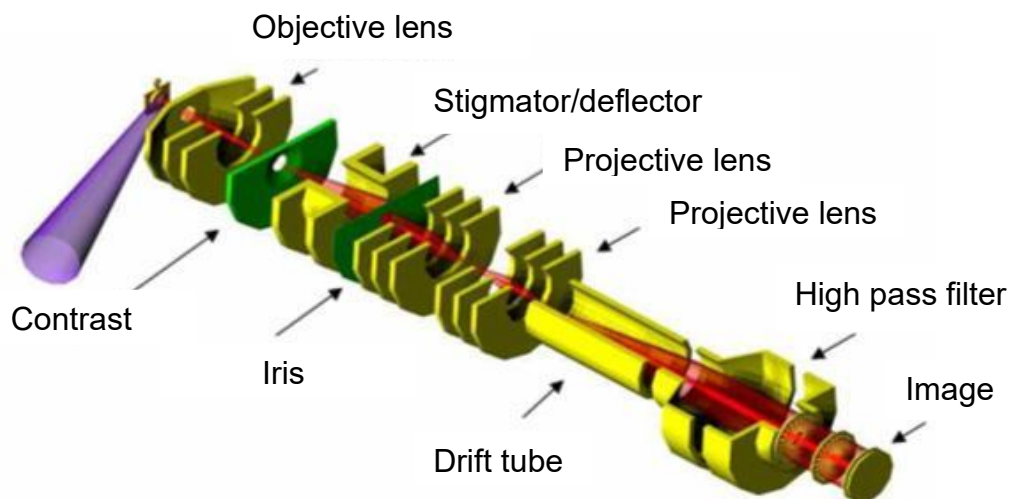


Figure 3.3: Schematic diagram of the photoemission electron microscopy (PEEM) optics. Reproduced with permission from [<http://efd.nsrcc.org.tw/EFD.php?num=242>].

The beamline used to collect the PEEM images in this thesis is also able to measure X-ray absorption spectra in electron yield mode by measuring the drain current from a sample over a range of photon energies which span an element's absorption edge. Both images and NEXAFS spectra from a PEEM endstation are shown in this thesis.

3.5.1 Data collection and processing

PEEM images and corresponding NEXAFS spectra were collected at the BL05B2 beamline at the National Synchrotron Radiation Research Centre (NSRRC) in Hsinchu, Taiwan [36]. The beamline is equipped with an elliptically polarised undulator and a spherical-grating monochromator, which results in a photon flux of 2×10^{12} photons/s at 800 eV in a $0.4 \text{ mm} \times 0.2 \text{ mm}$ spot size. The images are obtained by focussing the electrons emitted from the surface of the material through an electrostatic lens column and onto an aluminium coated YAG (yttrium aluminium garnet) fluorescent screen, which is mounted on a CCD detector, which collects images in total electron yield (TEY) mode. All PEEM images shown in this thesis have a field of view of $450 \text{ }\mu\text{m}$, with a resolution of 1000 pixels/image. NEXAFS spectra are obtained in total electron yield mode, using the drain current from the sample. Spectra are collected with a step size of 0.1 eV and a dwell time of 3 seconds to achieve an acceptable signal to noise ratio. An I_0 signal of the photon flux is collected simultaneously by a gold mesh. Samples were mounted to conducting sample holders using conductive carbon tape. The beamline endstation was operated at a vacuum of 10^{-9} Torr. The pixel intensity of images collected at absorption edges contain both absorption information and topographical effects caused by the geometry between the sample and the incident photon energy resulting in a larger photon flux at sharp surface features, and shadowing effects [37]. The topographical effects are counteracted by

the formula in Eq. (5), where I_A is the pixel intensity of the image taken at the peak energy, and I_B is the background image taken below the absorption energy. This provides a high contrast normalised image with an intensity range of -1 to 1, with minimal topographical effects. Spectra were processed as described previously in section 3.3.1.

$$I = \frac{I_A + I_B}{I_A - I_B} \quad \text{Eq. (5)}$$

3.6 Scanning transmission X-ray microscopy

Scanning transmission X-ray microscopy (STXM) is a relatively new microspectroscopy technique that is capable of analysing samples in environments other than the ultra-high vacuum environments required for XPS, NEXAFS and PEEM. A STXM beamline uses a zone plate to focus synchrotron radiation onto a small point on the sample. Images are generated by raster scanning the sample plate while the transmission of photons through the sample is measured by the detector.

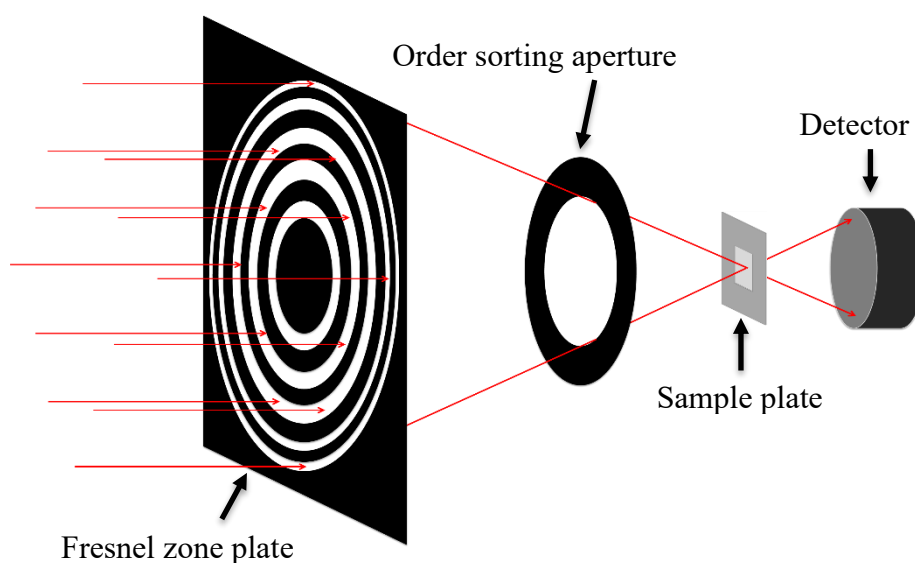


Figure 3.4: Schematic of key optical components of a STXM endstation.

To generate spectra from a point or an image, the incident photon energy is varied over an absorption edge. The detected transmission function (I_t) is converted to an absorption function, or optical density (OD) using the Beer-Lambert law, shown in Eq. (6), where I_o is the incident photon flux, and μd is the absorption function (μ) multiplied by the density of the material (d).

$$I_t = I_o e^{-\mu d} \quad \text{Eq. (6)}$$

There are multiple modes of operation for a STXM instrument; imaging at a fixed photon energy by rastering the sample window across a narrowly focussed beam; collecting spectra at a defined point or line across the sample; and collecting a stacked image. The stacked image is a series of rastered images collected over a chosen absorption edge. This creates a 3 dimensional image, where an absorption spectrum may be derived from each pixel in the image. STXM measures the transmission of photons through the sample, shown in Eq. (7). The transmission signal is then converted to the linear absorption scale, known as “optical density”, by dividing by the I_o (incident photon intensity) signal, and taking the natural logarithm, as shown in Eq. (8). For single images, unless the I_o is otherwise defined, it is taken as the maximum transmission signal in the unprocessed image, or better, the averaged pixel value over a region of the image which is determined to be a hole in the sample, as this is assumed to be the intensity of photon transmission through the window. The benefit of presenting images in optical density is that the scale is linear, rather than exponential, and therefore small changes in intensity due to thickness or changes in the absorption coefficient are linear and more easily visible.

$$I_t = I_o e^{-\mu d} \quad \text{Eq. (7)}$$

$$\text{OD} = -\ln\left(\frac{I_t}{I_o}\right) = \mu d \quad \text{Eq. (8)}$$

Spectra collected as line scans measure the transmission of photons across a defined photon energy range over a line across the sample. As with images, line scans are also converted to optical density, however the I_o signal may either be from a section of the line which passes over a “hole”, where maximum transmission occurs due to the absence of sample, or can be collected separately from a blank window, which accounts for attenuation due to the thickness of the window, and any contamination from the beamline which may contribute to the sample. The I_o signal used for stacks can be collected in the same way as for the line scans; either from a separate blank window, or from a “hole” in the sample.

Due to the design of the beamline optics and the sample plate, STXM can be used for samples which are difficult to analyse using the techniques previously described. The small spot size delivers a much lower radiation dose than a technique such as PEEM, while maintaining a good signal to noise ratio [38]. This makes the technique appropriate for samples such as polymers or biological samples which may otherwise suffer significant beam damage [39]. The development of sample holders extends the possibilities of sample environments to include wet cells [40], and more recently the boundaries of

this technique have been pushed further to include electrochemical analysis [41, 42], and with flow-through chemistry [43, 44]

3.6.1 Data collection

The data presented in Chapter 9 was collected at the Canadian Light Source STXM beamline 10ID1, or at the Swiss Light Source PolLux beamline. The CLS soft X-ray microscopy beamline has an Apple II Elliptically Polarizing Undulator light source which provides polarised photons in a range of 130 – 2700 eV. The spectral resolving power of the endstation for normal operation is $E/\Delta E = 3000$. The spatial resolution is 30 nm. The endstation is able to operate at atmospheric pressure, or under a vacuum of down to 10^{-2} Torr. Experiments were conducted with the chamber backfilled with helium at a pressure of approximately 130 Torr, as helium is transparent in the soft X-ray region [45].

The PolLux beamline at the Swiss Light Source uses polarized X-rays from a bending magnet source, which provides photons in an energy range of 250 – 1600 eV. The beamline is fitted with a spherical grating monochromator, with a spectral resolution of $E/\Delta E > 3000$. The spatial resolution is at least 40 nm. The vacuum of the beamline is separated from the endstation by a 100 nm thick Si_3N_4 membrane, which is located just upstream of the Fresnel Zone Plate, allowing the measurements to be made at atmospheric pressure, or in a vacuum of down to 10^{-6} Torr [46].

Since STXM is a relatively new technique, and the expansion of this technique to sulfide minerals is a key aspect of this thesis, the analysis of the results will be discussed in Chapter 9.

3.7 References

- [1] F. Xia, J. Zhou, J. Brugger, Y. Ngothai, B. O'Neill, G. Chen, A. Pring, Novel Route To Synthesize Complex Metal Sulfides: Hydrothermal Coupled Dissolution–Reprecipitation Replacement Reactions, *Chemistry of Materials*, 20 (2008) 2809-2817.
- [2] V. Drebushchak, T. Kravchenko, V. Pavlyuchenko, Synthesis of pure pentlandite in bulk, *Journal of Crystal Growth*, 193 (1998) 728-731.
- [3] S. Hagström, C. Nordling, K. Siegbahn, Electron spectroscopy for chemical analyses, *Physics Letters*, 9 (1964) 235-236.
- [4] S. Harmer, Personal Communication
- [5] S. Hüfner, *Photoelectron Spectroscopy*, 2nd ed., Springer-Verlag, Berlin, 1996.
- [6] D.A. Shirley, High-Resolution X-Ray Photoemission Spectrum of the Valence Bands of Gold, *Physical Review B*, 5 (1972) 4709-4714.
- [7] J.F. Moulder, W.F. Stickle, P.E. Sobol, K.D. Bomben, *Handbook of X-ray Photoelectron Spectroscopy*, Physical Electronics, Eden Prairie, Minnesota, 1992.
- [8] M.C. Biesinger, L.W.M. Lau, A.R. Gerson, R.S.C. Smart, Resolving surface chemical states in XPS analysis of first row transition metals, oxides and hydroxides: Sc, Ti, V, Cu and Zn, *Applied Surface Science*, 257 (2010) 887-898.

- [9] M.C. Biesinger, B.P. Payne, A.P. Grosvenor, L.W.M. Lau, A.R. Gerson, R.S.C. Smart, Resolving surface chemical states in XPS analysis of first row transition metals, oxides and hydroxides: Cr, Mn, Fe, Co and Ni, *Applied Surface Science*, 257 (2011) 2717-2730.
- [10] R.P. Gupta, S.K. Sen, Calculation of multiplet structure of core *p*-vacancy levels, *Physical Review B*, 10 (1974) 71-77.
- [11] F.K. de Groot, A., *Core Level Spectroscopy of Solids*, CRC Press, United States of America, 2008.
- [12] G. van der Laan, J. Zaanen, G. Sawatzky, R. Karnatak, J.-M. Esteve, Comparison of x-ray absorption with x-ray photoemission of nickel dihalides and NiO, *Physical Review B*, 33 (1986) 4253-4263.
- [13] W. Mönch, *Semiconductor Surfaces and Interfaces*, Springer-Verlag, Berlin, 1993.
- [14] Free Software Foundation, Compute inelastic mean free path of electron scattering, <http://electronsoftware.altervista.org/lab/IMFP.html>.
- [15] S. Tanuma, C.J. Powell, D.R. Penn, Calculations of electron inelastic mean free paths (IMFPs). IV. Evaluation of calculated IMFPs and of the predictive IMFP formula TPP-2 for electron energies between 50 and 2000 eV, *Surface and Interface Analysis*, 20 (1993) 77-89.
- [16] M. Tokonami, K. Nishiguchi, N. Morimoto, Crystal structure of a monoclinic pyrrhotite (Fe₇S₈), *American Mineralogist*, 57 (1972) 1066-1080.
- [17] D.A. Clark, Hysteresis properties of sized dispersed monoclinic pyrrhotite grains, *Geophysical Research Letters*, 11 (1984) 173-176.
- [18] B. Etschmann, A. Pring, A. Putnis, B.A. Grguric, A. Studer, A kinetic study of the exsolution of pentlandite (Ni,Fe)₉S₈ from the monosulfide solid solution (Fe,Ni)S, *American Mineralogist*, 89 (2004) 39-50.
- [19] W.L.C. Roberts, T. J., G.R. Rapp, *Encyclopedia of Minerals*, 2nd ed., Van Nostrand Reinhold, 1990.
- [20] B.C.C. Cowie, A. Tadich, L. Thomsen, The Current Performance of the Wide Range (90–2500 eV) Soft X-ray Beamline at the Australian Synchrotron, *AIP Conference Proceedings*, 1234 (2010) 307-310.
- [21] B. Cowie, unpublished beamline resolution calculator, Personal Communication
- [22] J. Cutler, D. Chapman, L. Dallin, R. Lamb, The Brightest Light in Canada: The Canadian Light Source, *Quantum Beam Science*, 1 (2017) 4.
- [23] Y.F. Hu, L. Zuin, R. Reininger, T.K. Sham, VLS-PGM Beamline at the Canadian Light Source, *AIP Conference Proceedings*, 2007.
- [24] Casa Software, CasaXPS, 2000.
- [25] D. Briggs, M.P. Seah, *Practical Surface Analysis, Auger and X-ray Photoelectron Spectroscopy*, 2nd ed. ed., Wiley & Sons, Chichester, England, 1990.
- [26] R.S.C. Smart, W.M. Skinner, A.R. Gerson, XPS of sulphide mineral surfaces: metal-deficient, polysulphides, defects and elemental sulphur, *Surface and Interface Analysis*, 28 (1999) 101-105.
- [27] J. Stöhr, *NEXAFS Spectroscopy*, Springer-Verlag, Berlin, 1992.
- [28] M. Abbate, J.B. Goedkoop, F.M.F. de Groot, M. Grioni, J.C. Fuggle, S. Hofmann, H. Petersen, M. Sacchi, Probing depth of soft x-ray absorption spectroscopy measured in total-electron-yield mode, *Surface and Interface Analysis*, 18 (1992) 65-69.
- [29] M. Kasrai, W.N. Lennard, R.W. Brunner, G.M. Bancroft, J.A. Bardwell, K.H. Tan, Sampling depth of total electron and fluorescence measurements in Si L- and K-edge absorption spectroscopy, *Applied Surface Science*, 99 (1996) 303-312.
- [30] P. Marcus, J.M. Grimal, The anodic dissolution and passivation of Ni-Cr-Fe alloys studied by ESCA, *Corrosion Science*, 33 (1992) 805-814.
- [31] L. Soriano, M. Abbate, F.M.F. de Groot, D. Alders, J.C. Fuggle, S. Hofmann, H. Petersen, W. Braun, Chemical analysis of passivated and oxidized layers on FeCr and FeTi alloys by soft x-ray absorption spectroscopy, 20 (1993) 21-26.
- [32] S.W. Goh, A.N. Buckley, R.N. Lamb, W.M. Skinner, A. Pring, H. Wang, L.-J. Fan, L.-Y. Jang, L.-J. Lai, Y.-w. Yang, Sulfur electronic environments in α -NiS and β -NiS: examination of the

- relationship between coordination number and core electron binding energies, *Phys Chem Minerals*, 33 (2006) 98-105.
- [33] U. Fano, Effects of Configuration Interaction on Intensities and Phase Shifts, *Physical Review*, 124 (1961) 1866-1878.
- [34] M.F. López, A. Höhr, C. Laubschat, M. Domke, G. Kaindl, Resonant Photoemission vs. Coster-Kronig Auger Decay At the L_{III} Thresholds of Ni Metal and CuO, *Europhysics Letters*, 20 (1992) 357-362.
- [35] S.W. Goh, A.N. Buckley, R.N. Lamb, L.-J. Fan, L.-Y. Jang, Y.-w. Yang, Pentlandite sulfur core electron binding energies, *Phys Chem Minerals*, 33 (2006) 445-456.
- [36] D.H. Wei, Y.-L. Chan, Y.-J. Hsu, Exploring the magnetic and organic microstructures with photoemission electron microscope, *Journal of Electron Spectroscopy and Related Phenomena*, 185 (2012) 429-435.
- [37] S. Günther, B. Kaulich, L. Gregoratti, M. Kiskinova, Photoelectron microscopy and applications in surface and materials science, *Progress in Surface Science*, 70 (2002) 187-260.
- [38] I. Koprinarov, A.P. Hitchcock, X-ray Spectromicroscopy of Polymers: An introduction for the non-specialist, <http://unicorn.mcmaster.ca/stxm-intro/polySTXMIintro-all.html>.
- [39] Y. Zubavichus, O. Fuchs, L. Weinhardt, C. Heske, E. Umbach, J.D. Denlinger, M. Grunze, Soft X-Ray-Induced Decomposition of Amino Acids: An XPS, Mass Spectrometry, and NEXAFS Study, *Radiation Research*, 161 (2004) 346-358.
- [40] M. Obst, A. Hitchcock, T. Ayers, C. Schietinger, C. Karunakaran, A novel wet cell for in situ 2D and 3D STXM studies, *Canadian Light Source activity report*, (2008) 142-143.
- [41] D. Guay, J. Stewart-Ornstein, X. Zhang, A.P. Hitchcock, In Situ Spatial and Time-Resolved Studies of Electrochemical Reactions by Scanning Transmission X-ray Microscopy, *Analytical Chemistry*, 77 (2005) 3479-3487.
- [42] A.P. Hitchcock, Z. Qin, S.M. Rosendahl, V. Lee, M. Reynolds, H. Hosseinkhannazer, Electrodeposition of Cu studied with in situ electrochemical scanning transmission x-ray microscopy, *AIP Conference Proceedings*, 1696 (2016) 020003.
- [43] V. Prabu, M. Obst, H. Hosseinkhannazer, M. Reynolds, S. Rosendahl, J. Wang, A.P. Hitchcock, Instrumentation for in situ flow electrochemical Scanning Transmission X-ray Microscopy (STXM), *Review of Scientific Instruments*, 89 (2018) 063702.
- [44] M. Obst, P. Ingino, A. Hitchcock, V. Prabu, A. Picard, Redox-Chemistry of Environmental Biofilms Probed on the Submicron Scale by in-situ Electrochemistry Scanning Transmission (soft) X-ray Microscopy, *Microscopy and Microanalysis*, 24 (2018) 502-505.
- [45] K.V. Kaznatcheev, C. Karunakaran, U.D. Lanke, S.G. Urquhart, M. Obst, A.P. Hitchcock, Soft X-ray spectromicroscopy beamline at the CLS: Commissioning results, *Nuclear Instruments and Methods in Physics Research A*, 582 (2007) 96-99.
- [46] U. Flechsig, C. Quitmann, J. Raabe, M. BöGe, R. Fink, H. Ade, The PolLux Microspectroscopy Beam line at the Swiss Light Source, *AIP Conference Proceedings*, 879 (2007).

4 PRISTINE FRACTURE SURFACES OF MONOCLINIC PYRRHOTITE

Pyrrhotite is an abundant terrestrial iron sulfide mineral which is commonly associated with valuable metal sulfide minerals such as pentlandite and is a carrier for platinum group metals. Pyrrhotite is one of the most commonly found sulfide minerals, and therefore is important for the mining and minerals processing industries. During mineral processing, pyrrhotite reacts and dissolves to produce acidic solutions that may contribute significantly to acid mine drainage and affect the recovery of valuable mineral phases. Pyrrhotite has also been a mineral of interest regarding pre-biotic reactions. There is a suggestion that the catalytic potential of pyrrhotite's surface may have played a role in the formation of the building blocks of living organisms [1]. A mineral's reactions are determined by its surface structure and electronic structure; therefore, these aspects are important areas of research for understanding the surface reactions.

Some studies have investigated the surface structure of pyrrhotite using XPS, but the spectra are difficult to interpret. The difficulty arises from the overlapping binding energies of multiple bulk and surface states in both the Fe and S $2p$ photoelectron spectra. The spectra are further convoluted by final state effects such as multiplet states and energy loss features which contribute to the spectra, which may be misinterpreted as additional states [2-4].

While some previous studies have investigated the surface structure of troilite (FeS) and monoclinic pyrrhotite and hexagonal pyrrhotites, none have been able to spectroscopically identify the species present on fracture surfaces [3, 4]. Other studies have investigated the electronic structure of pyrrhotite; investigating the bonding between Fe and S states [5-8], and identifying weak π - π bonding between Fe atoms adjacent in the c-axis [9]. No studies have yet addressed the relationship between the electronic structure of pyrrhotite and the effect of electron correlation on the photoelectron spectra and its effect on the interpretation of the presence of surface states.

The original contribution to knowledge presented in this chapter is the identification of the surface species present on fracture surfaces of monoclinic pyrrhotite using varying analysis depths to isolate the surface and bulk contributions to X-ray photoelectron spectra. This technique allows for the identification of the bulk pyrrhotite sulfide line shape. Detailed analyses of the valence states and the effect of electron correlation in transition metal sulfides are considered and inform a discussion about the peak line shape in photoelectron spectra.

4.1 Methods

The sample analysed in this chapter is a section of monoclinic pyrrhotite originating from the Naica Mine in Chihuahua, Mexico. The sample was analysed using X-ray diffraction to confirm the 4C crystal structure, and a total acid digest followed by inductively coupled plasma – mass spectrometry to determine the stoichiometry to be $\text{Fe}_{6.93}\text{S}_{8.00}$.

The core level and valence band X-ray photoelectron spectra, and the X-ray absorption spectra were collected at the Australian Synchrotron soft x-ray beamline (14ID) [10]. The binding energies of the photoelectron spectra were calibrated using the Au $4f_{7/2}$ peak of a gold standard and calibrating the peak 84.00 eV [11]. The pyrrhotite sample was fractured in the preparation chamber of the endstation under a vacuum of at least 10^{-8} Torr, as described in section 3.1.3. A survey spectrum for this sample was collected with $h\nu = 1487$ eV and is shown in Figure 4.1. There are no oxygen or carbon species evident in the survey spectrum around 530 eV or 285 eV respectively. The peaks in the survey spectrum can all be attributed to iron and sulfur species, and the ratio of the Fe $3p$ and S $2p$ features is consistent with the stoichiometry of the sample as measured by microprobe analysis.

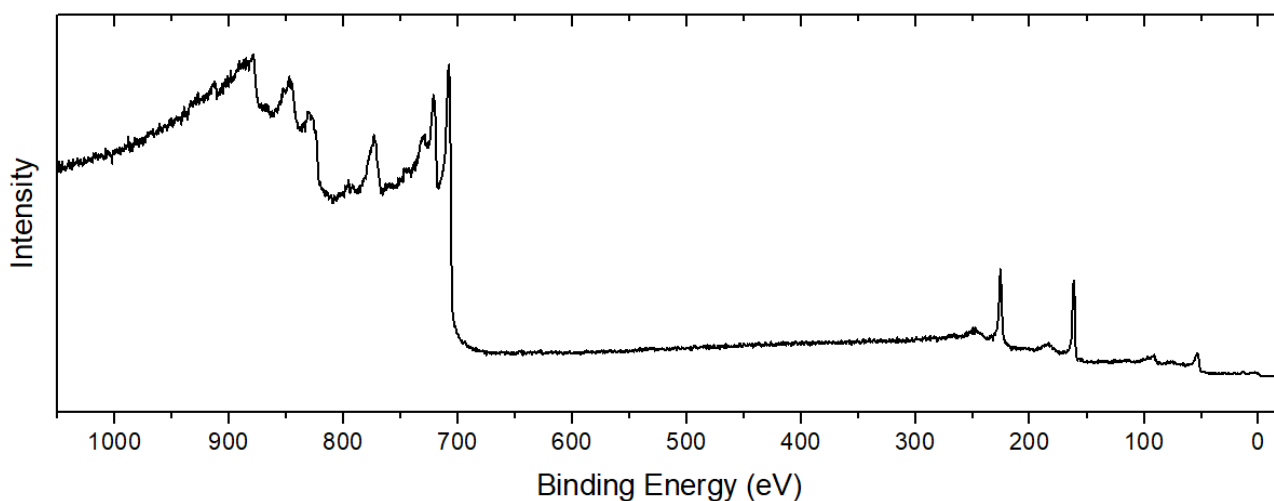


Figure 4.1: Survey spectrum for pristine vacuum fractured monoclinic pyrrhotite which shows no evidence of carbon or oxygen contamination at the surface. $h\nu = 1487$ eV.

Fe and S $2p$ photoelectron spectra were normalised to the bulk peaks to allow direct comparison between spectra. Each sulfur $2p$ spectrum has a Shirley background applied [12]. Where the S $2p$ spectrum has been fitted, each feature is fitted with two spin-orbit split peaks for the $2p_{3/2}$ and $2p_{1/2}$ peaks as described in section 3.2.4. Valence band spectra have been normalised to constant photon flux at a point a few eV below the onset of the spectrum to compare relative intensities of the features.

4.2 Analysis of sulfur states

Sulfur $2p$ photoelectron spectra were obtained with $h\nu = 260$ eV, 846 eV and 1487 eV and are shown in Figure 4.2. The $2p_{3/2}$ peak for bulk monosulfide is at 161.2 eV consistent with the bulk five-coordinate peak fitted to previously reported monoclinic pyrrhotite [3]. While these spectra have been collected with the same experimental conditions and acquisition parameters as the pentlandite spectra presented in Chapter 6 and recently published in Applied Surface Science [13], the line widths of the main peak shown in the three spectra in Figure 4.2 are considerably broader and vary between approximately 0.75 to 0.9 eV. The $h\nu = 260$ eV spectrum has a significantly broader line width of the main peak in comparison to the $h\nu = 846$ eV spectrum, and the minimum between the $2p_{3/2}$ and $2p_{1/2}$ peaks is not as great as in the bulk sensitive spectrum. A similar observation is made in the comparison of the S $2p$ spectra for chalcopyrite [14] and bornite [15]; the latter of which is seen to have a broader line width due to the surface features present. Therefore, the increase in the line width of the main peak in the spectra presented in Figure 4.2 is expected to be due to the increase in spectral contribution from surface features. All three spectra show an asymmetric line shape that extends in the high binding energy region to approximately 167 eV. These tails have previously been attributed to a Doniach-Sunjic line shape for conductors due to pyrrhotite's possible metallic nature [3, 4, 16]. However, the true shape of the pyrrhotite bulk monosulfide tail is difficult to determine due to the uncertainty in bulk features that should be fitted, and the overlap of the bulk features with surface disulfide and polysulfide features.

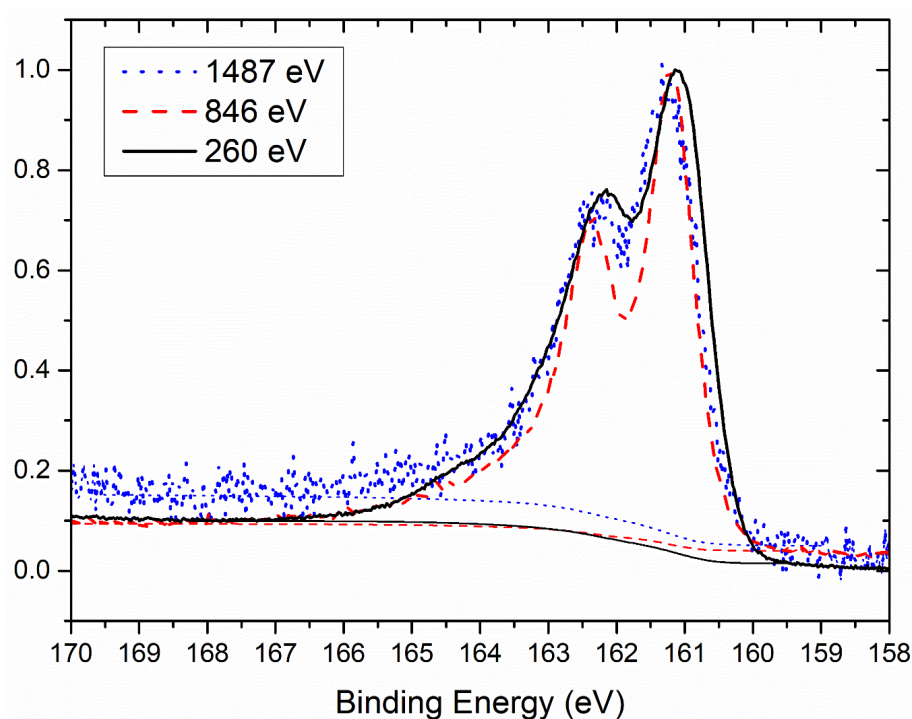


Figure 4.2: Vacuum fractured monoclinic pyrrhotite S $2p$ photoelectron spectra collected with $h\nu = 260$ eV, 846 eV, and 1487 eV.

4.2.1 Identifying the sulfur states on pyrrhotite fracture surfaces

A method of finding the binding energy of surface features is to calculate a difference spectrum from spectra of varying surface sensitivities. Each spectrum ($I(E)$) can be considered to be a convolution of bulk ($B(E)$) and surface states ($S(E)$) and therefore may be expressed in the simplified form shown in Eq. (9). In this equation, α and β are coefficients of the bulk and surface states and are dependent on the incident photon energy.

$$I(E) = \alpha B(E) + \beta S(E) \quad \text{Eq. (9)}$$

Therefore the 846 eV and 260 eV spectra can be shown by Eq. (10) and Eq. (11).

$$I_{846}(E) = \alpha_{846}B(E) + \beta_{846}S(E) \quad \text{Eq. (10)}$$

$$I_{260}(E) = \alpha_{260}B(E) + \beta_{260}S(E) \quad \text{Eq. (11)}$$

Since each spectrum is normalised to the bulk sulfide peak, it is expected that $\alpha_{846} \cong \alpha_{260}$, and that $\beta_{846} < \beta_{260}$. The difference spectrum, calculated by Eq. (12) and shown in Figure 4.3, is expected to represent the shape of the surface components of the spectrum.

$$\begin{aligned} \Delta I &= I_{260} - I_{846} && \text{Eq. (12)} \\ &= \alpha_{260}B + \beta_{260}S - \alpha_{846}B - \beta_{846}S \end{aligned}$$

$$\Delta I = (\beta_{260} - \beta_{846})S \quad (\beta_{260} - \beta_{846} > 0) \quad \text{Eq. (13)}$$

The 846 eV and 260 eV spectra were selected for this calculation, since the 1487 eV spectrum has a lower resolution and a greater line width, and therefore any difference spectrum calculated using the 1487 eV spectrum would have less detail. Furthermore, it can be seen in Figure 4.2 that the

background in the 1487 eV spectrum is significantly higher than for the 846 eV and 260 eV spectra, therefore using the 1487 eV spectrum will result in distortion of the difference spectrum.

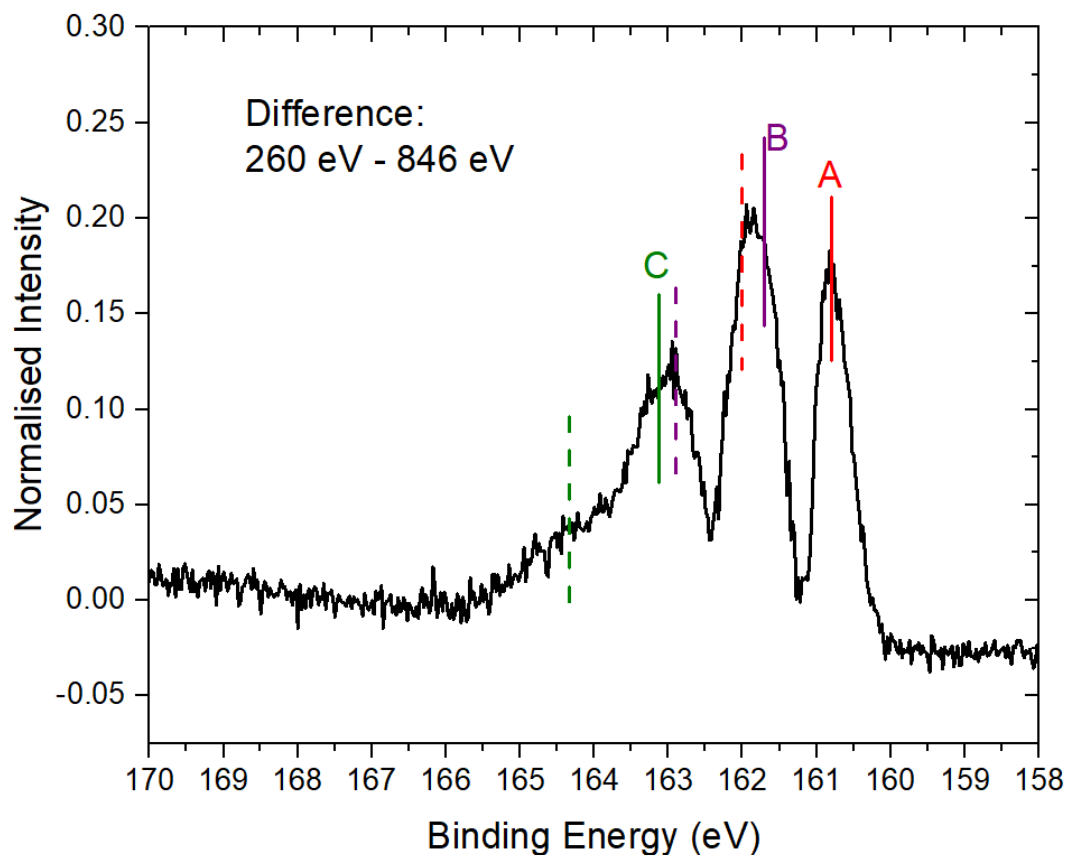


Figure 4.3: Difference spectrum calculated by subtracting S 2p 846 eV spectrum from 260 eV spectrum. The difference spectrum shows evidence of three doublet features labelled A, B and C.

The difference spectrum in Figure 4.3 shows three clear peaks. The features on the high binding energy side show some asymmetry, indicating that this may be due to a broad doublet. The negative intensity of the background on the low binding energy side is due to the normalisation of the two spectra and not a significant feature of this difference spectrum. Since each feature has a doublet at a binding energy 1.19 eV higher, and due to the overlap of some of these peaks, it is simplest to begin identifying doublets on the low binding energy side. The first clear peak is around 160.8 eV and is due to the $2p_{3/2}$ component of peak A as labelled in Figure 4.3. The $2p_{1/2}$ component of this peak is therefore expected at 162.0 eV and is marked with a vertical dashed line. The second peak in the spectrum is broader than the first, and is centred around 161.8 eV, rather than at 162.0 eV as is expected for the $2p_{1/2}$ components of peak A. Furthermore, the second peak has a greater intensity than the first peak, contrary to what is expected for the $2p_{1/2}$ doublet. Therefore, it is expected that there is a $2p_{3/2}$ peak of a second component contributing to the spectrum in this region. It is estimated that the binding energy of this component is around 161.7 eV, thus deducing the $2p_{1/2}$ component is

at 162.9 eV, as indicated in Figure 4.3. The third component, which is estimated to be broader than the first two based on the width of the high binding energy shoulder, is at a higher binding energy around 163 eV, labelled as peak C in Figure 4.3.

Since the difference spectrum is expected to represent the shape of the surface states only (Eq. (13)), this spectrum may be subtracted from one of the original spectra to obtain the shape of the bulk peak. This has been done by subtracting the difference spectrum from the $h\nu = 846$ eV spectrum, to obtain the shape shown in Figure 4.4. This shape is expected to represent the shape of the bulk monoclinic pyrrhotite sulfur spectrum, with no surface component. It is noted that the shape closely resembles the sulfur $2p$ spectrum of the structurally similar millerite (NiS) [17] more so than the Doniach-Sunjic line shape [16]. Unfortunately, the bulk line shape shown here gives no clear indication of the presence of multiple bulk components, as has been found for pentlandite [13, 18], and has been suggested for pyrrhotite [3]. The origin of this asymmetric line shape is discussed in more detail further in this chapter.

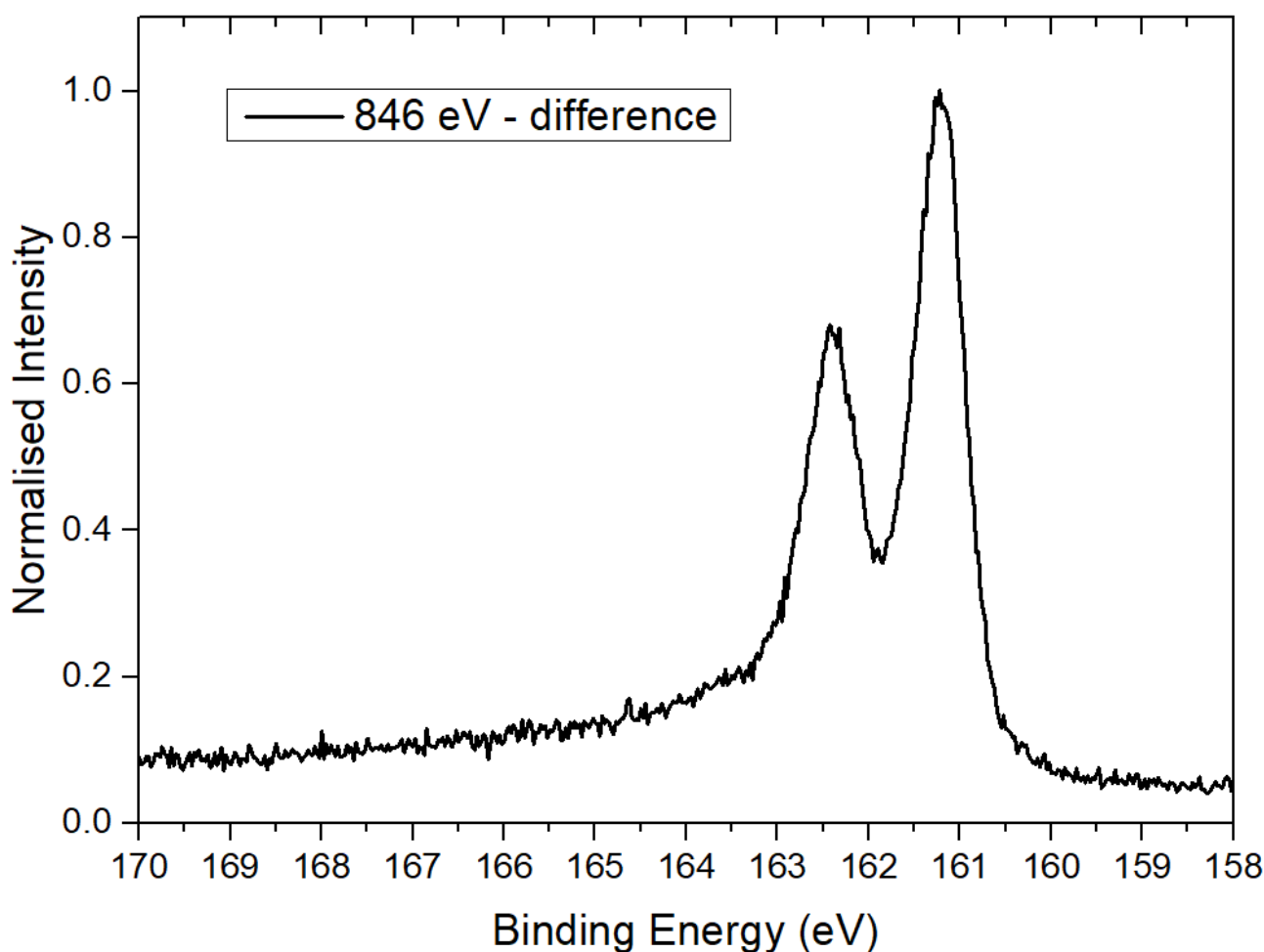


Figure 4.4: Bulk peak shape obtained by subtracting the difference spectrum (Figure 4.3) from the 846 eV spectrum.

4.2.2 Fitting pyrrhotite S 2p photoelectron spectra

The pyrrhotite S 2p spectra from Figure 4.2 have been fitted with the three surface components identified in Figure 4.3, in addition to the bulk peak shape identified in Figure 4.4. It is clear from the spectrum in Figure 4.4 that an asymmetric line shape is required, however only a few asymmetric line shapes have been developed [19], with a theoretical explanation given only for the Doniach-Sunjic line shape [16, 20]. Two methods have been used to fit the bulk sulfide line shape. The first is to use the hybrid Doniach-Sunjic/Gaussian-Lorentzian line shape “H(0.02, 70)GL(50)” [20]. This line shape was found to fit the $h\nu = 1487$ eV spectrum, which is expected to have the most bulk contribution. The line shape was then applied to the bulk contribution of the $h\nu = 846$ eV and 260 eV spectra. No extra doublets were required for the bulk sensitive spectrum, but doublets were required for the $h\nu = 846$ eV and 260 eV spectra at the energies identified in Figure 4.3. The fitted spectra are shown in Figure 4.5, with the quantification of these spectra shown in Table 4.1.

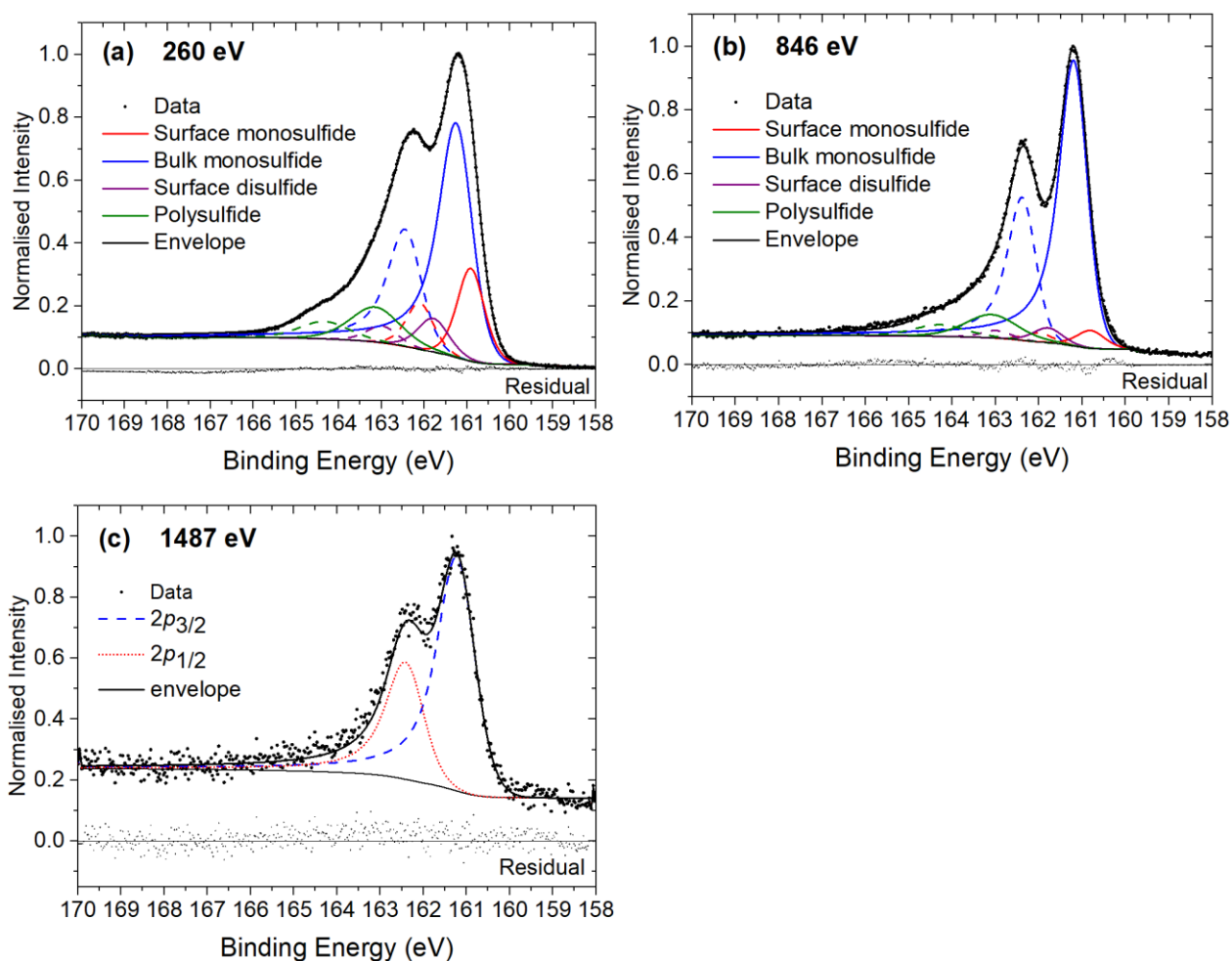


Figure 4.5: Sulfur 2p spectra for vacuum fractured monoclinic pyrrhotite, collected with $h\nu =$ (a) 260 eV, (b) 846 eV, and (c) 1487 eV, each fitted with asymmetric bulk peaks in addition to symmetric surface peaks as identified in Figure 4.3.

Table 4.1: Peak contributions to sulfur 2p spectra of pristine pyrrhotite, fitted with asymmetric bulk peaks.

Species	Binding Energy (FWHM) % contribution to fit			
	Photon Energy:	260	846	1487
Peak A		160.9 (0.75) <u>19.7</u>	160.8 (0.77) <u>5.1</u>	<u>0.0</u>
Bulk monosulfide		161.2 (0.88) <u>58.6</u>	161.2 (0.73) <u>78.3</u>	161.2 (0.99) <u>100</u>
Peak B		161.8 (0.85) <u>8.1</u>	161.8 (0.79) <u>4.3</u>	<u>0.0</u>
Peak C		163.1 (1.3) <u>13.6</u>	163.1 (1.3) <u>12.3</u>	<u>0.0</u>
Estimated % from surface monolayer		34.9	13.5	8.5

The binding energy of the surface peaks fitted in $h\nu = 260$ eV and 846 eV spectra in Figure 4.5a,b is consistent between both spectra and consistent with the difference spectrum in Figure 4.3. The residuals from the fitted spectra, shown on each graph below each fitted spectrum, are minimal and show no extra components. However, the small residual and consistent fit are not necessarily evidence of the validity of the fit, and the quantification of sulfur species in

Table 4.1 is therefore not necessarily reliable, specifically in the high binding energy region where disulfide and polysulfide species are expected to overlap with the tail of the bulk sulfide peak. Furthermore, the fitted contribution from peak C, assuming it is a surface contribution, does not follow that which is expected based on the estimated contribution from the surface layer, and no surface contribution is fitted in the $h\nu = 1487$ eV spectrum. Additionally, having fitted the tail with a hybrid Doniach-Sunjić line shape is certainly not evidence of the metallic nature of pyrrhotite, since fitting XPS line shapes cannot be used as a diagnostic tool for the nature of the sample.

The second method for fitting the bulk sulfide line shape is one similar to that used for fitting the asymmetric tails of pentlandite sulfur spectra [13]. This method uses an empirically-derived series of symmetric peaks to model the asymmetric tail. This tail shape has been modelled to fit the bulk line shape that was identified in Figure 4.4. The details of the series of symmetric peaks are shown in Table 4.2, where the parameters are set relative to those of the bulk $2p_{3/2}$ peak. The fit of these peaks to the bulk line shape are shown in Figure 4.6. The S 2p spectra were then fitted with this bulk line shape in addition to the three surface components identified in Figure 4.3, which were required in all three spectra, with differing intensities which varied with surface sensitivity. The fitted spectra are shown in Figure 4.6b-d.

Table 4.2: Peak parameters for symmetric peaks fitting the high binding energy tail of bulk pyrrhotite, relative to the bulk $2p_{3/2}$ peak.

	Area	FWHM	Position
Peak 1	$\times 0.13$	$\times 1.2$	+ 0.63
Peak 2	$\times 0.28$	$\times 2.2$	+ 1.66
Peak 3	$\times 0.28$	$\times 5.8$	+ 3.2

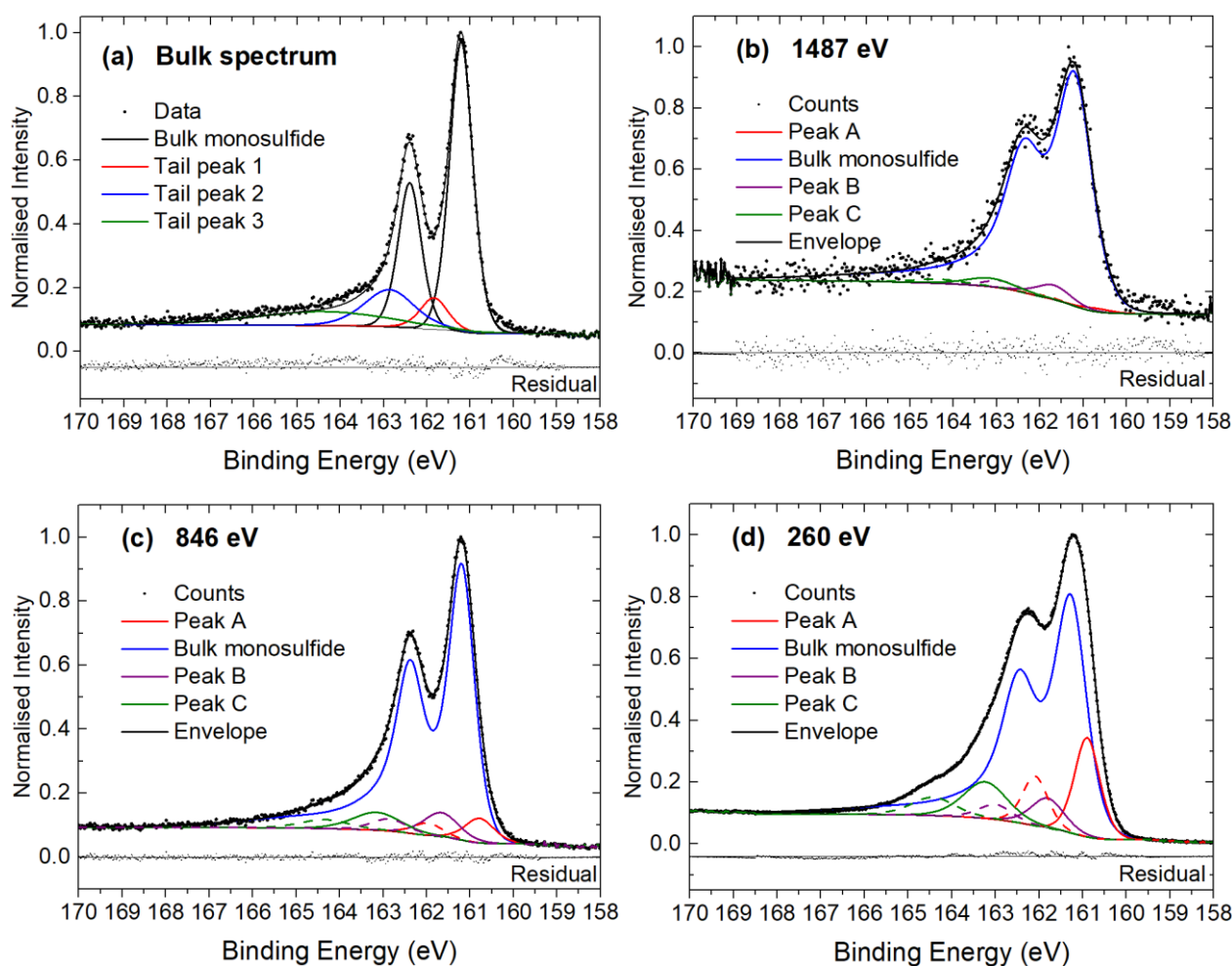


Figure 4.6: (a) Bulk peak shape obtained by subtracting the difference spectrum (Figure 4.3) from the 846 eV spectrum, and sulfur 2p photoelectron spectra collected with a photon energy of (b) 1487 eV, (c) 846 eV, and (d) 260 eV, each fitted with additional peaks to account for the high binding energy tail and surface components where necessary.

By fitting with the additional peaks to account for the high binding energy tail it is possible to obtain a fit for each spectrum with a small residual which is within the noise of each spectrum. However, unlike the fitted spectra in Figure 4.5 which only required surface species fitted to the more surface sensitive spectra, every spectrum in Figure 4.6 requires some surface component, including the $h\nu = 1487$ eV spectrum. The binding energy and contribution of each sulfur species fitted to the spectra in

Figure 4.6 are shown in Table 4.3. For comparison, the contribution of these species to the spectra fitted with the hybrid asymmetric peak shape (method 1) are also shown in Table 4.3.

Table 4.3: Peak contributions to the pyrrhotite sulfur 2p spectra fitted with empirical tail shapes. The “% contribution from asymmetric fit” data is taken from

Table 4.1 for comparison.

Species	Binding Energy (FWHM)			% contribution from asymmetric fit		
	% contribution			260	846	1487
Peak A	160.9 (0.68) <u>16.8</u>	160.8 (0.80) <u>5.9</u>	160.7 (0.80) <u>0.8</u>	<u>19.7</u>	<u>5.1</u>	-
Bulk monosulfide	161.2 (0.84) <u>65.9</u>	161.2 (0.69) <u>80.2</u>	161.2 (0.93) <u>91.3</u>	<u>58.6</u>	<u>78.3</u>	<u>100</u>
Peak B	161.8 (0.90) <u>6.6</u>	161.7 (0.95) <u>6.9</u>	161.7 (0.95) <u>4.4</u>	<u>8.1</u>	<u>4.3</u>	-
Peak C	163.2 (1.2) <u>10.7</u>	163.2 (1.3) <u>7.0</u>	163.2 (1.3) <u>3.5</u>	<u>13.6</u>	<u>12.3</u>	-
Estimated % from surface monolayer	34.9	13.5	8.5			

4.2.3 Assignment of S 2p peaks

A peak which is associated with a monomeric surface species has been previously identified in synchrotron studies of vacuum fractured pyrrhotite surfaces [3, 4] However, surface dimers or polymers could not be identified due to the overlap in binding energy of the relatively broad bulk monosulfide peak with the binding energy region in which polymerised sulfur species are expected. In this work, spectra obtained with varying surface sensitivities have been used to identify and extract the surface and bulk components of each spectrum. Synchrotron radiation is useful for this purpose [21] and is employed in this thesis, where the incident photon energy is selected to maximise the surface sensitivity of the spectra. Difference spectra between surface and bulk sensitive spectra definitively show the binding energies of surface components. By this method, it is shown here in Figure 4.3 that three components contribute to the surface sensitive $h\nu = 260$ eV spectrum more than the $h\nu = 846$ eV spectrum; one of which is at a binding energy lower than the bulk peak (at 160.8 eV, bulk peak at 161.2 eV), and the other two which have higher binding energies (at 161.8 eV and 163.1 eV respectively). Since the survey spectrum in Figure 4.1 shows no evidence of oxygen or carbon

Chapter 4: Pristine fracture surfaces of monoclinic pyrrhotite

species on the surface of this sample, the surface components observed in the S $2p$ spectrum must be formed due to surface stabilisation and not due to reaction of the surface with external oxidants.

Peak A in the difference spectrum has a lower binding energy than the bulk monosulfide peak and is estimated at 160.8 eV. The binding energy difference of 0.4 eV between this peak and the bulk sulfide peak is similar to uncoordinated surface monosulfide species such as those observed in some other minerals [14, 22, 23]. An undercoordinated sulfur species is likely to occur at a surface when a material such as pyrrhotite fractures along a cleavage plane that reveals a non-polar face, exposing both cation and anion species in approximately equal abundance. To form the lowest energy surface, the newly exposed face subsequently relaxes, where electrons that were previously shared in covalent bonds between neighbouring atoms relax into states closer to the more electronegative atom. In the case of pyrrhotite, the sulfur anion experiences the greatest electronegativity. Therefore, when the undercoordinated surface monosulfide forms due to rupture of the Fe-S bond, the sulfur anion will display a surface core level shift to a lower binding energy. This occurs due to the increased electron density around the sulfur atom, in comparison to the bulk anion. Therefore, peak A is assigned to an undercoordinated sulfur species, likely formed on a non-polar surface that undergoes relaxation rather than reconstructions.

Peak B is fitted to each spectrum with a binding energy of 161.8 eV, which is 0.6 eV higher than the bulk monosulfide peak. The increase in binding energy relative to the bulk peak indicates that there is a lower electron density around the emitted atom in comparison to the bulk sulfide. Since peak B is a surface feature, the binding energy shift is most likely due to a reconstruction of the pyrrhotite fracture surface and specifically due to sulfur polymerisation. As mentioned in section 2.5.1, surface reconstruction to form surface disulfide and polysulfide species has been observed for polar surfaces of other minerals such as millerite (NiS) [3], chalcopyrite [14], and bornite [15]. Although a binding energy less than 162.0 eV is generally considered to be low for bulk polymerised sulfur species [24], the binding energy of 161.8 eV is equal to that observed for the surface disulfide on the fracture surface of chalcopyrite [14] and similar to the surface disulfide observed on the galena (PbS) fracture surface [25]. Therefore, peak B fitted to the pyrrhotite S $2p$ spectrum at 161.8 eV is assigned to a surface disulfide species.

Peak C appears to be broader than peak A and B, observable in the broadness of the $2p_{1/2}$ component on the high binding energy side of the difference spectrum. Due to the overlap of the $2p_{1/2}$ component of peak B with the $2p_{3/2}$ component of peak C, the binding energy of this peak is difficult to determine solely from the difference spectrum. This peak has been fitted to each of the spectra around 163.1 eV,

indicating that it is due to polymerised sulfur species [24]. The width of this peak is somewhat larger than the other surface components, indicating a variety of oligomer lengths. While polysulfide species are common on oxidised sulfide surfaces, they are less common on vacuum fractured surfaces and generally form short chains such as the sulfur trimers formed on marcasite surfaces [23, 26]. The formation of the sulfur trimers on marcasite surfaces occurs by the unstable surface S^- species, which are formed by rupture of bulk disulfide bonds, reacting with the surface disulfide species to form sulfur trimers [26]. In the case of pyrite, these surface polymers are not formed and instead the S^- species stabilise through auto-redox reaction with Fe^{2+} to form S^{2-} and Fe^{3+} species on the surfaces [23, 26]. The mechanism for the formation of the surface polysulfide species on pyrrhotite cannot be the same as for marcasite, since pyrrhotite has no bulk disulfide species. Bulk pyrrhotite has only Fe-S bonds present in the structure (with evidence of some weak Fe-Fe bonding [9]), therefore S^{2-} species are expected to initially form on fracture surfaces due to the rupture of Fe-S bonds.

A scanning tunnelling microscopy (STM) study of the (001) fracture surface of monoclinic pyrrhotite [27] may offer some clues to the assignment of surface sulfur oligomers. Firstly, the study used scanning tunnelling spectroscopy to show that the (001) fracture surface is sulfur terminated, and supporting calculations indicated that the sulfur terminated surface is the most energetically favourable. With an excess of sulfur atoms at the surface, it is reasonable to expect some surface reconstruction of sulfur species occurs. Secondly, clusters of three sulfur atoms had formed on surface terraces. This occurred as a result of the relaxation of the upper surface layer, and the Fe layer below, both relaxing outwards from the bulk, thereby levelling out the sulfur atoms that were previously not level in the c-axis of the bulk structure. Finally, STM showed evidence of S-S bonds forming between the triangular clusters of sulfur atoms [27]. These observations may explain the contributions to peak A and more specifically peak B, however they offer little explanation to the formation of the longer chain polysulfide species at peak C. Pyrrhotite is known to have uneven fracture with no cleavage, and is therefore expected to reveal multiple fracture planes, with the possibility of both polar and non-polar faces. Therefore, the STM study of the (001) fracture surface cannot be expected to offer a full description of the uncontrolled fracture surface presented in this work. For a more complete understanding of the spectra and the mechanism of formation of the longer chain polysulfide species, more studies such as those using STM, combined with spectroscopy of a known surface are required.

4.2.4 Pyrrhotite bulk sulfide peak shape

Both of the two previous XPS studies of vacuum fractured pyrrhotite surfaces fitted multiple components to the bulk monosulfide peak, attributing them to 5-coordinate and 6-coordinate sulfur respectively [3, 4]. The two components were argued to be required to account for the relative

broadness of the bulk peak and its asymmetry on the high binding energy side. A broad peak has been observed for other sulfides, namely bornite, which has a broader bulk sulfide peak in comparison to similar minerals such as chalcopyrite [14, 15]. The increased width of the bornite sulfur $2p$ peak in comparison with other sulfide minerals was justified by the multitude of structurally discrete sulfur sites present in the bornite crystal structure and effect of the variation in electron density causing slight binding energy shifts, resulting in several inseparable XPS signals [15]. Consequently, the high binding energy signal in the bornite spectrum was attributed to a surface polymer arising from the reconstruction of the sulfur-rich fracture surface. In the previous studies of pyrrhotite sulfur spectra, the increased width of the peaks was attributed to the presence of multiple sulfur sites in the bulk structure, and slight variation in binding energy between these sites [3]. This assignment was justified by comparing the relative intensities of the peaks and their similarity to that expected for the sample that was being analysed. However, using relative heights of peaks is not a robust justification, especially when so few samples are being compared. Indeed, such an argument was used for the pentlandite sulfur spectrum, arguing that the peak at 161.4 eV was due to a 4-coordinate pentlandite sulfur [18], which was later shown to be due to a secondary oxidation product [28]. Furthermore, it has been shown that a difference in the number of bonding partners does not necessarily cause a binding energy shift, and that other factors such as bond length and ultimately electronegativity must be considered [29]. In the case of pyrrhotite, it has not been clear if the high binding energy tail to the bulk peak is due to a 6-coordinate bulk sulfide, or if it is due to energy-loss processes of the bulk peak, and that the similarity in fitted peak heights with the prevalence of the two bulk sulfide environments is simply fortuitous. The work by Skinner, Nesbitt and Pratt [4] which compared the sulfur spectra for troilite (FeS) and monoclinic pyrrhotite (Fe_7S_8) provided the most compelling evidence for the assignment of different binding energies for 5-coordinate and 6-coordinate bulk sulfide. However, even with two bulk components, there is still a high binding energy contribution which has not been accounted for. Nesbitt, Schaufuss, Scaini, Bancroft and Szargan [3] proposed that the contribution, which was observed in the region between 163.5 – 165.5 eV, may be due to either an inadequate Doniach-Sunjić contribution, or an energy loss feature such as has been observed for pyrite. A similar feature of the pentlandite spectrum has been observed [13, 18], and in Chapter 7 is attributed to the $\text{S } 3p \rightarrow \text{Fe } 3d$ ligand-to-metal charge-transfer final state. A similar feature may be present for pyrrhotite.

Figure 4.7 shows the sulfur $L_{2,3}$ edge absorption spectrum which may offer some clues to the origin of the high binding energy tail on the bulk sulfide peak. The absorption spectrum has been energy corrected such that the pre-edge peak labelled *a* aligns with the energy reported for the sulfur L edge absorption spectrum for another pyrrhotite sample [30]. The shape of the spectrum generally agrees

with pyrrhotite L edge spectrum previously published [8, 30], however the relative intensities of the peaks vary between the spectra in literature and that presented here. The onset of the absorption edge just below 162 eV is attributed to the transition of S 2*p* electrons to S 3*p* states and has a crystal field splitting estimated to be 1.3 eV, in agreement with estimations made in literature [5]. These S 2*p* states are generally agreed to be mixed with the unoccupied Fe 3*d* crystal-field band [8, 30]. The shoulder at 166 eV is assigned to the transition of S 2*p* electrons to S 3*s*-like states, and the structure at higher energies is due to the transition to empty S 3*d* states split into *t*_{2*g*} and *e*_g bands [8, 30]. The similarity of the splitting of the features labelled a and a' in Figure 4.7 and the crystal-field splitting predicted for the Fe 3*d* valence band [5] indicates that the unoccupied Fe 3*d* states may be hybridised with sulfur 3*p* and 3*s* states, and that the pyrrhotite conduction band is comprised of Fe *s* and *p* states strongly hybridised with sulfur 3*s*, 3*p* and 3*d* states.

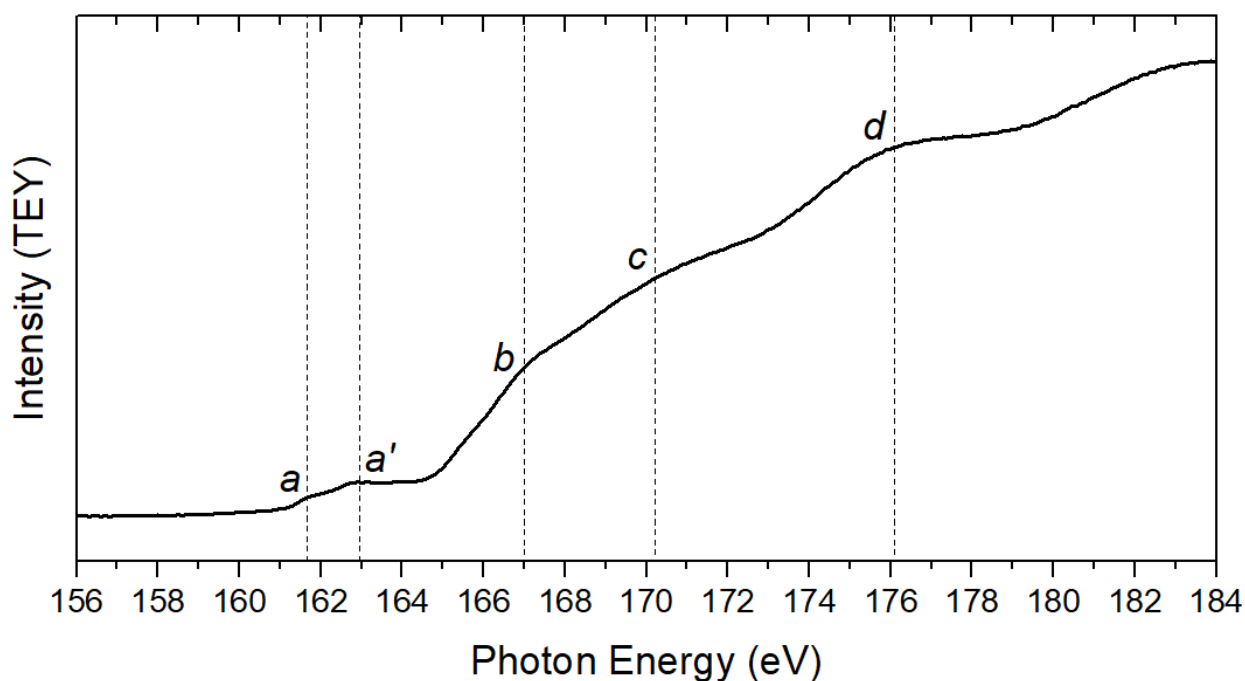


Figure 4.7: Sulfur L_{2,3} NEXAFS spectrum for vacuum fractured monoclinic pyrrhotite showing a spin-orbit splitting of 1.3 eV.

A ligand-to-metal charge-transfer (LMCT) state has previously been identified for the sulfide mineral chalcopyrite [31]. The S 3*p* → Fe 3*d* charge-transfer state which occurs due to the creation of the core hole during the photoemission process, was found to be the cause of the high binding energy tails observed in the core-level photoemission spectra for chalcopyrite, similar to that observed for the pyrrhotite sulfur spectrum. Therefore, it is possible that the high binding energy tail in the S 2*p* core-level spectrum occurs due to a LMCT final state.

4.3 Analysis of iron states

4.3.1 Fe 2p X-ray photoelectron spectra

Figure 4.8 shows the Fe 2p spectrum of the pristine vacuum fracture pyrrhotite sample collected with $h\nu = 846$ eV and 1487 eV. The Fe $2p_{3/2}$ peak is centred at 707.7 eV and the $2p_{1/2}$ peak around 721 eV, consistent with the Fe 2p spectrum for pyrrhotite after argon sputtering [32] and that of vacuum fractured pyrrhotite [2]. There is a low, broad, symmetric peak centred around 731 eV, which is due to a plasmon satellite from the $2p_{3/2}$ peak [6]. The surface sensitivity expected for the $h\nu = 1487$ eV spectrum is approximately 13% contribution from the surface monolayer, while the 846 eV spectrum is calculated to have approximately 32% from the surface monolayer, yet there is no significant difference in the shape of these two spectra. This indicates that there is negligible oxidation of Fe^{II} to Fe^{III} due to restructure at the surface, and that the electronic structure of the surface Fe states is approximately the same as those in the bulk.

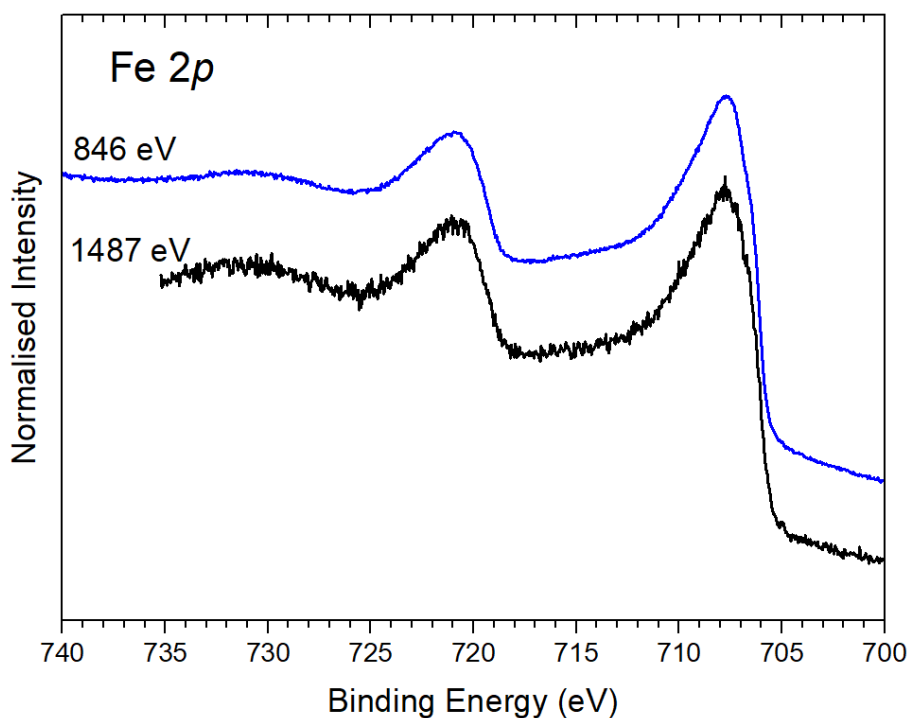


Figure 4.8: Fe 2p photoelectron spectrum for vacuum fractured pyrrhotite shows a broad Fe $2p_{3/2}$ peak at 707.7 eV. $h\nu = 846$ eV (blue, dotted), and 1487 eV (black, dashed).

The strong peak at 707.7 eV is consistent with the Fe^{II}-S present in the structure. The broad asymmetric tail is indicative of multiplet structure resulting from unpaired electrons in high-spin iron [33]. This confirms the assignment of high-spin Fe^{II}-S as proposed from calculations by Sakkopoulos, Vitoratos and Argyreas [5]. The broad high binding energy tails seen in Figure 4.8 are similar to those for tetrahedral Fe^{III}-S in chalcopyrite [29] and especially that of high-spin Fe^{II}-S in sphalerite [34]. In

contrast, pyrite and marcasite Fe 2*p* spectra both show sharp peaks with very little high binding energy multiplet structure, indicative of the low-spin Fe^{II}-S present in both the minerals' structures [23, 26].

The asymmetric tail is also partly due to the convolution of Fe^{II} and Fe^{III} contributions from the bulk [2]. Fe^{III}-S has previously been identified in the pyrrhotite spectra, with the main peak centred at 709.2 eV; a little higher than the Fe^{II}-S peak. Surface sensitive Fe 2*p* spectra for both pyrite and marcasite were used to determine the auto-redox reactions that occur on the fracture surfaces of these minerals, stabilising the surface S states by oxidation of Fe^{II} to Fe^{III}. The subsequent changes in the Fe 2*p* spectra showed an increase of Fe^{III} at the surface, with characteristic multiplet structure, in addition to increased high-spin Fe^{II} at the surface due to change in coordination [23]. No such changes are seen in the pyrrhotite spectra, where no significant differences are observed in the shape between the 1487 eV and 846 eV spectra, indicating that abundance of Fe^{III} species is the same at the surface as in the bulk. Therefore, no significant oxidation of Fe^{II} to Fe^{III} at the surface is expected, and the reconstruction of the sulfur species at the surface does not involve the surface iron species.

As seen in the S 2*p* core-level spectrum, there may also be final state effects contributing to the asymmetric tail in the Fe 2*p* spectrum. The following section investigates the electronic structure of this pyrrhotite sample using Fe L_{2,3} NEXAFS, and resonant photoemission spectroscopy of the valence band, collected with photon energies from over the L_{2,3} edge to highlight the valence states with Fe character.

The Fe L_{2,3} edge absorption spectrum for vacuum fractured pyrrhotite is shown in Figure 4.9. The L₃ peak is an asymmetric peak, broadened on the high energy side and with a small unresolved shoulder on the low energy side of the peak. The shape of the spectrum agrees with previously reported pyrrhotite Fe L edge spectra [7, 8, 29, 35]. The main L₃ peak, labelled B in Figure 4.9 has an absorption energy of 706.8 eV and is predominantly due to the transition of 2*p* electrons to the minority spin *e_gβ* orbitals of octahedral high-spin Fe^{II}-S [7, 8, 35]. The pre-edge shoulder, which is at approximately 705.1 eV; 1.7 eV lower than the main absorption peak, has previously been observed [7, 29]. The crystal field splitting of the Fe^{II} 3*d* orbitals of pyrrhotite has previously been calculated to be split by 1.8 eV [5], therefore the pre-edge feature at A has been attributed to partly filled *t_{2g}β* orbitals of high-spin Fe^{II}-S. Since Fe^{III}-S is also expected natively in the pyrrhotite structure, the broad shoulder at C is assigned to the *e_gβ* orbitals of high-spin Fe^{II}-S, and therefore some contribution at the main peak B is expected to be due to the *t_{2g}β* orbitals of high-spin Fe^{III}-S. There are weak contributions to the broad shoulder around D which are assigned to antibonding orbitals involving the Fe 4*s* and 4*p* states [7, 8].

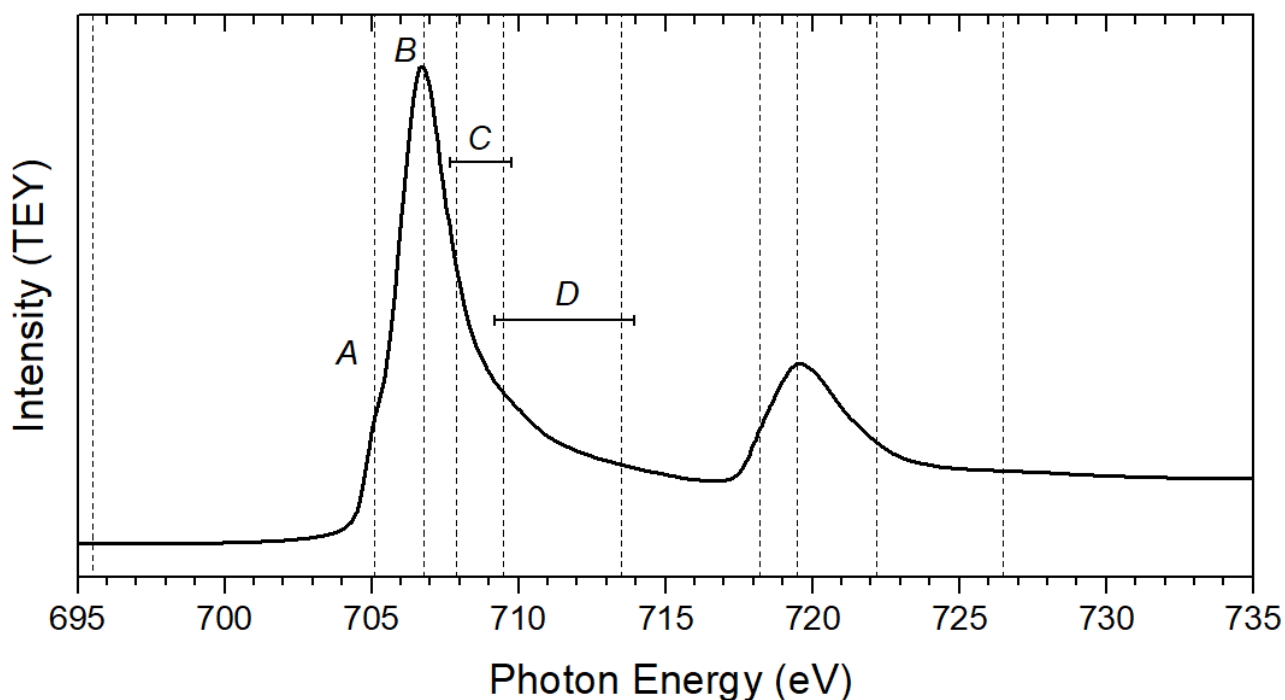


Figure 4.9: Fe $L_{2,3}$ NEXAFS spectrum for vacuum fractured pyrrhotite showing the L_3 peak at 706.8 eV with pre-edge peak at 705.1 eV.

Calculations of the valence band of an Fe^{2+} ion in octahedral coordination with sulfur determined that the majority-spin Fe $3d$ orbitals are 80% Fe in character, and that the minority-spin Fe $3d$ orbitals have even less sulfur character [36]. However, these calculations do not account for the distorted octahedra reported for pyrrhotite, or the regular iron deficiencies in the lattice, which are expected to affect the valence states. In contradiction to these calculations, the S L edge absorption spectrum presented in Figure 4.7, specifically the similarity in pre-edge crystal field splitting for the S and Fe L edge spectra, indicates that there is significant hybridization between the S $3p$ states and the Fe $3d$ valence band states.

4.3.2 Fe states in the pyrrhotite valence band

Figure 4.10 shows the valence band spectrum for pyrrhotite collected with a photon energy below the main absorption peak at $h\nu = 695.5$ eV. Key features of the valence band spectrum have been highlighted in Figure 4.10 by blue dotted lines. Assignments for the valence band peaks have been made based on ground state calculations for pyrrhotite in literature [5]. The pyrrhotite valence band spectrum has a strong broad peak around 4 eV with a shoulder around 6 eV. Both features are attributed to S $3p$ states [6, 9]. There is also a strong localised peak around 14 eV which is attributed to S $3s$ states. The fine structure in the upper valence band is attributed to the Fe $3d$ -like states. In particular, there is a sharp peak near the Fermi energy at 0.25 eV, which is attributed to the partly-

filled minority-spin $t_{2g}\beta$ states, while the $t_{2g}\alpha$ states are seen as a small shoulder at around 2.5 eV, as shown in Figure 4.10 [3, 6]. These features are separated by a local minimum. Previous literature has presented a pyrrhotite valence band spectrum which identifies a small peak at 1.0 eV within this local minimum, which is attributed to the Fe $e_g\alpha$ state [3]. This feature may be present in the spectrum in Figure 4.10, however may be obscured by the low signal to noise ratio.

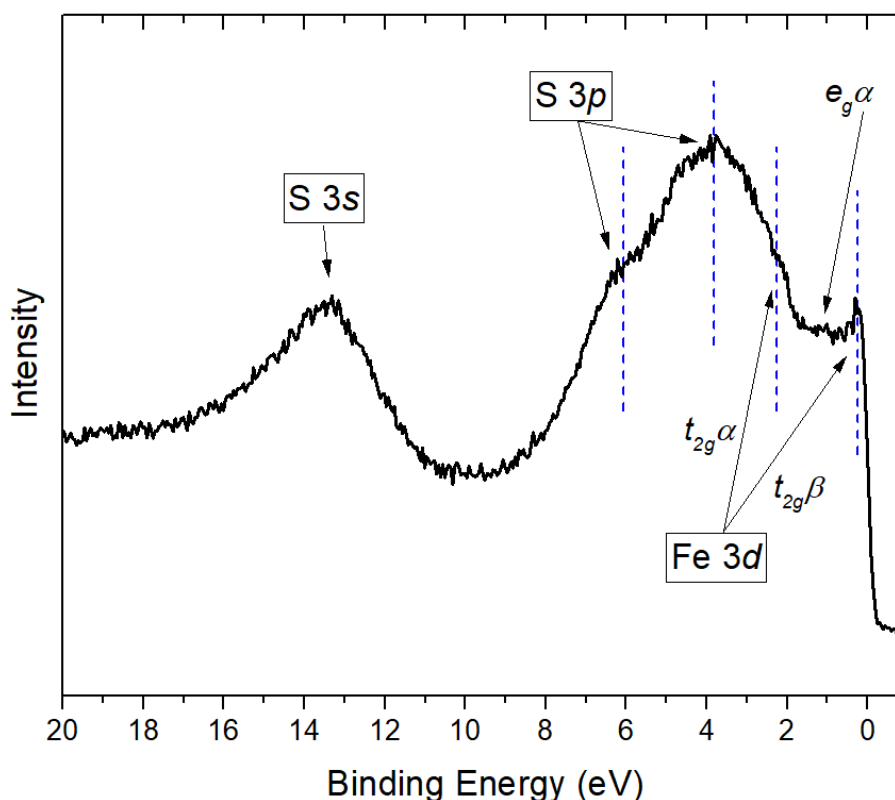


Figure 4.10: Pyrrhotite off-resonance ($h\nu = 695.5$ eV) valence band spectrum, showing Fe $3d$ states in the upper valence band, and S $3p$ and $3s$ states in the lower valence band. Key features are indicated by blue dotted lines at 0.25, 2.5, 3.8 and 6.0 eV.

4.3.3 Resonant valence band spectra over the Fe $2p$ absorption threshold

Figure 4.11 shows the resonant valence band spectra collected over the Fe $L_{2,3}$ absorption edge, with the absorption spectrum shown on the right. The photon energies used to collect each valence band spectrum are shown by dotted lines on the absorption spectrum and labelled on each valence band spectrum. Each valence band spectrum is normalised to constant flux and plotted on the same scale, vertically offset for clarity. The spectrum at the top of Figure 4.11 is the off-resonance valence band spectrum which was shown in Figure 4.10, collected with $h\nu = 695.5$ eV; below the onset of the absorption spectrum. The valence band spectrum collected with the pre-edge absorption energy of $h\nu = 705.1$ eV has increased in intensity across the whole spectrum in comparison to the off-resonance valence band spectrum. This is most notable in the lower valence band around 3 – 5 eV. The valence band spectrum collected at the peak absorption energy of $h\nu = 706.8$ eV shows an immense increase

in intensity in the lower valence band region, with the peak of this spectrum just below 5 eV. The increase in intensity is so great that to plot this spectrum on the same scale as the off-resonance spectrum causes the latter spectrum to appear insignificant. The intense signal seen in the $h\nu = 706.8$ eV spectrum is seen to move through the subsequent valence band spectrum with a photon energy dependence, and an intensity profile which follows the shape of the absorption spectrum, indicating that it is likely the Auger decay signal. The strength of this deexcitation channel at its maximum is estimated to be around 45 times greater than the intensity of the photoemission signal. In the valence band spectra collected with photon energies over the L_2 absorption edge, there is another increase in the lower valence band especially, which once again moves through subsequent spectra with a photon energy dependence. This second Auger-like signal is significantly less intense than that observed over the L_3 absorption edge.

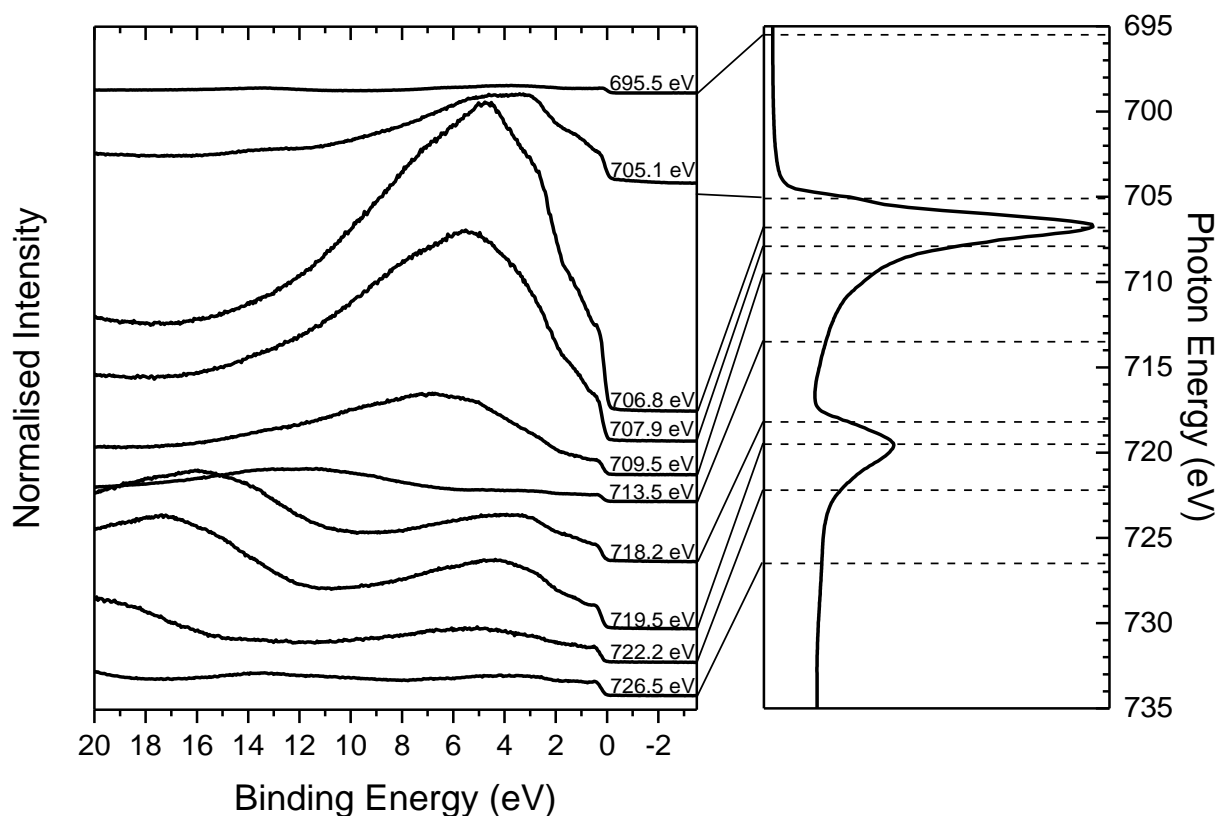


Figure 4.11: Pyrrhotite valence band spectra collected with photon energies across the Fe $2p$ absorption spectrum. A strong increase in seen in the lower valence band region at the absorption peak photon energy.

The nature of the Auger-like feature is investigated in Figure 4.12, where the off-resonance valence band spectrum has been subtracted from each subsequent valence band spectrum, and the result plotted in the kinetic energy scale. If there is no coherence and therefore no interaction between the photoemission and Auger deexcitation channels, then each valence band spectrum is expected to be a superposition of these two signals. In that case, by subtracting the off-resonance photoemission

Chapter 4: Pristine fracture surfaces of monoclinic pyrrhotite

signal from each subsequent spectrum, only the Auger signal would remain, in the absence of true resonance.

It can be seen in the spectra in Figure 4.12 that the photoemission signal is not completely removed and can still be observed in the spectra which are not completely overshadowed by the deexcitation channel. Key examples of this can be seen in the difference spectra originating from the $h\nu = 713.5$ eV, 722.2 eV, and 726.5 eV spectra, where the deexcitation channel has moved sufficiently away from the regular photoemission signal, but this photoemission signal is still visible in these spectra which have had the off-resonance spectrum subtracted. This shows that at photon energies above the absorption peak, the photoemission signal is enhanced across the whole spectrum, indicating that there are valence states across the upper and lower valence band which originate from Fe 3*d*-like states.

The difference spectra in Figure 4.12 which originate from spectra collected with photon energies above the absorption maximum show an Auger feature with a peak around 702 eV, and a second feature in the higher photon energy spectra with a peak around 715 eV. The main feature at 702 eV is consistent in each of the difference spectra, except for the spectrum collected with $h\nu = 705.1$ at the L₃ absorption pre-edge. In contrast, this spectrum has a different shape, with a second peak around 700 eV in the kinetic energy scale. This shows that at energies below the absorption peak, the deexcitation channel is not at a constant kinetic energy, but transitions to the constant kinetic energy regime at the absorption threshold.

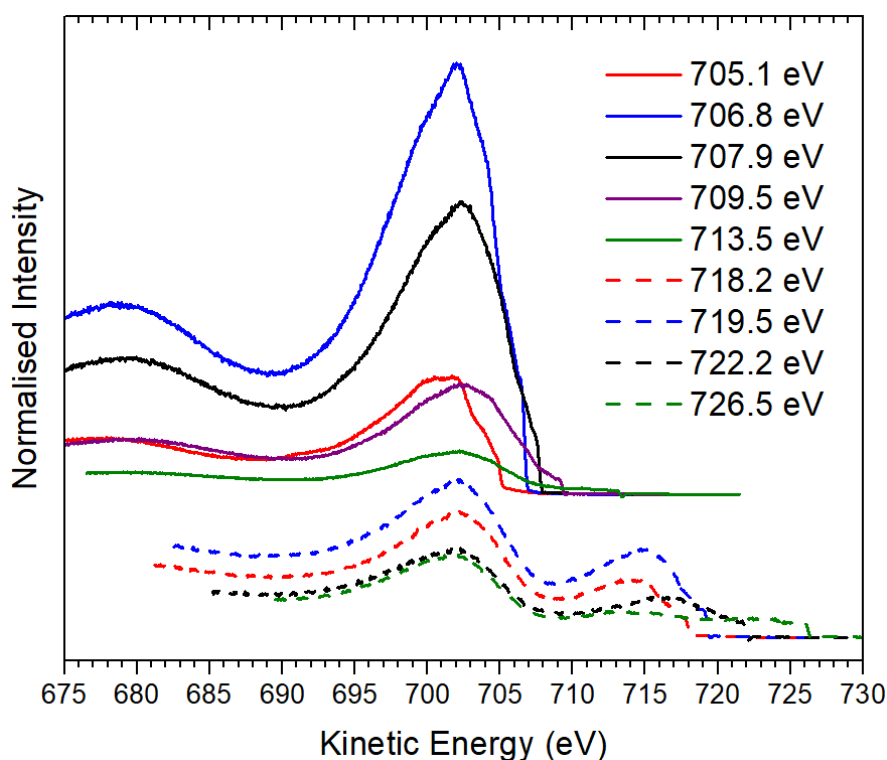


Figure 4.12: Resonant valence band spectra each with the off-resonance spectrum ($h\nu = 695.5$ eV) subtracted to show the constant LMM Auger feature moving through the spectra. The 705.1 – 713.5 eV spectra have been vertically offset for clarity.

The resonant valence band spectra shown in Figure 4.13 include the off-resonance spectrum scaled up by $10\times$ such that its features are visible, and the valence band spectra collected with photon energies at the L_3 pre-edge and L_3 absorption peak respectively. As previously described, the off-resonance valence band spectrum collected with a photon energy at the absorption edge has a peak at 4.7 eV due to the Auger deexcitation channel which is much stronger than the photoemission channel. There is also a shoulder to this peak at 3.0 eV, marked by a dotted line in Figure 4.13. The features at 4.7 eV and 3.0 eV are also seen in the spectrum collected with the pre-edge photon energy, however the relative intensities of these features differ between the two spectra.

The increase in the $h\nu = 705.1$ eV spectrum at 4.7 eV cannot be attributed to the Auger deexcitation channel, as seen in Figure 4.12. This may indicate either a Fe $3d$ derived state near this binding energy, or an interatomic resonant enhancement of the S $3d$ states, as first seen by Kay, Arenholz, Mun, García de Abajo, Fadley, Denecke, Hussain and Van Hove [37]. A previous resonant photoemission study of the pyrrhotite valence band had identified a satellite feature near 5 eV which was resonant over the $3p$ absorption edge [6]. This was only a weak resonance, indicating a weakly localised state, and it was not detected at all in the later study by Nesbitt, Schaufuss, Bancroft and Szargan [9] which also detected a resonant feature at 0.25 eV and attributed it to the $t_{2g}\beta$ orbitals contributing to the weak Fe-Fe π - π bonding. This study also showed that the feature at 2.5 eV has strong Fe $3d$ character and

Chapter 4: Pristine fracture surfaces of monoclinic pyrrhotite

is owing to the majority spin $t_{2g}\alpha$ orbitals. This feature could be contributing to the intensity of the $h\nu = 705.1$ eV and 706.8 eV spectra around that binding energy, contributing to the peak in the $h\nu = 705.1$ eV spectrum, and to the shoulder in the $h\nu = 706.8$ eV spectrum.

The current study is the first to detect a feature in the lower valence band around this energy that is resonant at photon energies corresponding to Fe core electron absorption. The lower valence band has been shown to generally have strong S $3p$ character, especially the feature at 4.5 eV [5, 9], and ground state calculations have shown that at higher binding energies around $5 - 7$ eV there are Fe $3d - S 3p$ bonding states [36]. However, such calculations do not account for final state effects, which can be significantly affected by electron correlations.

The satellite feature previously observed by Shimada, Mizokawa, Mamiya, Saitoh, Fujimori, Ono, Kakizaki, Ishii, Shirai and Kamimura [6] was attributed to a mixture of d^5 and $d^7\bar{L}^2$ final states. This feature was likely not observed in the study by Nesbitt, Schaufuss, Bancroft and Szargan [9] but is observed strongly in this study since the Fe L_3 absorption cross section is significantly larger than the absorption cross section for core level $3p$ electrons, used in previous studies [6, 9]. Since the absorption cross section is much larger any resonant effects would be more visible. The 4.7 eV feature is also obscured by the density of S $3p$ states and not easily detectable in non-resonant photoemission studies.

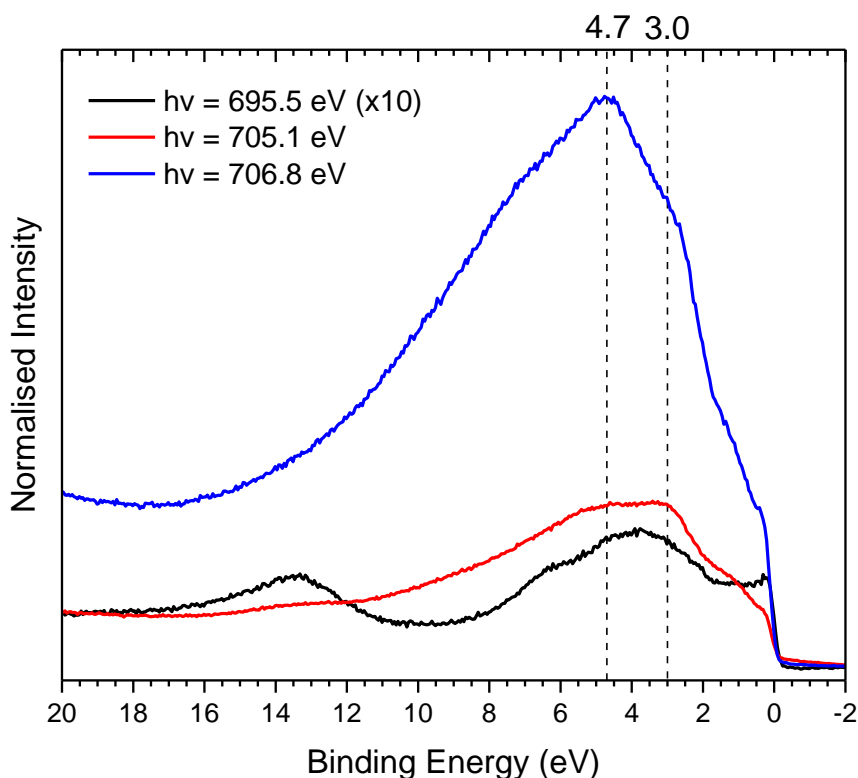


Figure 4.13: Resonant valence band spectra collected with $h\nu = 695.5$ eV (black), 705.1 eV (red) and 706.8 eV (blue). The binding energy of highlighted features is shown above the spectra. The $h\nu = 695.5$ eV spectrum has been scaled $\times 10$. The features at 4.7 eV and 3.0 eV binding energy have been highlighted.

The detection of a localised state in the lower valence band, in addition to the $t_{2g}\alpha$ state at 2.5 eV and the $t_{2g}\beta$ state contributing to the Fe-Fe π - π bonding at 0.25 eV [9], shows that electron correlation plays a role in the electronic structure of Fe_7S_8 pyrrhotite. The presence of weakly localised states indicates that Doniach-Sunjić line shapes are not appropriate for fitting core level photoelectron spectra such as those presented previously in this chapter. The high binding energy tail observed for pyrrhotite S $2p$ photoelectron spectrum can therefore be attributed to a final state effect arising from electron correlation in the valence band, such as the weak satellite structure seen in pyrrhotite's lower valence band.

4.4 Conclusions

This chapter has presented core-level and valence band photoemission spectra for a pristine vacuum fractured monoclinic pyrrhotite sample. The aim of this study was to investigate in detail the surface species present on pristine fractured pyrrhotite surfaces, and also investigate the effect of electron correlation on the spectral interpretation for pyrrhotite. The core-level X-ray photoelectron spectra were collected with varied photon energies, thus varying the sampling depth. This method allowed for the surface states to be distinguished from the bulk states present in each core-level spectrum. By this method it was shown for the first time that both disulfide and polysulfide species occur natively

in addition to a previously identified undercoordinated surface monosulfide species. A difference spectrum calculated by subtracting a more bulk sensitive spectrum from a surface sensitive spectrum identified a surface monosulfide at 160.8 eV, while surface disulfide and polysulfide species were identified at 161.8 eV and 163.1 eV respectively. Concurrently, the Fe species displayed no observable change to oxidation state or electronic structure at the surface in comparison to the bulk, indicating that the upper surface layer is dominated by sulfur species, and that the relaxation and reconstruction of this layer largely involves the sulfur species alone.

The line shape of the Fe 2*p* spectrum showed asymmetry on the high binding energy side which is attributed to the convolution of peaks due to Fe^{II} and some Fe^{III} species, and the multiplet structure expected due to high-spin Fe species in the bulk pyrrhotite structure. As in previous literature, this chapter also identified an asymmetric line shape in the sulfur 2*p*, the origin of which is less clear. Previous literature has fitted two components to the bulk sulfide line shape to account for both 5-coordinate and 6-coordinate sulfur in the bulk structure. However, this does not account for the high binding energy tail which extends out to 166 eV, which was identified in this chapter using the difference spectrum. Therefore, an alternative approach was made in this chapter, where a series of empirically derived symmetrical peaks was used to fit the asymmetric shape of the bulk sulfide line shape. This line shape was used to successfully fit the series of S 2*p* spectra collected for this sample, in addition to the surface components previously identified. Although this method was able to accurately fit the bulk component of the S 2*p* spectrum, it provides no explanation for the origin of the line shape.

The comparison of Fe and S L_{2,3} absorption edge spectra identified the possibility of a S 3*p* → Fe 3*d* ligand-to-metal charge-transfer final state, highlighted by the similarity in crystal field splitting energy observed in both spectra.

Resonant valence band photoemission spectroscopy showed that there are localised Fe-derived valence states in the lower valence band, which was previously understood to be occupied by a large density of S 3*p* states. The Fe-derived state observed at 4.7 eV in the lower valence band is in addition to other localised states observed in previous literature at 0.25 eV and 2.5 eV, attributed to the partially occupied *e_g* orbital and the *t_{2g}β* orbital contributing to the Fe-Fe π-π bonding, respectively. The 4.7 eV valence state shows that there is significant mixing between the Fe 3*d* and S 3*p* states, attributed to a ligand-to-metal charge-transfer final state. These valence states show that electron correlation plays an important role in the electronic structure of pyrrhotite and contributes to the photoemission final states.

This is an important result because it highlights the necessity to consider final state effects in the interpretation of core level and valence band spectra. Specifically, in the case of pyrrhotite sulfur spectra, the final state effects are seen to contribute significantly to the bulk sulfide line shape. Because the final state contribution to the bulk sulfide line shape overlaps with the binding energy of disulfide and polysulfide species, these naturally occurring surface species have previously been undetected. These final state effects are also important to consider when interpreting valence band spectra as the photon energy being used must be considered to avoid or account for any resonance effects that may occur due to the excitation of core electrons.

Finally, this chapter additionally highlights the need for caution when fitting spectra to identify surface species. Here, two fits were proposed for the S $2p$ spectra; the first which uses a Doniach-Sunjic hybrid line shape for the bulk sulfide peaks, and the second which used symmetric line shapes for the bulk peaks, and a series of empirically derived symmetric peaks to account for the high binding energy tail caused by final state effects. While both fits included all three surface components in the more surface sensitive spectra, the quantification arising from these fits differed significantly. It is expected that the quantification from the second fit, which used the series of symmetric peaks to model the bulk line shape, is more accurate, since the peak shape is designed to fit the bulk shape. Alternatively, using pre-designed line shapes such as the Doniach-Sunjic hybrid line shape used in this chapter, is unnecessarily constricting and may only accurately fit the bulk line shape fortuitously, rather than by design. The variation between the two fits highlights the limitation in quantifying species from fitted photoelectron spectra when the bulk line shape is not well defined.

4.5 References

- [1] R. Osterberg, On the prebiotic role of iron and sulfur, *Origins of Life and Evolution of the Biosphere*, 27 (1997) 481-484.
- [2] A.R. Pratt, I.J. Muir, H.W. Nesbitt, X-ray photoelectron and Auger electron spectroscopic studies of pyrrhotite and mechanism of air oxidation, *Geochimica et Cosmochimica Acta*, 58 (1994) 827-841.
- [3] H.W. Nesbitt, A.G. Schaufuss, M. Scaini, G.M. Bancroft, R. Szargan, XPS measurement of fivefold and sixfold coordinated sulfur in pyrrhotites and evidence for millerite and pyrrhotite surface species, *American Mineralogist*, 86 (2001) 318-326.
- [4] W.M. Skinner, H.W. Nesbitt, A.R. Pratt, XPS identification of bulk hole defects and itinerant Fe 3d electrons in natural troilite (FeS), *Geochimica et Cosmochimica Acta*, 68 (2004) 2259-2263.
- [5] S. Sakkopoulos, E. Vitoratos, T. Argyreas, Energy-band diagram for pyrrhotite, *Journal of Physics and Chemistry of Solids*, 45 (1984) 923-928.
- [6] K. Shimada, T. Mizokawa, K. Mamiya, T. Saitoh, A. Fujimori, K. Ono, A. Kakizaki, T. Ishii, M. Shirai, T. Kamimura, Spin-integrated and spin-resolved photoemission study of Fe chalcogenides, *Physical Review B*, 57 (1998) 8845-8853.

- [7] H. Miyauchi, T. Koide, T. Shidara, N. Nakajima, H. Kawabe, H. Fukutani, K. Shimada, A. Fujimori, K. Iio, T. Kamimura, Core-level magnetic circular dichroism in Fe_7S_8 and Fe_7Se_8 , *Journal of Electron Spectroscopy and Related Phenomena*, 78 (1996) 259-262.
- [8] Y. Mikhlin, Y. Tomashevich, Pristine and reacted surfaces of pyrrhotite and arsenopyrite as studied by X-ray absorption near-edge structure spectroscopy, *Phys Chem Minerals*, 32 (2005) 19-27.
- [9] H.W. Nesbitt, A.G. Schaufuss, G.M. Bancroft, R. Szargan, Crystal orbital contributions to the pyrrhotite valence band with XPS evidence for weak Fe-Fe π bond formation, *Phys Chem Minerals*, 29 (2002) 72-77.
- [10] Z.E. Pettifer, A Study of the Dissolution of Iron and Nickel Sulfides and the Effect of Mixed Mineral Systems [Honours thesis], Flinders University, *Some of the data of this sample was presented in a previous honours thesis, however the analysis is original to the present PhD thesis*, 2014.
- [11] D. Briggs, M.P. Seah, Practical Surface Analysis, Auger and X-ray Photoelectron Spectroscopy, 2nd ed. ed., Wiley & Sons, Chichester, England, 1990.
- [12] D.A. Shirley, High-Resolution X-Ray Photoemission Spectrum of the Valence Bands of Gold, *Physical Review B*, 5 (1972) 4709-4714.
- [13] Z.E. Pettifer, J.S. Quinton, W.M. Skinner, S.L. Harmer, New interpretation and approach to curve fitting synchrotron X-ray photoelectron spectra of $(\text{Fe,Ni})_9\text{S}_8$ fracture surfaces, *Applied Surface Science*, 504 (2020) 144458.
- [14] S.L. Harmer, A.R. Pratt, W.H. Nesbitt, M.E. Fleet, Sulfur species at chalcopyrite (CuFeS_2) fracture surfaces, *American Mineralogist*, 89 (2004) 1026-1032.
- [15] S.L. Harmer, A.R. Pratt, H.W. Nesbitt, M.E. Fleet, Reconstruction of fracture surfaces on bornite, *The Canadian Mineralogist*, 43 (2005) 1619-1630.
- [16] S. Doniach, M. Sunjic, Many-electron singularity in X-ray photoemission and X-ray line spectra from metals, *Journal of Physics C: Solid State Physics*, 3 (1970) 285-291.
- [17] D.L. Legrand, H.W. Nesbitt, G.M. Bancroft, X-ray photoelectron spectroscopic study of a pristine millerite (NiS) surface and the effect of air and water oxidation, *American Mineralogist*, 83 (1998) 1256-1265.
- [18] D.L. Legrand, G.M. Bancroft, H.W. Nesbitt, Surface characterization of pentlandite, $(\text{Fe,Ni})_9\text{S}_8$, by X-ray photoelectron spectroscopy, *International Journal of Mineral Processing*, 51 (1997) 217-228.
- [19] P.M.A. Sherwood, Data Analysis in XPS and AES, in: Practical Surface Analysis, John Wiley & Sons Ltd, Chichester, 1990, pp. 555-586.
- [20] N. Fairley, A. Carrick, *The Casa Cookbook*, Acolyte Science, United Kingdom, 2005.
- [21] K. Laajalehto, I. Kartio, E. Suoninen, XPS and SR-XPS techniques applied to sulphide mineral surfaces, *International Journal of Mineral Processing*, 51 (1997) 163-170.
- [22] M. Bronold, Y. Tamm, W. Jaegermann, Surface states on cubic d -band semiconductor pyrite (FeS_2), *Surface Science*, 314 (1994) 931-936.
- [23] S.L. Harmer, H.W. Nesbitt, Stabilization of pyrite (FeS_2), marcasite (FeS_2), arsenopyrite (FeAsS) and loellingite (FeAs_2) surfaces by polymerization and auto-redox reactions, *Surface Science*, 564 (2004) 38-52.
- [24] R.S.C. Smart, W.M. Skinner, A.R. Gerson, XPS of sulphide mineral surfaces: metal-deficient, polysulphides, defects and elemental sulphur, *Surface and Interface Analysis*, 28 (1999) 101-105.
- [25] A.N. Buckley, I.M. Kravets, A.V. Shchukarev, R. Woods, Interaction of Galena with hydrosulphide ions under controlled potentials, *Journal of Applied Electrochemistry*, 24 (1994) 513-520.
- [26] I. Uhlig, R. Szargan, H.W. Nesbitt, K. Laajalehto, Surface states and reactivity of pyrite and marcasite, *Applied Surface Science*, 179 (2001) 222-229.
- [27] U. Becker, A.W. Munz, A.R. Lennie, G. Thornton, D.J. Vaughan, The atomic and electronic structure of the (001) surface of monoclinic pyrrhotite (Fe_7S_8) as studied using STM, LEED and quantum mechanical calculations, *Surface Science*, 389 (1997) 66-87.

Chapter 4: Pristine fracture surfaces of monoclinic pyrrhotite

- [28] S.W. Goh, A.N. Buckley, R.N. Lamb, L.-J. Fan, L.-Y. Jang, Y.-w. Yang, Pentlandite sulfur core electron binding energies, *Phys Chem Minerals*, 33 (2006) 445-456.
- [29] S.W. Goh, A.N. Buckley, R.N. Lamb, R.A. Rosenberg, D. Moran, The oxidation states of copper and iron in mineral sulfides, and the oxides formed on initial exposure of chalcopyrite and bornite to air, *Geochimica et Cosmochimica Acta*, 70 (2006) 2210-2228.
- [30] D. Li, M. Bancroft, M. Kasrai, M. Fleet, X. Feng, K. Tan, S K- and S L-edge X-ray absorption spectroscopy of metal sulfides and sulfates: applications in mineralogy and geochemistry, *The Canadian Mineralogist*, 33 (1995) 949-960.
- [31] M. Fujisawa, S. Suga, T. Mizokawa, A. Fujimori, K. Sato, Electronic structures of CuFeS_2 and $\text{CuAl}_{0.9}\text{Fe}_{0.1}\text{S}_2$ studied by electron and optical spectroscopies, *Physical Review B*, 49 (1994) 7155-7164.
- [32] A. Buckley, R. Woods, X-ray photoelectron spectroscopy of oxidized pyrrhotite surfaces: I. Exposure to air, *Applications of Surface Science*, 22/23 (1985) 280-287.
- [33] R.P. Gupta, S.K. Sen, Calculation of multiplet structure of core p -vacancy levels, *Physical Review B*, 10 (1974) 71-77.
- [34] S.L. Harmer, A. Mierczynska-Vasilev, D.A. Beattie, J.G. Shapter, The effect of bulk iron concentration and heterogeneities on the copper activation of sphalerite, *Minerals Engineering*, 21 (2008) 1005-1012.
- [35] R.G. Acres, S.L. Harmer, D.A. Beattie, Synchrotron PEEM and ToF-SIMS study of oxidized heterogeneous pentlandite, pyrrhotite and chalcopyrite, *Journal of Synchrotron Radiation*, 17 (2010) 606-615.
- [36] J.A. Tossell, SCF- $X\alpha$ scattered wave MO studies of the electronic structure of ferrous iron in octahedral coordination with sulfur, *The Journal of Chemical Physics*, 66 (1977) 5712-5719.
- [37] A. Kay, E. Arenholz, S. Mun, F.J. García de Abajo, C.S. Fadley, R. Denecke, Z. Hussain, M.A. Van Hove, Multi-Atom Resonant Photoemission: A Method for Determining Near-Neighbor Atomic Identities and Bonding, *Science*, 281 (1998) 679.

5 OXIDISED SURFACES OF MONOCLINIC PYRRHOTITE

Pyrrhotite surfaces are an area of interest in mineral studies due to the natural abundance of pyrrhotite, its close association with other economically relevant minerals, catalytic activity, and the role it may have played in pre-biotic chemistry. Furthermore, since pyrrhotite is naturally reactive, understanding the way its surfaces react upon exposure to various oxidants is equally as important. The previous chapter investigated the surface and electronic structure of a monoclinic pyrrhotite sample which had been fractured in high vacuum and analysed before exposure to air or other external oxidants. This chapter shifts the focus to altered pyrrhotite surfaces, to understand the physical and chemical origin of features observed in X-ray photoelectron and X-ray absorption (NEXAFS) spectra. The aim of this is to simultaneously improve the interpretation of complex spectra, thus providing more robust analytic tools for sulfide minerals, while developing the current understanding of how pyrrhotite surfaces react under such conditions.

The initial exposure of pyrrhotite surfaces to water results in adsorption of hydroxyl ions to the iron vacancies in the lattice, coinciding with an increase in disulfide species [1]. When pyrrhotite is oxidised in water or air over the time period of a few days, an amorphous sulfur rich upper surface layer forms with a thickness of less than 2 nm and does not further oxidise significantly after a few days [2]. The sulfur-rich layer forms by migration of Fe species from the bulk to the surface to be oxidised to form a Fe oxide and hydroxide surface [3]. The sulfur-rich layer has a ratio of Fe:S close to 1:2, and this ratio gradually changes composition to pyrrhotite in the bulk [3]. XRD studies have shown that this layer is mostly amorphous [2].

After exposure to acidic conditions the sulfur-rich upper surface layer is shown by XRD studies to form a crystalline structure which more closely resembles the NaCl structure than the NiAs structure to which pyrrhotite is typically compared [2]. The structure has been shown to have polymerised sulfur and low-spin Fe(II), in contradiction to the high-spin Fe^{II} found in bulk pyrrhotite. It is expected that the transition to low-spin is due to the reduction in Fe-S bond length and a change in coordination [4].

The original contribution to knowledge within this chapter is to develop a deeper understanding and interpretation of data through cross-examination of prevailing reported ideas with new higher resolution results presented here. The aim is to reconsider evidence presented in previous studies with the new interpretation of pyrrhotite core level spectra and electronic structure presented in Chapter 4. This will help in identifying species in photoelectron spectra, which are difficult to resolve due to the

overlap in binding energies of peaks associated with different species, which also overlap with complex final state effects that feature in spectral peaks. By identifying species present in synchrotron data, these species can be justified and included in the analysis of spectra obtained with conventional lab methods, thus enhancing the interpretation of all future conventional photoelectron studies of sulfide minerals.

5.1 Methods

The monoclinic sample investigated in this chapter is from the same source as the pyrrhotite sample investigated in the previous chapter. Both the polished pyrrhotite and pyrrhotite reacted in pH 1 H₂SO₄ were shaped and polished using the method described in section 3.1.3 After polishing, one sample was then exposed to pH 1 H₂SO₄ solution for 1 hour at ambient temperature and will be referred to as pyrrhotite in pH 1 H₂SO₄. The samples were carefully dried with lint-free laboratory tissue, ensuring the analysis surface was not disturbed, before being inserted into the vacuum chamber of the synchrotron endstation.

Synchrotron XPS (SXPS) spectra were collected at the Australian Synchrotron soft X-ray beamline [5]. Spectra collected for the polished sample includes a survey spectrum and sulfur 2*p* spectrum collected with $h\nu = 1487$ eV and 260 eV. The same spectra were collected for pyrrhotite in pH 1 H₂SO₄, in addition to an Fe 2*p* spectrum collected with $h\nu = 1487$ eV. The energy scale of each $h\nu = 1487$ eV spectrum was calibrated to the C 1*s* peak in the survey spectrum at 284.8 eV [6]. The $h\nu = 260$ eV spectra were calibrated by aligning the sulfate peaks in each $h\nu = 260$ eV spectrum with those in the $h\nu = 1487$ eV spectrum of the same sample.

Spectra were fitted using CasaXPS software [7]. After fitting a background to each spectrum, a GL(50) line shape was used for each peak, and a series of symmetric peaks used to model the tail of the bulk sulfide component, as was devised in Chapter 4.

The NEXAFS spectra and corresponding images presented in this chapter were collected at the PEEM beamline (BL05B2) at the NSRRC as described in section 3.5 [5]. The Fe L edge absorption spectrum was calibrated by comparison to a spectrum from the same mineral prepared in the same way, collected at the Australian Synchrotron soft X-ray beamline. The main peak of the oxygen K edge spectrum was set to 0 eV to report relative energies of other features. The PEEM images shown in this chapter were also collected at the BL05B2 beamline with a 450 μm field of view. Images were taken below each absorption edge as a background image showing primarily topography of the

sample surface. These background images were used to remove this topography from the images collected at the absorption edge, such that only the distribution of chemical states remains. The images presented have had the background images removed as described in Eq. (5) in section 3.5.1.

5.2 Monoclinic pyrrhotite

The species present at the near-surface of the sample were quantified using the survey spectra collected with $h\nu = 1487$ eV, shown in Figure 5.1. Iron, sulfur, carbon and oxygen species are observed on both the polished pyrrhotite and pyrrhotite in pH 1 H_2SO_4 , and the quantification of these species is shown in Table 5.1. Both samples show a little more than 40% contribution from carbon species. This is expected to arise from a combination of polishing, and the presence of adventitious carbon. The polished sample shows 30 at % contribution from oxygen species, and a slightly greater ratio of iron to sulfur species. The sample of pyrrhotite in pH 1 H_2SO_4 has a ratio of sulfur to iron similar to what is expected from the bulk pyrrhotite stoichiometry of Fe_7S_8 . This sample also has comparatively less oxygen contribution to the survey spectrum, with only 11.8 at % oxygen contribution, compared to 30 at % for the polished sample.

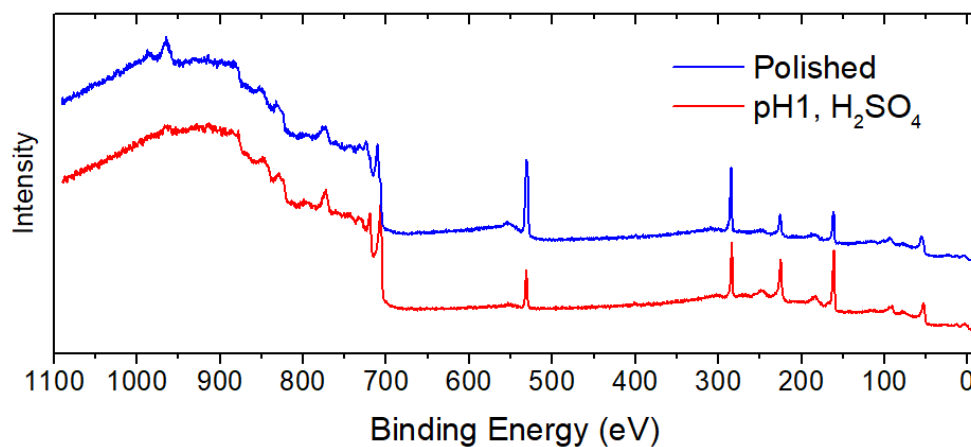


Figure 5.1: Survey spectra of polished monoclinic pyrrhotite and monoclinic pyrrhotite exposed to pH 1 H_2SO_4 for 1 hour, each obtained with $h\nu = 1487$ eV.

Table 5.1: Atomic % elements for the samples of polished pyrrhotite and pyrrhotite in pH 1 H_2SO_4 for 1 hour.

Species	Polished pyrrhotite	Pyrrhotite, pH 1 H_2SO_4
Fe 3p	16.9 %	21.6 %
S 3p	11.0 %	24.1 %
C 1s	42.0 %	42.5 %
O 1s	30.1 %	11.8 %

The sulfur $2p$ spectra collected with $h\nu = 260$ eV and 1487 eV for both the polished pyrrhotite and pyrrhotite in pH 1 H_2SO_4 are shown in Figure 5.2. Also included in Figure 5.2 are the S $2p$ spectra from the vacuum fractured monoclinic sample of Chapter 4 for comparison. The spectra collected with $h\nu = 1487$ eV from the polished pyrrhotite and pyrrhotite in pH 1 H_2SO_4 show a decrease in the minimum between the two main peaks around 162 eV, indicating an increase in disulfide and polysulfide species in the pyrrhotite in pH 1 H_2SO_4 sample. Also seen is the emergence of sulfate species at 168 eV. The spectra from both oxidised samples collected with $h\nu = 260$ eV show a remarkable difference in comparison to the vacuum fractured spectrum. While the vacuum fractured pyrrhotite $h\nu = 260$ eV spectrum has a similar shape to the bulk S $2p$ spectrum, the polished pyrrhotite sample shows an apparent increase in disulfide and polysulfide species at the surface, resulting in a flat-top spectral shape with the highest peak just below 163 eV, and clear evidence of both sulfite (SO_3^{2-} , 166.5 eV) and sulfate (SO_4^{2-} , 168 eV) species. The $h\nu = 260$ eV spectrum of pyrrhotite in pH 1 H_2SO_4 shows distinct peaks at a low binding energy near the energy of the bulk peak, which appear to have a higher resolution than the polished and the vacuum fractured pyrrhotite $h\nu = 260$ eV spectra. The peak of the spectrum for pyrrhotite in pH 1 H_2SO_4 is at 163 eV, indicating a strong presence of polysulfide species, and with clear evidence of sulfate species in the high binding energy region.

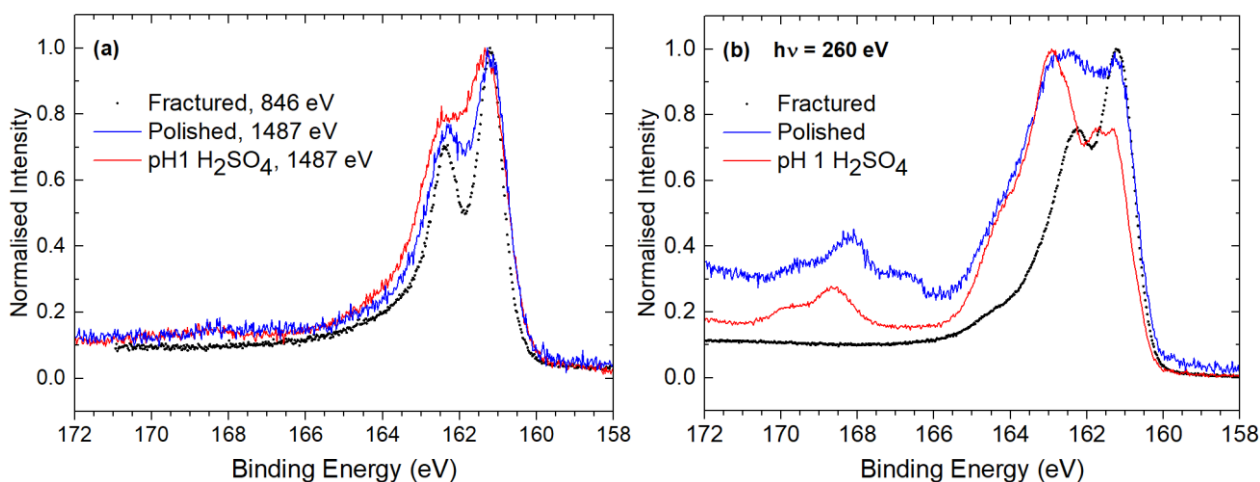


Figure 5.2: S $2p$ photoelectron spectra for polished pyrrhotite and pyrrhotite in pH 1 H_2SO_4 collected with (a) $h\nu = 1487$ eV, and (b) $h\nu = 260$ eV. The S $2p$ spectra from the fractured pyrrhotite sample of Chapter 4 have been included for comparison.

5.2.1 Polished monoclinic pyrrhotite surfaces

There was no high resolution Fe $2p$ spectrum collected for the polished sample, however from the survey spectrum there are some significant observations that can be made. The main Fe $2p_{3/2}$ peak is centred around 711 eV, indicating the presence of Fe^{III} -OOH species [8]. There is a low binding

energy shoulder present around 707.5 eV, attributable to bulk pyrrhotite Fe-S species. Since no high resolution spectrum was collected, no observations can be made regarding high- or low-spin iron.

The $h\nu = 1487$ eV S $2p$ spectrum has been fitted with six components. The first doublet represents the bulk monosulfide, and contribution 85% to the spectrum (Figure 5.3a). A second doublet at 161.8 eV, which contributes 8.5% to the sulfur spectrum, is required to account for the decreased minimum between the bulk sulfur $2p_{3/2}$ and $2p_{1/2}$ peaks and has been attributed to disulfide. A sulfur-oxy component is also required to account for the slight increase in intensity in the 166 – 169 eV region, and although this could be fitted with a single doublet species, in this case has been fitted with a sulfite component at 166.7 eV and a sulfate at 168.2 eV [8] to maintain consistency with the fitted $h\nu = 260$ eV spectrum. Similarly, the sulfur components in Figure 5.3 attributed to polysulfide and elemental sulfur are small enough that the need to include them in the fit is not clear from the $h\nu = 1487$ eV spectrum alone.

The $h\nu = 260$ eV spectrum is more difficult to fit accurately due to the large secondary electron background at binding energies greater than the main peak. Three separate methods are used here to model this background; using a Shirley background (Figure 5.3b), a Tougaard background (Figure 5.3c), and a linear background (Figure 5.3d). Of these three background fitting methods, only the Shirley and Tougaard backgrounds have a theoretical description. The Shirley background considers the inelastically scattered photoelectrons contributing to higher binding energies in the spectrum [9]. While the Tougaard background considered the inelastically scattered electrons which lose kinetic energy, but also the elastically scattered photoelectrons which have an increased path length and therefore increase the number of inelastic scattering events [10].

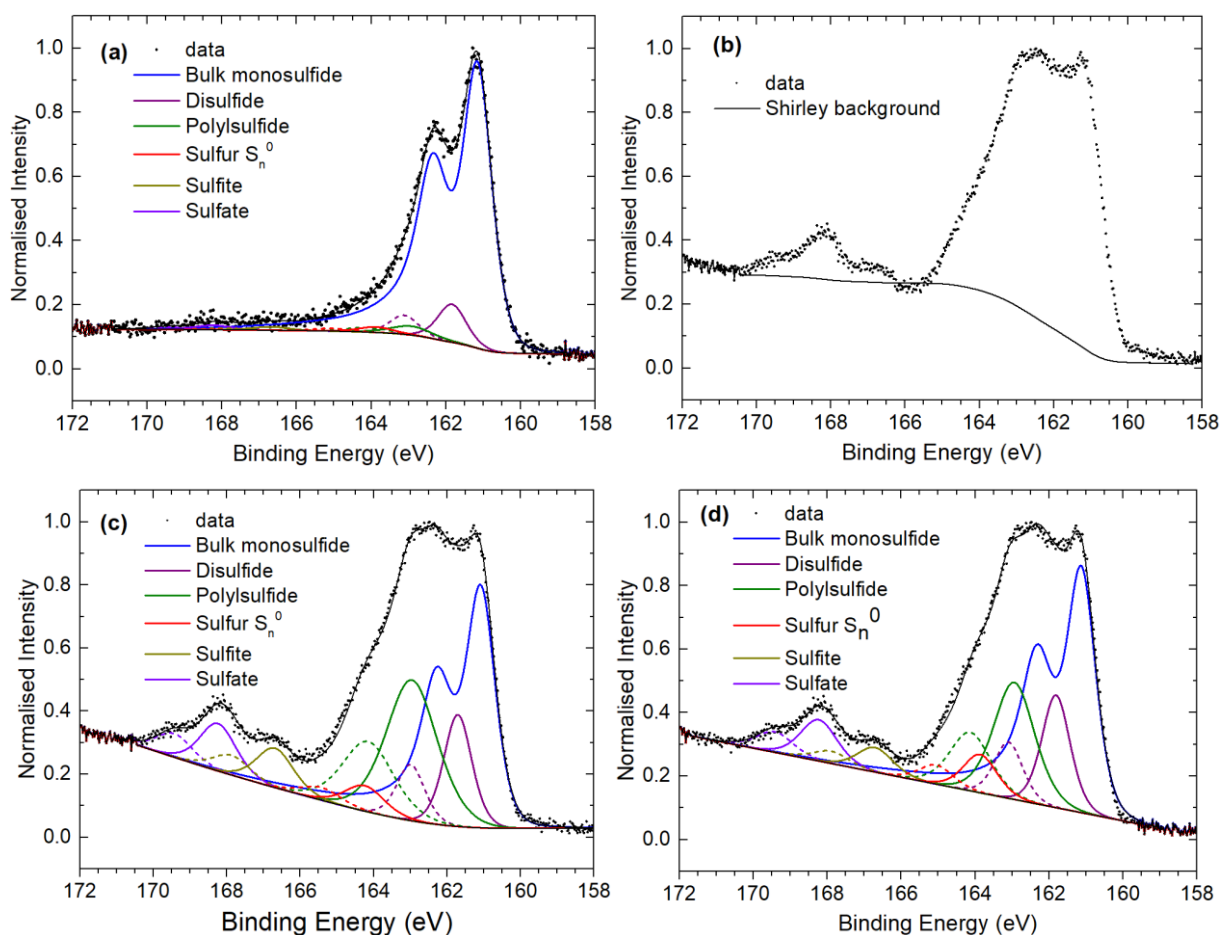


Figure 5.3: Fitted S $2p$ spectra of polished monoclinic pyrrhotite collected with (a) $h\nu = 1487$ eV, and (b) $h\nu = 260$ eV fitted with a Shirley background [9], (c) fitted with a Tougaard background [10], and (d) fitted with a linear background.

The Shirley model is the most commonly used for background subtraction when fitting photoelectron spectra. This is shown for the current data in Figure 5.3b. However, in this instance the Shirley background cannot be accurately applied to model the secondary electron background present in the spectrum in Figure 5.3b. This is evidenced by the overfitting of the background to the spectrum, specifically in the binding energy region between 166 eV and 167 eV, where the fitted background clearly strikes through the spectral peak, which is an unreasonable result and will lead to incorrect analysis when attempting to deconvolute the peaks of the various contributing species.

The Tougaard background has a far more in-depth consideration for both elastic and inelastic scattering of photoelectrons during their transport to the surface, in comparison to the Shirley background [10]. Tougaard proposes an algorithm for modelling the background created by inelastically scattered electrons, which is appropriate for most samples [11]. While not used extensively, this method for background fitting has been shown to give more accurate quantitative results than the Shirley method [12, 13], and has been used to determine the thickness, distribution,

and mechanism of film growth on surfaces [14-17]. The key difference between the Shirley and Tougaard background methods is that while the Shirley background is considered reasonable for homogeneous samples, the Tougaard method can be used for samples with non-homogeneous distribution of species through the sample.

A linear background subtraction has also been tested in Figure 5.3d for comparison, since the Tougaard background typically requires a much larger region below and above the spectrum to obtain an accurate result. While the linear background has no theoretical description, the background directly above and below the S $2p$ photoelectron spectrum appears to be linear, and therefore a linear background fitted underneath the measured spectrum may be reasonable.

The $h\nu = 260$ eV spectrum has been fitted with peaks for both the Tougaard and linear background methods, and the contribution from each species is shown in Table 5.2. In each case, the $h\nu = 260$ eV spectrum has been fitted with disulfide and polysulfide components in addition to the bulk monosulfide as is required to fit the intensity of the spectrum in the region 162 – 165 eV. Both sulfite and sulfate components are also required to fit the structure in the high binding energy region and have been fitted at 166.7 eV and 168.2 eV respectively. An extra component is required around 164 eV in both Figure 5.3c and d, which is in the binding energy region often attributed to elemental sulfur [18]. The assignment of this peak to elemental sulfur is not straightforward, since elemental sulfur is volatile in vacuum and is therefore not expected in photoelectron spectra unless the samples are cooled. There are a number of possible explanations for this peak. Firstly, inaccuracies in the background correction will propagate into errors in the fitted spectra. While it is possible that the Tougaard method underestimates the background in the region 165 – 166 eV, thus necessitating the use of an elemental sulfur feature, the linear background, which is higher in this region, also requires an elemental sulfur feature. It is therefore more likely that this peak is not simply an artefact of the background correction, but can be attributed to a sulfur component of the sample.

There are two possible sulfur assignments for the peak fitted at 164 eV. Previous literature has postulated that the amorphous sulfur rich layer contains long polysulfide chains with bond lengths similar to that of elemental sulfur [4]. It is possible that the 163 – 165 eV region should be entirely attributed to iron polysulfide species with a range of oligomer chain lengths, and consequently a range of sulfur $2p$ binding energies. This explanation is not considered likely, since an attempt was made to fit the spectrum with a broader polysulfide component and no extra component for elemental sulfur. No good fit could be attained using this method. The alternative, and more likely explanation is that the peak around 164 eV is attributable to elemental sulfur (S_n^0), which has not volatilized in the

vacuum. This may be due to the uppermost oxide layer, which is mostly devoid of sulfur, which has been found to form after air-oxidation of pyrrhotite surfaces [19]. If the upper surface layer is extensive enough, it may be physically trapping the elemental sulfur species which are formed during oxidation of the surface. The strong secondary electron background observed in the $h\nu = 260$ eV S $2p$ spectrum is likely also caused by the chemically and structurally distinct surface overlayer. An alternative explanation for the entrapment of elemental sulfur species is the assumed amorphous structure of the sulfur rich layer, as was observed for air oxidised pyrrhotite samples analysed using X-ray diffraction [2]. As the sulfur rich underlayer develops during polishing, it is possible that the elemental sulfur produced is trapped in pockets formed in the amorphous sulfur rich phase. A similar conclusion has previously been offered for the observation of elemental sulfur in ultra-high vacuum conditions on bioleached mineral surfaces; where the elemental sulfur was proposed to be trapped within other surface compounds as the surface phase developed [20].

The $h\nu = 1487$ eV spectrum has been fitted with the same peaks used in the $h\nu = 260$ eV spectrum, adjusting the heights as necessary. The results from fitting these spectra, and the atomic % contribution to the overall surface calculated from the $h\nu = 1487$ eV spectrum are shown in Table 5.2. While the bulk monosulfide component accounts for almost 10 at % for the overall sample, each of the other sulfur components accounts for less than 1% of the total atomic contribution. This data supports the observations reported in literature of an overlayer of an iron deficient sulfide consisting of disulfide species and long chain polysulfide species, which gradually returns to the bulk pyrrhotite structure at depth.

Table 5.2: Fitted components of the polished monoclinic S $2p$ spectrum, including the binding energy (BE), peak width (FWHM), % contribution represents the contribution of that species to each spectrum, with Tougaard background removal(T), and linear background removal (L), and overall atomic % contribution calculated from the $h\nu = 1487$ eV spectrum.

Species	Binding Energy (FWHM)	% contribution			At % (1487 eV)
		260 eV (Tougaard)	260 eV (Linear)	1487 eV	
Bulk monosulfide (S^{2-})	161.2 (0.90)	38.4	43.4	83.2	9.15
Disulfide (S_2^{2-})	161.8 (0.90)	13.3	15.8	9.0	0.99
Polysulfide (S_n^{2-})	162.9 (1.3)	30.6	22.6	5.0	0.55
Elemental Sulfur	163.9 (1.1)	4.2	6.7	0.9	0.10
Sulfite (SO_3^{2-})	166.7 (1.2)	6.2	4.2	0.6	0.07
Sulfate (SO_4^{2-})	168.2 (1.2)	7.3	7.3	1.3	0.14

Previous studies of air oxidised pyrrhotites have reported the uppermost layers to consist of a thin layer of saturated carbon, carbonate and sulfate species, which overlies an Fe-oxide/oxyhydroxide layer [2, 3, 21]. Angle-resolved XPS has shown that the oxygen species do not diffuse appreciably into the iron deficient sulfide layer and are primarily found in the upper layer of iron oxyhydroxide (FeOOH) species.

The results presented here do not include high-resolution spectra of carbon or oxygen species, therefore no comment can be made about the chemical state of oxygen and carbon species. Neither is there direct evidence of the distribution of measured species within and across the sample. However, the shape of the inelastic background observed in the S $2p$ $h\nu = 260$ eV spectrum is evidence of an overlayer of species other than the sulfide species which constitute a significant proportion of the sulfur signal.

The Fe $2p$ peak in the survey spectrum in Figure 5.1 is observed at a binding energy higher than that for vacuum fractured pyrrhotite; at 711 eV, consistent with Fe-oxyhydroxide species [19]. This is consistent with the reports in previous literature of the Fe-oxyhydroxide overlayer. The results presented here point towards the pyrrhotite surface and near-surface layers being similar to those of other air oxidised pyrrhotite samples [2, 3, 21]. There, the origin of the feature in the S $2p$ spectrum around 164 eV is proposed to be due to elemental sulfur in the sulfur rich near surface layer, which is formed when the Fe ions diffuse to the surface to oxidise to Fe-oxyhydroxide species. The elemental sulfur is detected in the photoelectron spectra, despite its volatility in vacuum and lack of sample cooling, due to being physically trapped by the Fe-oxyhydroxide overlayer which is sufficiently extensive.

5.2.2 Surface of monoclinic pyrrhotite in pH 1 H₂SO₄

The Fe $2p$ spectrum for pyrrhotite in pH 1 H₂SO₄ is compared to the Fe $2p$ spectrum for vacuum fractured pyrrhotite in Figure 5.4. The resolution of the spectrum for this sample appears to be better than that for the fractured sample, despite the samples being collected on the same beamline with the same instrumental settings. It is expected that this is due to the nature of the surface of the samples. The surface of the vacuum fractured pyrrhotite sample is not expected to be perfectly flat since pyrrhotite has no cleavage, while the surface of the pyrrhotite sample in pH 1 H₂SO₄ had been polished to a high shine before reacting with acidic solution and was still visibly smooth after reaction. The Fe $2p_{3/2}$ peak for this sample is also narrower than that for the vacuum fractured sample, which is considerably broad due to the multiplet structure owing to the high-spin Fe^{II}-S in bulk pyrrhotite

and a convolution of Fe^{II}-S and Fe^{III}-S found natively in bulk pyrrhotite. The width of the Fe 2p_{3/2} peak on the low binding energy side is at least partly owing to the Fe-Fe π-π bonding which is less prominent in more iron deficient pyrrhotites, and most prominent in troilite (FeS) [22]. The Fe 2p_{3/2} peak of this sample is similarly centred at 707.7 eV, but has a sharp leading edge. There is also less intensity on the high binding energy side but with a shoulder emerging around 710 eV. Previous studies have shown that the Fe:S ratio in the sulfur rich layer of pyrrhotite samples which have been similarly reacted in acid becomes close to 1:2 at the near surface [3]. The decrease in iron in this layer would likely result in less Fe-Fe π-π bonding, causing a decrease in the low binding energy feature and give the Fe 2p_{3/2} peak a sharper leading edge. Mössbauer studies have shown that the iron in the sulfur rich layer of pyrrhotite reacted in HCl solution is primarily low-spin Fe^{II}-S, with a shorter Fe-S bond length than found in bulk pyrrhotite, as shown by S K edge absorption spectra [4]. If a similar transformation of the near surface layers of the pyrrhotite sample analysed here has taken place, the transition from high- to low-spin Fe^{II}-S would explain the decrease in intensity in the overall width of the main peak. The emergence of the shoulder around 710 eV is attributable to the presence of Fe-oxide/oxyhydroxide species [23].

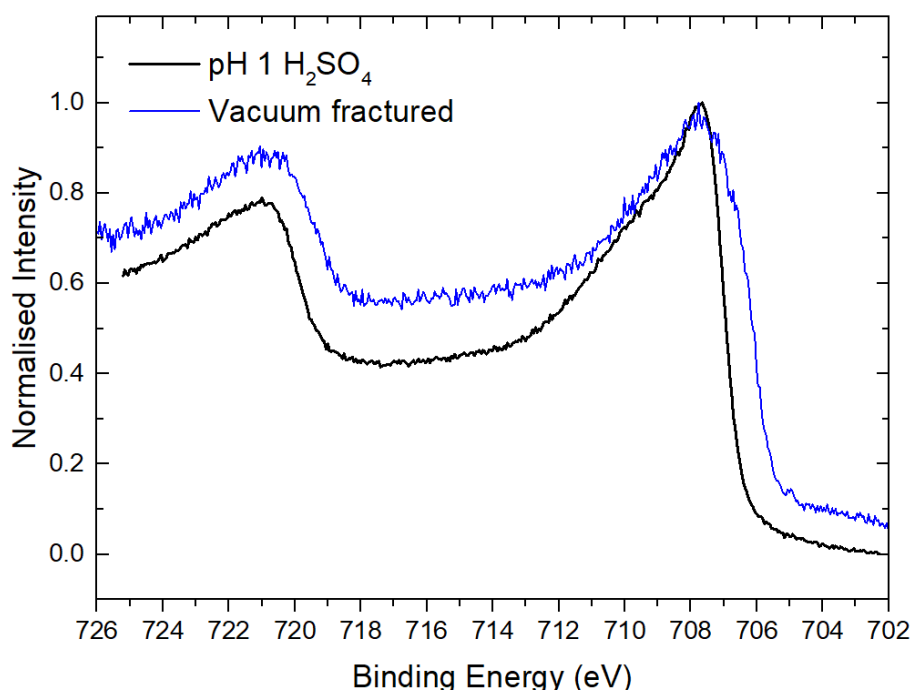


Figure 5.4: Fe 2p spectra for pyrrhotite exposed to pH 1 H₂SO₄ for 1 hour (black) and vacuum fractured (blue) monoclinic pyrrhotite from Chapter 4.

The $h\nu = 1487$ eV S 2p spectrum has a similar shape to the bulk S 2p spectra of the vacuum fractured and polished pyrrhotite samples, but with a decrease in the minimum between the 2p_{3/2} and 2p_{1/2} components. There is also additional intensity in the 163 – 165 eV region, indicating a greater

presence of disulfide and polysulfide species than in the vacuum fractured and polished pyrrhotite sample. In comparison to the polished sample, the sample of pyrrhotite in pH 1 H_2SO_4 has a similar percentage of sulfur-oxy species contributing to the S $2p$ spectrum (1.9% in the polished sample compared to 2.4% for pyrrhotite in H_2SO_4). However, the atomic % contribution to the overall sample from the sulfur-oxy species is significantly greater in the acid reacted sample (0.2% in the polished sample compared to 0.6% for pyrrhotite in H_2SO_4).

As in the polished sample, the sulfur features that are additional to the bulk monosulfide in the sample of pyrrhotite in H_2SO_4 are not clear from the $h\nu = 1487$ eV spectrum alone, and the fitted peaks from the $h\nu = 260$ eV spectrum are applied to the $h\nu = 1487$ eV spectrum, with the heights adjusted as necessary.

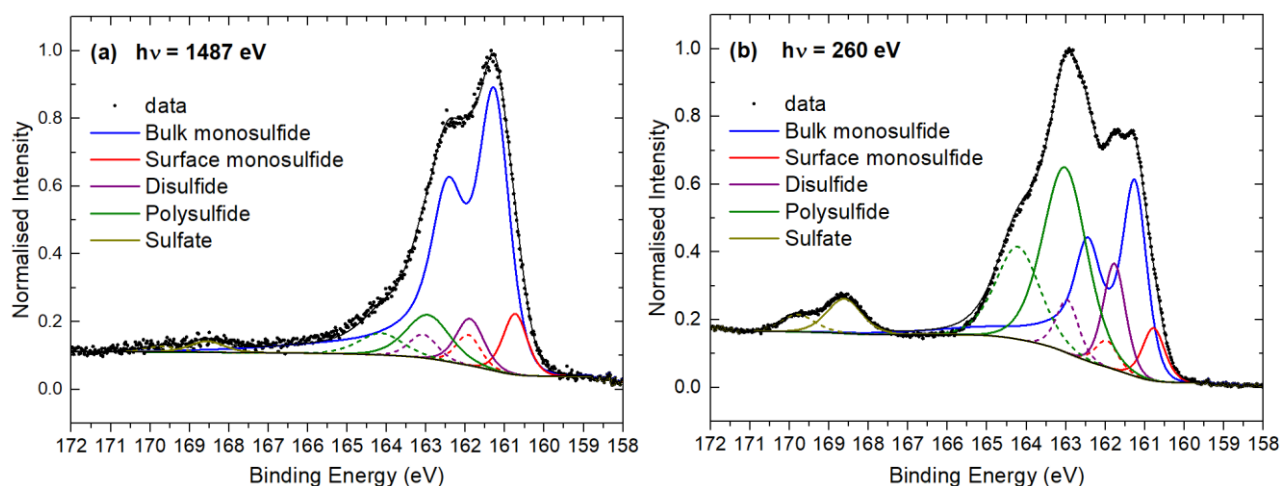


Figure 5.5: Fitted S $2p$ spectra of monoclinic pyrrhotite exposed to pH 1 H_2SO_4 for 1 hour, collected with $h\nu =$ (a) 1487 eV and (b) 260 eV.

The $h\nu = 260$ eV spectrum in Figure 5.5b shows a curious double peak feature in the 161 – 162 eV region which is either not present or not resolved in the S $2p$ spectra for either the vacuum fractured or the polished pyrrhotite samples. The energies of the two peaks are similar to the bulk monosulfide and the disulfide species fitted to the vacuum fractured sulfur spectrum and have been fitted as such in the spectrum in Figure 5.5b. An extra peak on the low binding energy side of this spectrum has been fitted to account for the small inflection in this region and contributes to 6% of the total fit. The binding energy of this peak is consistent with the undercoordinated surface monosulfide species fitted to the vacuum fractured $h\nu = 260$ eV sulfur spectrum. The inclusion of this peak necessitates a narrower line width for the bulk monosulfide and disulfide peaks, which is required to recreate the double peak feature in the 161 – 162 eV region of the spectrum. The binding energies of the bulk monosulfide and disulfide peaks are consistent with those fitted to the spectra of the vacuum fractured

and polished pyrrhotite samples, and account for 34% and 12% of the total spectral fit respectively. The main peak of the $h\nu = 260$ eV spectrum is well fitted with a broad polysulfide component fitted at 163.0 eV and constitutes 42% of the $h\nu = 260$ eV sulfur spectrum. A single sulfur-oxy species is required at 168.6 eV and is attributed to sulfate (SO_4^{2-}) species.

Unlike in the polished pyrrhotite sample, no extra peaks were required to fit the $h\nu = 260$ eV spectrum, such as those attributed to elemental sulfur. It may initially seem that this may be due to the choice of Shirley background in the $h\nu = 260$ eV spectrum for pyrrhotite in H_2SO_4 , however the increased background due to secondary electrons is not as obvious in this spectrum as it was for the polished sample. Therefore, the Shirley background was chosen as it best fitted the background of the spectrum, is consistent with other spectra presented in this work, and with spectra shown in previous literature. The difference in the heights of the backgrounds between the two samples is expected to be due to the increase in total path length of electrons and therefore the loss of kinetic energy due to a chemically distinct overlayer.

Since a Shirley background was sufficient for the sample of pyrrhotite in pH 1 H_2SO_4 , which did not have such a significant contribution to the background compared to the polished sample, the background indicates that there is not a significant overlayer for this sample, as there was observed for the polished sample. This coincides with the lack of elemental sulfur observed in the S $2p$ spectrum for the sample of pyrrhotite in H_2SO_4 . Since this sample was polished in the same way as the polished sample, elemental sulfur can be expected to have been produced and trapped in the same way. However, during the reaction with sulfuric acid, the sample has changed such that the elemental sulfur is either consumed, leached into solution, or is able to escape into atmosphere or in the vacuum chamber of the end station.

As previously shown in Table 5.1, the total contribution to the sample from the sulfate species is observed to be significantly higher in the sample reacted in sulfuric acid than in the polished sample. It is possible that a significant contribution to the sulfate species arises from the sulfuric acid solution. In contrast, this pyrrhotite sample has a significantly lower contribution from oxygen species than in the polished sample, despite the relative increase in sulfur-oxy species. This indicates that it is the Fe-oxyhydroxide overlayer which is being removed due to the reaction with acidic solution. The removal of the oxyhydroxide overlayer coincides with the reduction in the inelastic background in the low photon energy S $2p$ spectrum, indicating that the background in the low photon energy S $2p$ spectrum for the polished sample is due to the presence of a significantly extensive Fe-oxyhydroxide overlayer.

Table 5.3: Fitted components of the S 2*p* spectra of monoclinic pyrrhotite in pH 1 H₂SO₄ for 1 hour. The binding energy (BE), peak width (FWHM), % contribution to the fit for both *hν* = 1487 eV and 260 eV spectra, and overall atomic % contribution to the sample calculated from the *hν* = 1487 eV spectrum.

Species	Binding Energy (FWHM)	% contribution		At % (1487 eV)
		260 eV	1487 eV	
Surface monosulfide	160.7 (0.73)	6.0	9.1	2.2
Bulk monosulfide	161.8 (0.89)	33.7	68.8	17
Disulfide	162.9 (0.82)	12.1	7.9	1.9
Polysulfide	163.9 (1.3)	42.0	11.8	2.8
Sulfate	168.2 (1.1)	6.2	2.4	0.6

5.2.3 NEXAFS spectra and PEEM images of pyrrhotite immersed in pH 1 H₂SO₄ for 1 hour

The Fe L_{2,3} edge NEXAFS spectrum for pyrrhotite in pH 1 H₂SO₄ is shown in Figure 5.6a with the spectrum for vacuum fractured monoclinic pyrrhotite. The spectrum for pyrrhotite in H₂SO₄ shows a slight shift of the main absorption peak to a higher absorption energy and an increase in intensity around 710 eV in comparison to the vacuum fractured pyrrhotite. This increase at 710 eV is attributed to an increase in Fe^{III} species [24], which is partly due to the creation of Fe-oxyhydroxide species evident in the Fe 2*p* photoelectron spectrum. The pre-edge shoulder at 705 eV is less clear in the oxidised sample, indicating a decrease in the transition of 2*p* electrons to the Fe^{II}-S *t*_{2g}*β* state. This is consistent with a transition of high-spin Fe^{II}-S to low-spin Fe^{II}-S, as the Fe *t*_{2g} band becomes more filled, resulting in a less intense peak relating to this transition. Similarly, the slight shift in the position of the main L₃ absorption peak may be due to the change in proportion of high- to low-spin Fe^{II}-S. The shift in peak position may also represent a change in relative intensity of Fe^{II} to Fe^{III} species to favour the latter.

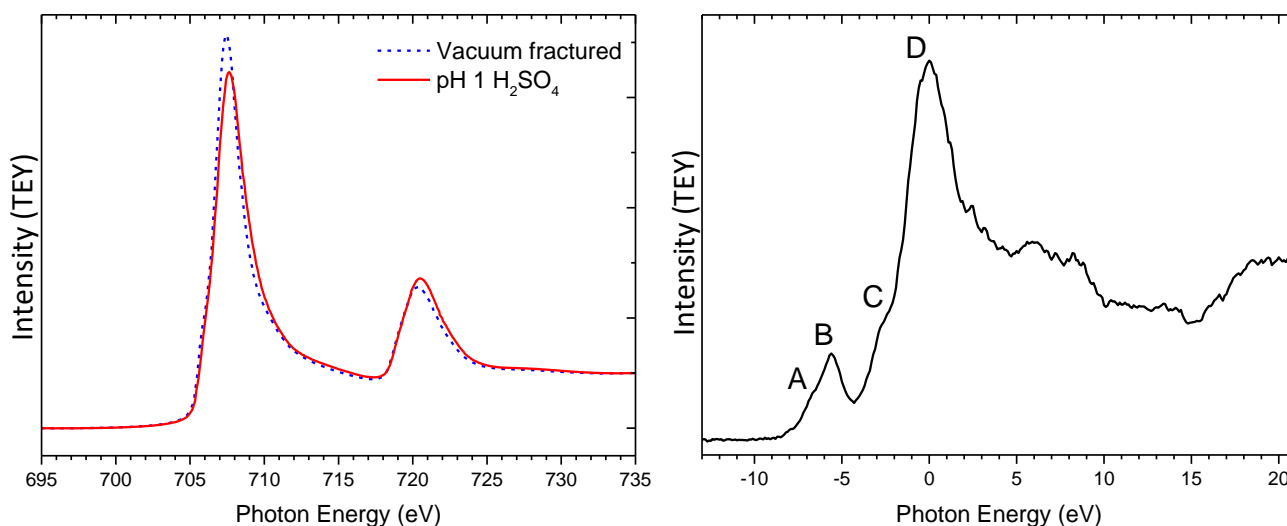


Figure 5.6: (a) Fe $L_{2,3}$ edge NEXAFS spectra for vacuum fractured pyrrhotite and pyrrhotite in pH 1 H_2SO_4 , (b) Oxygen K edge NEXAFS for pyrrhotite in pH 1 H_2SO_4 .

The oxygen K edge spectrum has a main peak at D, and a small peak at an energy approximately 5 eV lower. Both of these peaks have additional structure, with a pre-edge shoulder to the main peak at C, approximately 6.5 eV below the main peak. The structure around peak D and up to 15 eV above has been assigned to transitions from O $2p$ states hybridised with unoccupied metal $4s$ and $4p$ states [25]. The energy difference between peaks A and B is approximately 1 eV, which is consistent with the calculations of the pyrrhotite iron valence states [26] and consistent with the results in the previous chapter. Therefore, peaks A and B are attributed to the O $2p$ orbitals which are mixed with the Fe $3d$ t_{2g} and e_g orbitals respectively. The relative height of the main peak and the peak around B reflects the number of unoccupied metal $3d$ states available for electrons to transition to the final state, and the spectrum shows that the transition of electrons into the conduction band is more likely, as the Fe $3d$ -like states are mostly filled. This spectrum shows that the oxygen species are strongly associated with the covalent Fe-O bonding reported for the upper surface layer of oxidised pyrrhotite. However, the little difference between the Fe L edge spectra of the vacuum fractured sample, and pyrrhotite in pH 1 H_2SO_4 indicates that the Fe-O species contribute only a small proportion of the Fe species in the sample. This is consistent with the thin Fe-O overlayer proposed in literature.

The PEEM images presented in Figure 5.7 are taken at the Fe L pre-edge shoulder, the L_3 absorption peak, and the main O K edge absorption peak respectively, each with the same 450 μm field of view. Each of these images has had the topography removed using a background image taken below each absorption edge. The feature seen running diagonally across the field of view is likely from a scratch remaining from the polishing procedure. The surface also has a speckled appearance, which aligns with regions of strong absorption at the O K edge. It is not clear from the images if the speckled effect

is from pitting of the surface, or if it is from island growth of oxygen species. These images show that the oxygen species aggregate in small regions across the sample rather than in an even surface layer. This speckled appearance shows that the Fe-oxyhydroxide species exist predominantly in patches. This is consistent with the hypothesis that after reaction with acidic solution, the Fe-oxyhydroxide layer is not sufficiently extensive to trap elemental sulfur in the sulfur rich underlayer. The Fe absorption image in Figure 5.7b shows stronger absorption in regions where there is less oxygen, indicating that the Fe L edge NEXAFS spectrum is predominantly from pyrrhotite Fe-S species.

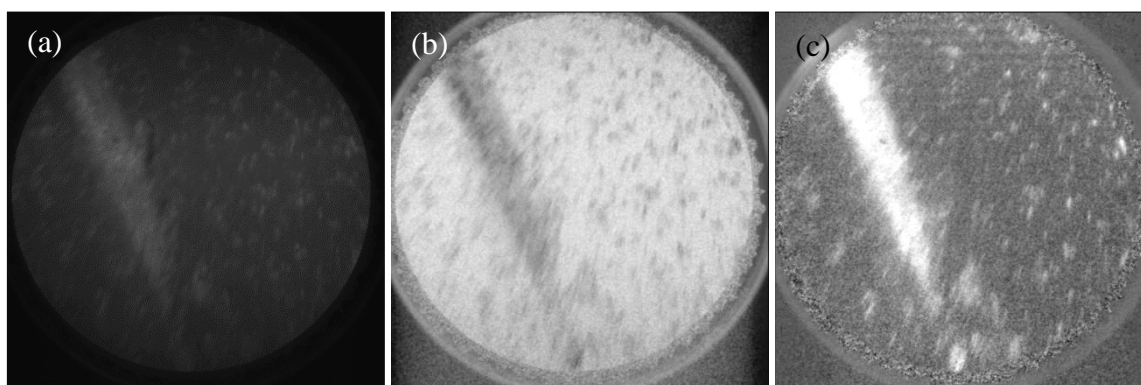


Figure 5.7: Images of monoclinic pyrrhotite surface after 1 hour in pH 1 H₂SO₄, collected (a) below the iron absorption edge, (b) at the iron absorption edge (background removed) and (c) at the oxygen absorption edge (background removed). Field of view = 450 μ m.

5.3 Conclusion

This chapter has presented photoelectron spectra for polished pyrrhotite and pyrrhotite after 1 hour in pH 1 H₂SO₄, with NEXAFS spectra and PEEM images over the iron L and oxygen K absorption edges for the sample in sulfuric acid. Survey spectra were used to quantify the contributions to each sample's surface from individual elements, showing strong contributions from carbon in both samples, and oxygen in the polished sample, while Fe 2*p* core level spectra showed the Fe species in the polished sample to be largely be due to iron oxyhydroxide species, and the sample reacted in acidic solution to be largely iron sulfide species. A detailed analysis of the sulfur 2*p* core level spectra, using both surface sensitive and more bulk sensitive photon energies, revealed the sulfur species present on the surface of the sample, including an elemental sulfur component in the polished sample, but not the sample in sulfuric acid.

Overall, the results showed that the surface of the polished sample resembled surfaces of other air oxidised pyrrhotite samples presented in literature. Specifically, the survey spectrum showed a large proportion of carbon and oxygen species at the surface, with an increased proportion of iron in comparison to the expected bulk. This result is consistent with the air oxidised pyrrhotite samples

presented in previous studies by Buckley and Woods [21], Jones, LeCount, Smart and White [2] and Mycroft, Nesbitt and Pratt [3], on which a layer of iron oxyhydroxide species develops as the iron ions diffuse through the bulk towards the surface to react with oxygen. The Fe $2p$ peak in the survey spectrum was at a binding energy consistent with Fe oxyhydroxide species, and very little evidence of pyrrhotite Fe-S species remained, indicating that the iron oxyhydroxide layer was significantly thick and extensive. The S $2p$ spectrum of the polished pyrrhotite sample had a contribution from elemental sulfur, which is initially surprising since elemental sulfur is typically not expected on a sample in ultra-high vacuum at ambient temperature. It is likely that this species is physically trapped by a combination of the amorphous sulfur rich underlayer which has formed due to oxidation of the surface during polishing, and a physical barrier that is possibly provided by an extensive layer of Fe-oxyhydroxides. The low photon energy S $2p$ spectrum showed a strong inelastic background in the low photon energy spectrum, which is evidence of a significant overlayer of elementally distinct species, which does not contribute significantly to the peaks in the spectrum. Rather, this overlayer contributes to the background by increasing the path length and therefore the inelastic collisions of the photoelectrons. It is suggested that the overlayer contributing to the background in the S $2p$ spectrum is largely the iron oxyhydroxide overlayer, and that this layer is also possibly contributing to the entrapment of elemental sulfur within the near surface region of the sample.

After reacting with acidic solution, the surface of the sample had significantly lower contribution from oxygen species, and the ratio of iron to sulfur was similar to that expected from bulk pyrrhotite. This showed that the iron oxyhydroxide overlayer which was created by polishing the sample is largely removed upon reaction with acidic solution. The Fe $2p$ spectrum supported this observation, as the shape of the $2p_{3/2}$ peak was similar to that of bulk pyrrhotite, with only a small contribution from Fe oxyhydroxide species. Concurrently, the S $2p$ spectrum showed contributions from disulfide and polysulfide species, but no contribution from elemental sulfur. The low photon energy S $2p$ spectrum also showed significantly less inelastic background than was seen for the polished sample. This showed that the overlayer which was present on the polished sample was not as extensive on the sample in sulfuric acid. The sulfur rich underlayer was still present, evidenced by the strong contribution to the low photon energy S $2p$ spectrum from polysulfide species, yet no elemental sulfur was detected. This reinforces the proposition that it is the iron oxyhydroxide overlayer, and not the sulfur rich near surface layer which is trapping the elemental sulfur in the polished sample. The NEXAFS spectra and PEEM images supported this theory, as iron oxyhydroxide species were observed on the surface of pyrrhotite in acidic solution but were not extensive across the sample. Rather, they existed in patches, and did not contribute significantly to the Fe L edge spectrum. This

showed that while some oxyhydroxide species exist on the surface, they are not extensive, and have been removed in the reaction in acidic solution such that the Fe-S near surface layer is exposed.

A significant outcome of this chapter is the ability to accurately fit the S 2*p* spectra, and the detail of the sample surface that could be gained from the analysis of these spectra. The significant inelastic background in the low photon energy S 2*p* spectrum for the polished sample highlighted the importance of considering the most appropriate background to use for a spectrum, and what that might physically mean for a sample. Although there has been significant work in this field, the information that is contained in the background of a sample is often not considered, despite the effect it may have on the fit of a core level spectrum, and the additional information that may be gained about the surface of the sample. The method used for fitting the S 2*p* spectra is also a significant outcome of this chapter. The higher binding energy sulfur species are often difficult to accurately fit in conventional photoelectron spectra due to the overlap of species and the undefined shape of the bulk sulfide tail. By using the bulk pyrrhotite line shape which was found empirically in Chapter 4, these higher binding energy species such as disulfide, polysulfide and elemental sulfur species could be fitted with greater accuracy. Furthermore, the comparison of the low photon energy, surface sensitive spectra with the spectra collected with conventional photon energy provided more confidence in fitting minority species which could not otherwise be justified in conventional photoelectron spectra. These results will inform future analysis of similar samples, thereby enhancing the advantage of conventional photoelectron spectroscopy.

5.4 References

- [1] S.W. Knipe, J.R. Mycroft, A.R. Pratt, H.W. Nesbitt, G.M. Bancroft, X-ray photoelectron spectroscopic study of water adsorption on iron sulphide minerals, *Geochimica et Cosmochimica Acta*, 59 (1995) 1079-1090.
- [2] C.F. Jones, S. LeCount, R.S.C. Smart, T.J. White, Compositional and structural alteration of pyrrhotite surfaces in solution: XPS and XRD studies, *Applied Surface Science*, 55 (1992) 65-85.
- [3] J.R. Mycroft, H.W. Nesbitt, A.R. Pratt, X-ray photoelectron and Auger electron spectroscopy of air-oxidized pyrrhotite: Distribution of oxidized species with depth, *Geochimica et Cosmochimica Acta*, 59 (1995) 721-733.
- [4] Y.L. Mikhlin, Y.V. Tomashevich, G.L. Pashkov, A.V. Okotrub, I.P. Asanov, L.N. Mazalov, Electronic structure of the non-equilibrium iron-deficient layer of hexagonal pyrrhotite, *Applied Surface Science*, 125 (1998) 73-84.
- [5] Z.E. Pettifer, A Study of the Dissolution of Iron and Nickel Sulfides and the Effect of Mixed Mineral Systems [Honours thesis], Flinders University, *Some of the data of this sample was presented in a previous honours thesis, however the analysis is original to the present PhD thesis*, 2014.
- [6] J.F. Moulder, W.F. Stickle, P.E. Sobol, K.D. Bomben, *Handbook of X-ray Photoelectron Spectroscopy*, Physical Electronics, Eden Prairie, Minnesota, 1992.
- [7] Casa Software, CasaXPS, 2000.

- [8] M. Descostes, F. Mercier, N. Thromat, C. Beaucaire, M. Gautier-Soyer, Use of XPS in the determination of chemical environment and oxidation state of iron and sulfur samples: constitution of a data basis in binding energies for Fe and S reference compounds and applications to the evidence of surface species of an oxidized pyrite in a carbonate medium, *Applied Surface Science*, 165 (2000) 288-302.
- [9] D.A. Shirley, High-Resolution X-Ray Photoemission Spectrum of the Valence Bands of Gold, *Physical Review B*, 5 (1972) 4709-4714.
- [10] S. Tougaard, P. Sigmund, Influence of elastic and inelastic scattering on energy spectra of electrons emitted from solids, *Physical Review B*, 25 (1982) 4452-4466.
- [11] S. Tougaard, Practical algorithm for background subtraction, *Surface Science*, 216 (1989) 343-360.
- [12] M. Repoux, Comparison of background removal methods for XPS, *Surface and Interface Analysis*, 18 (1992) 567-570.
- [13] B.S. Norgren, M.A.J. Somers, J.H.W. De Wit, Application of Tougaard Background Subtraction to XPS Spectra of Passivated Fe-17 Cr, *Surface and Interface Analysis*, 21 (1994) 378-381.
- [14] S. Tougaard, H.S. Hansen, Yb growth on Ni(100) studied by XPS inelastic background analysis, *Surface Science*, 236 (1990) 271-281.
- [15] M.R. Alexander, G.E. Thompson, X. Zhou, G. Beamson, N. Fairley, Quantification of oxide film thickness at the surface of aluminium using XPS, *Surface and Interface Analysis*, 34 (2002) 485-489.
- [16] S. Tougaard, Energy loss in XPS: Fundamental processes and applications for quantification, non-destructive depth profiling and 3D imaging, *Journal of Electron Spectroscopy and Related Phenomena*, 178-179 (2010) 128-153.
- [17] S. Tougaard, Improved XPS analysis by visual inspection of the survey spectrum, *Surface and Interface Analysis*, 50 (2018) 657-666.
- [18] R.S.C. Smart, W.M. Skinner, A.R. Gerson, XPS of sulphide mineral surfaces: metal-deficient, polysulphides, defects and elemental sulphur, *Surface and Interface Analysis*, 28 (1999) 101-105.
- [19] A.R. Pratt, I.J. Muir, H.W. Nesbitt, X-ray photoelectron and Auger electron spectroscopic studies of pyrrhotite and mechanism of air oxidation, *Geochimica et Cosmochimica Acta*, 58 (1994) 827-841.
- [20] M. Khoshkhoo, M. Dopson, A. Shchukarev, Å. Sandström, Chalcopyrite leaching and bioleaching: An X-ray photoelectron spectroscopic (XPS) investigation on the nature of hindered dissolution, *Hydrometallurgy*, 149 (2014) 220-227.
- [21] A. Buckley, R. Woods, X-ray photoelectron spectroscopy of oxidized pyrrhotite surfaces: I. Exposure to air, *Applications of Surface Science*, 22/23 (1985) 280-287.
- [22] W.M. Skinner, H.W. Nesbitt, A.R. Pratt, XPS identification of bulk hole defects and itinerant Fe 3d electrons in natural troilite (FeS), *Geochimica et Cosmochimica Acta*, 68 (2004) 2259-2263.
- [23] A.P. Grosvenor, B.A. Kobe, M.C. Biesinger, N.S. McIntyre, Investigation of multiplet splitting of Fe 2p XPS spectra and bonding in iron compounds, *Surface and Interface Analysis*, 36 (2004) 1564-1574.
- [24] Y. Mikhlin, Y. Tomashevich, Pristine and reacted surfaces of pyrrhotite and arsenopyrite as studied by X-ray absorption near-edge structure spectroscopy, *Phys Chem Minerals*, 32 (2005) 19-27.
- [25] F. de Groot, M. Grioni, J. Fuggle, J. Ghijsen, G. Sawatzky, H. Petersen, Oxygen 1s x-ray-absorption edges of transition-metal oxides, *Physical Review B*, 40 (1989) 5715-5723.
- [26] S. Sakkopoulos, E. Vitoratos, T. Argyreas, Energy-band diagram for pyrrhotite, *Journal of Physics and Chemistry of Solids*, 45 (1984) 923-928.

6 PRISTINE FRACTURE SURFACES OF PENTLANDITE

6.1 Introduction

The interpretation of photoelectron spectra for pentlandite has been a point of discussion in published literature since the first observation of pentlandite photoelectron spectra by Richardson and Vaughan [1]. Subsequent studies reported sulfur spectra similar to each other but asserted differing assignments of states to the features in the spectra. Common to all modern observations of the pentlandite sulfur spectrum is a dominant peak at 162.2 eV binding energy, assigned to the bulk sulfide, and a smaller peak on the low binding energy side around 161.4 eV. It is the assignment of this second peak that is contentious among experts in the field [2, 3] assigning this feature to an oxidised sulfide feature, such as that observed in the transformation from pentlandite to violarite [1]. Other literature has suggested that the two sulfur features can be attributed to 5-coordinate and 4-coordinate bulk sulfide respectively [4, 5]. Although it has been shown that there is no general relationship between coordination and binding energy, there may be a difference in binding energy between the 4- and 5-coordinate sulfur sites in pentlandite based on bond length, or more accurately, electronegativity [6]. Since the publications of these mentioned studies there has been considerable improvements in the spectral resolution available, especially with the use of synchrotron radiation XPS (SXPS), which this chapter utilises to address this contention in the literature.

The pentlandite structure has been described in detail in section 2.3. The uncertainty in distribution of Fe and Ni cations in the pentlandite lattice complicates the interpretation of photoelectron spectra and it is difficult to predict the electronic structure of the material. The expectation of metal-metal bonding between adjacent tetrahedral cations has given rise to discussion of the metallic nature of pentlandite and the subsequent fitting of pentlandite S 2*p* spectra with asymmetric Doniach-Sunjic tails [4]. The asymmetric nature of the tails arises from the readjustment of valence band electrons in the final state as a result of the creation of a core hole [7]. However, more recently sulfide semiconductors similar to pentlandite have displayed more discrete energy loss features in their S 2*p* spectra [8-11]. As seen in previous chapters, any inaccuracy in the selection of the tail shape will likely overshadow the contribution from possible surface states at binding energies higher than the bulk peak, thus creating more uncertainty in the interpretation of S 2*p* spectra.

Choosing the appropriate line shape to use for fitting spectra is a perplexing issue surrounding the pentlandite photoelectron spectra and is not isolated to this mineral, but is an issue for transition metal compounds in general [12, 13]. The previously mentioned pentlandite studies have identified broad tails on the high binding energy side of the sulfide peaks. Analogous features have previously been

Chapter 6: Pristine fracture surfaces of pentlandite

observed for other similar sulfides for example such as chalcopyrite [8] and bornite [9]. Due to the resolution available for previous pentlandite studies, the overlap between different sulfide states and the relatively high binding energy of the bulk sulfide, up to this point it has been unclear if the broad high binding energy tails are due to products of surface reconstruction such as disulfide and polysulfide species, or if the tails are a bulk sulfide feature. By identifying the surface features in the sulfur spectrum, this chapter also aims to address the origin of this high binding energy tail.

6.1.1 Methods

Both samples presented in this chapter were cut from the same synthetic pentlandite mineral. Analysis revealed a stoichiometry of $\text{Fe}_{4.4}\text{Ni}_{4.6}\text{S}_{8.1}$ throughout the mineral. Each sample was notched then fractured under high vacuum, and the exposed surface analysed without exposure to atmosphere. This process is described in detail in the methods section. The samples were fractured and analysed at separate times and are referred to in this chapter as “Pn1” and Pn2” respectively.

For comparison between samples each spectrum was normalised to the bulk peak and the intensity scale is therefore arbitrary. The spectra taken with each photon energy were energy corrected using the valence band spectra which are presented in Chapter 7. Each of the sulfur $2p$ spectra have been fitted with a Shirley background [14] before fitting individual components.

6.2 Photoelectron spectra of the “Pn1” fractured surface

The survey spectrum for Pn1 is shown in Figure 6.1 below, with approximate quantification from the spectrum shown in Table 6.1. The quantification has used relative sensitivity factors (RSF) based on a photon energy of 1487 eV. The quantification is expected to be reasonable at this photon energy since the photoionization cross section of each of the subshells used for the quantification increases at a similar rate from $h\nu = 1487$ eV to $h\nu = 1400$ eV [15].

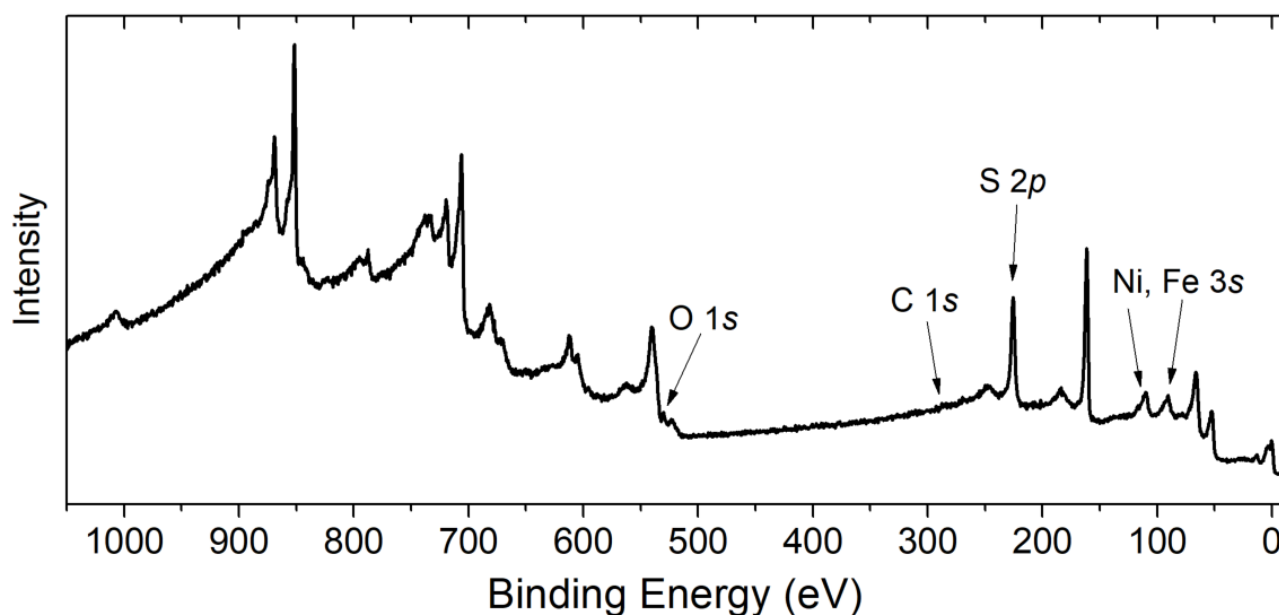


Figure 6.1: Survey spectrum for vacuum fractured Pn1 sample, showing no apparent contribution from carbon or oxygen species, $h\nu = 1400$ eV.

Due to the overlap with the Ni LMM Auger at 540 eV (binding energy) the oxygen 1s peak at 530 eV is difficult to quantify. There is a small peak around 285 eV due to a small amount of carbon on the sample, however the peak is barely noticeable above the noise in the 1400 eV spectrum. The approximate quantification of atomic species based on the 1400 eV spectrum is shown in Table 6.1. The Fe and Ni 3s peaks were used to quantify the cations, due to the significant background overlapping with the 3p states, and the Auger components overlapping with the 2p states. The quantification results show that there is very little carbon and oxygen species present on the surface, indicating that the sample is relatively pristine.

Table 6.1: Approximate quantification from the $h\nu = 1400$ eV survey spectrum for Pn1.

Peak	At% contribution
Fe 3s	27.7
Ni 3s	31.2
S 2p	37.7
O 1s	1.6
C 1s	1.7

6.2.1 Pn1 Fe & Ni 2p SXPS

Both Fe 2p spectra presented in Figure 6.2(a) show a peak centred at 707.3 eV for divalent iron sulfide in pentlandite [2-4] with a tail that extends to approximately 714 eV. The peak binding energy is

similar to high-spin divalent iron $\text{Fe}^{\text{II}}\text{-S}$ that is octahedrally coordinated to sulfur in pentlandite and pyrrhotite [16] and trivalent tetrahedrally coordinated iron $\text{Fe}^{\text{III}}\text{-S}$ in chalcopyrite (CuFeS_2) [3]. The broad shape of the peak can be explained by multiplet splitting of the spectral line and supports the designation of high spin divalent iron [17]. While the 1400 eV spectrum has approximately 10% of the signal from the surface, the 1110 eV and 846 eV spectra are expected to have approximately 15% and 26% contribution from the surface, respectively. The 1110 eV and 846 eV spectra show increased intensity at 710 eV, indicating oxidation of the iron sites at the surface [16, 18, 19]. This corresponds to the estimated 1% oxygen and 1.5% carbon species observed in the survey spectrum. There is an increase in intensity at 708 eV in the 1110 eV and 846 eV spectra which is attributed to divalent iron oxide species [20]. Since the sample was fractured in vacuum, and due to pentlandite's propensity to oxidise along grain boundaries, it is expected that the oxidation observed at the iron sites is confined to the grain boundaries and is not extensive across the surface.

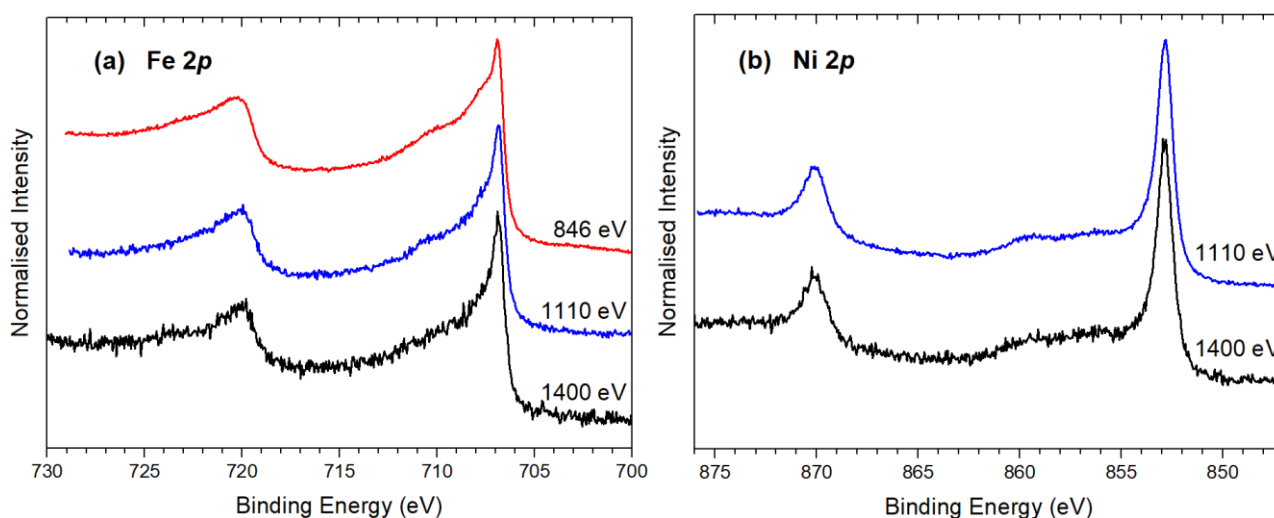


Figure 6.2: (a) Fe 2p XPS spectra of pristine pentlandite collected with $h\nu = 846$ eV, 1110 eV, and 1400 eV, (b) Ni 2p XPS spectra collected with $h\nu = 1110$ eV, and 1400 eV.

The 1110 eV and 1400 eV Ni 2p spectra, shown in Figure 6.2b, both show a strong peak centred at a binding energy of 852.8 eV, which is consistent with divalent Ni-S [1, 2, 4]. The tail of the Ni 2p spectrum has more structure than the Fe 2p spectrum, with two broad peaks observable around 856 eV and 860 eV. The higher binding energy peak has a separation from the main peak of 6 eV which is similar to the satellite seen in the 2p spectrum for nickel metal. This has been attributed to the $3d^9 4s^2$ final state, while the main peak is attributed to the $3d^{10} 4s$ final state [21]. The two high binding energy peaks observed in Figure 6.2(b) show no observable difference in shape or relative intensity between the 1400 eV spectrum and the 1110 eV spectrum, indicating that these peaks are bulk features. This indicates that there is no alteration of the nickel sites at the surface due to either oxidation or surface electronic structure changes relative to the bulk. The absence of oxidised nickel

products confirms that the iron in the pentlandite lattice oxidises preferentially over the nickel, as has previously been suggested [1, 2].

6.2.2 Pn1 Sulfur 2p spectra

Figure 6.3 displays a series of S 2p photoemission spectra collected from *in situ* vacuum fractured pentlandite with incident photon energies of 260, 400, 600, 846, and 1400 eV. As shown in Table 6.2, an incident photon energy of 260 eV yields S 2p photoelectrons with a kinetic energy of 100 eV, from a depth of 5.2 Å. Approximately 30% of those photoelectrons arise from the surface monolayer [22, 23]. Comparably, an incident photon energy of 1400 eV yields S 2p photoelectrons with kinetic energy of 1240 eV, which results in the photoelectrons arising from a depth of 23.3 Å, with less than 10% of these electrons originating in the surface monolayer. Therefore, the variation in surface sensitivity of the spectra presented may be used to isolate the species due to surface and bulk contributions.

Shown in Figure 6.3, each spectrum exhibits three doublets and a high binding energy tail that extends out to 168 eV. Each S 2p_{3/2} peak has been labelled A, B and C from low to high binding energy (Figure 6.3(a) to (e)). Each peak was fitted with symmetric doublets, providing a good fit at low binding energies up to around 162.5 eV, but a poor fit at higher energies due to the significant high binding energy tail.

The 2p_{3/2} peak, 'A' is located at a binding energy of 161.1 eV and has the smallest contribution of 15% to the 260 eV spectrum, and decreases consistently to 5% at 1400 eV spectrum due to the change in IMFP of the photoelectrons [23]. The decrease in intensity indicates this feature is a surface-derived feature. Table 1 shows that peak A accounts for a little more than half of the expected surface signal in each of the spectra.

Peak B is located at 161.7 eV and is clearly visible in each spectrum. The intensity of this feature exhibits some dependence on photon energy. It contributes to 40.4% of the total fit in the 260 eV spectrum and decreases to 26% in the 1400 eV spectrum. Unlike peak A, peak B does not trend to 0% contribution in the most bulk sensitive spectrum. Therefore, peak B is likely a combination of both surface and bulk features.

The primary feature in each spectrum is labelled peak C and has a 2p_{3/2} binding energy of 162.2 eV, consistent with that of bulk pentlandite monosulfide previously described in literature [2-4].

Table 6.2: Contribution of each component to the fitted S 2p spectra, and estimated contribution from the first monolayer for each spectrum.

Species	Binding Energy (FWHM) % contribution to				
	fit				
Photon Energy =	260	400	600	846	1400
'A' - Surface 3-coordinate	161.1 (0.42) <u>15.0</u>	161.1 (0.43) <u>11.6</u>	161.1 (0.43) <u>8.2</u>	161.1 (0.48) <u>8.2</u>	161.1 (0.53) <u>5.0</u>
'B' - Bulk & surface 4-coordinate	161.6 (0.52) <u>40.4</u>	161.7 (0.53) <u>39.3</u>	161.7 (0.52) <u>37.5</u>	161.7 (0.53) <u>32.9</u>	161.7 (0.53) <u>26.0</u>
'C' - Bulk 5-coordinate	162.2 (0.50) <u>44.6</u>	162.2 (0.44) <u>4</u> <u>9.1</u>	162.2 (0.43) <u>54.3</u>	162.2 (0.43) <u>58.9</u>	162.2 (0.51) <u>69.0</u>
Inelastic mean free path of photoelectrons (Å)	5.2	7.5	10.9	15.0	23.3
Estimated % from surface monolayer	29.2	21.3	15.2	11.3	7.4

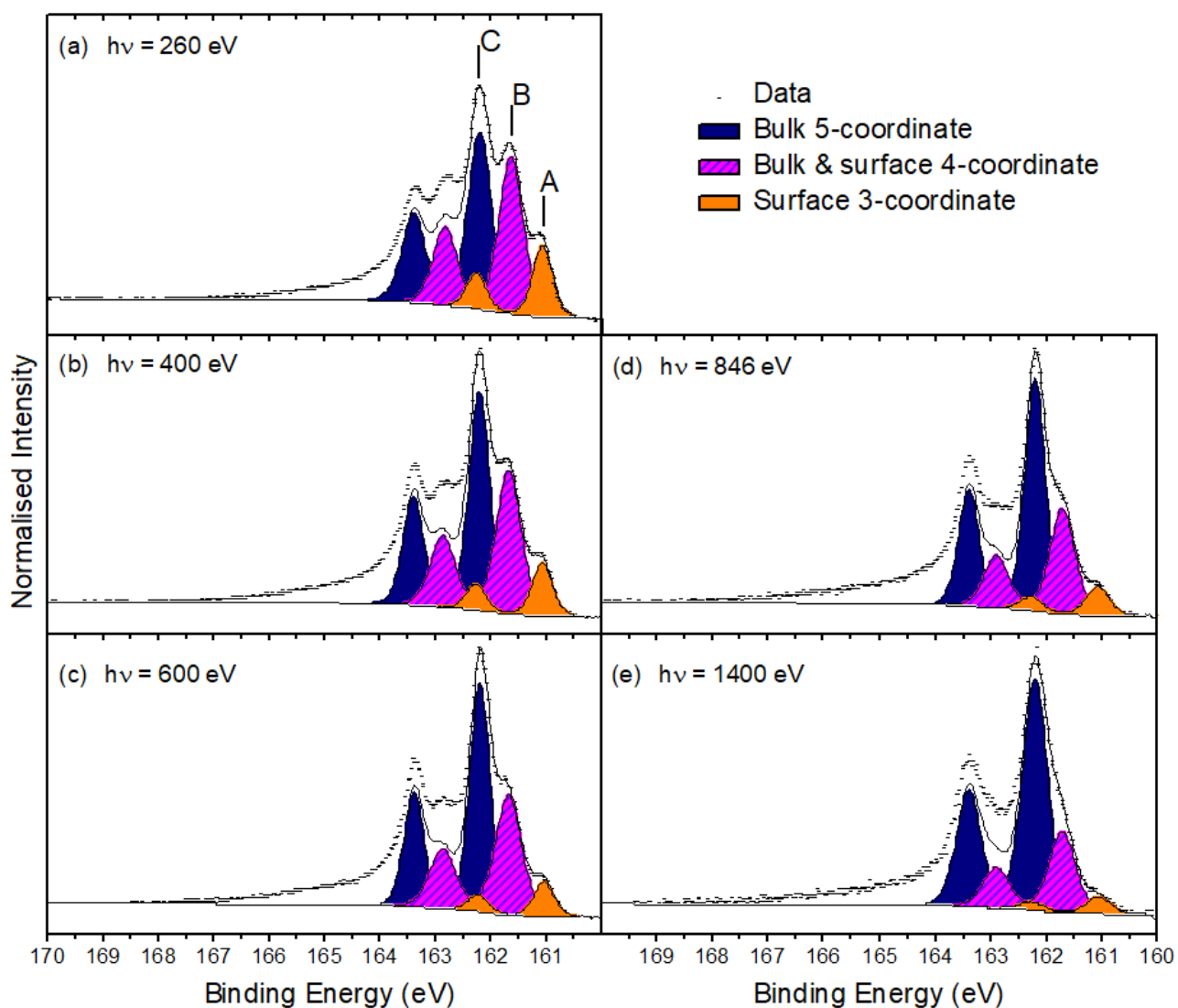


Figure 6.3: S $2p$ synchrotron X-ray photoelectron spectra collected from *in situ* fractured pentlandite ($\text{Fe}_{4.4}\text{Ni}_{4.6}\text{S}_8$) obtained with $h\nu =$ (a) 260 eV, (b) 400 eV, (c) 600 eV, (d) 846 eV, and (e) 1400 eV, each fitted with three symmetric doublets.

To determine the nature of the high binding energy tail, residual spectra were generated by subtracting the fitted spectra shown in Figure 6.3. The residual spectra shown in Figure 6.4 have a doublet-like feature at 162.6 and 163.8 eV and a broad high binding energy tail that extends out to 168 eV with no obvious structure beyond 164 eV. The binding energy of the doublet-like feature is consistent with possible disulfide or polysulfide species, arising from either surface reconstruction as a result of vacuum-fracture, or oxidation [24]. However, there is very little dependence on photon energy and hence surface sensitivity on the intensity profile of the residual spectra, therefore the majority of the signal in these residual spectra is expected to be due to bulk effects rather than surface reconstruction.

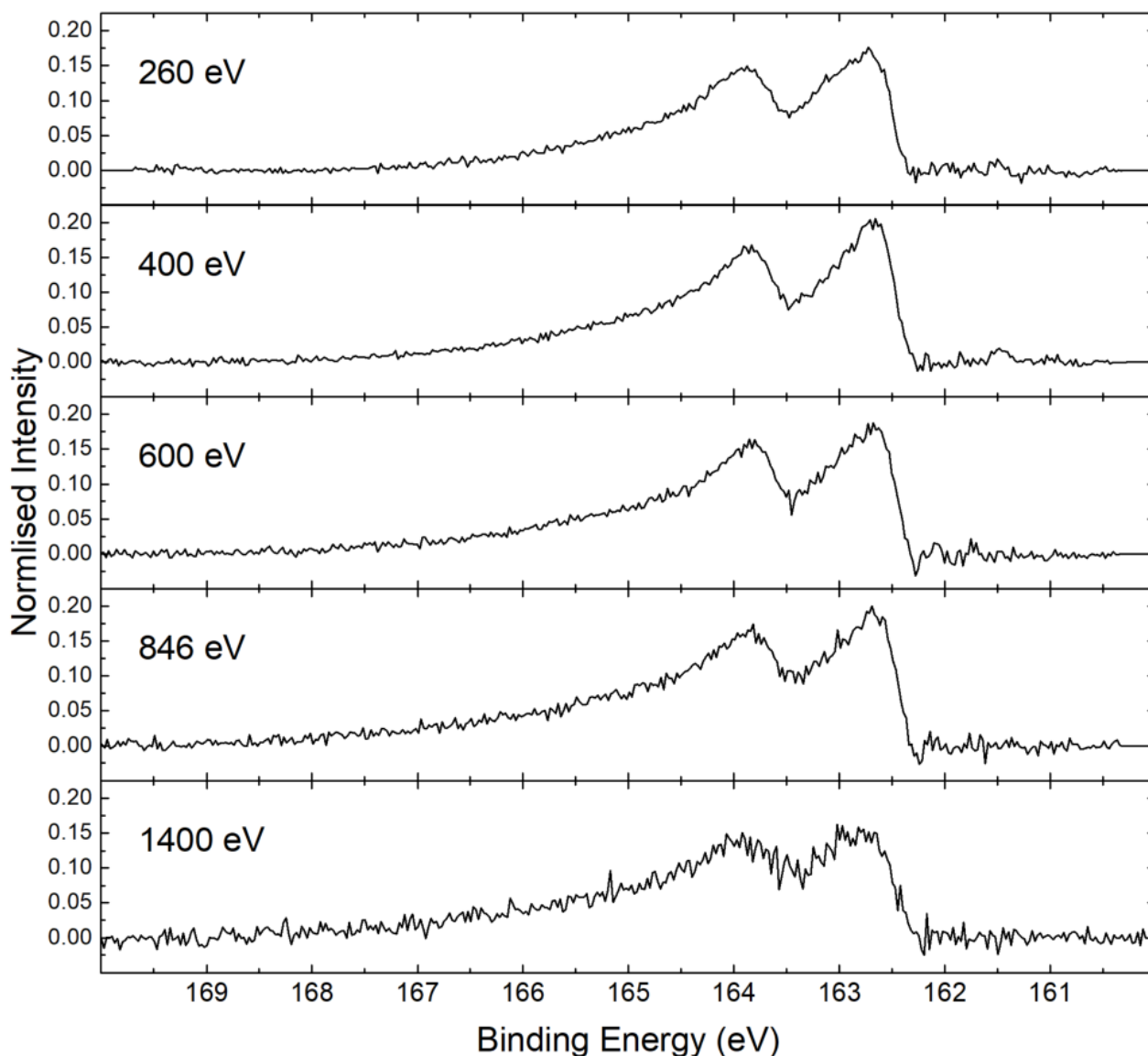


Figure 6.4: Residual signal from the Pn1 S $2p$ spectra taken at each incident photon energy, after subtraction of the fitted spectra with three symmetric spin-orbit-split doublets.

6.2.3 Pn1 valence band

Valence band spectra (0-18 eV) were collected with 260, 400, 600, 846, and 1110 eV incident photon energies. Each spectrum shown in Figure 6.5(a) shows three distinct features; the upper valence band shows the strongest peak around 1.1 eV binding energy, which is dominated by metal d states, while the lower valence band shows significant intensity in the region between 4 – 8 eV, dominated by S $3p$ states, and a small peak at 13 – 16 eV due to S $3s$ states, as have been shown previously by calculations [25]. It has also been shown by calculations that the energy difference between the S $3s$ states and the metal valence orbitals prevents significant mixing between these states, and that most of the bonding occurs between the metal $4s$ and $3d$, and the S $3p$ orbitals [26].

The overall intensity of each valence band spectrum decreases with increasing photon energy, especially in the broad region at 4 – 8 eV, which has mostly S 3*p* character, and the main peak at 1.1 eV, which is due to the e_g orbitals of the octahedral cations [27]. In comparison, the intensity of the peak at 13 – 16 eV attributable to the presence of S 3*s* states shows little change across each of the spectra. The intensity of each spectrum is largely influenced by the change in photoionization cross section of the atomic subshells, calculated by Yeh and Lindau [15] and shown in Figure 6.5(b). As the photon energy is increased, the decrease in photoionization cross section for Fe and Ni 3*d* orbitals is greater than that for the S 3*s*, and to a lesser extent, the S 3*p* subshells. There is also expected to be a contribution from the change in surface sensitivity of each valence band spectrum. The 260 eV spectrum is estimated to have approximately 20% contribution from the first surface monolayer, while the 846 eV spectrum has just less than 10% surface contribution. In contrast, the photoionization cross sections for any of the atomic subshells shown in Figure 6.5(b) differs by a factor of 10 between the 260 eV and 846 eV spectra and is therefore expected to overshadow the difference in valence band spectra that occurs due to surface sensitivity.

The inset to Figure 6.5(a) shows the upper valence band region for the 260 to 846 eV spectra that have been normalised to the main peak at 1.1 eV. A slight variation can be observed between these spectra at 0.3 – 0.5 eV, where the largest difference in intensity is seen between the 600 eV and 846 eV spectra. The contribution at 0.5 eV is due to electrons in tetrahedral metal t_{2g} orbitals hybridised with sulfur S 3*p* orbitals [28], which is enhanced by the relatively increased photoionization cross section at 846 eV in comparison to the lower photon energies.

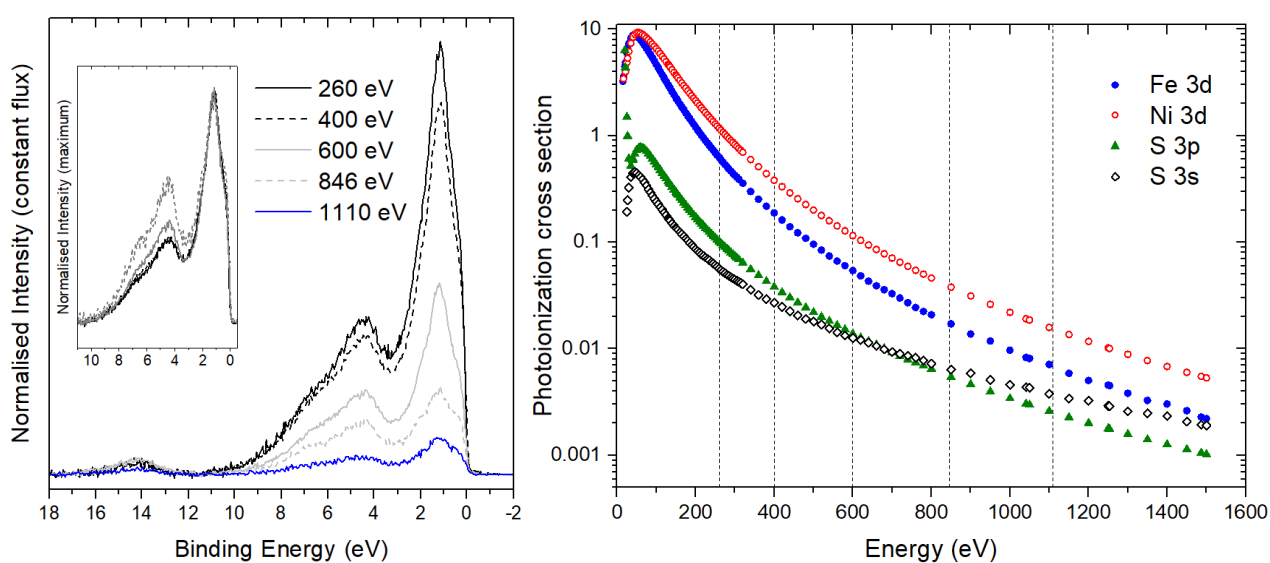


Figure 6.5: (a) X-ray valence band spectra of *in-situ* fractured Pn1 collected at photon varied photon energies. (b) photoionization cross sections of selected atomic subshells, from [15]

6.2.4 Assignment of sulfur peaks

The fracture surfaces of several transition metal sulfides have been investigated using SXPS and show evidence of surface monomer species and polysulfide species as a result of relaxation and restructure of the fracture surfaces [8-10, 29-32]. Non-polar fracture surfaces, consisting of both metal and sulfur terminations, typically result in under-coordinated sulfur monomer species on the surface, bonded to a single cation, with a lower binding energy than the bulk sulfide species due to the increased electron distribution around the sulfur atom [21, 22]. In contrast, polar surfaces are expected to undergo a surface reconstruction, which results in the formation of surface sulfur dimer and polymer species, which shift to higher binding energies [22].

There are 13 possible distinct fracture surfaces from the low Miller Index planes [100], [110], and [111] for the pentlandite structure [33]. Three of the four possible fracture surfaces parallel to the [100] plane are polar surfaces of either metal or sulfur character, while the third surface is an evenly distributed non-polar surface. Parallel to the [110] plane, there are two distinct non-polar fracture surfaces, one of which exhibits cations and face-capping sulfur, the other exhibits cations with both face-capping and linking sulfur sites at the surface. Finally, each of the seven possible fracture surfaces in the [111] plane are polar surfaces which exhibit both face-capping and linking sulfur environments within the first monolayer. It is expected that with uneven fracture, a combination of polar and non-polar surfaces will be exposed, and both face-capping and linking sulfur environments will be present at the surface.

6.2.5 Surface monosulfide species

Each S $2p$ spectrum shows three distinct peaks that are most prominent in the 260 eV photon energy spectrum. The lowest binding energy $2p_{3/2}$ peak is at 161.1 eV and is assigned to an under-coordinated surface monomer. An under-coordinated anionic surface monomer is expected to have an increased electron density compared to the bulk anions due to the loss of bonding partner, and therefore a decrease in binding energy is observed relative to the bulk anionic species. The binding energy difference observed for other surface monosulfide species is as small as 0.5 eV for chalcopyrite [8] and hexagonal pyrrhotite [29], and up to 0.7 eV in pyrite [34]. A binding energy difference of 0.6 eV between peak A and peak B in these results is therefore considered reasonable for a core-level shifted surface monosulfide species of the bulk component of peak B. While previous studies of pentlandite surfaces have shown clear evidence of only two sulfur environments, none have shown surfaces as pristine as those presented here. A study of the incipient oxidation of pyrite surfaces shows that the under-coordinated surface monosulfide species are the most reactive upon exposure to air, and after only one minute in atmosphere, the surface monosulfide species have almost completely oxidised to

form sulfate species [32]. Similarly, for pentlandite, in less pristine conditions, this surface monosulfide species could be quickly oxidised during sample preparation and therefore not detected.

6.2.6 Surface and bulk contributions to peak B

The intensity of peak B at 161.7 eV shows a clear surface dependency as it changes relative to the bulk peak with the change in incident photon energy. However, the contribution from this feature, in addition to that from peak A, is significantly greater than the calculated signal from the first surface monolayer (Table 6.2). Furthermore, while the signal from peak A decreases to almost 0% in the most bulk sensitive spectrum, in the same spectrum, the signal from peak B accounts for one third of the intensity of the total signal. The peak fitted to this feature is also observed to be slightly broader than the other two features, hinting that there is more than one contribution to this feature. This indicates that while peak B has some dependence on surface sensitivity, there must also be some contribution from the bulk.

The binding energy of peak B is 0.5 eV lower than the bulk monosulfide peak C at 162.2 eV. Since the binding energy is lower, this indicates an increase in electron density around the surface species, indicative of a second surface monosulfide species. Therefore, the surface component of peak B is assigned to under-coordinated face-capping sulfur, which is coordinated with 5 cations in the bulk, but only 4 cations at the surface. Consequently, the surface feature at 161.1 eV is due to under-coordinated sulfur atoms that have only 3 bonding partners at the fracture surface.

It follows that the bulk contribution to peak B must be due to a distinction of two sulfur environments in the bulk pentlandite structure; namely face-capping (5-coordinate) sulfur and linking (4-coordinate) sulfur. The clear presence of these two surface monomers is indicative of a non-polar surface, such as the example (110) fracture plane shown in Figure 6.6. The structure in Figure 6.6 shows bulk face-capping sulfur (dark blue) and bulk linking sulfur (purple), in addition to 4-coordinate (magenta) and 3-coordinate (orange) surface monomers. This surface is similar to that investigated by density functional theory calculations of a pentlandite fracture surface, which showed that upon fracture, the uppermost layer relaxes to form three surface layers and consequently, both bulk sulfur environments form under-coordinated surface species [28]. The results presented here highlight these two surface states, however it is expected that due to pentlandite's uneven fracture, a combination of possible non-polar surfaces is exposed, producing both surface monomers.

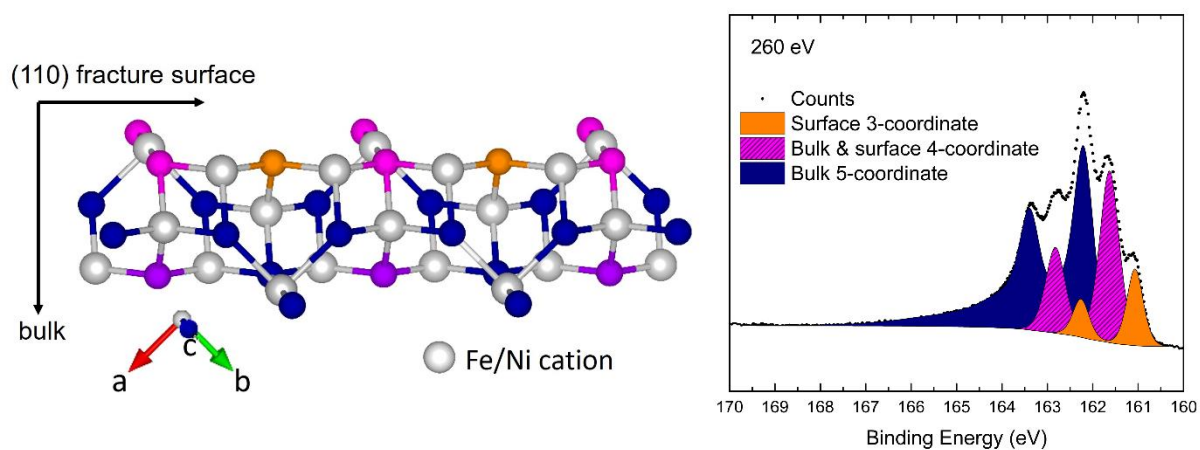


Figure 6.6: (a) Pentlandite crystal structure terminated at the (110) fracture plane, (b) $h\nu = 260$ eV S $2p$ spectrum fitted with three monosulfide components, and an asymmetric bulk tail, described in section 6.2.7.

Previous studies have observed two distinct peaks in the pentlandite sulfur $2p$ spectrum. While the peak at 162.2 eV (peak C) is attributed to the bulk pentlandite sulfide, the assignment of the feature reported in other work at 161.4 eV has been disputed. Legrand, Bancroft and Nesbitt proposed that the peak at 161.4 eV was due to 4-coordinate bulk monosulfide, while the peak at 162.2 eV is due to 5-coordinate monosulfide [4]. However, the height of the peak at 161.4 eV has been seen to vary [2, 3, 5], and in particular, Goh et al. showed that this feature increased relative to the bulk peak with increasing exposure to air, therefore concluding that it is due to a violarite-like oxidation product [3]. Goh et al. also proposed that if the 4-coordinate bulk sulfide species had a binding energy separate to the 5-coordinate species, it is likely to be at a binding energy around 161.8 eV, however the resolution that is required to resolve a peak within 0.5 eV of the bulk peak was not available at the time [3]. It must also be noted that the binding energy for a sulfur atom is not determined exclusively by the number of coordinating atoms, as has been shown for NiS structures with sulfur in 5-coordinate and 6-coordinate environments respectively [6]. Rather, the binding energy of a species is determined by the electron density surrounding the atom, which is also influenced by bond length. It is fortuitous that the 4-coordinate bulk sulfur and 4-coordinate surface monomer species of pentlandite have similar binding energy values.

6.2.7 Pentlandite's sulfur high binding energy tail

The residuals spectra in Figure 6.4, indicates that the origin of the high binding energy tail is from a bulk energy loss process. Previous studies have claimed pentlandite has a metallic nature due to the short interatomic distances between tetrahedral metal atoms [35]. Similar asymmetric tail shapes have been demonstrated for millerite and pyrrhotite [29], both of which show similar metallicity [36, 37]. Other transition metal chalcogenides including pyrite, chalcopyrite, marcasite, arsenopyrite and loellengite, display similar high binding energy tails [10]. The asymmetric tail shape of the

Chapter 6: Pristine fracture surfaces of pentlandite

chalcopyrite spectrum has been found to be due to an energy loss process which arises from the ligand to metal charge transfer (LMCT) $S\ 3p \rightarrow Fe\ 3d$ states, and has been fitted with a single broad peak approximately 3 eV higher in binding energy than the bulk peak [8, 11]. The comparison of the valence band spectra shown in Table 6.5 indicates that for pentlandite there may indeed be some hybridisation of the metal t_{2g} states with the $S\ 3p$ orbitals for the tetrahedral cations in particular.

The high BE tail in the pentlandite $S\ 2p$ spectrum has previously been fit with a combination of asymmetric line shapes for the bulk peaks, and extra features to account for a contribution from polymerised sulfur species [3, 4]. The use of additional doublets for polymerised sulfur is reasonable in other studies where significant surface oxidation is expected to occur due to abrading prior to analysis. In contrast, this study is expected to have minimal contribution from oxidised surface products since the sample was fractured and maintained under ultra-high and therefore had little chance to oxidise in the short time before analysis. The uncertainty in the tail shape for bulk species makes the analysis of species in the high binding energy region difficult, therefore a calculated approach to analysing the tail region has been implemented.

An empirical approach has been employed to fit the high binding energy tails in each of the sulfur spectra. Since the tail is attributed to bulk processes, a series of symmetric peaks were added on the high binding energy side of the bulk peak and the parameters of these peaks fixed to the bulk peak. The parameters for the tail peaks were initially found for the 1400 eV spectrum since this spectrum has the least surface sensitivity and therefore the least opportunity for errors arising from the overlap of the surface components with the bulk peak. These peaks were applied to subsequent spectra and the peaks for the surface and bulk features were altered as little as required to achieve the best possible fit. The parameters used for the tail peak, which are shown in Table 6.3, are reported relative to the parameters of the bulk peak C.

Table 6.3: Parameters used for the three peaks used to fit the tail region. Values are relative to the bulk peak at 162.2 eV.

	Area	FWHM	Position
Tail 1	$\times 0.3$	$\times 1.6$	+ 0.5 eV
Tail 2	$\times 0.5$	$\times 2.8$	+ 1.6 eV
Tail 3	$\times 0.3$	$\times 5.0$	+ 3.0 eV

Figure 6.7 shows an example of the 1400 eV spectrum fitted with the three peaks in the tail region. The fit in Figure 6.7 shows the asymmetric shape of the bulk 5-coordinate peak that is obtained when

using the three peaks to fit the tail region as described. Figure 6.8 displays the residual signal from each spectrum after fitting the tail region. The intensity of each of the residual spectra is within the range of ± 0.04 , indicating a reasonably good fit in each spectrum. The region beyond 164 eV shows a reasonable fit for each spectrum, resulting in a minimal residual, with a variation in intensity within ± 0.02 . The peaks slightly over-fit the tail region in the 260 eV spectrum, which is due to an inaccuracy in the background selection due to a broad energy loss peak feature around 180 eV, which is most significant in the low kinetic energy spectrum. The peaks slightly under-fit the tail region in the 846 eV spectrum, and although an explanation for this is less clear, it is likely due to inaccuracies in the fit of the three features.

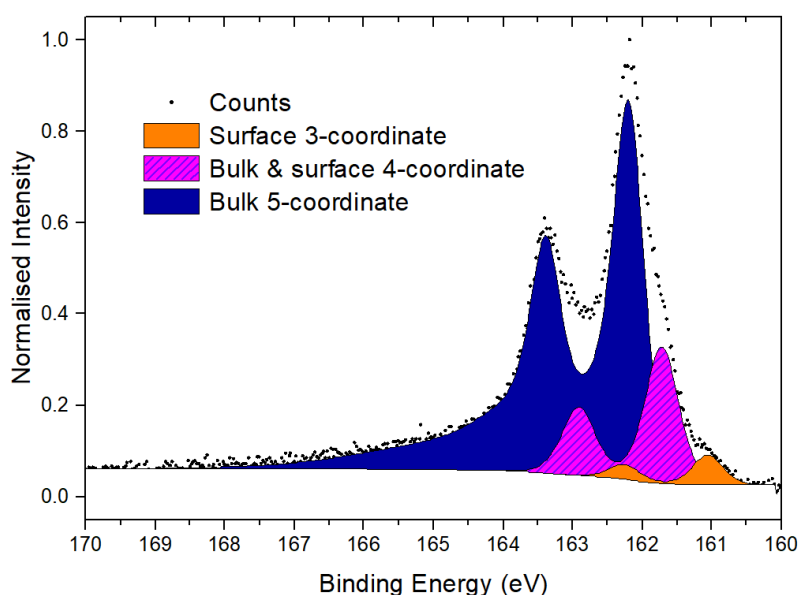


Figure 6.7: Sulfur 2p spectrum of pentlandite obtained with 1400 eV incident photon energy, fitted with three distinct features and the asymmetric tail shape described in Table 6.3.

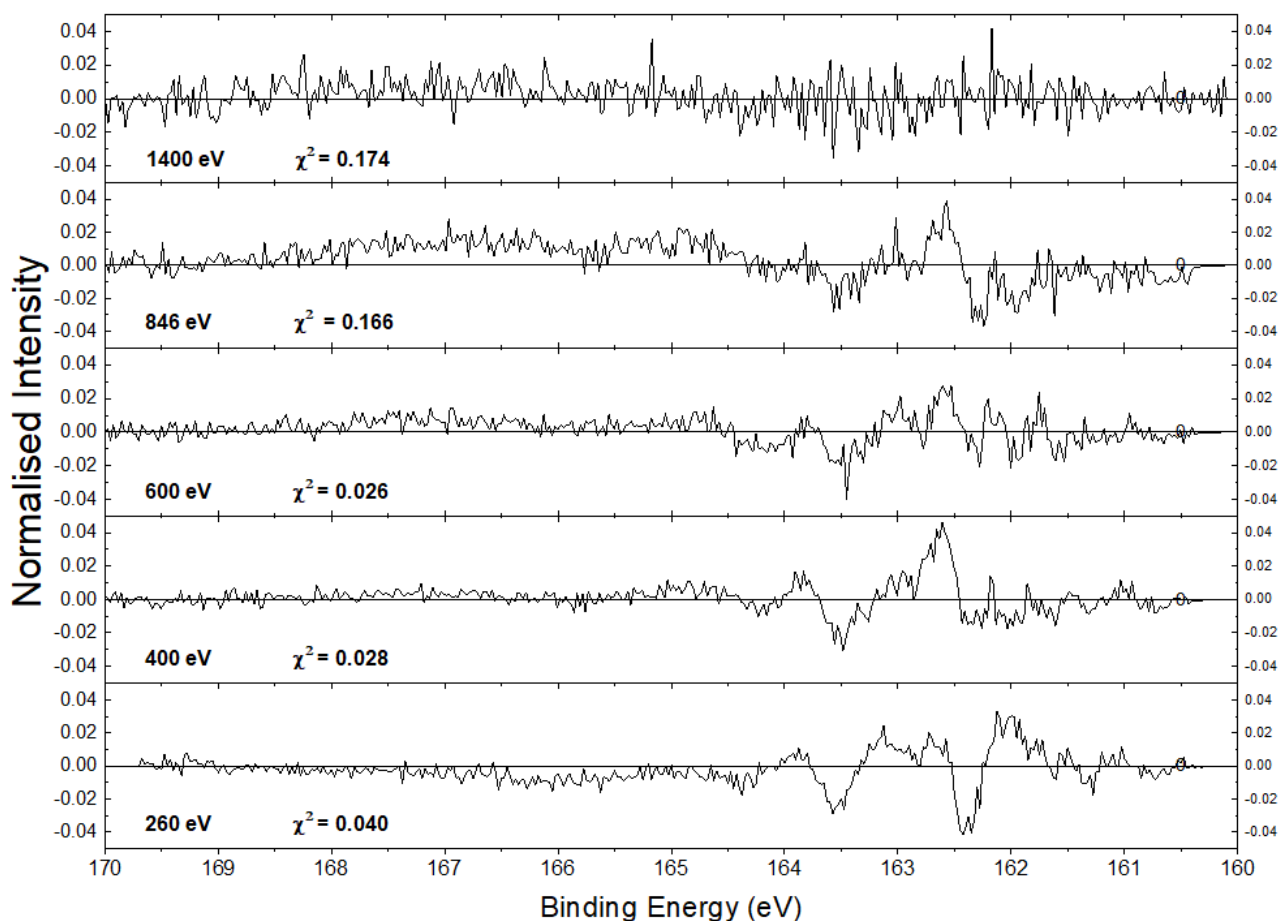


Figure 6.8: Stack plot of S $2p$ residual signal after subtracting the three tail peaks and fitted monosulfide species from each spectrum.

Other than the 1400 eV case, each residual spectrum in Figure 6.8 has some intensity between 162 and 164 eV illustrating the mismatch between the fitted peaks and the original data spectrum. The 260 eV residual has a doublet shape with an energy separation consistent with a S $2p$ doublet. The binding energy of this feature is consistent with a possible surface disulfide feature [24]. The goodness of each fit is measured by the chi-squared (χ^2) value shown on each residual spectrum in Figure 6.8, and shows a χ^2 value of less than 0.2 for the 1400 eV and 846 eV residuals, and less than 0.05 for the other residual spectra.

To ascertain the surface species resulting from reconstruction of the fracture surface, difference spectra have been calculated by subtracting the normalised 1400 eV and 846 eV spectra from the 260 eV spectrum, respectively, shown in Figure 6.9. It is expected that the surface species are represented in these difference spectra as positive peaks. Both spectra show a clear peak at 161.1 eV and a second peak above 161.5 eV, corresponding to the $2p_{3/2}$ peaks A and B from Figure 6.3 that represent surface 3-coordinate sulfur and surface and bulk 4-coordinate sulfur respectively. The third peak at 162.7 eV in Figure 6.9 is attributed to the $2p_{1/2}$ component of peak B. The $2p_{1/2}$ component of peak A is just

visible in the 260-1400 eV spectrum in the minimum near 162 eV. Both difference spectra show a positive background in the region between 164 eV and 170 eV, which does not change between the two difference spectra. The origin of this non-zero background is the slightly larger background that can be observed in the 260 eV spectrum in comparison to the other spectra, which is due to a broad satellite structure at 20 eV above the main peak, which is stronger for the 260 eV spectrum.

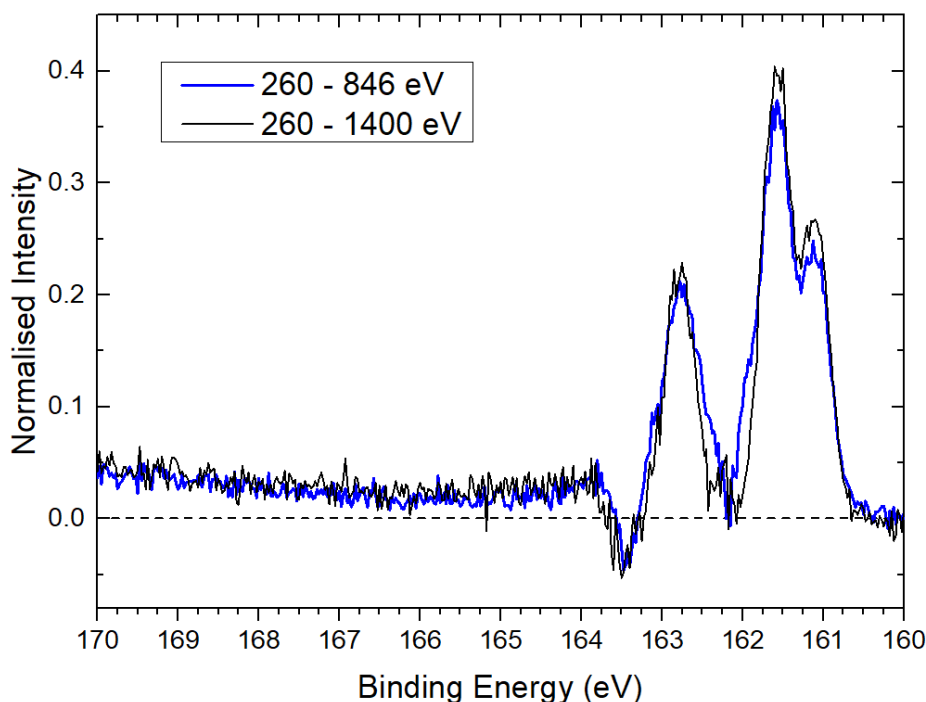


Figure 6.9: Difference between $h\nu = 260$ eV spectrum and $h\nu = 1400$ eV spectrum and $h\nu = 846$ eV spectrum respectively. All spectra are normalised to the bulk peak.

Since neither of the difference spectra show evidence of surface features additional to those already discussed, it can be concluded that no additional components such as for disulfide or polysulfide species are required to fit the sulfur spectra. Consequently, the structure seen in the residual spectra in Figure 6.8 is due to small inaccuracies in the fitted peaks, rather than additional sulfur components. The percentage contribution for each component shown in Table 6.4 includes the empirically-derived asymmetric tail in the 5-coordinate bulk contribution. It is acknowledged that the asymmetric tail is not necessarily attributed only to the 5-coordinate peak, and likely has a contribution from the 4-coordinate bulk species also. Therefore, the precise distribution of the reported contribution from bulk and surface states is unclear, however the data shown in Table 6.4 has been included to demonstrate that with the broad tails fitted, the quantification of the surface and bulk states is reasonable.

Table 6.4: Quantification of the percentage contribution of each feature to the fit, with the 5-coordinate bulk peak fitted with the empirically-derived asymmetric tails described in Table 6.3.

Species (Binding Energy)	PE (eV) =	% contribution to fit				
		260	400	600	846	1400
'A' - Surface 3-coordinate	(161.1 eV)	11.7	8.7	6.4	5.2	4.0
'B' - Bulk & surface 4-coordinate	(161.7 eV)	33.1	30.1	26.1	23.7	19.4
'C' - Bulk 5-coordinate	(162.2 eV)	55.2	61.2	67.5	71.0	76.6
Estimated % from surface monolayer		29.2	21.3	15.2	11.3	7.4

6.3 Consistency of vacuum fracture method: Comparison to "Pn2"

The spectra in the following section are obtained from a sample with a stoichiometry of $\text{Fe}_{4.4}\text{Ni}_{4.6}\text{S}_{8.1}$. The survey spectrum shown in Figure 6.10 was taken with $h\nu = 1600$ eV and clearly shows the presence of carbon and oxygen species. The peaks which are indicated in Figure 6.10 were used to approximately quantify the species in the sample. The approximately quantification is shown in Table 6.5.

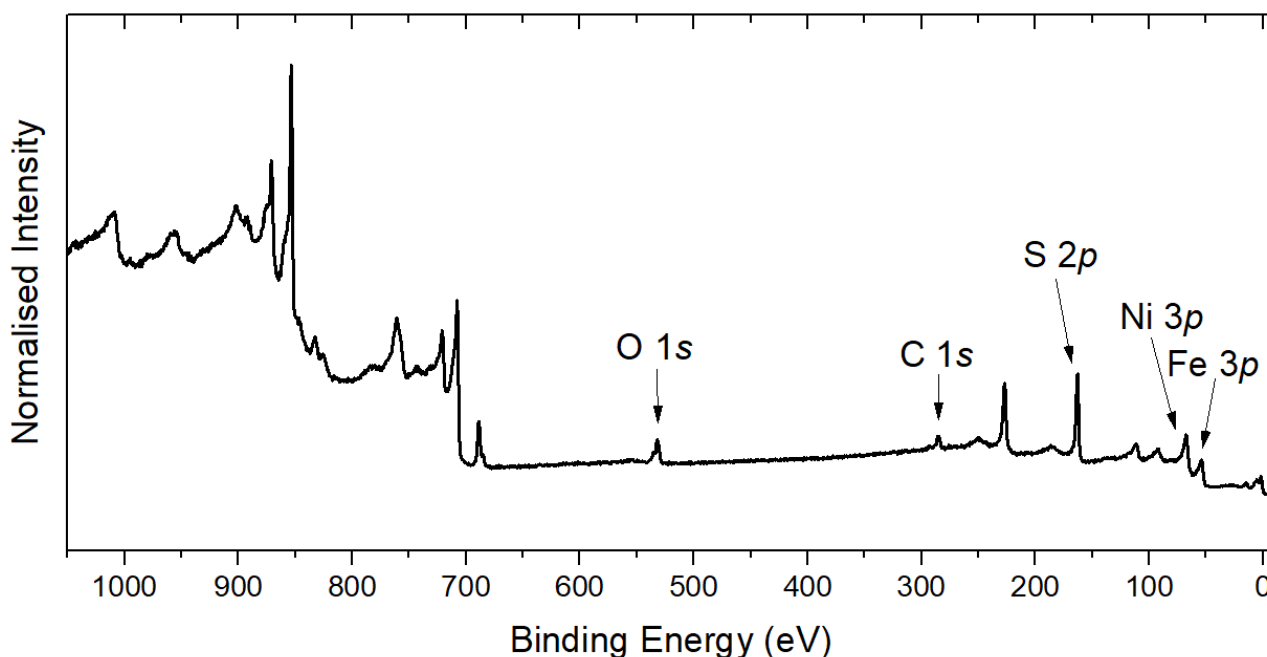


Figure 6.10: Survey spectrum of vacuum fractured "Pn2" obtained with $h\nu = 1600$ eV, indicating some small contribution from carbon and oxygen species.

The approximate quantification shown in Table 6.5 reports a ratio of Fe:Ni:S that transcribes to a stoichiometry of $\text{Fe}_{4.5}\text{Ni}_{4.9}\text{S}_{7.7}$ in comparison to the stoichiometry of $\text{Fe}_{4.4}\text{Ni}_{4.6}\text{S}_{8.1}$ found by microprobe analysis. The results shown in this table should be reasonable since the ratios of the photoionization cross sections for the atomic subshells used in the quantification are similar at $h\nu =$

1600 eV and $h\nu = 1487$ eV, therefore the RSF values should be similar. The ratio of Fe:Ni which is measured by XPS survey analysis is almost identical to that measured by microprobe analysis, however less sulfur signal is observed by XPS than is expected. The estimated contribution from oxygen and carbon species is reported to be just less than 14% and a little more than 15% respectively. Comparing the quantification of the Pn2 spectrum with the Pn1 spectrum shows that Pn2 has significantly more carbon and oxygen species. This may be an indication that Pn2 has oxidised more than Pn1, or may simply represent residual hydrocarbons, either deposited on the surface during fracture, or already existing along pre-exposed grain boundaries.

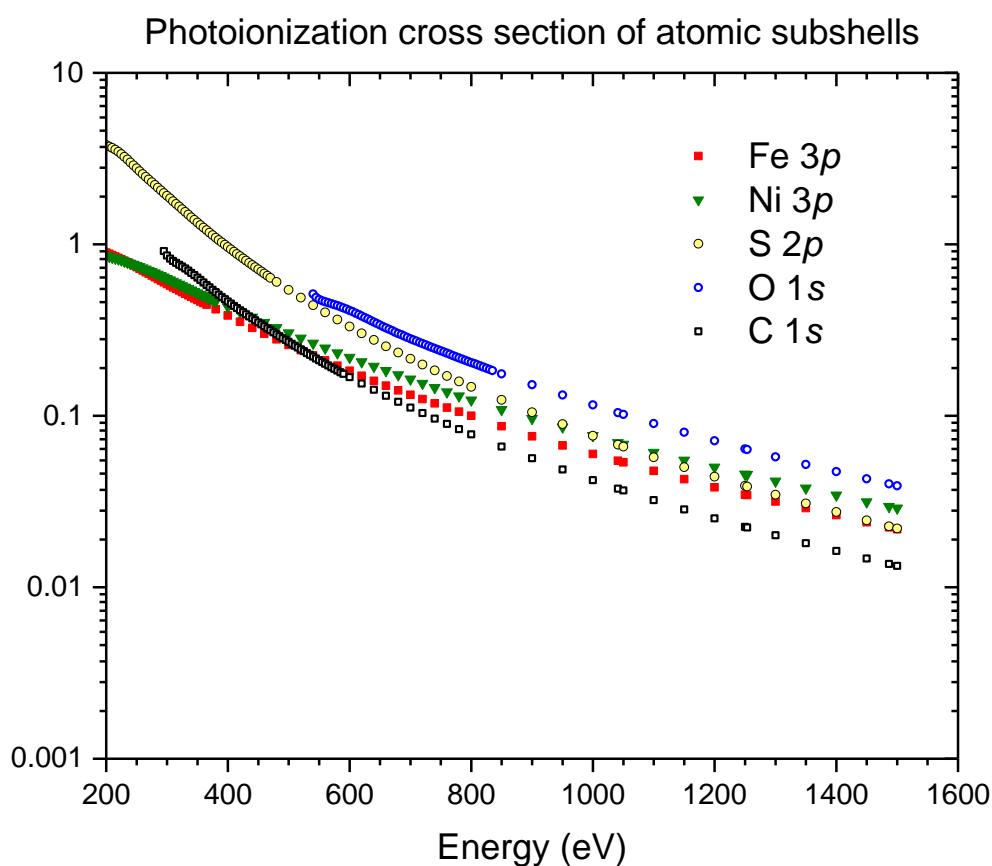


Figure 6.11: Photoionization cross section of atomic subshells [15] used for approximate quantification of the XPS survey spectrum.

Table 6.5: Approximate atomic % contribution of species for the $h\nu = 1600$ eV survey spectrum.

Peak	At% contribution
Fe 3p	18.7
Ni 3p	20.3
S 2p	31.9
O 1s	13.8
C 1s	15.3

6.3.1 Pn2 Fe & Ni 2p spectra

The Fe and Ni 2p spectra for Pn2 were collected with $h\nu = 850$ eV, 1050 eV and 1530 eV to reveal changes in the spectra due to change in surface sensitivity, and are shown in Figure 6.12. The Fe $2p_{3/2}$ peak is located at 707.0 eV, similar to that of Pn1 presented in the previous section. There is a tail on the high binding energy side that extends out to approximately 715 eV with some obvious structure as a shoulder around 708 eV, which has previously been attributed to divalent iron oxide species [20], and a broad peak around 710 eV, the binding energy of which is consistent with trivalent iron oxides and oxyhydroxides [16, 38]. The Fe 2p spectrum with $h\nu = 850$ eV has a larger background and a S LMM Auger peak observable around 702 eV binding energy. However, disregarding the difference in background, there is no change to the spectral shape between the three spectra taken with different photon energies. Therefore, the structure observed in the high binding energy tail at 708 eV and 710 eV is attributed to multiplet structure of the divalent Fe-S species. The conclusion can be made that this Fe 2p spectrum is less oxidised than that presented for the previous sample, based on the consistent spectral shape between the spectra collected with different sampling depths. The multiplet structure is also more obvious in the spectrum for this sample than for the previous sample. It is therefore reasonable to propose that the bulk Fe 2p peak has distinct multiplet structure in the tail, which was inhibited in the previous sample by the additional components due to oxidised iron species.

The Ni spectrum shown in Figure 6.12(b) has a sharp $2p_{3/2}$ peak at 853.0 eV which is consistent with the Ni spectrum presented for the previous sample. There are two clear broad peaks on the high binding energy side of the Ni $2p_{3/2}$ peak centred around 856 eV and 860 eV respectively. The Ni 2p spectrum does not show any change in spectral shape as a function of photon energy, indicating that there is no oxidation of the Ni sites as for the Fe sites, within the detection limits. This is consistent with the Ni 2p spectrum presented for the previous sample.

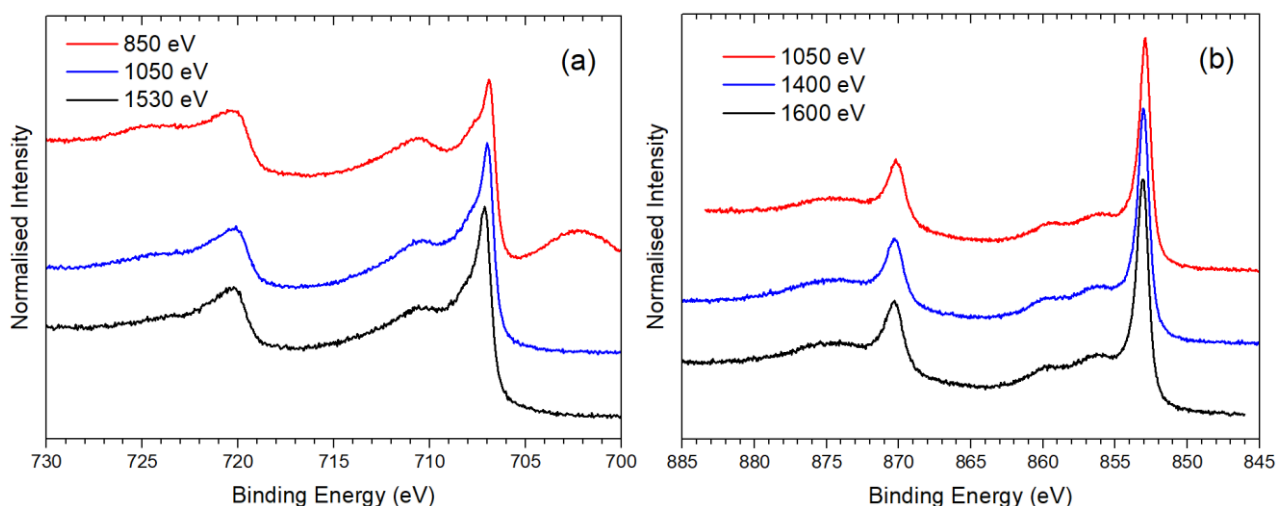


Figure 6.12: (a) Fe 3*p* photoelectron spectra obtained with $h\nu = 850$ eV (red), 1050 eV (blue) and 1530 eV (black), and (b) Ni 2*p* photoelectron spectra obtained with $h\nu = 1050$ eV (red), 1400 eV (blue), and 1600 eV (black).

Fe and Ni $L_{2,3}$ NEXAFS spectra were also obtained for this sample, and are shown in Figure 6.13. The energy scale of these two spectra has been corrected to match the Fe and Ni NEXAFS spectra shown in Chapter 7 for a similar vacuum fractured pentlandite sample. The Fe L_3 edge has a sharp peak at 706.8 eV with an asymmetric shoulder on the high photon energy side. It appears as though there may be some structure in the high energy shoulder around 711 and 713 eV. There may also be some inflection on the low photon energy side of the L_3 peak, similar to that previously observed for a natural pentlandite sample [39]. The shape of the Fe L edge spectrum is generally similar to that of the pyrrhotite spectrum, although the shoulder on the high energy of the L_3 peak appears to be stronger in the pentlandite spectrum than in the pyrrhotite spectrum. The Ni $L_{2,3}$ spectrum shown in Figure 6.13(b) has a sharp L_3 peak with no obvious shoulders, followed by a low, broad feature on the high photon energy side. This is similar to the Ni L_3 spectrum presented for α - and β -NiS, although the broad feature is stronger in the pentlandite spectrum [6].

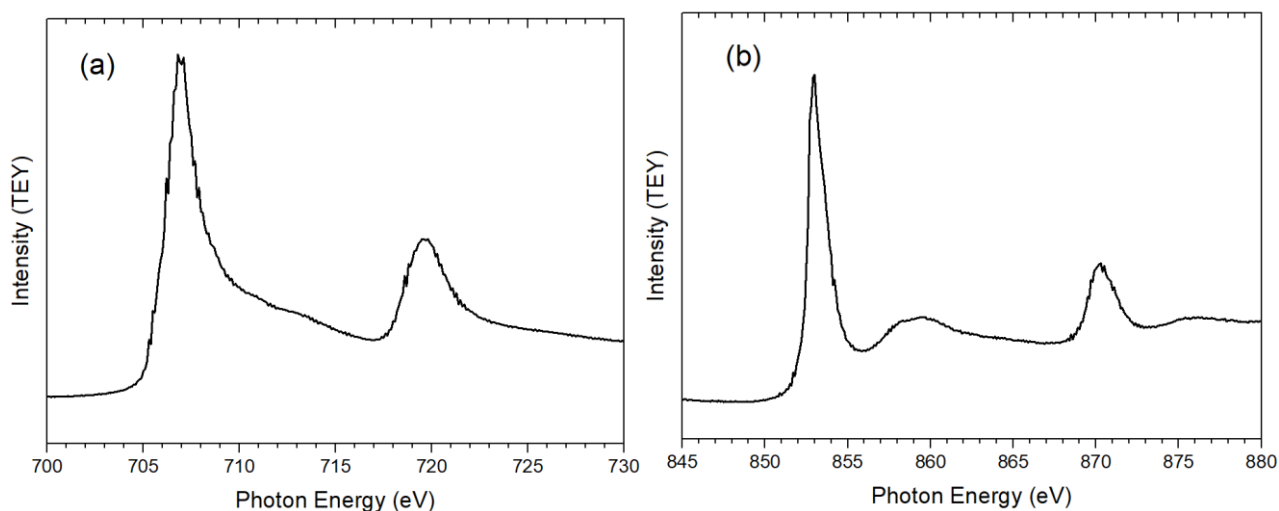


Figure 6.13: (a) Fe L_{2,3} NEXAFS spectrum, (b) Ni L_{2,3} NEXAFS spectrum of Pn2.

6.3.2 Sulfur 2p spectra

Sulfur 2p photoelectron spectra were collected using $h\nu = 260, 400, 600, 850$ and 1050 eV. Each spectrum has been fitted with three doublet components, with the binding energy of the $2p_{3/2}$ components at 161.1, 161.7 and 162.2 eV respectively. These binding energies are equivalent to the three components fitted in the S 2p spectrum of the sample in the previous section. The third component, which is attributed to bulk 5-coordinate monosulfide has been fitted with the asymmetric tail shape that was devised for the previous sample and detailed in Table 6.3. The fitted spectra are shown in Figure 6.14 and the quantification from these fitted spectra is shown in Table 6.6.

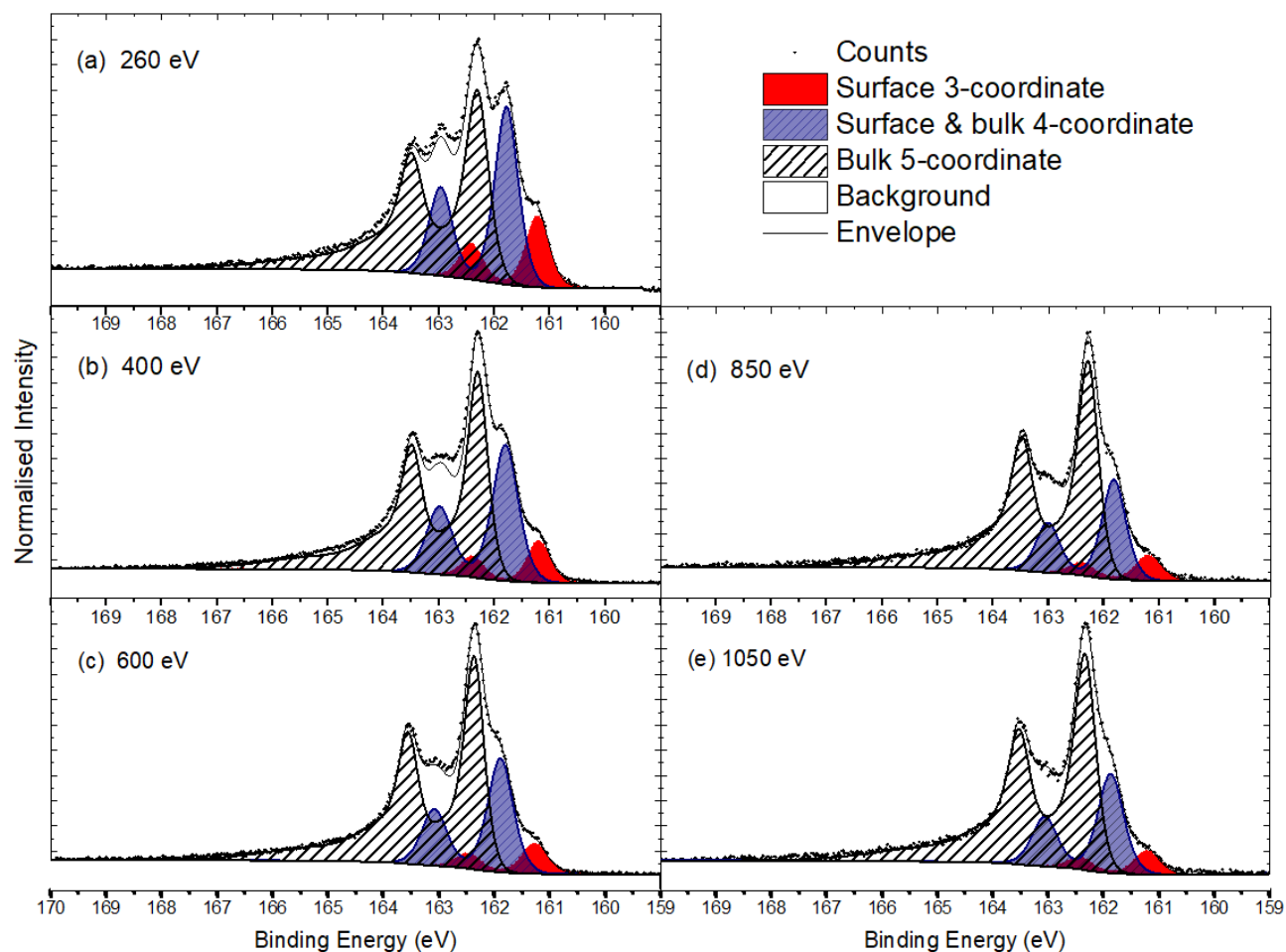


Figure 6.14: Fitted sulfur $2p$ spectra collected with $h\nu =$ (a) 260 eV, (b) 400 eV, (c) 600 eV, (d) 850 eV, and (e) 1050 eV.

Table 6.6: Contribution from each of the features to the fitted spectra shown in Figure 6.14. The tail components are included in the bulk 5-coordinate contribution.

Species (Binding Energy)	PE (eV) =	% contribution to fit				
		260	400	600	850	1050
Surface 3-coordinate	(161.1 eV)	13.0	8.4	7.3	6.3	5.6
Surface & bulk 4-coordinate	(161.7 eV)	32.7	31.5	27.3	23.3	23.9
Bulk 5-coordinate	(162.2 eV)	54.3	60.1	65.4	70.4	70.5
Estimated % from first surface monolayer		29.2	21.3	15.2	11.3	9.5

6.3.3 Additional surface components

The three monosulfide species used to fit the spectra in Figure 6.14 fit the higher photon energy spectra reasonably well, however there is a noticeable residual in the $h\nu = 260$ and 400 eV spectra in particular in the binding energy region between 163 – 165 eV. The residual after fitting the three components is shown for each spectrum in Figure 6.15. The residual is the largest for the $h\nu = 260$

eV spectrum and decreases with decreasing surface sensitivity, where it is within the noise of the $h\nu = 850$ and 1050 eV spectra. The shape of the residual, where observable, shows that there is at least one more S $2p$ component present in these spectra, with a $2p_{3/2}$ peak at around 162.6 eV, attributable to disulfide species [24]. Just visible in the residual of the $h\nu = 260$ and 400 eV spectra is a small feature around 165 eV, which is expected to be the $2p_{1/2}$ peak of a second feature which is attributable to polysulfide species.

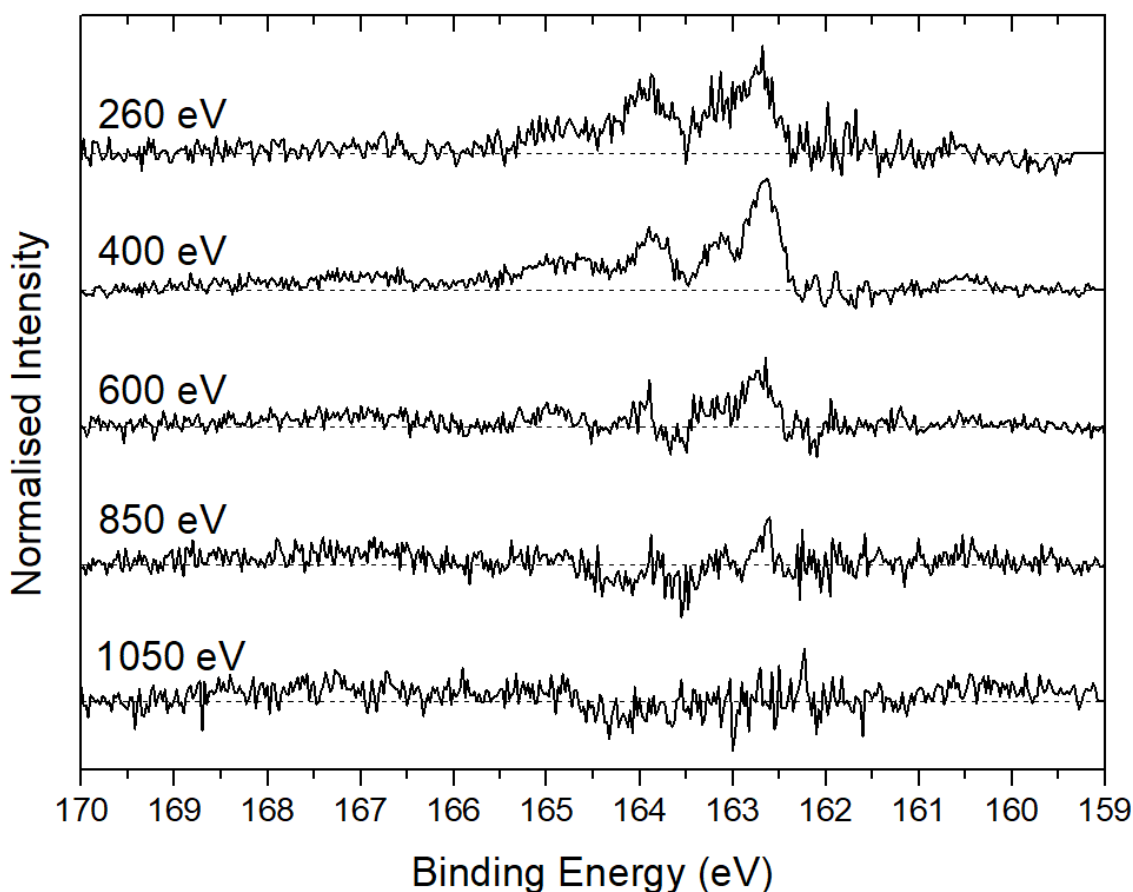


Figure 6.15: Residual signal from subtracting fitted components from the S $2p$ spectra in Figure 6.14.

The disulfide and polysulfide species observed in the residual spectra have been fitted for the $h\nu = 260$ and 400 eV spectra, and the 600 eV spectrum has been fitted with a disulfide component. In the $h\nu = 850$ and 1050 eV spectra the signal from the polymerised sulfur components is sufficiently small to be within the spectral noise and therefore these components have not been fitted for these two photon energies. The spectra fitted with the polymerised sulfur components are shown in Figure 6.16 while the quantification of these species is shown in Table 6.7.

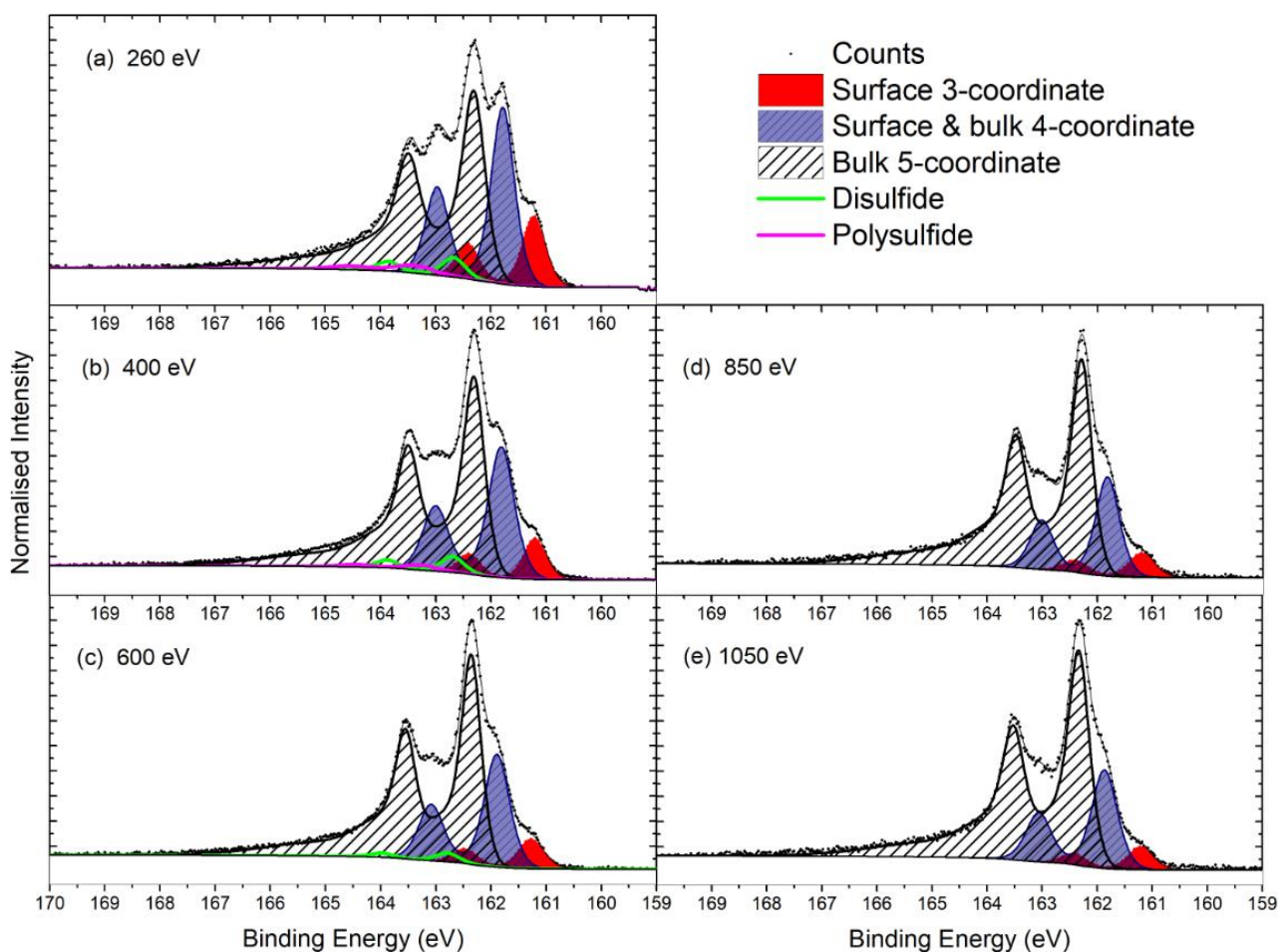


Figure 6.16: Pn2 S $2p$ spectra fitted with polymerised surface components in addition to the observed surface and bulk components.

Table 6.7: Contribution from each of the features to the fitted spectra shown in Figure 6.16. The tail components are included in the bulk 5-coordinate contribution.

Species (Binding Energy)	Binding Energy (FWHM)	% contribution to fit				
		260	400	600	850	1050
Surface 3-coordinate	161.1 eV (0.50)	12.3	8.0	7.1	6.3	5.6
Surface & bulk 4-coordinate	161.7 eV (0.52)	30.8	29.2	26.9	23.3	23.9
Bulk 5-coordinate	162.2 eV (0.44)	51.1	58.0	64.0	70.4	70.5
Disulfide	162.6 eV (0.50)	3.5	3.2	2.0	0.0	0.0
Polysulfide	163.2 eV (0.77)	2.3	1.6	0.0	0.0	0.0

This polymerisation of sulfur species may either be caused by the reaction of the surface with the carbon and oxygen species observable in the survey spectrum, or it may be due to the exposure of polar surfaces that subsequently reconstruct without the influence of external oxidants. The contribution from the carbon and oxygen species estimated in the survey spectrum together equals

almost the entire signal from the sulfur spectrum, while the polymerised sulfur species contribute only a very minor amount to the overall sulfur species. Additionally, no S-O species such as sulfite or sulfate species are observable in the spectra in Figure 6.14. Therefore, if the polymerised sulfur species are attributable to the carbon and oxygen species, it is an incomplete explanation of the carbon and oxygen, and it is more likely that the carbon and oxygen species form an adventitious layer over some of the sample's surface, possibly along grain boundaries. Furthermore, it appears from the Fe and Ni $2p$ spectra that the adventitious species have reacted very little with the cations, indicating that the adventitious species are isolated in cracks and grain boundaries, rather than spread extensively across the surface of the analysis area.

The second possibility is that the adventitious species observed on this sample interact very little with the pentlandite structure, and that the reconstruction of sulfur species that is observed occurs without the aid of external oxidants. As seen for the pyrrhotite surface in Chapter 4 and numerous other sulfide minerals (for example [8-10, 31, 32, 40]), such a reconstruction occurs when cleaving the sample exposes a fracture plane with a polar surface, which reconstructs to form the most stable surface structure. It is possible that the exposed surface that was analysed for Pn1 fortuitously consisted of only non-polar surfaces, while the exposed surface of Pn2 consists of both polar and non-polar surfaces.

6.3.4 Pn2 valence band

Figure 6.17 shows the valence band spectra for Pn2 collected with the same photon energies used for the sulfur spectra for this sample. These spectra are similar to the valence band spectra shown for Pn1, as they show distinct changes to the intensity due to the change in photoionization cross section of the subshells. The inset to Figure 6.17 shows the upper valence band of the $h\nu = 260, 400$ and 600 eV spectra that have been normalised to the main peak in the upper valence band. This shows that relative to the upper valence band, the broad band above 4 eV binding energy decreases with increasing photon energy. Since this is a relatively small change in intensity, and due to the normalisation method for these spectra, the change in intensity of the broad feature around 5 eV may be attributed to surface species. This is consistent with the calculations which indicate that this region is dominated by S $3p$ states, and the observation from the sulfur $2p$ results of polymerised sulfur species on the surface. In contrast to the valence band spectra from Pn1, these spectra show no difference in the shape of the upper valence band, specifically around 0.5 eV where small deviations were observed for Pn1. This indicates that those small changes in spectral shape observed in the Pn1 valence band spectra in Figure 6.5(a) are likely due to the slight oxidation of iron sites that was observed from the Fe $2p$ spectrum for Pn1, and hence why it is not observed for the valence band

spectra of the Pn2 sample. Importantly, this indicates that the states contributing to the valence band around 0.5 eV are Fe-dominated states, which vary in intensity for a sample that has some slight oxidation of the Fe sites.

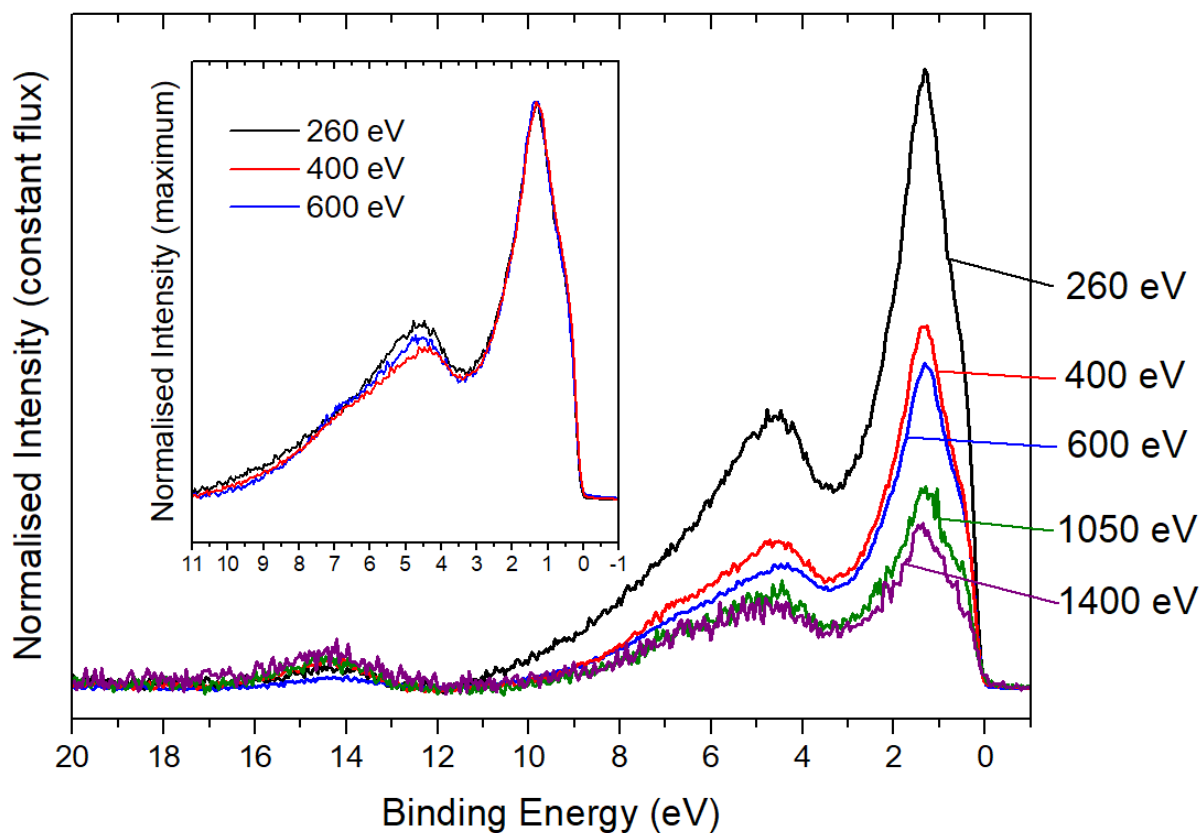


Figure 6.17: X-ray valence band spectra of in situ fractured Pentlandite 2 obtained with $h\nu = 260, 400, 600, 1050$ and 1400 eV. Inset: Valence band spectra normalised to the upper valence band peak.

The comparison of these two pentlandite samples is a valuable assessment to make since the samples are identical in their synthesis and preparation and differ only in their inadvertent surface oxidation. This allows an insight into the validity of the vacuum fracture method for pentlandite, despite this method previously being dismissed due to pentlandite's propensity to fracture along pre-oxidised grains [2]. It is unclear from these results if the reconstruction of the sulfur species on the surface of Pn2 is due to the reconstruction of polar fracture surfaces, or if it is caused by external oxidants. This comparison has shown that while some oxidised surfaces may exist around fracture planes, the extent of the surface alteration due to this is minimal, and only observable with high resolution techniques and analysis. The presentation of pristine, or near-pristine pentlandite spectra made in this chapter is of great benefit to help understand the features observed in spectra of altered pentlandite surfaces. This will aid in identifying alteration products and consequently understanding the analysed surfaces in future studies.

Chapter 6: Pristine fracture surfaces of pentlandite

The comparison of fitted S 2*p* spectra from these two pentlandite samples also gives an indication of the error associated with fitting high resolution spectra. It is difficult to isolate the error in the fit from the variation in samples, but considering the similarity of the two pentlandite samples shown in this chapter, an estimation can still be made. While Pn1 was shown to have no contribution from disulfide and polysulfide species, Pn2 had a small contribution on the surface from polymerised sulfur, amounting to a combined total of less than 6% of the fitted species in the most surface sensitive spectrum. There was no observable contribution in the two most bulk sensitive spectra for Pn2. By comparing the Pn1 $h\nu = 846$ eV fitted spectrum with the Pn2 $h\nu = 850$ eV fitted spectrum, we see that the discrepancy between the fits is up to 1% of the total fitted species. An error of approximately 1 – 2% in the fitted components throughout this thesis is therefore expected to be a reasonable estimate.

6.4 Conclusions

This chapter presents photoelectron spectra from two vacuum fractured synthetic pentlandite samples. Prior to this work, there has been no reports of pristine pentlandite surfaces, as most studies have prepared the pentlandite samples by abrasion resulting in surface oxidation. The original contribution to knowledge presented in this chapter is the analysis of the pristine, or near-pristine samples using synchrotron radiation of varied photon energies. This method has identified the bulk and surface contributions to Fe, Ni and S 2*p* photoelectron spectra. The first sample showed evidence of slight oxidation of the Fe sites, but no changes to Ni or S species due to oxidation. Two surface species were identified in the S 2*p* spectrum, which were attributed to 3- and 4-coordinate undercoordinated surface monosulfide species. This showed that the fracture surface experienced relaxation rather than reconstruction to form a stable surface. This conclusion altered the previous understanding about the assignment of S 2*p* states for pentlandite. In contrast, the second pentlandite sample showed no evidence of oxidation of the Fe or Ni sites, but showed evidence of reconstruction of the sulfur species at the surface. This indicates that the pentlandite surface may have multiple fracture planes that cause the surface to stabilise either through relaxation or by reconstruction.

By identifying the bulk and surface contributions to the S 2*p* spectrum, a fitting method was developed to fit the broad asymmetric tail observed on the high binding energy side of the bulk monosulfide species. A series of empirical symmetric peaks have been proposed to fit the bulk contribution, which was used for the second sample to identify the disulfide and polysulfide species in the surface sensitive spectra. This fitting method is significant for future studies that wish to use photoelectron spectroscopy to characterise pentlandite surfaces. Although fitting the asymmetric tail does not provide any evidence of the origin of the tail, valence band spectra show that the cation and anion valence states are potentially significantly mixing. The Fe L edge absorption spectrum also

shows a pre-edge feature similar to that seen for pyrrhotite and other sulfide minerals. This shows that the broad tails in the S 2*p* spectrum arise from ligand to metal charge transfer final states. A deeper analysis of the pentlandite valence band spectrum is required to give a deeper insight into this process, which is addressed in the next chapter.

6.5 References

- [1] S. Richardson, D.J. Vaughan, Surface alteration of pentlandite and spectroscopic evidence for secondary violarite formation, *Mineralogical magazine*, 53 (1989) 213-222.
- [2] A.N. Buckley, R. Woods, Surface composition of pentlandite under flotation-related conditions, *Surface and Interface Analysis*, 17 (1991) 675-680.
- [3] S.W. Goh, A.N. Buckley, R.N. Lamb, L.-J. Fan, L.-Y. Jang, Y.-w. Yang, Pentlandite sulfur core electron binding energies, *Phys Chem Minerals*, 33 (2006) 445-456.
- [4] D.L. Legrand, G.M. Bancroft, H.W. Nesbitt, Surface characterization of pentlandite, (Fe,Ni)₉S₈, by X-ray photoelectron spectroscopy, *International Journal of Mineral Processing*, 51 (1997) 217-228.
- [5] D. Legrand, G. Bancroft, H. Nesbitt, Oxidation/alteration of pentlandite and pyrrhotite surfaces at pH 9.3: Part 1. Assignment of XPS spectra and chemical trends, *American Mineralogist*, 90 (2005) 1042-1054.
- [6] S.W. Goh, A.N. Buckley, R.N. Lamb, W.M. Skinner, A. Pring, H. Wang, L.-J. Fan, L.-Y. Jang, L.-J. Lai, Y.-w. Yang, Sulfur electronic environments in α -NiS and β -NiS: examination of the relationship between coordination number and core electron binding energies, *Phys Chem Minerals*, 33 (2006) 98-105.
- [7] S. Doniach, M. Sunjic, Many-electron singularity in X-ray photoemission and X-ray line spectra from metals, *Journal of Physics C: Solid State Physics*, 3 (1970) 285-291.
- [8] S.L. Harmer, A.R. Pratt, W.H. Nesbitt, M.E. Fleet, Sulfur species at chalcopyrite (CuFeS₂) fracture surfaces, *American Mineralogist*, 89 (2004) 1026-1032.
- [9] S.L. Harmer, A.R. Pratt, H.W. Nesbitt, M.E. Fleet, Reconstruction of fracture surfaces on bornite, *The Canadian Mineralogist*, 43 (2005) 1619-1630.
- [10] S.L. Harmer, H.W. Nesbitt, Stabilization of pyrite (FeS₂), marcasite (FeS₂), arsenopyrite (FeAsS) and loellingite (FeAs₂) surfaces by polymerization and auto-redox reactions, *Surface Science*, 564 (2004) 38-52.
- [11] M. Fujisawa, S. Suga, T. Mizokawa, A. Fujimori, K. Sato, Electronic structures of CuFeS₂ and CuAl_{0.9}Fe_{0.1}S₂ studied by electron and optical spectroscopies, *Physical Review B*, 49 (1994) 7155-7164.
- [12] M.C. Biesinger, L.W.M. Lau, A.R. Gerson, R.S.C. Smart, Resolving surface chemical states in XPS analysis of first row transition metals, oxides and hydroxides: Sc, Ti, V, Cu and Zn, *Applied Surface Science*, 257 (2010) 887-898.
- [13] M.C. Biesinger, B.P. Payne, A.P. Grosvenor, L.W.M. Lau, A.R. Gerson, R.S.C. Smart, Resolving surface chemical states in XPS analysis of first row transition metals, oxides and hydroxides: Cr, Mn, Fe, Co and Ni, *Applied Surface Science*, 257 (2011) 2717-2730.
- [14] D.A. Shirley, High-Resolution X-Ray Photoemission Spectrum of the Valence Bands of Gold, *Physical Review B*, 5 (1972) 4709-4714.
- [15] J.J. Yeh, I. Lindau, Atomic subshell photoionization cross sections and asymmetry parameters: $1 \leq Z \leq 103$, *Atomic Data and Nuclear Data Tables*, 32 (1985) 1-155.
- [16] A.R. Pratt, I.J. Muir, H.W. Nesbitt, X-ray photoelectron and Auger electron spectroscopic studies of pyrrhotite and mechanism of air oxidation, *Geochimica et Cosmochimica Acta*, 58 (1994) 827-841.
- [17] R.P. Gupta, S.K. Sen, Calculation of multiplet structure of core *p*-vacancy levels, *Physical Review B*, 10 (1974) 71-77.

- [18] A. Shchukarev, J.F. Boily, XPS study of the hematite–aqueous solution interface, *Surface and Interface Analysis*, 40 (2008) 349-353.
- [19] A.P. Grosvenor, B.A. Kobe, M.C. Biesinger, N.S. McIntyre, Investigation of multiplet splitting of Fe 2p XPS spectra and bonding in iron compounds, *Surface and Interface Analysis*, 36 (2004) 1564-1574.
- [20] N.S. McIntyre, D.G. Zetaruk, X-ray photoelectron spectroscopic studies of iron oxides, *Analytical Chemistry*, 49 (1977) 1521-1529.
- [21] S. Hüfner, *Photoelectron Spectroscopy*, 2nd ed., Springer-Verlag, Berlin, 1996.
- [22] W. Mönch, *Semiconductor Surfaces and Interfaces*, Springer-Verlag, Berlin, 1993.
- [23] S. Tanuma, C.J. Powell, D.R. Penn, Calculations of electron inelastic mean free paths. II. Data for 27 elements over the 50-2000 eV range, *Surface and Interface Analysis*, 17 (1991) 911-926.
- [24] R.S.C. Smart, W.M. Skinner, A.R. Gerson, XPS of sulphide mineral surfaces: metal-deficient, polysulphides, defects and elemental sulphur, *Surface and Interface Analysis*, 28 (1999) 101-105.
- [25] H.R. Chauke, D. Nguyen-Manh, P.E. Ngoepe, D.G. Pettifor, S.G. Fries, Electronic structure and stability of the pentlandites Co_9S_8 and $(\text{Fe},\text{Ni})_9\text{S}_8$, *Physical Review B*, 66 (2002) 155105.
- [26] G.G. Hoffman, J.K. Bashkin, M. Karplus, Electronic structure of icosahedral cobalt-sulfur clusters, *Journal of the American Chemical Society*, 112 (1990) 8705-8714.
- [27] M. Fronzi, S.A. Tawfik, C. Stampfl, M.J. Ford, Magnetic properties of stoichiometric and defective Co_9S_8 , *Physical Chemistry Chemical Physics*, 20 (2018) 2356-2362.
- [28] P.P. Mkhonto, H.R. Chauke, P.E. Ngoepe, Ab initio Studies of O_2 Adsorption on (110) Nickel-Rich Pentlandite ($\text{Fe}_4\text{Ni}_5\text{S}_8$) Mineral Surface, *Minerals*, 5 (2015) 665-678.
- [29] H.W. Nesbitt, A.G. Schaufuss, M. Scaini, G.M. Bancroft, R. Szargan, XPS measurement of fivefold and sixfold coordinated sulfur in pyrrhotites and evidence for millerite and pyrrhotite surface species, *American Mineralogist*, 86 (2001) 318-326.
- [30] H.W. Nesbitt, G.M. Bancroft, A.R. Pratt, M.J. Scaini, Sulfur and iron surface states on fractured pyrite surfaces, *American Mineralogist*, 83 (1998) 1067-1076.
- [31] I. Uhlig, R. Szargan, H.W. Nesbitt, K. Laajalehto, Surface states and reactivity of pyrite and marcasite, *Applied Surface Science*, 179 (2001) 222-229.
- [32] A.G. Schaufuß, H.W. Nesbitt, I. Kartio, K. Laajalehto, G.M. Bancroft, R. Szargan, Incipient oxidation of fractured pyrite surfaces in air, *Journal of Electron Spectroscopy and Related Phenomena*, 96 (1998) 69-82.
- [33] C.N. Waterson, J.O. Sindt, J. Cheng, P.A. Tasker, C.A. Morrison, First-principles study on ligand binding and positional disorder in pentlandite, *The Journal of Physical Chemistry C*, 119 (2015) 25457-25468.
- [34] M. Bronold, Y. Tomm, W. Jaegermann, Surface states on cubic *d*-band semiconductor pyrite (FeS_2), *Surface Science*, 314 (1994) 931-936.
- [35] V. Rajamani, C.T. Prewitt, Crystal chemistry of natural pentlandites, *The Canadian Mineralogist*, 12 (1973) 178-187.
- [36] V. Rajamani, C.T. Prewitt, The crystal structure of millerite, *The Canadian Mineralogist*, 12 (1974) 253-257.
- [37] M. Tokonami, K. Nishiguchi, N. Morimoto, Crystal structure of a monoclinic pyrrhotite (Fe_7S_8), *American Mineralogist*, 57 (1972) 1066-1080.
- [38] A.P. Grosvenor, B.A. Kobe, N.S. McIntyre, Studies of the oxidation of iron by water vapour using X-ray photoelectron spectroscopy and QUASES™, *Surface Science*, 572 (2004) 217-227.
- [39] R.G. Acres, S.L. Harmer, D.A. Beattie, Synchrotron PEEM and ToF-SIMS study of oxidized heterogeneous pentlandite, pyrrhotite and chalcopyrite, *Journal of Synchrotron Radiation*, 17 (2010) 606-615.
- [40] U. Becker, A.W. Munz, A.R. Lennie, G. Thornton, D.J. Vaughan, The atomic and electronic structure of the (001) surface of monoclinic pyrrhotite (Fe_7S_8) as studied using STM, LEED and quantum mechanical calculations, *Surface Science*, 389 (1997) 66-87.

7 ELECTRONIC STRUCTURE OF PRISTINE PENTLANDITE SURFACES

7.1 Introduction

There is increasing interest in using pentlandite and similar structures as a catalyst for the hydrogen evolution reaction [1-5]. With this gaining interest comes a requirement to understand the catalytic activity of this mineral. The previous chapter largely described the surface structure of vacuum fractured pentlandite, and while this is important, it only aids in partway understanding the reactions that occur at the surface. The aim of this chapter is to investigate the electronic structure of pentlandite and how it may affect the reactions that occur at the surface of this complex mineral. To date there have been a number of calculations presented in the literature for density of states of pentlandite and similar structures [6-10]. However, until the results presented in the previous chapter, some of which have been recently published [11], there have been no other reported experimental observations of the valence band of pentlandite. Therefore, the original contribution to knowledge that is presented in this chapter is an experimental investigation of the valence band density of states of pentlandite. This is achieved through two separate techniques. The first technique is resonant photoemission spectroscopy, which aims to identify the states in the experimental valence band that can be attributed to Fe and Ni states respectively. The second technique investigates the valence band of a series of pentlandite samples with varied stoichiometry; analysing the variation in intensity of states as a result of changing photoionization cross section and making a comparison between samples with varied stoichiometries. By these methods it is shown in this chapter the regions of pentlandite's valence band that are dominated by Ni, Fe and S valence states respectively, and provides greater insight into the electronic structure of pentlandite.

7.2 Resonant valence band study of pentlandite electronic structure

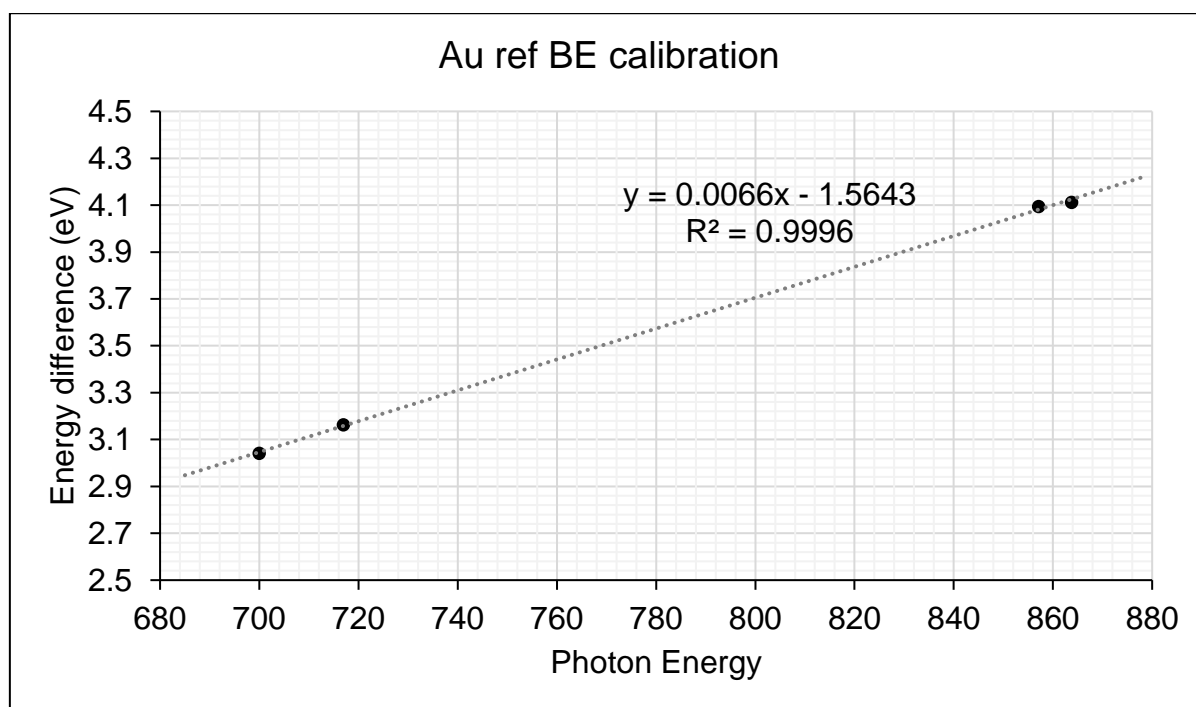
Resonant photoemission spectroscopy has been used for understanding the electronic structure of various other samples. By combining atom-specific X-ray absorption spectroscopy with photoelectron spectroscopy in the valence band region, the atomic character of valence band states may be investigated. This is a strength of the technique, especially for complex structures such as pentlandite, which potentially have broad bands and overlapping states, and are consequently difficult to explicate.

While the term 'resonance' is used to describe resonant photoemission spectroscopy, this technique does not always reveal 'true resonance' in the valence band spectra, as true resonance is only observed for valence states with specific qualities. Many publications (such as references [12-16]) use the term 'resonance' to refer to the enhancement of the photoemission spectrum that results from the onset of

the normal Auger decay signal as the photon energy is varied over the absorption edge. Quite often this effect is simply a superposition of the two channels and does not represent a ‘true resonance’. The stricter definition is that which refers to the interaction between the photoemission channel and the deexcitation (Auger decay) which follow the X-ray absorption process. The interaction arises from the two channels having the same initial and final states, and requires the two channels to be coherent [17]. The effect is an increase (resonance) or decrease (anti-resonance) in the spectrum that is additional to the superposition of the individual channels. True resonance is often characterised by a decrease just below, and a significant increase above the absorption threshold photon energy. This intensity profile is referred to as a Fano-profile [18]. In the following data the term ‘resonant valence band spectra’ is used to describe the process of collecting the data, rather than the outcome. However, when discussing the change in features in these spectra, the term ‘resonance’ is reserved for the stricter definition.

7.2.1 Methods

The sample analysed in this section was cut from the same mineral used in the previous chapter and has the same stoichiometry of $\text{Fe}_{4.4}\text{Ni}_{4.6}\text{S}_{8.1}$. The spectra shown in this section were collected at the Australian Synchrotron Soft x-ray beamline [19]. The photon energy of the beamline was calibrated by observing the absorption spectra of internal Fe and Ni metal standards, calibrating the main peaks to 706.8 eV [20] and 852.7 eV [21] respectively. The binding energy scales of the valence band spectra were calibrated using a series of Au $4f_{7/2}$ spectra calibrated to 84.00 eV [22], which were collected with photon energies similar to those of the valence band spectra. A linear relationship between the photon energy and the necessary binding energy correction was created, by which the binding energy scales of the valence band spectra were corrected. This linear relationship is shown in Figure 7.1, while the energy calibration required for each Au $4f_{7/2}$ spectrum is shown in Table 7.1. Each valence band spectrum was normalised to constant flux at a few eV below the onset of the valence band in the binding energy scale in each spectrum.

Figure 7.1: Binding energy calibration from Au $4f_{7/2}$ reference spectra.Table 7.1: Au $4f_{7/2}$ reference for energy calibration.

Photon energy	Measured energy	Correction
700.0 eV	87.04 eV	- 3.04 eV
717.0 eV	87.16 eV	- 3.16 eV
857.1 eV	88.09 eV	- 4.09 eV
864.8 eV	88.11 eV	- 4.11 eV
Slope	0.006587	
Intercept	-1.56432	

The survey spectrum for this sample is shown in Figure 7.2 while the quantification of species from this survey spectrum is shown in Table 7.2. The At% contribution to the survey spectrum shows an approximately equal ratio of iron to nickel, and a ratio of sulfur to metal (Fe+Ni) only slightly less than that expected from the sample's stoichiometry. There is clear evidence of carbon and oxygen species in the survey spectrum, which equates to 3.8% oxygen and 13.6% carbon detected at the surface. While this is greater than the estimated carbon and oxygen species in Pn1, it is less than those detected in Pn2 of the previous chapter.

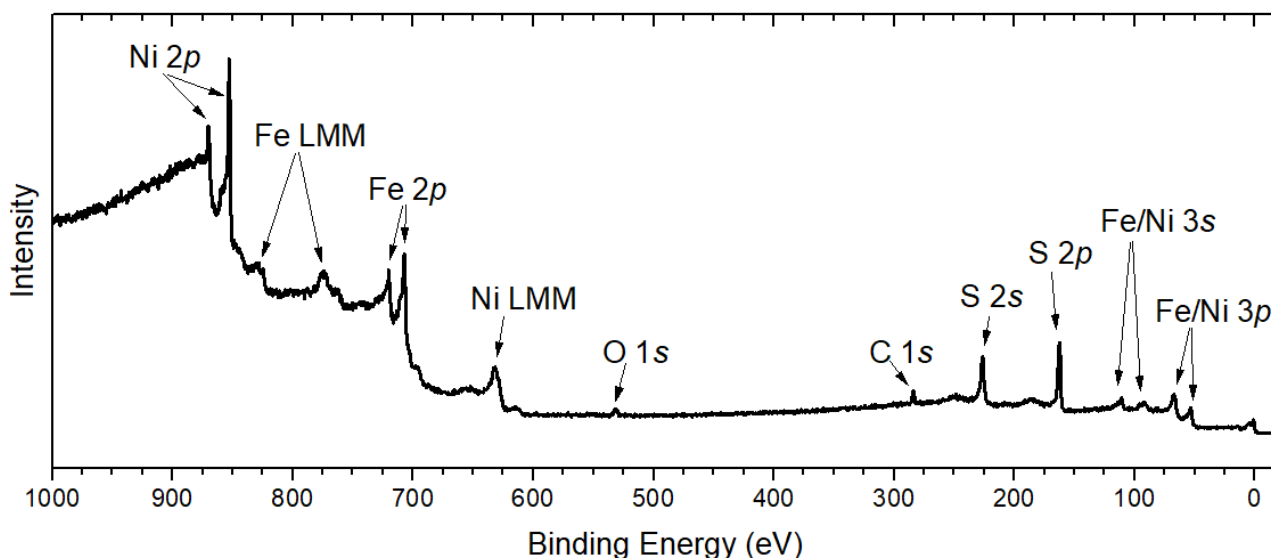
Figure 7.2: Survey spectrum of vacuum fractured pentlandite, $h\nu = 1487$ eV.

Table 7.2: Atomic % contribution from species to survey spectrum shown in Figure 7.2.

Species	At% contribution
Fe 3p	20.4
Ni 3p	20.1
S 2p	42.1
O 1s	3.8
C 1s	13.6

The Fe 2p and Ni 2p spectra from this pentlandite sample are shown in Figure 7.3 with the spectra from the two vacuum fractured pentlandite samples from the previous chapter. The Fe 2p spectrum in Figure 7.3ai has a peak at 707.1 eV consistent with the $2p_{3/2}$ peak of the previous two pentlandite samples, also shown in Figure 7.3aii,iii. The peak in Figure 7.3ai is seen to be broader than the peak in the two previous pentlandite samples. There is an asymmetric tail on the high binding energy side of this peak which extends out to 715 eV. The shape of the tail is similar to that observed for Pn1, and there is no obvious structure as can be seen in the Fe $2p_{3/2}$ tail in Pn2. The broadness of the peak in Figure 7.3a,i and the lack of structure in the high binding energy tail indicates that the Fe species are slightly oxidised, more so than both Pn1 and Pn2 samples.

The Ni 2p spectrum shown in Figure 7.3bi has a peak at 853.0 eV with some low intensity structure on the high binding energy side. The spectrum is consistent with the 2p peak of pentlandite Ni^{II}-S shown for Pn1 and Pn2 samples. The similarity in the peak energy, shape, and structure of the high binding energy tail indicates there is little to no oxidation of the Ni sites at the surface.

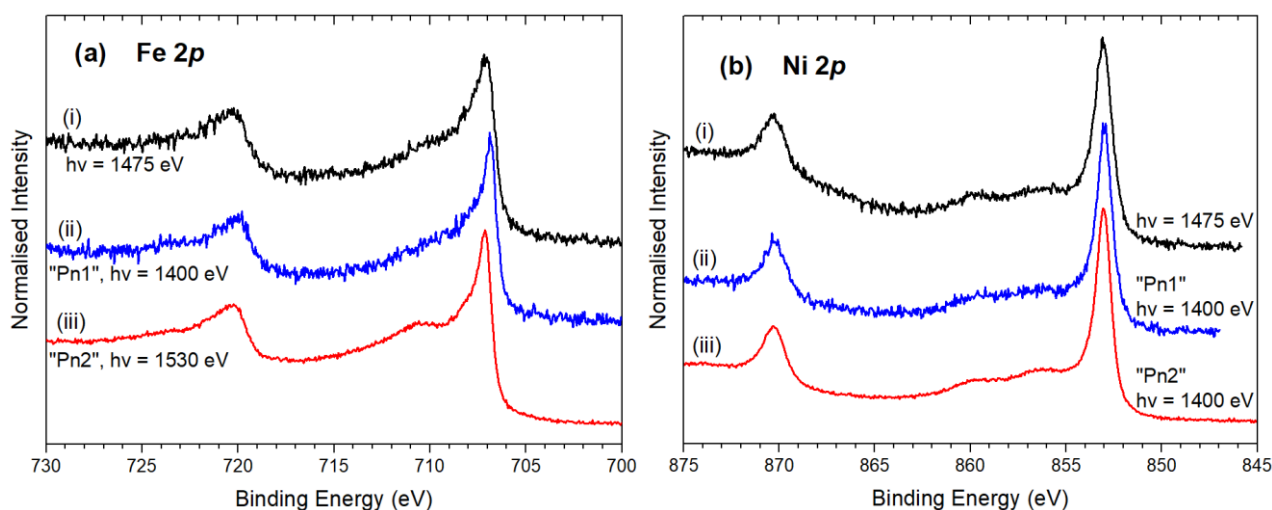


Figure 7.3: (a) Fe $2p$ and (b) Ni $2p$ spectra from three vacuum fractured pentlandite samples show the iron sites on the pentlandite surface are partly oxidised.

A S $2p$ spectrum was collected for this sample with $h\nu = 1475$ eV. The spectrum was fitted using the method devised in Chapter 6, with three doublets attributed to surface 3-coordinate monosulfide, overlapping surface and bulk 4-coordinate sulfide, and bulk 5-coordinate monosulfide species, respectively. The empirically derived asymmetric tail has been included in the bulk 5-coordinate component in the fitted spectrum shown in Figure 7.4. The % contribution from each of these features to the overall fitted S $2p$ spectrum shown in Table 7.3 is similar to that of the high photon energy spectra for Pn1 and Pn2 shown in Chapter 6. Although there is no clear evidence in this spectrum of disulfide and polysulfide species, the contribution from the surface features in this spectrum is expected to be approximately 7% of the total sulfur signal. When polymerised sulfur species were observed for Pn2 in Chapter 6 they could only be observed in the most surface sensitive spectra, and there was no evidence of them in the $h\nu = 1050$ eV spectrum. Therefore, if there are similar amounts of disulfide and polysulfide species on the surface of this sample as were observed for Pn2, they would not be observable in the spectrum shown in Figure 7.4. Yet, this spectrum does show that the sulfide species have not been altered significantly.

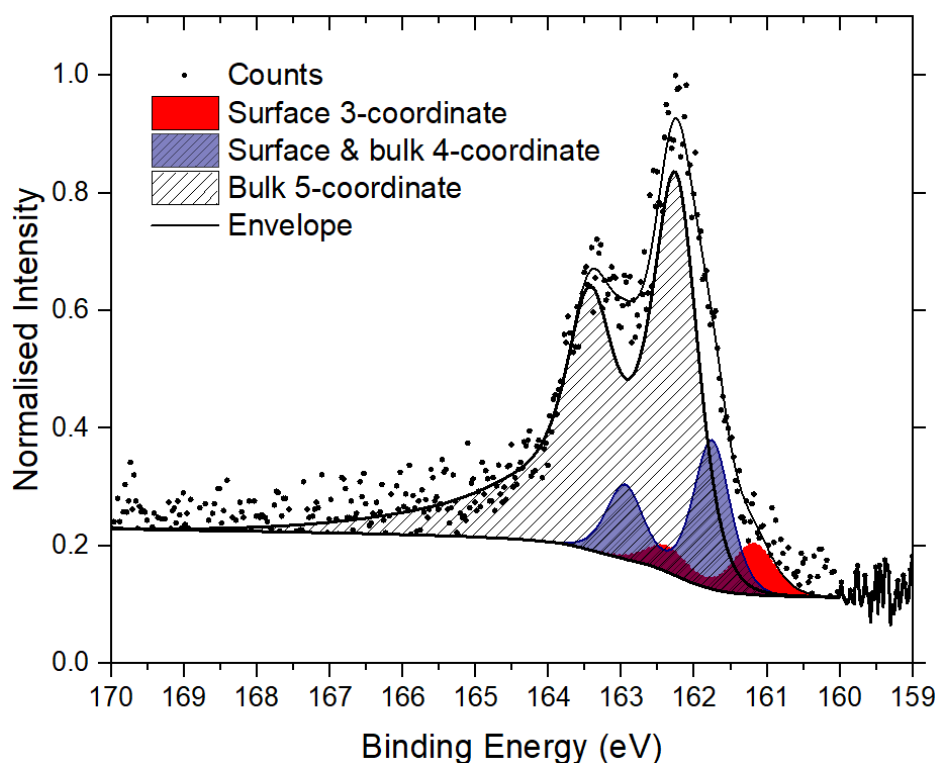


Figure 7.4: S $2p$ spectrum for vacuum fractured pentlandite showing no evidence of polymerised sulfur, $h\nu = 1475$ eV.

Table 7.3: Quantification of % contribution of each feature to the fitted S $2p$ spectrum.

Species (Binding Energy)	Binding Energy (FWHM)	% contribution to fit
		$h\nu = 1475$
Surface 3-coordinate	161.1 eV (0.65)	6.2
Surface & bulk 4-coordinate	161.7 eV (0.59)	16.4
Bulk 5-coordinate	162.2 eV (0.67)	77.4

7.2.2 Observation of Fe, Ni and S L edge NEXAFS spectra

The Fe $L_{2,3}$ X-ray absorption spectrum for this pentlandite sample is shown in Figure 7.5. The main L_3 absorption peak is at 706.8 eV, which is equal to that of the metal Fe standards and consistent with the L_3 absorption peak for Pn2 in the previous chapter and the only other pentlandite Fe L edge NEXAFS spectrum previously presented in literature [23]. Since the Fe $2p$ binding energy is at 707.1 eV, the absorption peak at 706.8 eV in Figure 7.5 can be attributed to transitions from the $2p$ orbital to unoccupied bound states. Unlike the Fe L edge spectrum for Pn2 and that presented in literature [23], the spectrum in Figure 7.5. has a distinct high energy shoulder around 708 eV. Previous Fe L edge spectroscopy has observed the main peak of Fe^{III} at a similar energy in hematite (Fe₂O₃) [20, 24] and in FeOOH [25]. The presence of this strong shoulder in the spectrum in Figure 7.5 where it

is not seen in the Pn2 absorption spectrum in Chapter 6 can be explained by the oxidation of Fe states expected at the surface of this sample, where no such oxidation was observed for the Pn2 sample. The oxidation of Fe sites is seen to broaden the $2p_{3/2}$ peak in the photoelectron spectrum. However, this only has a small effect in the photoelectron spectrum due to the overlap of Fe^{II} multiplet features with the Fe^{III} signal. Contrastingly, the presence of Fe^{III} species has a much clearer effect on the X-ray absorption spectrum due to the distance between absorption energies for Fe^{II} and Fe^{III} species, possible changes in symmetry at the oxidised sites, and the increased opportunities for absorption to unoccupied states for Fe^{III} species. There is a small inflection that can be seen on the leading edge of the main absorption peak around 705 eV. This feature is not as obvious as the pre-edge peak in the Pn2 sample in the previous chapter or the spectrum presented in literature [23]. It is possible that the strong contribution to the spectrum by Fe^{III} species is somewhat overshadowing the pre-edge feature, rather than entirely suppressing this state.

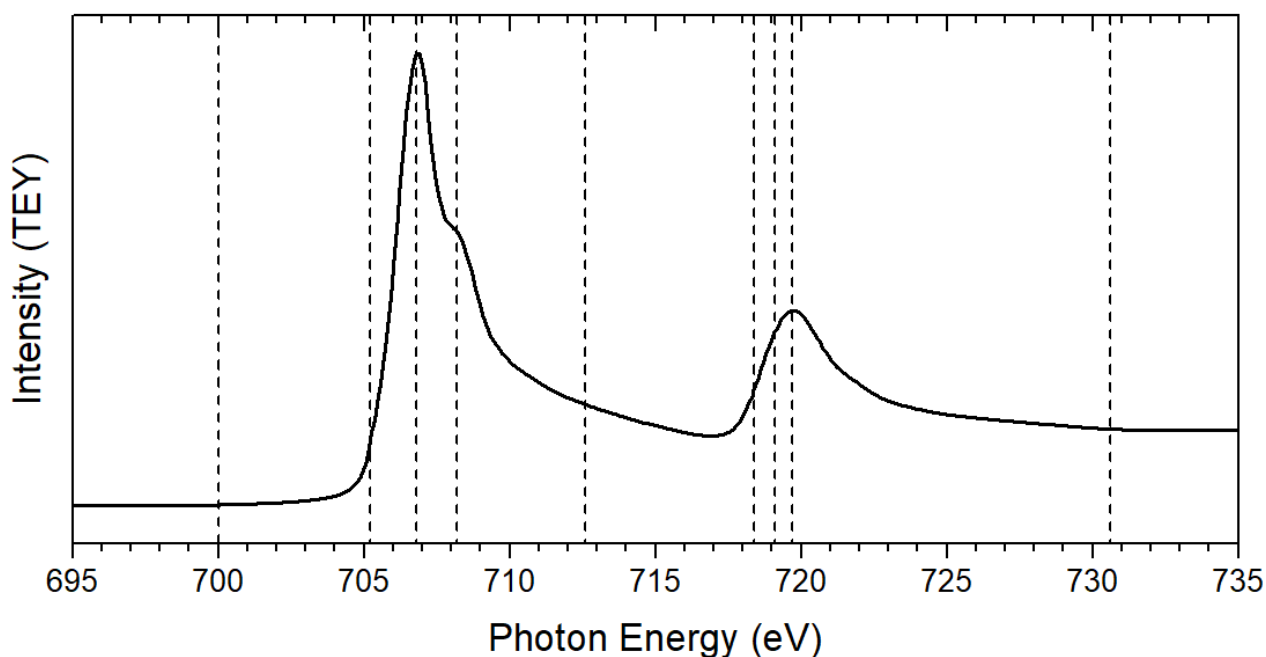


Figure 7.5: Fe $L_{2,3}$ absorption spectrum for vacuum fractured pentlandite shows evidence of both Fe^{II} and Fe^{III} components.

The Ni L_3 absorption energy is observed at 853.0 eV, shown in Figure 7.6 and is consistent with the previously reported Ni L edge spectrum for Pn2, that presented previously in literature [23], and that of Ni^{II} -S in millerite (NiS) [26]. The energy of the main absorption peak is the same as the binding energy for the $2p$ photoelectron peak (853.0 eV), indicating that this absorption peak may be due to transitions to the continuum, and would therefore result in the appearance of the Auger decay channel in the valence band spectrum collected at that photon energy. The L_3 absorption peak is a sharp asymmetric peak with slight broadening on the high energy side. A broad low intensity feature is

observed around 859 eV, similar to the feature observed in the millerite absorption spectrum [26]. The Ni L edge spectra have been investigated generally for nickel dihalides (NiF_2 , NiCl_2 , NiBr_2 and NiI_2) and NiO [27]. This study showed that for the compounds with greater electronegativity there was a small sharp peak on the high energy side of the Ni L_3 maximum, which was attributed to multiplet states. By decreasing the electronegativity of the ligand, the multiplet structure decreased, causing the decrease in the multiplet contribution to the spectra, and simultaneously increased the satellite structure, seen as a low intensity broad peak at some distance from the main absorption peak. The pentlandite Ni L edge spectrum shown in Figure 7.6 has no distinct high energy contribution such as those associated with the multiplet structure, but shows a clear broad peak approximately 6 eV above the main absorption peak. This energy separation is similar to that seen for the satellite peaks observed in the more covalent nickel dihalides, and especially that of NiO. If the trend in covalency observed by van der Laan, Zaanen, Sawatzky, Karnatak and Esteva [27] is expected to continue for group IV nickel compounds (NiO, NiS etc), then NiS is expected to be more covalent with less multiplet structure and a stronger satellite structure in the absorption spectrum. The observation of the Ni L edge spectrum, in comparison with the previously published NiO spectra supports this theory.

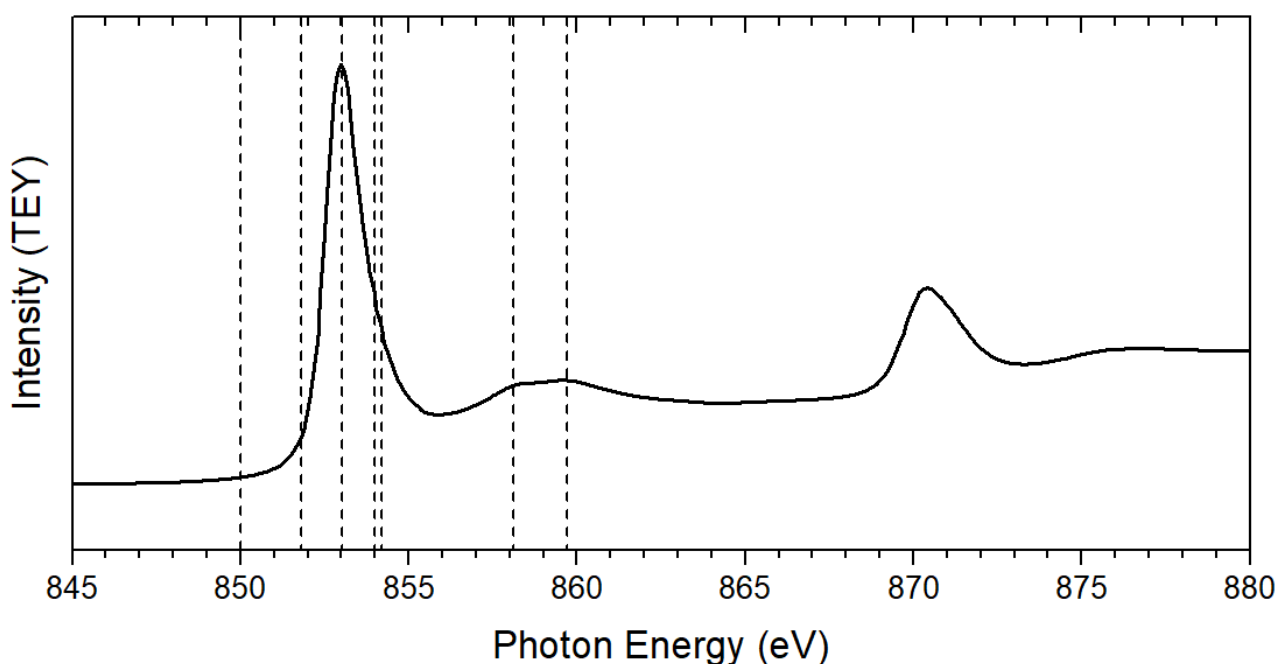


Figure 7.6: Ni $L_{2,3}$ absorption spectrum for vacuum fractured pentlandite shows a broad contribution due to multiplet structure arising from Ni-S covalency.

The S $L_{2,3}$ absorption spectrum for pentlandite is shown in Figure 7.7 and is the first known reported L edge spectrum for pentlandite. The absorption spectrum consists of some low intensity fine structure in around 163 eV. This structure is split into a doublet, indicating that this feature is due to

the transition of S $2p_{2/3}$ and $2p_{1/2}$ electrons to $3s$ or $3d$ states respectively. The energy of this spin-orbit splitting is estimated to be 1.2 eV, which is similar to the spin-orbit splitting of 1.3 eV for the pyrrhotite S $L_{2,3}$ edge absorption spectrum in Chapter 4. This indicates there may be a strong covalency between the sulfur ligand and metal states. It is difficult to compare this spin-orbit splitting energy to the energy difference between the Fe absorption peak and the pre-edge energy since the pre-edge feature is so small. However, the pre-edge peak of the Pn2 Fe X-ray absorption spectrum shown in Chapter 6 is estimated to be approximately 1.2 eV below the main absorption peak. In contrast, no pre-edge peak has been observed for the pentlandite Ni L edge absorption spectrum. This indicates that there is a ligand to metal charge transfer state between the sulfur and iron atoms. Other features observable in the spectrum in Figure 7.7 include broad shoulders 6 eV and 8 eV higher than the onset of the absorption spectrum, respectively labelled 'b' and 'c', and another broad, strong peak approximately 14 eV above the onset of the spectrum labelled 'd'. The shape and relative energies of the features in the pentlandite spectrum are strikingly similar to the pyrrhotite spectrum shown previously in Chapter 4 and to that of chalcopyrite, which also has a notably similar S $L_{2,3}$ absorption spectrum [28]. Therefore, the peaks labelled in Figure 7.7 are attributed to transitions of S $2p$ electrons to empty S $3s$ - and $3p$ -like states at 'b' and 'c' respectively, and the peak at 'd' is attributed to transitions to empty S $3d$ states.

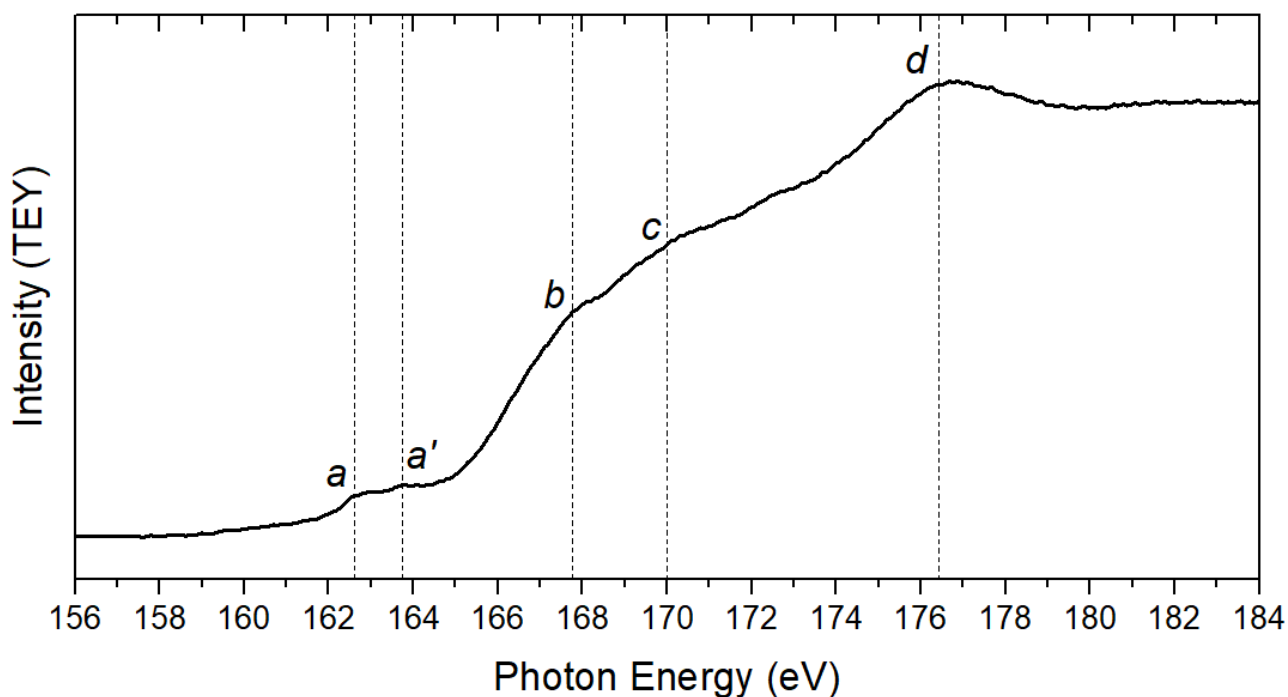


Figure 7.7: S $L_{2,3}$ absorption spectrum for vacuum fractured pentlandite.

7.2.3 Description of valence band for pentlandite

The photoelectron spectrum taken in the valence band region for pentlandite is shown in Figure 7.8, collected with $h\nu = 695.6$ eV; below the Fe absorption edge. The shape of the valence band spectrum has three distinct features. The upper valence band has a strong peak at 1.1 eV with a shoulder around 0.3 eV. This region is expected to be dominated by octahedral metal $3d$ states [8], particularly from the e_g orbitals [29]. The lower valence band has a peak at 4.4 eV with a shoulder around 6.3 eV. This broad peak is separated from the upper valence band by a local minimum around 3 eV, and from calculations is expected to be largely due to S $3p$ -like states from 4-coordinate and 5-coordinate bulk sulfur [8], with some contributions from tetrahedral $3d$ states [29]. There is another peak further from the Fermi energy at around 14 eV which is attributed largely to S $3s$ states [8]. It has been shown by previous calculations that the energy difference between the S $3s$ states and the metal valence states is great enough to prevent significant mixing between these orbitals [7]. The variation in intensity seen in the valence band spectra for Pn1 and Pn2 in Chapter 6 in comparison with the photoionization cross sections of atomic orbitals supports the general assignment of metal $3d$ states and sulfur $3p$ states to the upper valence band and the lower valence band between 3 – 8 eV respectively.

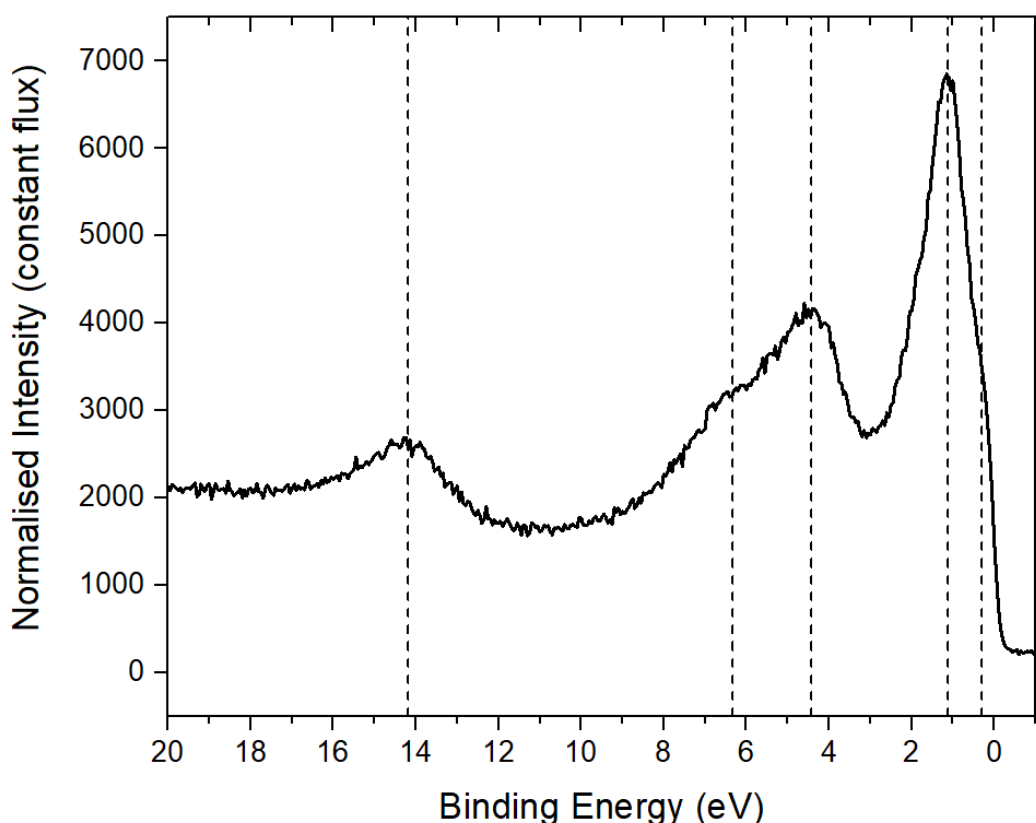


Figure 7.8: Pentlandite valence band photoelectron spectrum, $h\nu = 695.6$ eV.

7.2.4 Resonant valence band spectra at the Fe 2*p* absorption threshold

The Fe L edge absorption spectrum for pentlandite is shown on the right side of Figure 7.9, with the resonant photoemission spectra shown on the left. The photon energies used to collect the photoemission spectra are indicated by dotted lines connecting to the absorption spectrum. The spectrum at the top of Figure 7.9 is the same spectrum shown in Figure 7.8 and was collected with $h\nu = 695.6$ eV before the onset of the absorption spectrum. The next photoemission spectrum was collected with $h\nu = 705.2$ eV, which is the energy at which the pre-edge absorption peak is estimated to be. This spectrum appears to have a flat top between 1 – 6 eV. The next spectrum was collected with $h\nu = 706.8$ eV and shows a broad peak at 4.4 eV, with a shoulder around 7 eV. This structure is seen to move through the following spectra at what appears to be constant kinetic energy, with an intensity profile which generally follows the intensity of the absorption spectrum. Therefore, these features are expected to be due to the normal Auger decay channel.

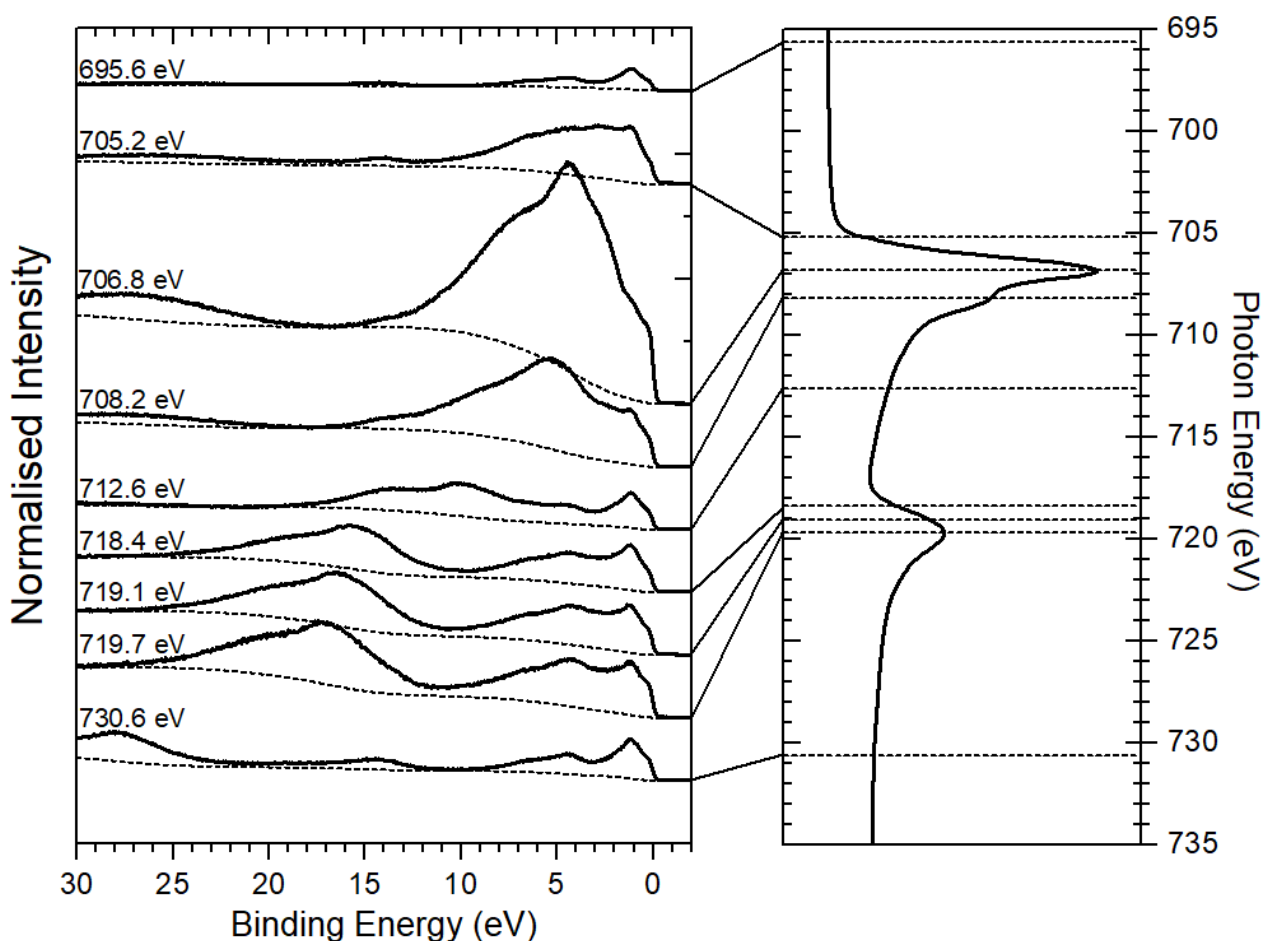


Figure 7.9: Photoelectron spectra collected with photon energies across the Fe 2*p* absorption spectrum show an increase in intensity of the lower valence band at photon energies at and above the L₃ absorption peak.

The fine structure of the $h\nu = 705.2$ eV and 706.8 eV spectra are investigated in Figure 7.10, which shows these two spectra with the off-resonance valence band spectrum. The spectrum taken with the

pre-edge peak energy shows some structure in the region between 1 – 5 eV, with a local maximum at 2.8 eV where the local minimum is in the off-resonance spectrum. In addition to the Auger-like feature at 4.4 eV in the $h\nu = 706.8$ eV spectrum, there is some additional structure on the Fermi energy side at 2.8 eV, and a shoulder at 1.1 eV and 0.2 eV, as indicated by dotted lines in Figure 7.10. The latter two binding energies are consistent with structure observed in the upper valence band of the off-resonance spectrum and are therefore expected to arise from the photoemission signal.

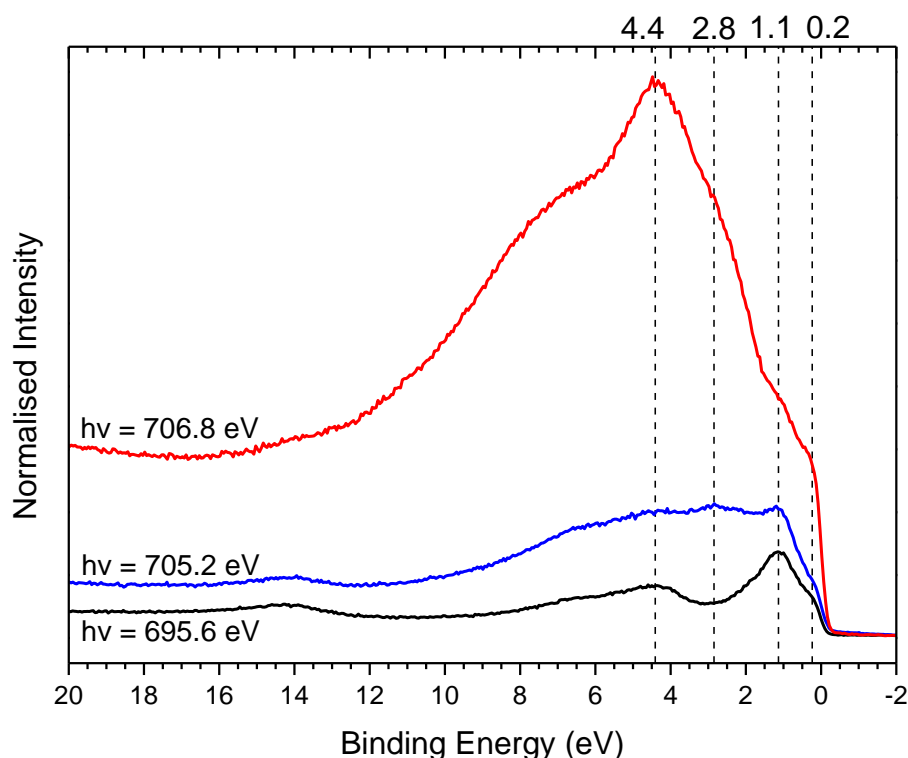


Figure 7.10: Photoelectron spectra collected with $h\nu = 695.6$ eV (off-resonance), 705.2 eV (pre-edge) and 706.8 eV (peak energy). The binding energies of specific features are labelled above the graph in eV.

To determine if the enhancement in the photoemission spectrum is due to resonance or simply the superposition of an Auger signal on the photoemission spectrum, the off-resonance photoemission spectrum has been subtracted from each subsequent spectrum, and the resulting spectra presented in Figure 7.11. These spectra are plotted in the kinetic energy scale to highlight the constant kinetic energy feature that moves through the photoemission spectrum. If the enhancement in each resonant valence band spectrum is only a superposition of the constant binding energy photoemission signal and the constant kinetic energy Auger decay spectrum, then only the Auger signal should be observed in the spectra in Figure 7.11. Indeed, there are no features observed in the spectra in Figure 7.11 that are not constant kinetic energy features. There is a strong peak at 702 eV (kinetic energy) visible for each spectrum, and a second, smaller feature with a peak just above 715 eV visible for the spectra collected with photon energies near the L_2 absorption edge. This shows that there is no interference

between the photoemission and deexcitation channels and therefore no true resonance resulting in a Fano-profile. The photoemission and deexcitation channels are non-coherent and do not interfere with one another, resulting in the enhancement of the spectra which arises from a superposition of the two channels. The loss of coherence of these two channels arises from the charge-transfer between the Fe $3d$ and S $3p$ states [30].

As far as is observable, the states in the upper valence band, which are expected to be strongly octahedral metal character, appear unaffected by the change in photon energies over the $L_{2,3}$ absorption edge. However, the constant kinetic energy deexcitation peak appears strongly in the photoemission spectrum at 4.4 eV. This region of the valence band spectrum is due to a strong density of sulfur states, especially from the 4-coordinate sulfur atoms which link the cube clusters through the tetrahedral metal atoms [8]. This shows that the initial and final states of the Fe Auger signal and the photoemission signal at this energy are the same. Due to the density of metal tetrahedral t_{2g} states calculated to be at that energy [29], the state at 4.4 eV in the valence band is most likely attributed to the charge-transfer between the tetrahedral Fe t_{2g} band and the 4-coordinate ‘linking’ sulfur $3p$ valence band, but may also have some contribution from an interatomic resonant enhancement of the S $3p$ states [31].

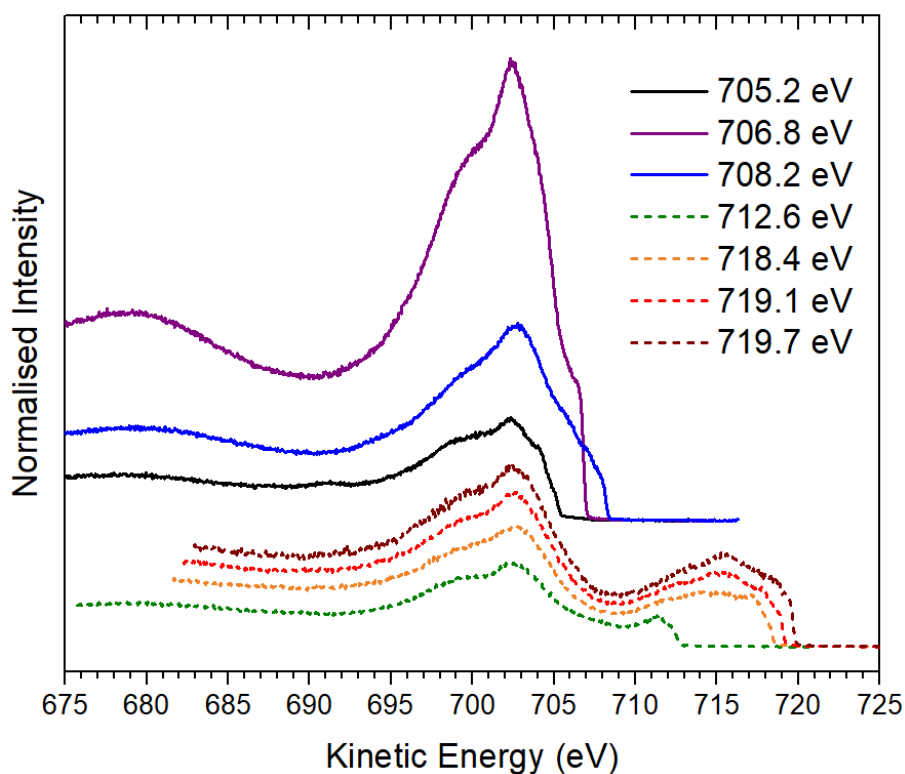


Figure 7.11: Resonant valence band spectra each with the off-resonance spectrum ($h\nu = 695.6$ eV) subtracted to show the constant kinetic energy Auger feature moving through the spectra. The 705.2 – 708.2 eV spectra have been vertically offset for clarity.

7.2.5 Resonant valence band spectra at the Ni 2*p* absorption threshold

The valence band photoemission spectra taken with photon energies ranging over the Ni absorption edge are shown in Figure 7.12. The first spectrum at the top of Figure 7.12 is an off-resonance spectrum collected with $h\nu = 845.9$ eV and is consistent with the off-resonance spectrum shown previously in Figure 7.10. The spectrum collected with $h\nu = 851.8$ eV below the absorption edge shows an enhancement of the photoemission spectrum around 7 eV, while the upper valence band appears to be subdued. The spectrum collected with $h\nu = 853.0$ eV at the absorption peak has a strong peak at 8 eV with a shoulder around 5 eV. This asymmetric shape is seen to move through the subsequent valence band spectra at what appears to be a constant kinetic energy and an intensity which follows the intensity of the absorption spectrum.

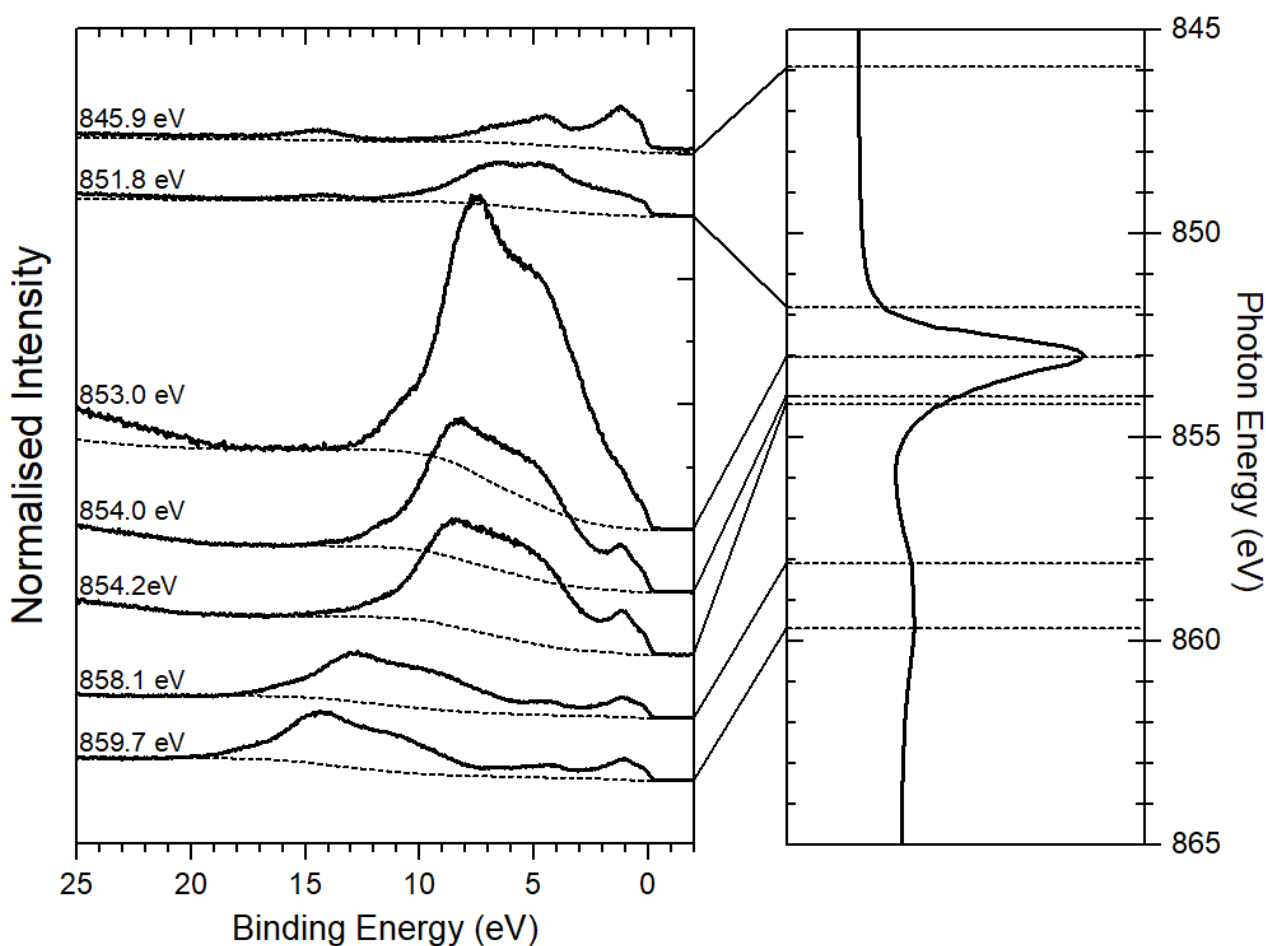


Figure 7.12: Photoelectron spectra collected with photon energies across the Ni 2*p* absorption spectrum show a strong increase in intensity for photon energies at and above the L₃ absorption edge.

The fine structure of the valence band spectra collected below and at the Ni L₃ absorption edge is shown in more detail in Figure 7.13. The photoemission spectrum collected directly below the Ni absorption edge has a diminished upper valence band (at 1.1 eV) in comparison to the off-resonance valence band spectrum, with an increase in the lower valence band at 4.5 eV and 6.6 eV. In

comparison, the 1.1 eV feature in the spectrum taken at the absorption edge has approximately the same intensity as is seen in the off-resonance photoemission signal. This diminished feature below the absorption edge may be an indication of either a resonance or anti-resonance Fano-profile [18].

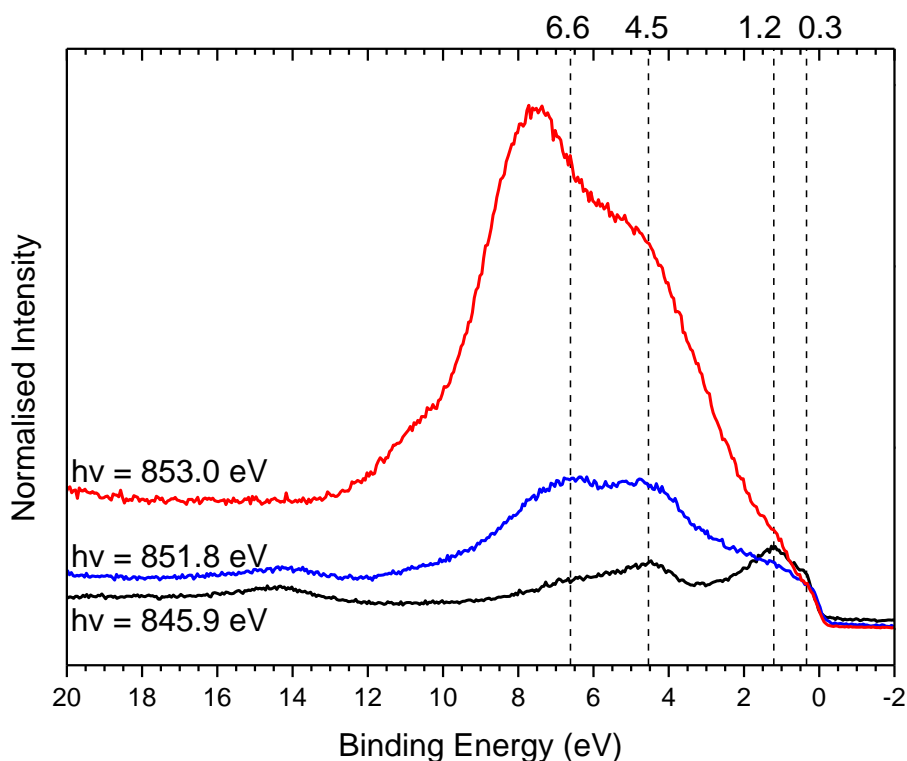


Figure 7.13: Photoelectron spectra collected with $h\nu = 845.9$ eV (off-resonance), 851.8 eV (pre-edge) and 853.0 eV (peak energy). The binding energies of specific features are labelled above the graph in eV.

Figure 7.14 shows the photoemission spectra collected with photon energies over the absorption edge with the off-resonance spectrum subtracted. In contrast to the similar spectra shown for the Fe absorption edge, the spectra in Figure 7.14 appear to have some contributions other than the constant kinetic energy Auger feature. Each spectrum has a strong peak in the constant kinetic energy feature at 845.5 eV with a shoulder around 848 eV, with the exception of the $h\nu = 851.8$ eV spectrum. The spectrum originating from the $h\nu = 851.8$ eV spectrum has a similar spectral shape, but the main peak is at 844.5 eV with a shoulder 0.5 eV below the shoulder of the constant kinetic energy feature which is consistent with the LMM Auger electrons. This shows that the deexcitation feature is photon energy dependent below the L_3 absorption peak, but constant kinetic energy above. This indicates some interference between the deexcitation channel and the photoemission states in the region 4 – 7 eV. Further indication of interference can be seen in the negative peak in the $h\nu = 851.8$ eV spectrum around 850.6 eV in the kinetic energy scale. This negative peak represents the diminished upper valence band peak just above 1 eV. A typical Fano-profile consists of a dip in intensity below the absorption edge, followed by a resonant enhancement at and above the absorption edge [18].

However, it is possible for the channels to interfere and cause a negative resonance, which may be characterised by a decrease in the intensity just below the absorption threshold with very little enhancement at or above the threshold [18, 32]. The coherence of this photoemission state with the deexcitation channel that follow the Ni L edge absorption indicates that the peak at 1.1 eV has strong nickel character.

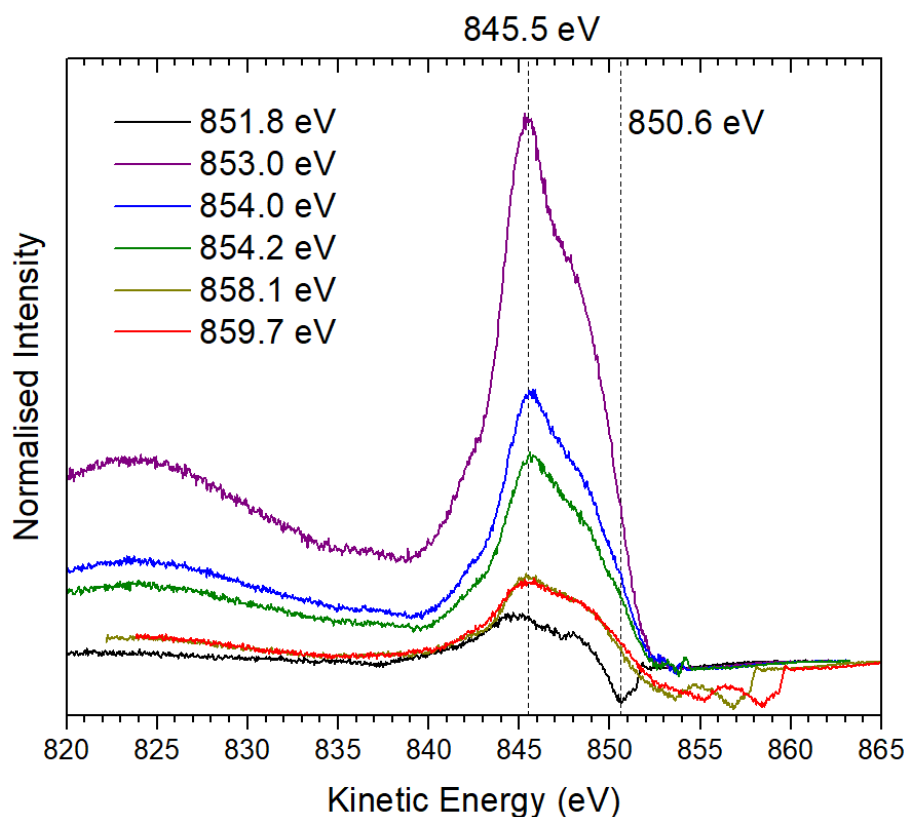


Figure 7.14: Resonant valence band spectra collected with photon energies over the Ni absorption edge each with the off-resonance spectrum ($h\nu = 845.9$ eV) subtracted to show the constant kinetic energy Auger feature moving through the spectra.

7.2.6 Conclusions from resonant valence band photoemission spectroscopy

The resonant valence band spectra for pentlandite have been investigated from the Fe and Ni L edge absorption spectra. This has led to the identification of the regions of the valence band photoemission spectrum that can be attributed to states with strong Fe or Ni character respectively. Firstly, the S $L_{2,3}$ absorption spectrum was presented for the first time in the literature and showed a spin-orbit splitting consistent with the separation of the Fe L edge peak and pre-edge energy. This showed evidence of a possible ligand to metal charge-transfer state between the sulfur and Fe metal atoms.

The resonant valence band spectra over the Fe L edge absorption threshold showed no clear indications of true resonance and the enhancements of the valence band were due to an incoherent

superposition of the photoemission and deexcitation channels. This was supported by the spectra with the photoemission signal removed, where only the constant kinetic energy Auger feature remained. The energy of the Auger enhancement indicated that the Fe valence states overlap with the S 3*p* valence states at 4.4 eV in the valence band spectrum. This signal is attributed to the ligand to metal charge transfer state between the tetrahedral Fe *t*_{2g} states and the S 3*d* states of the 4-coordinate linking sulfur sites. No strict resonance was observed for this feature, indicating that the photoemission and deexcitation signals have a loss of coherence due to the delocalisation of this state.

The nickel resonant valence band spectra showed a decrease in the 1.1 eV photoemission feature just below the absorption threshold, with no clear increase of this feature at or above the threshold. This is an indication of coherence between the 1.1 eV photoemission feature and the deexcitation channel, even if it is not a typical Fano-resonance, characterised by the strong increase in intensity above the threshold. The true nature of this state requires further investigation to elucidate, but showed that this feature at 1.1 eV in the valence band has a strong nickel character. Evidence of coherence between the photoemission and deexcitation channels was observed in the lower valence band region, specifically between 4 – 7 eV. This was characterised by an enhancement of the photoemission spectrum that was not consistent with the superposition of an Auger feature. The enhancement of the valence band was observed to be photon energy dependent below the absorption threshold, and transitioned to a constant kinetic energy feature above the L₃ absorption threshold. The resonance observed for the resonant photoemission spectra for nickel indicates that the nickel valence states are at least weakly localised, whereas the iron states are less localised.

7.3 Effect of stoichiometry on the valence band of pentlandite

7.3.1 Introduction

The effect of changing the ratio of iron and nickel, and other cations such as cobalt or silver in the pentlandite lattice has been an area of interest in several studies primarily surrounding the issue of the preference for Fe or Ni cations in the octahedral sites in the pentlandite lattice [33-35]. Some studies suggest that iron preferentially occupies the octahedral sites of natural pentlandite [35-37]. A more recent study which specifically investigated the cation ordering in fresh and annealed synthetic pentlandite samples found a disordered distribution of cations in both types of sample [38]. Additionally, microprobe studies of natural pentlandites found that the relative ratios of iron, nickel and cobalt cations provides an effective *d*-electron concentration per unit formula of close to 65, which corresponds to the ideal (Co₉)¹⁶⁺ such as is found in the only stable monometallic pentlandite [6]. A recent DFT calculation of pentlandite cation distribution found that the most stable distribution is one in which the cations are heterogeneously dispersed in the bulk, rather than clustered with like

atoms, but gives no indication about long-range ordering [10]. Calculations of the pentlandite valence band have found that the stable stoichiometries result from the Fermi level lying within a pseudo-gap in the density of states [8]. Therefore, it is possible and not unreasonable to expect that on the micro scale there would be a variation in local cation distribution and therefore density of states. However, the spot size over which these samples were analysed was up to $500 \times 500 \mu\text{m}$, and therefore any variation in local cation distribution is expected to have a minimal effect on the spectra.

A previous study by Fujimori, Mamiya, Mizokawa, Miyadai, Sekiguchi, Takahashi, Mori and Suga [39] has investigated the trends in the valence band spectra for pyrite-type FeS_2 , CoS_2 and NiS_2 as a result of the addition of an extra electron to each unit cell [39]. In this study it was observed that FeS_2 had the sharpest peak in the upper valence band due to the full t_{2g} and empty e_g band. With the addition of an electron the e_g band in CoS_2 and another in NiS_2 the peak in the upper valence band shows a broadening due to the exchange splitting and spin polarization of the e_g band. Additionally, a shoulder develops on the Fermi energy side of the main peak with increase in cation atomic number, which is most obvious in the NiS_2 spectrum, as a result of the successive filling of the e_g band [39]. While these minerals have significantly different structures and density of states to pentlandite, a similar trend may be observable in pentlandite samples with differing stoichiometries and different densities of valence d electrons.

7.3.2 Methods

The spectra in the following sections were measured from a series of synthetic pentlandite samples with varying ratios of Fe, Ni and S, to investigate the effect on the valence band photoemission spectrum by changing pentlandite's stoichiometry. Figure 7.15 shows the stoichiometry of the samples used in this section, and the stoichiometry of the vacuum fractured sample used in the previous section. The exact stoichiometries of the samples are listed in Table 7.5 with an overview of the observations made from the survey Fe/Ni $3p$ and S $2p$ spectra. These samples were analysed at the Canadian Light Source using the methods described in section 3.2.3. The samples were fractured in a nitrogen-filled glove bag immediately prior to analysis. Photoelectron spectra in the valence band region of these samples were collected using low photon energies. The photon energies were varied between spectra to attempt to isolate metal- and sulfur-like states based on the change in photoionization cross sections of different states. The photoionization cross sections of selected atomic valence orbitals are shown in Figure 7.16, calculated from reference [40].

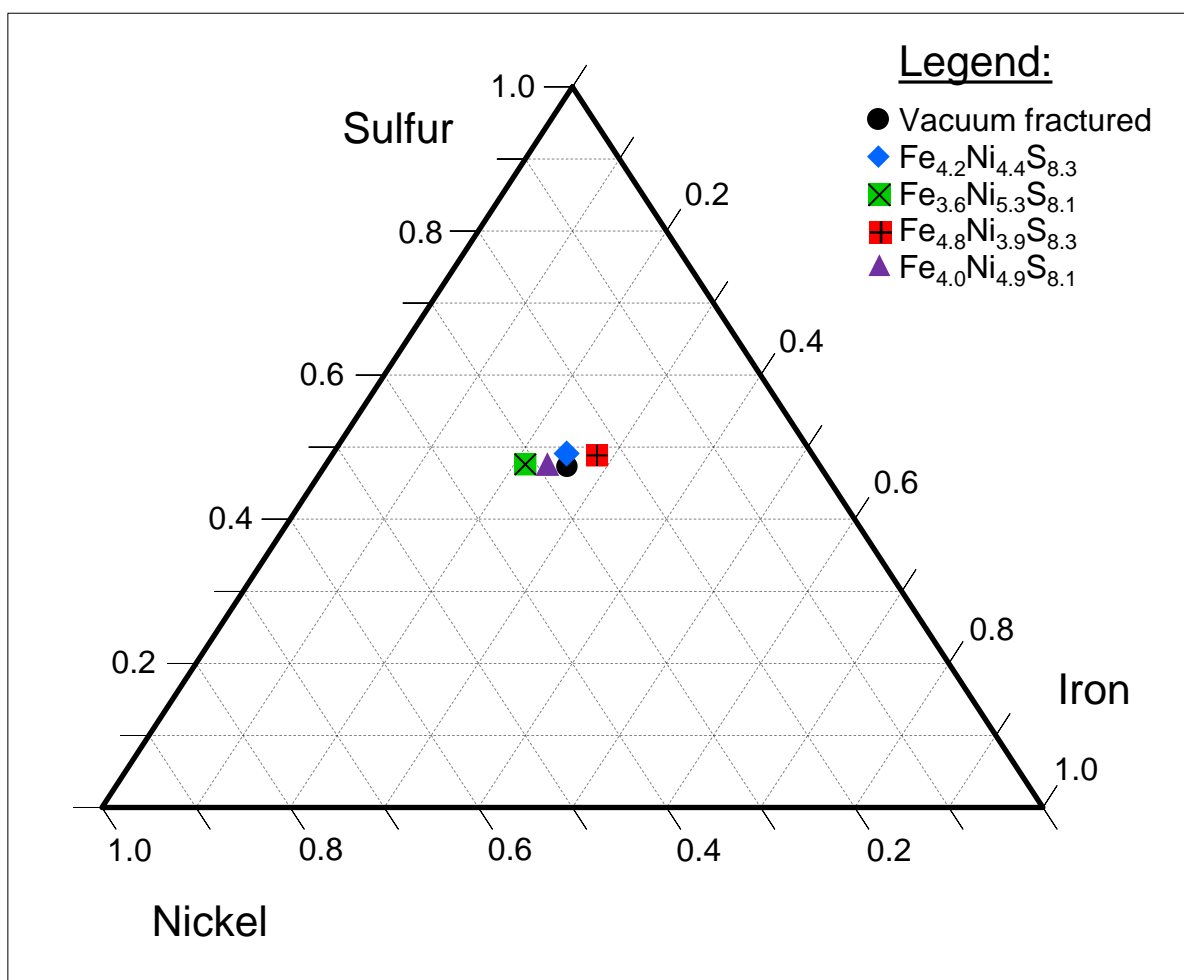


Figure 7.15: Ternary plot showing the stoichiometry of pentlandite samples used in this chapter as a proportion of sulfur, iron and nickel.

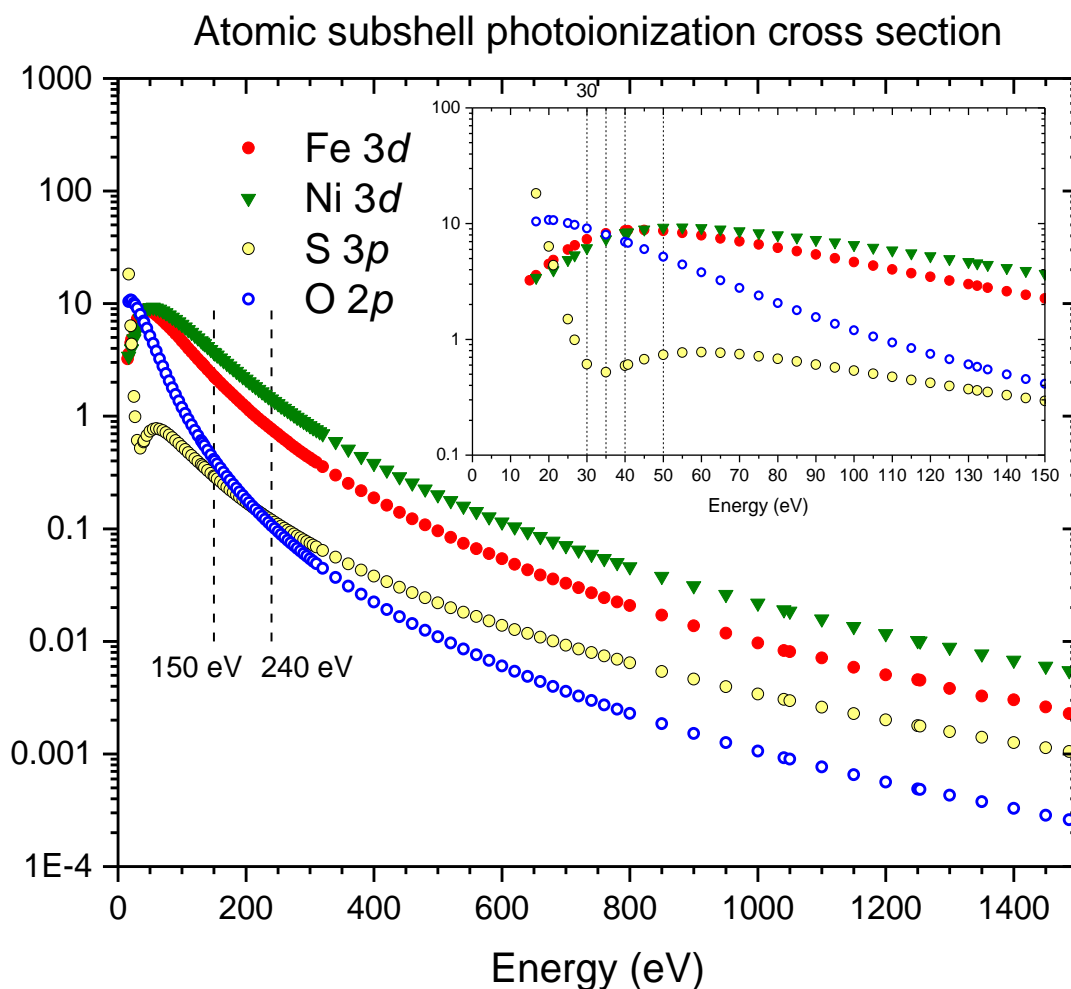


Figure 7.16: Photoionization cross section of valence level atomic subshells [40].

7.3.3 Comparison of survey and core level photoelectron spectra

The survey spectra from the four synthetic pentlandite samples used in this section are shown in Figure 7.17, collected with $h\nu = 240$ eV. The main features of each spectrum include a strong peak near 160 eV from the S $2p$, a broad asymmetric peak around 90 eV (kinetic energy = 150 eV) due to sulfur Auger electrons, two small peaks at 70 and 55 eV due to the Ni and Fe $3p$ respectively, and the valence band below 10 eV. Each spectrum also shows a low, broad peak around 25 eV which is attributed to the O $2s$, indicating that each of the samples has some oxygen contamination. The survey spectrum for $\text{Fe}_{4.2}\text{Ni}_{4.4}\text{S}_{8.3}$ also has a sharp peak just above 100 eV which is not seen in the other survey spectra. This is attributed to Si $2p$ photoelectrons. The Si is evidence of contamination from SiO_2 (glass) fibres used in the synthesis of these samples. The SiO_2 species are expected to be inert and not interact with the pentlandite structure, however it causes some intensity in the higher binding energies of the valence band spectra. Indeed, it can be seen from the $\text{Fe}_{4.2}\text{Ni}_{4.4}\text{S}_{8.3}$ survey spectrum that the S $3s$ peak in the valence band spectrum (expected around 15 eV) and the O $2s$ peak around 25 eV are not distinct and overlap. This overlap is observed only for $\text{Fe}_{4.2}\text{Ni}_{4.4}\text{S}_{8.3}$ and is therefore

expected to be due to the SiO₂ valence electrons which have their greatest intensity at energies above 10 eV [41]. The contribution to the valence band from the SiO₂ valence electrons should be minimal below 10 eV. Since no Si photoelectron peak is observed in the survey spectrum for the other three samples, the O 2s signal must originate from oxidation of part of the sample.

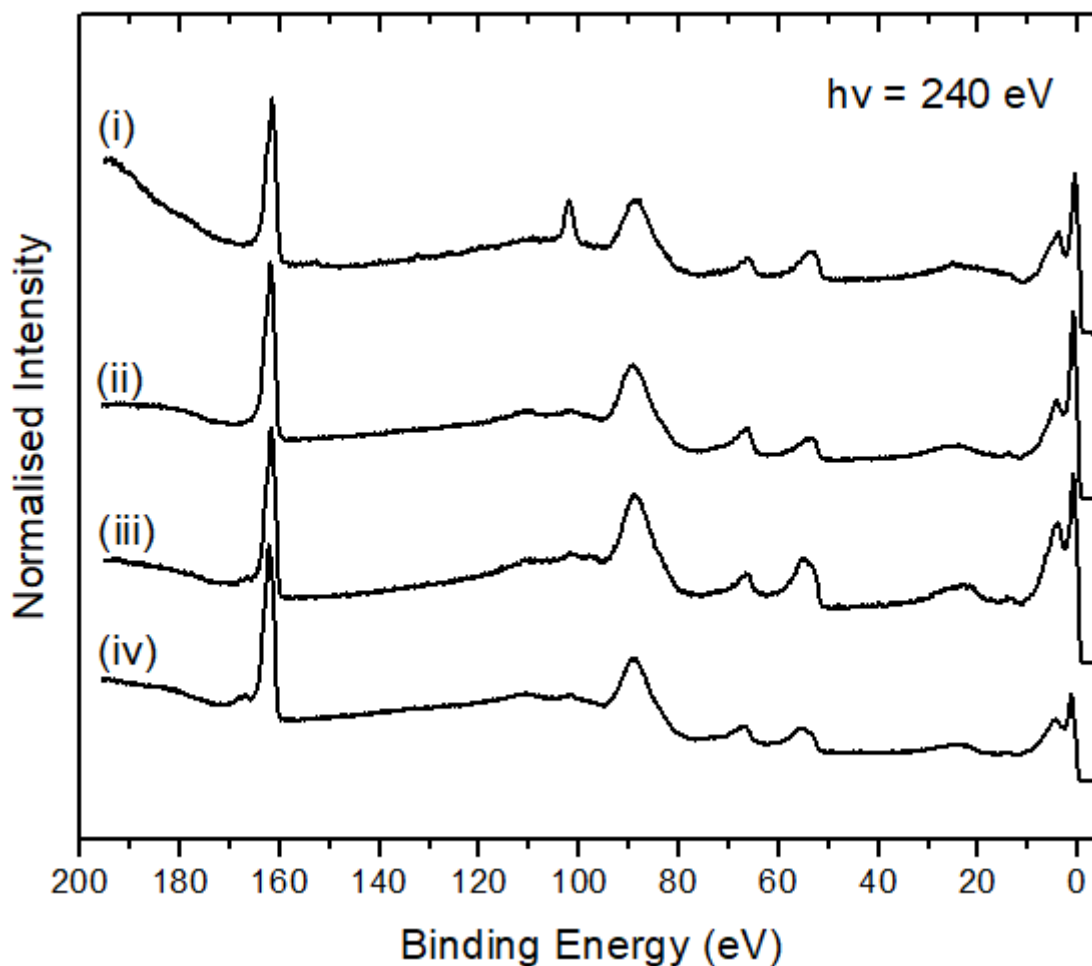


Figure 7.17: Survey spectra for the four pentlandite samples: (i) Fe_{4.2}Ni_{4.4}S_{8.3}, (ii) Fe_{3.6}Ni_{5.3}S_{8.1}, (iii) Fe_{4.8}Ni_{3.9}S_{8.3}, (iv) Fe_{4.0}Ni_{4.9}S_{8.1}. Si contamination is only observed in (i). For each spectrum, $h\nu = 240$ eV.

Fe and Ni 3*p* spectra were collected for each sample and are shown in Figure 7.18a. To allow for a direct comparison between the $h\nu = 240$ and 150 eV spectra of the same sample, the spectra have been normalised to the Fe 3*p* peak and had a Shirley background subtracted. The Fe 3*p* spectra for Fe_{4.2}Ni_{4.4}S_{8.3} and Fe_{3.6}Ni_{5.3}S_{8.1} show the main peak centred at 54 eV with asymmetry on the high binding energy side of this peak. The asymmetry is caused partly by multiplet structure such as is seen in the 2*p* spectrum, however a large contribution to the asymmetry is the overlap of the 3*p*_{1/2} peak with the stronger 3*p*_{3/2} peak. The transition metals 3*p* peaks are not well studied for sulfide minerals other than pyrite, but a comparison can be made with transition metal oxides, as the oxides are likely to form under the right conditions. Furthermore, comparison of the 3*p* peaks with those of

the transition metal oxides may give some indication of the valency of the cations in the current samples. The binding energy of the $3p_{3/2}$ peak is a little higher than that of unoxidized pyrite, which is just below 53 eV [42], but is consistent with Fe^{II} in hematite (Fe_2O_3), observed at 53.7 eV [43]. The higher binding energy in comparison to pyrite may be due to a broadening of the spectrum due to multiple Fe^{II} states and multiplet structure that would broaden the spectrum on the high binding energy side. The binding energy is significantly lower than Fe^{III} observed in magnetite (Fe_3O_4) at 55.6 eV [43, 44] and is therefore not likely to be due to oxidised Fe^{III} species. Furthermore, there is no obvious change in spectral shape between the $h\nu = 240$ eV and $h\nu = 150$ eV spectra, indicating that the surface structure does not deviate significantly from the bulk structure in these two samples. In contrast, the Fe $3p$ spectra for $\text{Fe}_{4.8}\text{Ni}_{3.9}\text{S}_{8.3}$ and $\text{Fe}_{4.0}\text{Ni}_{4.9}\text{S}_{8.1}$ have a different shape with the main peak at a higher binding energy near 55 eV and a shoulder on the low binding energy side. This is more consistent with the $3p$ spectrum for Fe^{III} observed in Fe_2O_3 [43, 44] and likely represents oxidation of the iron sites. Additionally, the shape of this peak differs notably between $h\nu = 150$ and 240 eV for both $\text{Fe}_{4.8}\text{Ni}_{3.9}\text{S}_{8.3}$ and $\text{Fe}_{4.0}\text{Ni}_{4.9}\text{S}_{8.1}$, with an increase in the peak at 55 eV for the more surface sensitive spectrum. This shows that the Fe states are somewhat oxidised in $\text{Fe}_{4.8}\text{Ni}_{3.9}\text{S}_{8.3}$ and $\text{Fe}_{4.0}\text{Ni}_{4.9}\text{S}_{8.1}$.

The Ni $3p$ spectra have a peak at 66 eV with a clear shoulder on the high binding energy side around 68 eV. This shape is similar to that seen for NiO [45] and for $\beta\text{-Ni}(\text{OH})_2$ [46], although the Ni-O species have much higher Ni $3p$ binding energies at 75 eV and 76 eV respectively. Like the Fe $3p$ spectra for $\text{Fe}_{4.2}\text{Ni}_{4.4}\text{S}_{8.3}$ and $\text{Fe}_{3.6}\text{Ni}_{5.3}\text{S}_{8.1}$, the Ni $3p$ spectra show no noticeable difference in spectral shape between the $h\nu = 240$ and 150 eV spectra, however the intensity of the Ni $3p$ peak relative to the Fe $3p$ peak (to which the spectra are normalised) vary. For each of the four samples, the intensity of the Ni $3p$ peak is greater in the $h\nu = 240$ eV spectrum than in the $h\nu = 150$ eV spectrum relative to the Fe $3p$ peak. This indicates that in each of the four samples the intensity from Fe species is relatively greater at the surface than in the bulk. This variation in intensity is most notable in $\text{Fe}_{3.6}\text{Ni}_{5.3}\text{S}_{8.1}$, followed by $\text{Fe}_{4.0}\text{Ni}_{4.9}\text{S}_{8.1}$. This shows that for all pentlandite samples the Fe species migrate towards the surface, possibly due to oxidation, but this effect is most noticeable in nickel-rich samples. The shape of the Ni $3p$ peak appears to be consistent between the $h\nu = 240$ and 150 eV spectra for each of the samples, indicating that there are no noticeable changes between the surface and bulk Ni species.

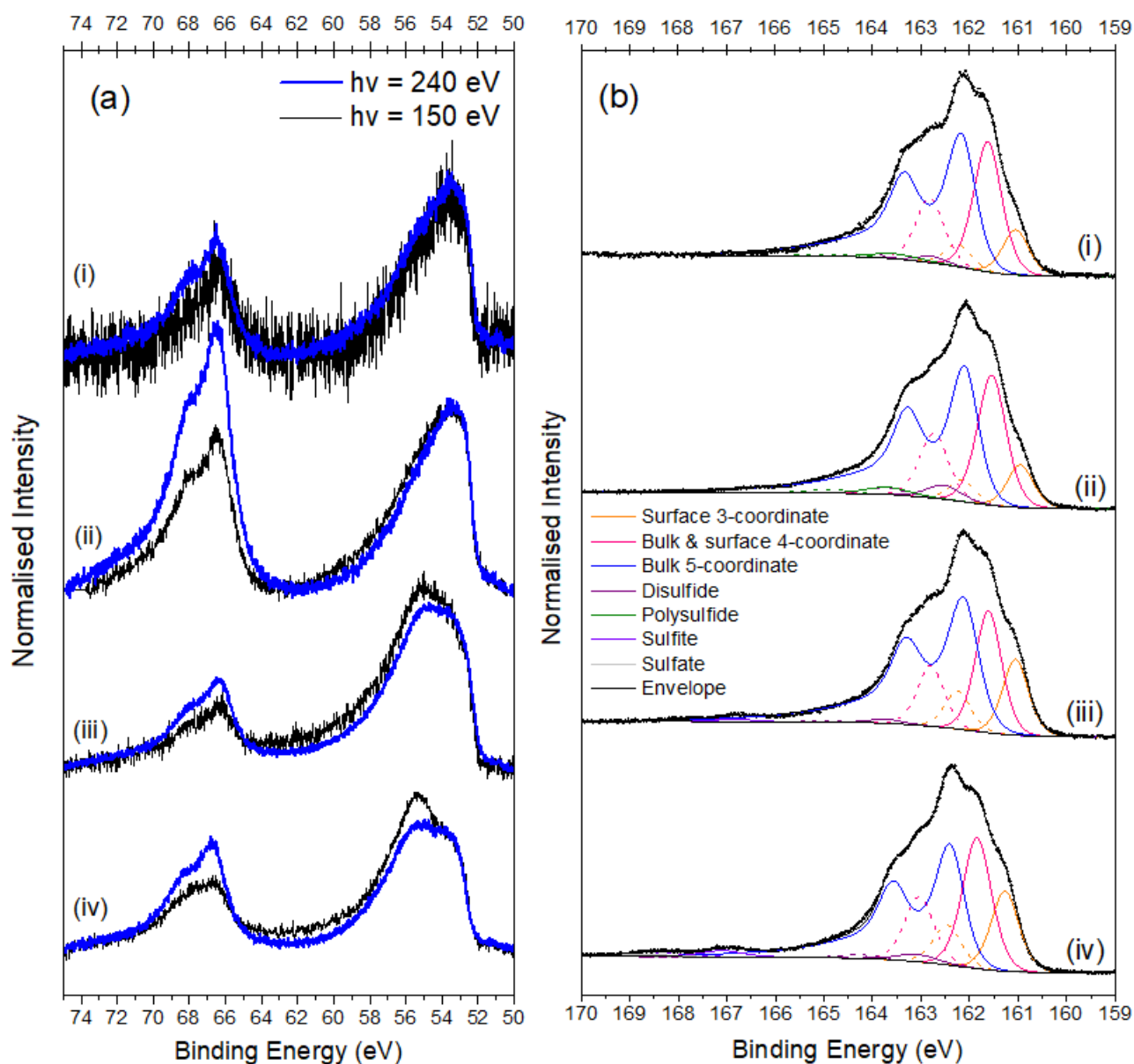


Figure 7.18: (a) Fe/Ni 3p spectra with background removed for $h\nu = 150$ eV and 240 eV, showing changes to Fe and Ni species at the surface. (b) Fitted S 2p spectra showing sulfur species present at the surface. (i) $\text{Fe}_{4.2}\text{Ni}_{4.4}\text{S}_{8.3}$, (ii) $\text{Fe}_{3.6}\text{Ni}_{5.3}\text{S}_{8.1}$, (iii) $\text{Fe}_{4.8}\text{Ni}_{3.9}\text{S}_{8.3}$, (iv) $\text{Fe}_{4.0}\text{Ni}_{4.9}\text{S}_{8.1}$.

The S 2p spectra for all four samples have been fitted using the fitting method devised in Chapter 6, and the fitted spectra are shown in Figure 7.18b, with the binding energy of the $2p_{3/2}$ component of each feature and the quantification of the fitted spectra detailed in Table 7.4. The widths of the S 2p peaks are up to 0.2 eV greater than those observed in the previous chapter due to the increased exit slit width necessary for reasonable flux at that photon energy. Due to the close binding energy of adjacent peaks and the overlap between features, having an accurate fitting method is particularly important to be able to fit and quantify the features in these spectra.

The S 2p spectrum for each sample has been fitted with a $2p_{3/2}$ peak around 161.1 eV, a second peak around 161.6 eV and a main peak at 162.2 eV. These three features are consistent with the surface 3-

coordinate monosulfide, surface and bulk 4-coordinate monosulfide, and bulk 5-coordinate monosulfide species respectively, which were observed for vacuum fractured pentlandite in the previous chapter, and these peaks have therefore been assigned to these features as detailed in Table 7.4. Additional peaks have been fitted to the $\text{Fe}_{4.2}\text{Ni}_{4.4}\text{S}_{8.3}$ spectrum at 162.8 eV and at 163.5 eV and attributed to disulfide and polysulfide components, respectively. The total contribution to the sulfur spectrum from polymerised sulfur species (disulfide + polysulfide) is 4% for this sample, which is significantly less than that observed for the vacuum fractured sample Pn2 shown in the previous chapter (which was approximately 8% for the $h\nu = 260$ eV spectrum). The proportion of 3-, 4- and 5-coordinate species fitted to the S 2*p* spectrum for $\text{Fe}_{4.2}\text{Ni}_{4.4}\text{S}_{8.3}$ is similar to that fitted for Pn2 in the previous chapter, although there is proportionally more 4- and 5-coordinate sulfur and less 3-coordinate monosulfide fitted to $\text{Fe}_{4.2}\text{Ni}_{4.4}\text{S}_{8.3}$ in comparison to the vacuum fractured Pn2.

$\text{Fe}_{3.6}\text{Ni}_{5.3}\text{S}_{8.1}$ also has disulfide and polysulfide components fitted to the S 2*p* spectrum at 162.5 eV and 163.7 eV respectively. Although no other species were fitted, a close inspection of the $\text{Fe}_{3.6}\text{Ni}_{5.3}\text{S}_{8.1}$ spectrum in Figure 7.18b shows that there might be a small inflection in the spectrum around 166 eV, which would indicate the presence of sulfur-oxy species such as sulfite (SO_3^{2-}). If such species are present on this sample, the quantity is so small that their resulting intensity is below the limits of detection and within the noise of the spectrum. A total amount of 7.1% polymerised sulfur is fitted to the $\text{Fe}_{3.6}\text{Ni}_{5.3}\text{S}_{8.1}$ S 2*p* spectrum, which is approximately 3% more than for $\text{Fe}_{4.2}\text{Ni}_{4.4}\text{S}_{8.3}$. The proportion of 3-, 4- and 5-coordinate sulfur species is similar between the two samples, however the increase in polymerised sulfur species in $\text{Fe}_{3.6}\text{Ni}_{5.3}\text{S}_{8.1}$ is accompanied by a slight decrease in the bulk 5-coordinate sulfur species.

The $\text{Fe}_{4.8}\text{Ni}_{3.9}\text{S}_{8.3}$ S 2*p* spectrum has been fitted with a disulfide component at 162.7 eV but no polysulfide component. Almost 1% of the total sulfur fitted is due to a doublet at 166.8 eV which is consistent with sulfur-oxy species and has been attributed to sulfite (SO_3^{2-}) species. The proportion of 3-, 4- and 5-coordinate sulfur is substantially different in $\text{Fe}_{4.8}\text{Ni}_{3.9}\text{S}_{8.3}$ than in $\text{Fe}_{4.2}\text{Ni}_{4.4}\text{S}_{8.3}$ or $\text{Fe}_{3.6}\text{Ni}_{5.3}\text{S}_{8.1}$. While the % contribution from the 5-coordinate bulk monosulfide is similar for $\text{Fe}_{4.2}\text{Ni}_{4.4}\text{S}_{8.3}$ and $\text{Fe}_{3.6}\text{Ni}_{5.3}\text{S}_{8.1}$, the contribution from the 4-coordinate monosulfide is somewhat less, and the contribution from the 3-coordinate surface monosulfide species is substantially greater than that seen for $\text{Fe}_{4.2}\text{Ni}_{4.4}\text{S}_{8.3}$ and $\text{Fe}_{3.6}\text{Ni}_{5.3}\text{S}_{8.1}$. Considering this with the observed oxidation of Fe species, this may indicate an oxidation pathway in which the iron species oxidise at the surface, causing an increase in 3-coordinate under-coordinate surface monosulfide species in addition to sulfur-oxy species.

Chapter 7: Electronic structure of pristine pentlandite surfaces

Fe_{4.0}Ni_{4.9}S₈. has a disulfide but no polysulfide component fitted to the S 2*p* spectrum, and similar to Fe_{4.8}Ni_{3.9}S_{8.3}, has clear evidence of sulfur-oxy species. Although there is no polysulfide component fitted, the binding energy of the fitted disulfide species is necessarily high to provide a good fit to the spectrum. The high binding energy indicates that this doublet may account for disulfide species and longer polysulfide chains, although since this feature only contributes 2.6% to the total fit, the error in this peak may be relatively high. The sulfur-oxy species in this sample are more well resolved and components were fitted for two species at 166.9 eV and 168.5 eV. These components have been attributed to sulfite and sulfate (SO₄²⁻) species respectively, and together they contribute 3.1% of the total S 2*p* fit.

Table 7.4: Binding energy and % contribution to fitted S 2*p* spectrum for each sample.

Species	Pn2	Fe _{4.2} Ni _{4.4} S _{8.3}		Fe _{3.6} Ni _{5.3} S _{8.1}		Fe _{4.8} Ni _{3.9} S _{8.3}		Fe _{4.0} Ni _{4.9} S _{8.1}	
	%	BE (FWHM)	%	BE (FWHM)	%	BE (FWHM)	%	BE (FWHM)	%
Surface 3-coordinate	12.4	161.0 (0.64)	10.8	161.0 (0.63)	10.0	161.1 (0.62)	17.4	161.1 (0.68)	19.0
Surface & bulk 4-coordinate	31.4	161.6 (0.68)	33.5	161.6 (0.69)	33.2	161.6 (0.64)	28.7	161.6 (0.71)	32.3
Bulk 5-coordinate	48.1	162.2 (0.67)	51.7	162.1 (0.65)	49.7	162.1 (0.71)	51.9	162.2 (0.66)	42.9
Disulfide	6.2	162.8 (0.71)	1.8	162.5 (0.82)	4.3	162.7 (0.85)	1.2	162.8 (1.0)	2.6
Polysulfide	1.9	163.5 (1.2)	2.2	163.7 (1.1)	2.8	163.7 (0.85)	0.0	(NA)	0.0
Sulfite	0.0	(NA)	0.0	(NA)	0.0	166.8 (0.93)	0.8	166.9 (1.0)	2.3
Sulfate	0.0	(NA)	0.0	(NA)	0.0	(NA)	0.0	168.5 (1.1)	0.9

An overview of the estimated concentration of species observed in the survey spectra and the observation of impurities and oxidised species is detailed in Table 7.5. The atomic % concentration of species shows 65 – 80% oxygen contribution in each of the samples. This appears to be a large

contribution; however, the sampling depth of the survey spectrum is in the range 15 – 22 Å, and the oxygen species are expected to be concentrated at the surface of the sample. The sampling depth is also important to consider regarding the ratio of nickel and iron species. In most of the samples there is more iron than nickel observed in each survey spectrum, with the exception of Fe_{4.0}Ni_{4.9}S_{8.1}, which has more than twice as much contribution from nickel species than from iron. Even in the iron rich sample, the ratio of iron to nickel observed in the survey spectrum is greater than is expected from the measured stoichiometry. This shows that in the stoichiometric sample, the iron rich sample and in the most nickel rich sample (Fe_{3.6}Ni_{5.3}S_{8.1}), the iron species have accumulated near the surface of each sample. This may account for the observed alteration of iron species in these three samples. In contrast, Fe_{4.0}Ni_{4.9}S_{8.1} shows a greater contribution from nickel than from iron species; the ratio of which is even greater than is expected from the measured stoichiometry, and there may be evidence in the high resolution Ni 3*p* spectrum for changes to the Ni species at the surface.

Table 7.5: Overview of observations of survey and core level spectra for pentlandite samples.

Stoichiometry	At% conc.				SiO ₂	Oxidised		S _x O _y ²⁻
	S 2 <i>p</i>	Ni 3 <i>p</i>	Fe 3 <i>p</i>	O 2 <i>s</i>		Fe	Ni	
Fe _{4.2} Ni _{4.4} S _{8.3}	12.4	2.4	7.5	77.7	Y	N	N	N
Fe _{3.6} Ni _{5.3} S _{8.1}	16.0	4.9	6.2	72.9	N	N	N	N*
Fe _{4.8} Ni _{3.9} S _{8.3}	9.6	2.4	8.8	79.2	N	Y	N	Y
Fe _{4.0} Ni _{4.9} S _{8.1}	21.0	8.8	3.8	66.4	N	Y	Y**	Y

* The S 2*p* spectrum for Fe_{3.6}Ni_{5.3}S_{8.1} shows a small inflection between 166 – 167 eV binding energy, which may indicate sulfite species. However, the intensity of this feature is so small that it cannot be accurately fitted, therefore it is not reported in this table or in the quantification of sulfur features.

** As discussed in the text above, there may be some alteration of the Ni sites in this sample, but the change in spectral shape is small and may be due to the background removal.

Considering the observed oxidation and surface alteration of the four samples, the analysis of the valence band spectra for these samples will follow the proposed narrative: A comparison of the valence band spectra for Fe_{4.2}Ni_{4.4}S_{8.3} and Fe_{3.6}Ni_{5.3}S_{8.1} will highlight if there is any contribution to the valence band photoemission spectrum due to the presence of SiO₂ species. Furthermore, the variation in stoichiometry between these two samples may reveal localised regions of the valence band with significant Fe or Ni contributions. Comparing the valence band spectra for Fe_{3.6}Ni_{5.3}S_{8.1} and Fe_{4.8}Ni_{3.9}S_{8.3} will show the effect on the valence band due to the oxidation of surface Fe states and the emergence of sulfite species. Finally, a comparison of Fe_{4.8}Ni_{3.9}S_{8.3} and Fe_{4.0}Ni_{4.9}S_{8.1} will show

the effect on the valence band of additional oxidation resulting in the presence of sulfate species in addition to sulfite species, and the possible oxidation of Ni species in addition to oxidised Fe species at the surface.

7.3.4 Comparison of $\text{Fe}_{4.2}\text{Ni}_{4.4}\text{S}_{8.3}$ and $\text{Fe}_{3.6}\text{Ni}_{5.3}\text{S}_{8.1}$

The photoelectron spectrum of the valence band region for $\text{Fe}_{4.2}\text{Ni}_{4.4}\text{S}_{8.3}$ is shown in Figure 7.19a also with the low energy valence band spectrum of Pn1 from the previous chapter (dotted line). Each of these spectra have been normalised to constant flux, therefore the overall intensity of each spectrum is determined by the photoionization cross section of the subshells that contribute to the spectrum. The photoionization cross section of the Fe, Ni and S atomic valence subshells decrease at a similar rate from $h\nu = 150$ eV to 240 eV, as shown in Figure 7.16. Accordingly, the overall intensity of the valence band spectra shown in Figure 7.19a decrease with increasing photon energy. As previously discussed, the upper valence band consists of a main peak at 1.1 eV, with a shoulder on the Fermi energy side around 0.5 eV which contributes to significant intensity near the Fermi energy. The upper valence band is generally attributed largely to metal $3d$ states, and the resonant valence band section showed that the peak at 1.1 eV has strong Ni character. There is a slight shoulder feature observable on the high energy side of the main peak around 2 eV in the $h\nu = 150$ eV spectrum, but is not clearly visible in the $h\nu = 240$ eV spectrum. The origin of this feature is currently unclear. The lower valence band consists of a broad feature which peaks around 5 eV and extends to 10 eV, which is largely attributed to S $3p$ valence states [8], however the resonant valence band section showed evidence of both nickel and iron states in this region. There is a local minimum at 3 eV separating the upper valence band, however the relatively large intensity at this local minimum indicates that there is significant overlap between the metal $3d$ and S $3p$ states. There is also a small feature around 14 – 16 eV due to S $3s$ states [7, 8], but as previously observed in the survey spectra for $\text{Fe}_{4.2}\text{Ni}_{4.4}\text{S}_{8.3}$, this feature is somewhat overshadowed by the O $2s$ photoelectrons which form a broad peak around 25 eV. These O $2s$ photoelectrons are contributing largely to the background observed in the valence band spectrum seen in Figure 7.19a.

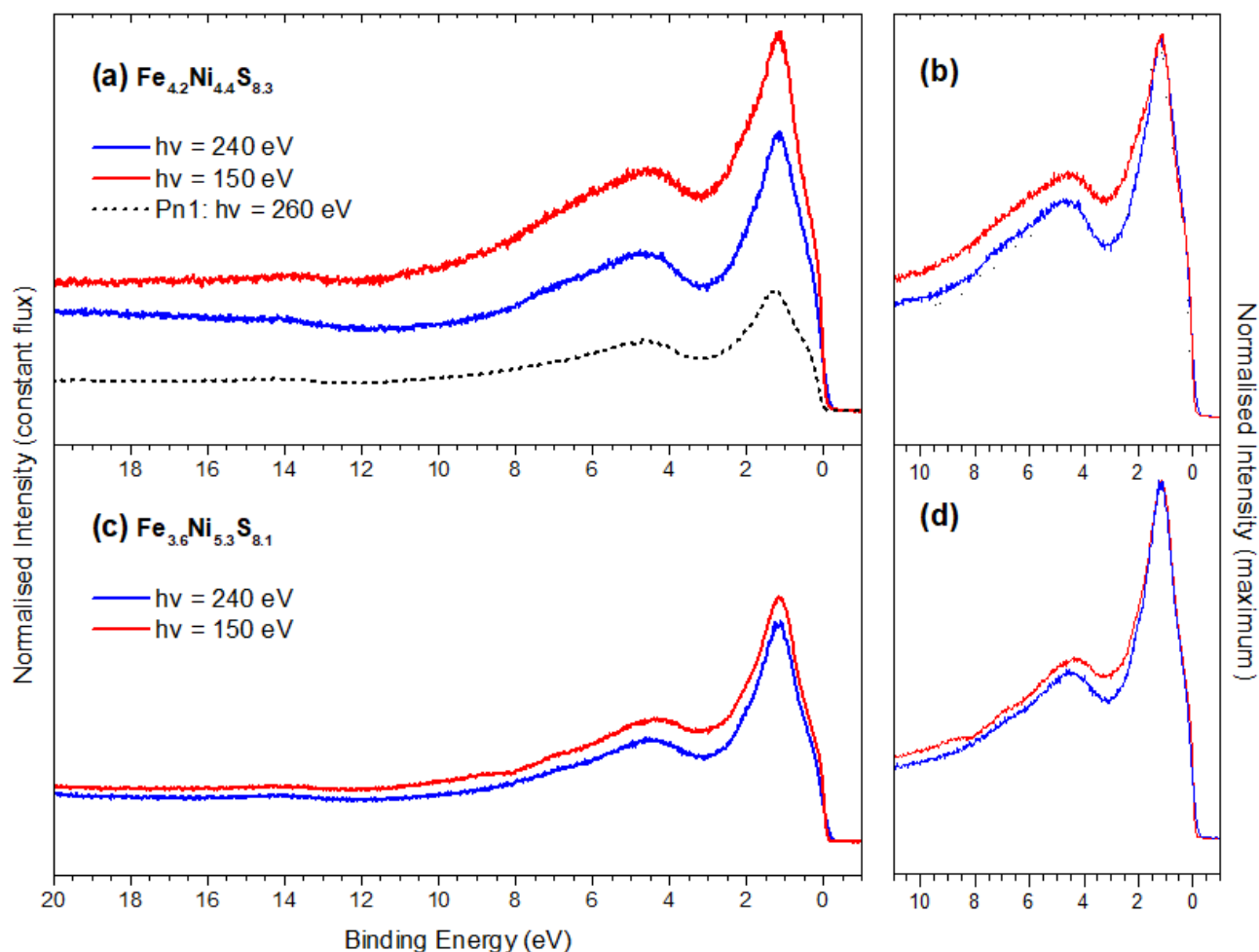


Figure 7.19: Photoemission spectra in the valence band region for (a) $\text{Fe}_{4.2}\text{Ni}_{4.4}\text{S}_{8.3}$ normalised to constant flux and (b) normalised to the main peak, and (c) $\text{Fe}_{3.6}\text{Ni}_{5.3}\text{S}_{8.1}$ normalised to constant flux and (d) normalised to the main peak.

The spectra shown in Figure 7.19b are the same as those shown in Figure 7.19a but have been normalised to the main peak at 1.1 eV such that the spectra can be directly compared. No change in shape is observable in the upper valence band, but there is additional intensity in the $h\nu = 150$ eV spectrum in the lower valence band at energies above 2 eV. There are two possible explanations for this difference in intensity. The first explanation, based on the photoionization cross sections shown in Figure 7.16, is that the region above 2 eV can be attributed to oxygen species, since the cross section for atomic O 2p states is relatively higher than the Fe, Ni and S valence states at $h\nu = 150$ eV in comparison to $h\nu = 240$ eV. The second explanation is that the formation of disulfide and polysulfide species causes an increase in the photoionization cross section of sulfur states at lower photon energies, thus causing an increase in intensity in this region of the valence band due to polymerised sulfur species.

The latter hypothesis can be tested by comparing the valence band spectra of the two vacuum fractured samples of the previous chapter, only one of which has polymerised sulfur at the surface.

This comparison is made in Figure 7.20. Figure 7.20a shows a series of valence band spectra for a vacuum fractured pentlandite which has no surface polymerised sulfur (Pn1 from Chapter 6), while Figure 7.20b shows similar valence band spectra for a vacuum fractured pentlandite sample with up to 8% of the sulfur signal at $h\nu = 260$ eV contributed to by polymerised sulfur (Pn2 from Chapter 6). Each of these spectra have been normalised to the main peak at 1.1 eV, and the intensity of each region is therefore being compared to the main peak.

The valence band spectra in Figure 7.20a, for the sample with no polymerised sulfur, show greater intensity in the region between 3 – 7 eV for the higher photon energies. This is due to the decrease in Fe and Ni 3d photoionization cross section relative to the S 3p orbitals. In contrast, the valence band spectra in Figure 7.20b, for the sample which did show polymerised sulfur, have increased intensity in the 3 – 6 eV region for the lower photon energy spectra, indicating that the polymerised sulfur species have a relatively higher photoionization cross section at lower photon energies than monosulfide species. Considering the mixing of the S 3p states with Fe and Ni states in this region, it is reasonable that the photoionization cross section of disulfide and polysulfide states would follow the S 3p atomic cross section more closely than the monosulfide species. Therefore, the increased intensity in the $\text{Fe}_{4.2}\text{Ni}_{4.4}\text{S}_{8.3}$ $h\nu = 150$ eV spectrum in Figure 7.19b, at least in the region 3 – 6 eV, can be attributed to disulfide and polysulfide species at the surface of the sample.

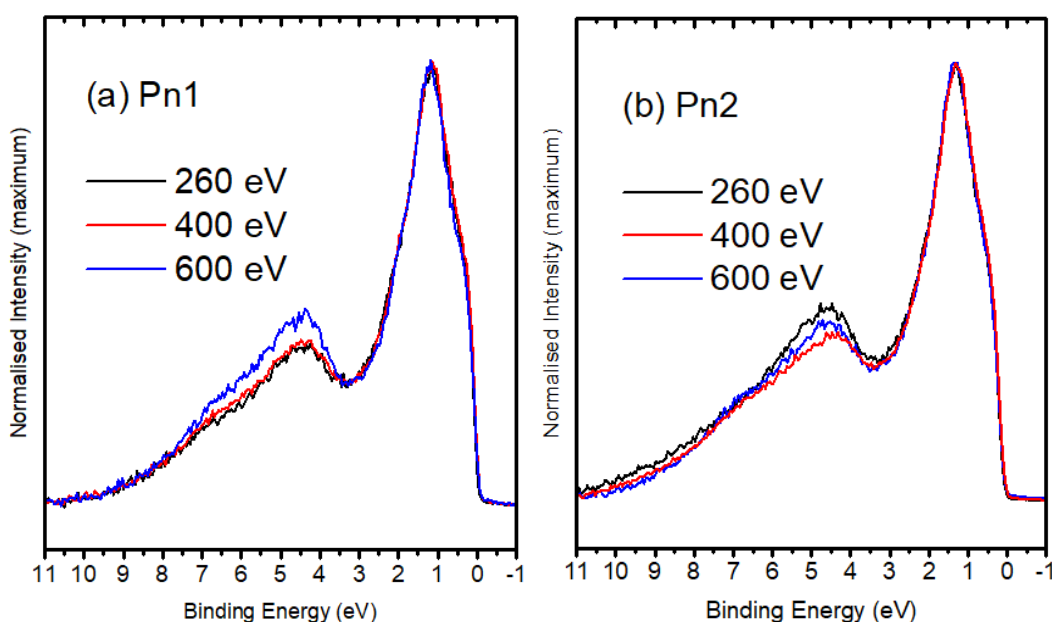


Figure 7.20: Photoelectron spectra of the valence band region of (a) Pn1 and (b) Pn2, normalised to the main peak at 1.1 eV. The change in the relative intensities of the lower valence band between the two samples is attributed to polymerised sulfur.

The features in the valence band spectrum for $\text{Fe}_{3.6}\text{Ni}_{5.3}\text{S}_{8.1}$ shown in Figure 7.19c are similar to those of $\text{Fe}_{4.2}\text{Ni}_{4.4}\text{S}_{8.3}$, however there appears to be some additional structure between 5 – 10 eV, which is not observable in $\text{Fe}_{4.2}\text{Ni}_{4.4}\text{S}_{8.3}$. The intensity ratio of the upper and lower valence band regions also appears to be greater in the $\text{Fe}_{3.6}\text{Ni}_{5.3}\text{S}_{8.1}$ sample compared to $\text{Fe}_{4.2}\text{Ni}_{4.4}\text{S}_{8.3}$. This is likely to be due to the SiO_2 contamination in $\text{Fe}_{4.2}\text{Ni}_{4.4}\text{S}_{8.3}$ which is expected to contribute to the background [47], thereby increasing the apparent intensity of the lower valence band. The fine structure which is observed at 5 – 10 eV for $\text{Fe}_{3.6}\text{Ni}_{5.3}\text{S}_{8.1}$ may also be overshadowed by minor contributions to the valence band in this region from SiO_2 valence states.

The valence band spectra taken with photon energies in the range of $h\nu = 30 - 50$ eV are shown for $\text{Fe}_{4.2}\text{Ni}_{4.4}\text{S}_{8.3}$ and $\text{Fe}_{3.6}\text{Ni}_{5.3}\text{S}_{8.1}$ in Figure 7.21a and Figure 7.21b respectively. The valence band spectra for $\text{Fe}_{4.2}\text{Ni}_{4.4}\text{S}_{8.3}$ show some weak structure in the upper valence band, whereas most of the intensity of the spectrum is located between 4 – 11 eV. The intensity of the spectrum is seen to increase with an increase in photon energy from $h\nu = 30$ eV to $h\nu = 50$ eV. This generally follows the shape of the Fe, Ni and S valence orbital cross sections, shown in the inset to Figure 7.16. There is a minimum in the photoionization cross section for S $3p$ states at 30 eV photon energy, however the valence band spectra in Figure 7.21a are all seen to increase with increasing photon energy in the S $3p$ region. This shows that the states which are expected to be strongly S $3p$ -like are hybridised with Fe and Ni states enough to eliminate this feature in the cross section. The intensity of each spectrum in the region above 11 eV varies unpredictably with photon energy, however this is expected to be due to the background caused by the SiO_2 contamination.

The valence band spectrum for $\text{Fe}_{3.6}\text{Ni}_{5.3}\text{S}_{8.1}$ also shows an increase in the intensity of the upper valence band with increasing photon energy, which is particularly prominent in the $h\nu = 50$ eV spectrum. Three of the four $\text{Fe}_{3.6}\text{Ni}_{5.3}\text{S}_{8.1}$ spectra curiously intersect at a point around 4 eV binding energy, where the intensity at lower energies (the upper valence band) increase with an increase in photon energy, but at higher binding energies the reverse is true. In the lower valence band at energies about 5 eV, the intensity of each spectrum is similar, but decreases slightly with increase in photon energy. There are two possible explanations for this behaviour in the valence band. The first is that the increase in relative cross section at lower photon energies may be indicative of the cross section of S $3p$ states for polymerised sulfur. The second explanation is that the slightly higher relative cross section for Fe $3d$ states (relative to Ni $3d$ states) may be represented in the cross over point in Figure 7.21b. This assertion supports the conclusion from the resonant valence band section which showed that the upper valence band has strong Ni $3d$ character, and indicates that the lower valence band region has more Fe $3d$ - and S $3p$ -like character from around 4 eV and beyond.

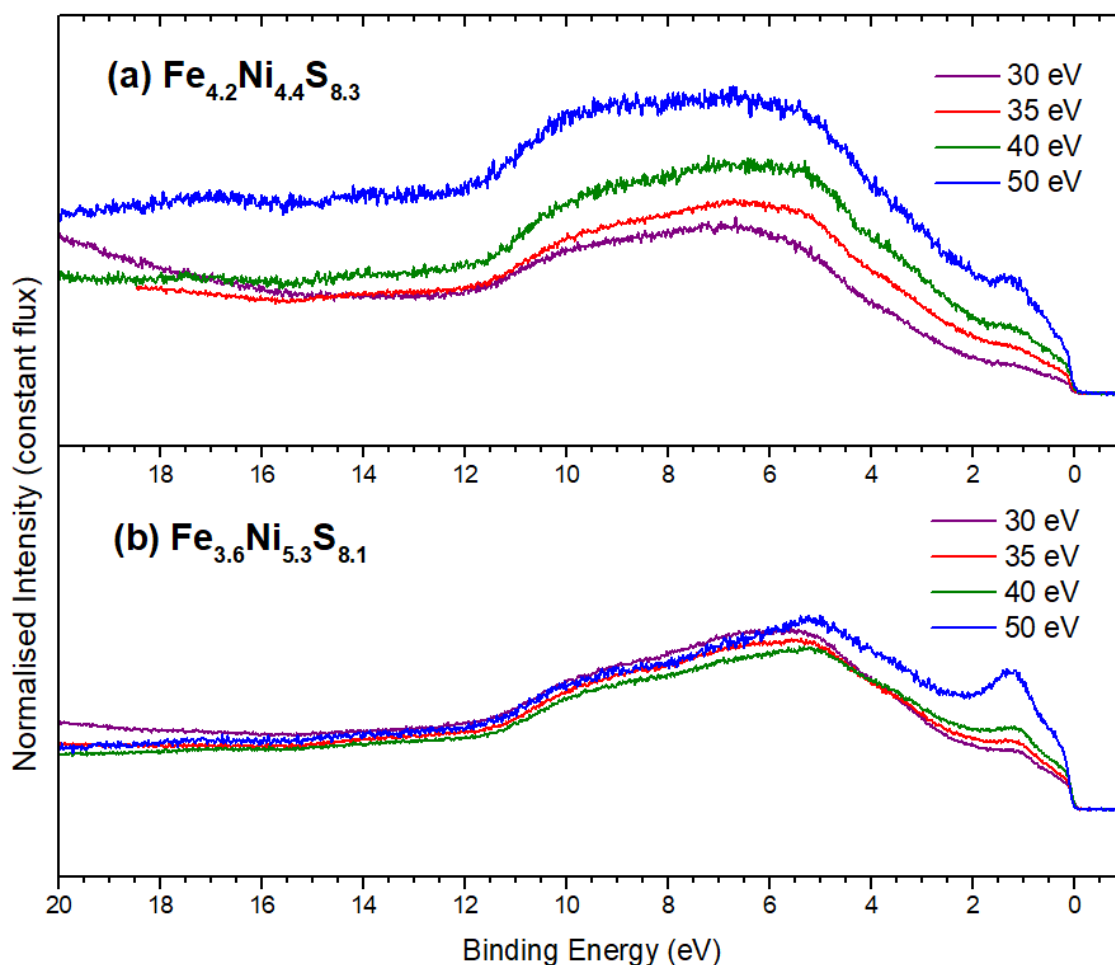


Figure 7.21: Photoemission spectra in the valence band region for (a) $\text{Fe}_{4.2}\text{Ni}_{4.4}\text{S}_{8.3}$ and (b) $\text{Fe}_{3.6}\text{Ni}_{5.3}\text{S}_{8.1}$ collected with $h\nu = 30, 35, 40,$ and 50 eV. The background in the $\text{Fe}_{4.2}\text{Ni}_{4.4}\text{S}_{8.3}$ valence band spectra is attributed to Si contamination.

1.1.1 Comparison of $\text{Fe}_{3.6}\text{Ni}_{5.3}\text{S}_{8.1}$ and $\text{Fe}_{4.8}\text{Ni}_{3.9}\text{S}_{8.3}$ and $\text{Fe}_{4.0}\text{Ni}_{4.9}\text{S}_{8.1}$

Figure 7.22 shows the valence band spectra collected with $h\nu = 150$ eV and 240 eV for $\text{Fe}_{3.6}\text{Ni}_{5.3}\text{S}_{8.1}$, $\text{Fe}_{4.8}\text{Ni}_{3.9}\text{S}_{8.3}$ and $\text{Fe}_{4.0}\text{Ni}_{4.9}\text{S}_{8.1}$. The key differences between these samples that were previously highlighted are firstly the stoichiometries of these samples. $\text{Fe}_{4.8}\text{Ni}_{3.9}\text{S}_{8.3}$ has a greater proportion of Fe to Ni in the bulk stoichiometry. $\text{Fe}_{3.6}\text{Ni}_{5.3}\text{S}_{8.1}$ and $\text{Fe}_{4.0}\text{Ni}_{4.9}\text{S}_{8.1}$ have a greater proportion of nickel to iron in the bulk stoichiometry, and $\text{Fe}_{3.6}\text{Ni}_{5.3}\text{S}_{8.1}$ has a greater proportion of nickel than $\text{Fe}_{4.0}\text{Ni}_{4.9}\text{S}_{8.1}$. The second difference between these samples is that $\text{Fe}_{3.6}\text{Ni}_{5.3}\text{S}_{8.1}$ shows no oxidation of the Fe states at the surface, while $\text{Fe}_{4.8}\text{Ni}_{3.9}\text{S}_{8.3}$ and $\text{Fe}_{4.0}\text{Ni}_{4.9}\text{S}_{8.1}$ do. The final notable difference is in the sulfur species observed for these samples. The S $2p$ spectrum for $\text{Fe}_{3.6}\text{Ni}_{5.3}\text{S}_{8.1}$ was fitted with disulfide and polysulfide species in addition to the monosulfide species observed for vacuum fractured pentlandite. The S $2p$ spectra for $\text{Fe}_{4.8}\text{Ni}_{3.9}\text{S}_{8.3}$ and $\text{Fe}_{4.0}\text{Ni}_{4.9}\text{S}_{8.1}$ showed sulfite species and also sulfate species in $\text{Fe}_{4.0}\text{Ni}_{4.9}\text{S}_{8.1}$. $\text{Fe}_{4.8}\text{Ni}_{3.9}\text{S}_{8.3}$ and $\text{Fe}_{4.0}\text{Ni}_{4.9}\text{S}_{8.1}$ were also fitted with a greater ratio

of 3- and 4-coordinate species to the bulk 5-coordinate monosulfide species, in comparison to the $\text{Fe}_{4.2}\text{Ni}_{4.4}\text{S}_{8.3}$, $\text{Fe}_{3.6}\text{Ni}_{5.3}\text{S}_{8.1}$ and vacuum fractured samples.

The valence band spectra for the three samples shown in Figure 7.22 have the same general shape as has been seen for all previous pentlandite valence band spectra presented. There are however two notable differences observable in these spectra. The first is the appearance of a shoulder at 2 eV in the $\text{Fe}_{4.8}\text{Ni}_{3.9}\text{S}_{8.3}$ $h\nu = 150$ eV spectrum, which was also observed in the $\text{Fe}_{4.2}\text{Ni}_{4.4}\text{S}_{8.3}$ $h\nu = 150$ eV spectrum, but not in any other spectra presented in this chapter or for the vacuum fractured pentlandite samples in the previous chapter. The second key difference is the change in relative intensity of the upper and lower valence band regions between the samples.

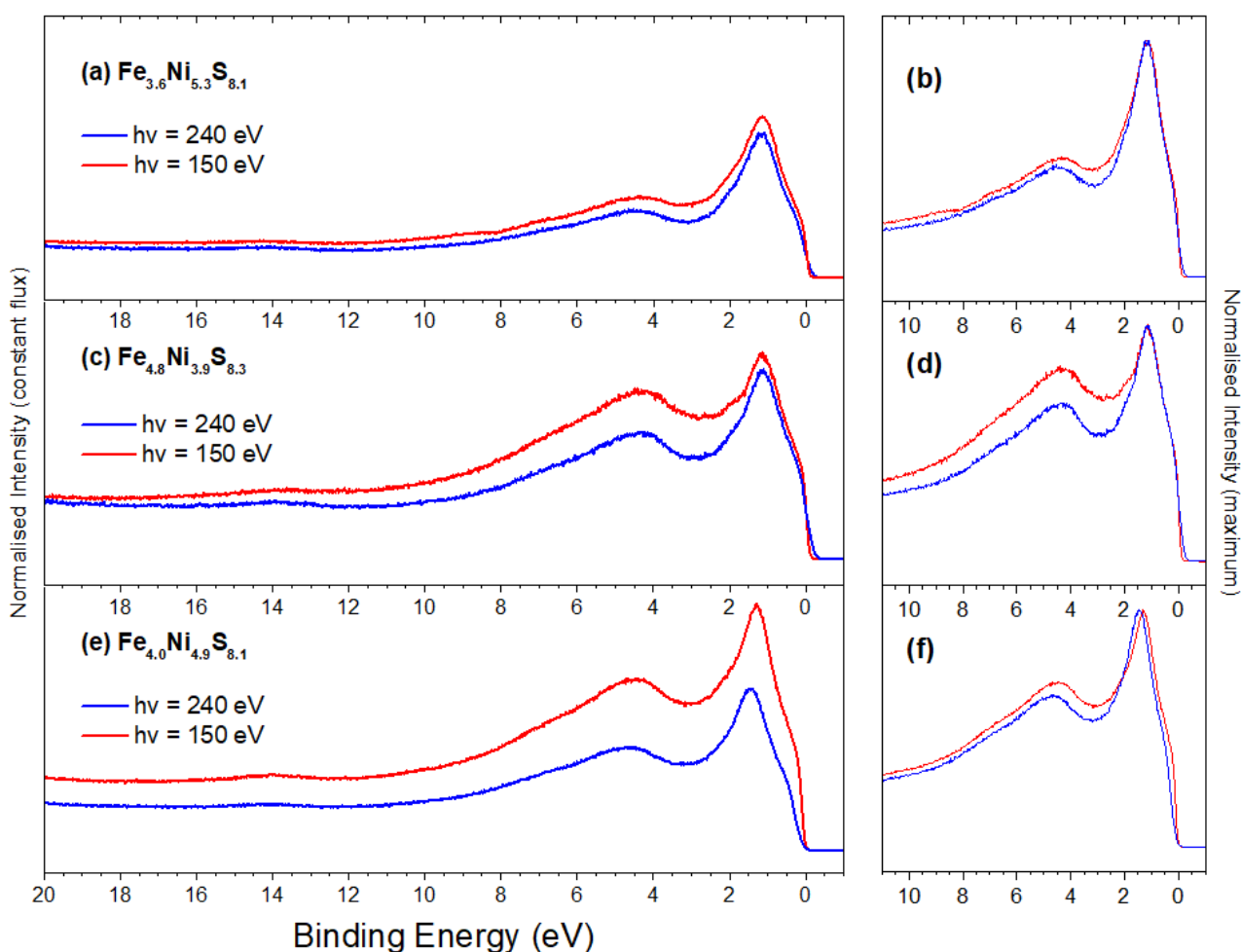


Figure 7.22: Pentlandite photoemission spectra in the valence band region for (a) $\text{Fe}_{3.6}\text{Ni}_{5.3}\text{S}_{8.1}$ normalised to constant flux and (b) normalised to the main peak, (c) $\text{Fe}_{4.8}\text{Ni}_{3.9}\text{S}_{8.3}$ normalised to constant flux and (d) normalised to the main peak, and (e) $\text{Fe}_{4.0}\text{Ni}_{4.9}\text{S}_{8.1}$ normalised to constant flux and (f) normalised to the main peak.

7.3.4.1 Shoulder at 2 eV

In the $\text{Fe}_{4.8}\text{Ni}_{3.9}\text{S}_{8.3}$ $h\nu = 150$ eV spectrum there is a shoulder on the high binding energy side of the upper valence band peak at around 2 eV. Upon close inspection, this shoulder is likely contributing to the broadening of the upper valence band peak in the $h\nu = 240$ eV spectrum, however it is less definitive in this spectrum. Additionally, by close inspection of the $\text{Fe}_{4.0}\text{Ni}_{4.9}\text{S}_{8.1}$ spectrum in the same region, this same feature may also be visible for $\text{Fe}_{4.0}\text{Ni}_{4.9}\text{S}_{8.1}$. Since both $\text{Fe}_{4.8}\text{Ni}_{3.9}\text{S}_{8.3}$ and $\text{Fe}_{4.0}\text{Ni}_{4.9}\text{S}_{8.1}$ showed evidence of oxidised iron species, the feature at 2 eV in the valence band spectrum is attributed to oxidised iron states. This feature is most visible in the $h\nu = 150$ eV spectra because the photoionization cross section for oxygen valence orbitals (shown in Figure 7.16) is higher at 150 eV than 240 eV in comparison to Fe, Ni and S valence orbitals. Considering the peak at 1.1 eV has a strong Ni-like character, as shown previously in this chapter, it is reasonable that the feature at 2 eV is less prominent in $\text{Fe}_{4.0}\text{Ni}_{4.9}\text{S}_{8.1}$, since the contribution from Fe states will generally be less than for $\text{Fe}_{4.8}\text{Ni}_{3.9}\text{S}_{8.3}$ due to the stoichiometry.

7.3.4.2 Relative intensity of upper and lower valence band regions

A difference in relative intensity of the upper and lower valence band regions is seen for the two spectra collected for each sample, and the strength of this effect is seen to differ between the three samples shown in Figure 7.22. The spectra in Figure 7.22(b, d & f) are normalised to the peak at 1.1 eV and best show the relative intensity between the upper and lower valence band regions for the spectra for all three samples. The lower valence band region is relatively higher in the $h\nu = 150$ eV spectrum for all three samples, although the effect is greatest in $\text{Fe}_{4.8}\text{Ni}_{3.9}\text{S}_{8.3}$. The effect appears to be similar in both $\text{Fe}_{3.6}\text{Ni}_{5.3}\text{S}_{8.1}$ and $\text{Fe}_{4.0}\text{Ni}_{4.9}\text{S}_{8.1}$, although the latter has a relatively more intense lower valence band than $\text{Fe}_{3.6}\text{Ni}_{5.3}\text{S}_{8.1}$ in both spectra.

Since $\text{Fe}_{3.6}\text{Ni}_{5.3}\text{S}_{8.1}$ has the least ratio of Fe to Ni in the bulk stoichiometry, followed by $\text{Fe}_{4.0}\text{Ni}_{4.9}\text{S}_{8.1}$, this effect can be attributed to the differing stoichiometries of these samples. The trend observed is that the samples with the greater ratio of Fe have a greater intensity in the lower valence band, especially in the $h\nu = 150$ eV spectrum. In $\text{Fe}_{4.2}\text{Ni}_{4.4}\text{S}_{8.3}$ it was postulated that the increase in the lower valence band region was either due to polymerised sulfur, or due to states of more Fe $3d$ character. Since $\text{Fe}_{4.8}\text{Ni}_{3.9}\text{S}_{8.3}$ and $\text{Fe}_{4.0}\text{Ni}_{4.9}\text{S}_{8.1}$ were observed to have comparatively little polymerised sulfur species, the intensity of the lower valence band region is attributed to a higher proportion of Fe states due to the stoichiometry of the samples. A second possibility is that the increase in relative intensity of the lower valence band is related to the increased ratio of 3- and 4-coordinate species in comparison to the 5-coordinate species for $\text{Fe}_{4.8}\text{Ni}_{3.9}\text{S}_{8.3}$ and $\text{Fe}_{4.0}\text{Ni}_{4.9}\text{S}_{8.1}$, and that these species have a greater contribution to the lower valence band. This is possible, since the results from the resonant

photoemission spectroscopy indicated a mixing of Fe 3*d* states with 4-coordinate sulfur 3*d* states in the lower valence band region. The strength of these mixed Fe 3*d* and 4-coordinate sulfur states would be increased both by the increase in 4-coordinate species and the increase in the ratio of Fe to Ni in the sample's stoichiometry.

Valence band spectra of the Fe_{3.6}Ni_{5.3}S_{8.1}, Fe_{4.8}Ni_{3.9}S_{8.3}, and Fe_{4.0}Ni_{4.9}S_{8.1} collected with $h\nu = 30, 35, 40$ and 50 eV are shown in Figure 7.23a, b, and c respectively. The general shape of the valence band spectra between Fe_{3.6}Ni_{5.3}S_{8.1} and Fe_{4.8}Ni_{3.9}S_{8.3} is the same, with a relatively low intensity upper valence band peaking just above 1 eV, followed by the higher intensity lower valence band extending from 3 – 12 eV, with a peak around 5.5 eV. The noticeable difference between the Fe_{3.6}Ni_{5.3}S_{8.1} and Fe_{4.8}Ni_{3.9}S_{8.3} valence band spectra in Figure 7.23 is the relative heights of the upper and lower valence band regions. The lower valence band has relatively higher intensity in the Fe_{4.8}Ni_{3.9}S_{8.3} spectra, which is consistent with previously made assertions that the lower valence band has strong Fe 3*d* character. There also appears to be a 'crossover point' for the spectra at around 5 eV in the Fe_{4.8}Ni_{3.9}S_{8.3} spectra, such as was observed and previously discussed for the Fe_{3.6}Ni_{5.3}S_{8.1} spectra. Below this crossover point, the lower photon energy spectra have lower intensity, while above this point, the lower photon energy spectra have a higher intensity than the higher photon energy spectra. The existence of this crossover point has been attributed to the change in the valence band spectrum from states of strong Ni 3*d* character in the upper valence band, to states of stronger Fe 3*d* character in the lower valence band. This point is less clear in the Fe_{4.8}Ni_{3.9}S_{8.3} spectra, which can be attributed to the oxidation of Fe states which was observed in the core level spectra.

The shapes of the valence band spectra for Fe_{4.0}Ni_{4.9}S_{8.1} are strikingly different to that of the previous samples. The lower valence band between the Fermi energy and up to 2 eV is subdued in comparison to the previous samples. The lower valence band still has a peak just above 5 eV, but this peak is significantly broader than that seen for previous samples. In addition, there is a strong shoulder at 10 eV that is prominent in all of the Fe_{4.0}Ni_{4.9}S_{8.1} spectra and a shoulder at 3 eV in the $h\nu = 50$ eV spectrum in particular. There is an emergence of sulfate species at the surface of Fe_{4.0}Ni_{4.9}S_{8.1}, which other pentlandites have not shown. Due to the striking difference in the valence band shape, the peak at 10 eV is attributed to the sulfate species, which have most likely bonded to Fe sites. This is consistent with previously published experimental valence band spectra of iron sulfate species, where a significant density of states was observed in the region 3 – 15 eV, with the greatest intensity at 10 eV [48]. Since the density of states for sulfate species are expected to contribute to the entire lower valence band region, the shoulder at 3 eV is also attributed to sulfate species. It is reasonable that these features are most observable in the $h\nu = 50$ eV spectrum, as there is a local maximum in the

photoionization cross section of S 3*p* atomic subshells, while the O 2*p* and Fe 3*d* cross sections are still high (inset to Figure 7.16). Therefore, the combination of these cross sections would likely peak around 50 eV and it is conceivable that the density of iron sulfate states would be most observable in the $h\nu = 50$ eV spectrum.

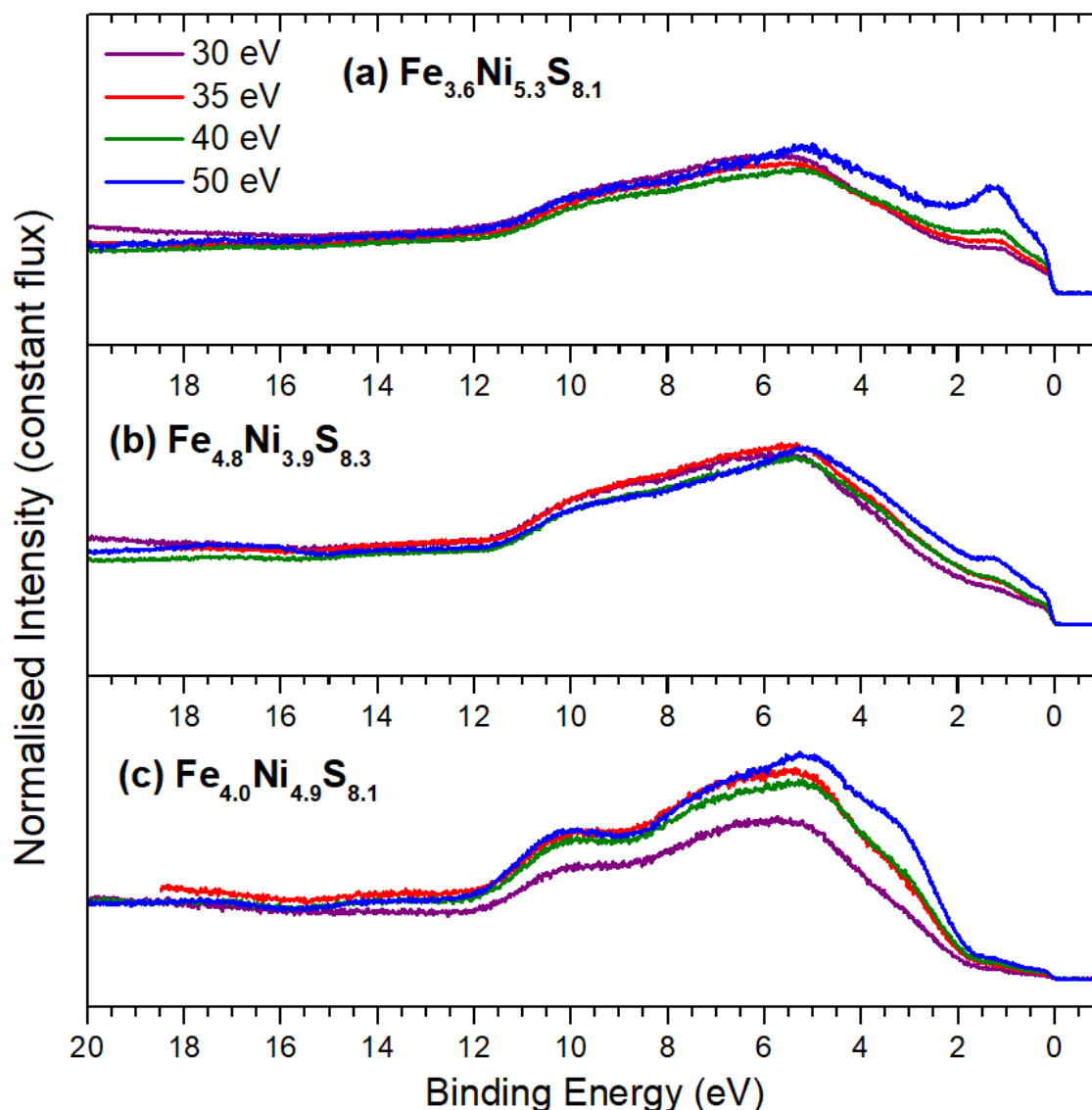


Figure 7.23: Photoemission spectra in the valence band region of (a) $\text{Fe}_{3.6}\text{Ni}_{5.3}\text{S}_{8.1}$, (b) $\text{Fe}_{4.8}\text{Ni}_{3.9}\text{S}_{8.3}$ and (c) $\text{Fe}_{4.0}\text{Ni}_{4.9}\text{S}_{8.1}$ collected with $h\nu = 30, 35, 40,$ and 50 eV show a striking difference between the $\text{Fe}_{4.0}\text{Ni}_{4.9}\text{S}_{8.1}$ valence band spectrum, which is largely attributed to sulfate species, and the $\text{Fe}_{3.6}\text{Ni}_{5.3}\text{S}_{8.1}$ and $\text{Fe}_{4.8}\text{Ni}_{3.9}\text{S}_{8.3}$ valence band spectra.

7.4 Conclusion

The results presented in this section are the first known experimental investigation of the electronic structure of pentlandite. The valence band spectrum of Pn1 from Chapter 6 has been recently published [11], and there have been a few calculations relating to pentlandite's valence band [7-10]. However, this chapter has been the first investigation to attempt to verify such calculations and

thoroughly investigate the features in the valence band spectrum. Resonant photoemission spectroscopy was used to isolate the states contributing to the valence band spectrum that originated from Fe or Ni atoms, and to provide insight into the nature of those states. This was subsequently verified by valence band photoemission spectroscopy using a low incident photon energy for a series of synthetic pentlandite samples with varied stoichiometries.

The upper valence band in the photoemission spectrum was shown to be largely of Ni character. Resonant photoemission spectroscopy showed some coherence between the upper valence band states and the Ni Auger-like deexcitation which follows the X-ray absorption process. The photoelectron spectra in the valence band region for the samples of varied stoichiometry also showed the upper valence band to have strong nickel character, as this feature was seen to be more intense in samples with a greater ratio of Ni to Fe in their measured stoichiometry. The upper valence band was also observed to have a shoulder around 2 eV for samples which showed evidence of oxidation of the Fe states at the surface. The feature at 2 eV was therefore attributed to oxidised Fe species.

The lower valence band has been calculated to have strong contributions from S 3*p* states [8]. The observation of X-ray absorption spectra revealed a ligand to metal charge-transfer state between the S and Fe atoms. Resonant photoemission spectroscopy subsequently showed the Fe 3*d*-derived states to overlap with S 3*p* states in the lower valence band at 4.4 eV. This photoemission feature was seen to be incoherent with Auger decay channel due to the charge-transfer between Fe and S valence states. Ni 3*d* derived states were also observed in the lower valence band, but are sufficiently localized for there to be coherence between the photoemission and deexcitation (Auger) channels, evident by their resonance behaviour. These Ni states therefore cannot be attributed to a ligand to metal charge-transfer.

The photoelectron study of pentlandites with varied stoichiometries showed that the contributions to the lower valence band have more Fe character than the upper valence band. Polymerised sulfur such as disulfide and polysulfide species were also observed to contribute to the lower valence band, especially in the region 3 – 6 eV.

While there were both Fe and Ni states observed in the lower valence band for all samples, the photoelectron study of pentlandites with varied stoichiometries showed that the lower valence band had stronger Fe character. The surface of one sample had oxidised sufficiently for sulfate species to be observed in the S 2*p* spectrum. These sulfate species contributed significantly to the low photon energy valence band spectra, especially at 3 eV and 10 eV. This is an original contribution to

knowledge in this field, as calculations of pentlandite's valence band have not been able to determine with clarity the band structure or the atomic origin of features in the valence band. The presentation of these valence band spectra and the conclusions regarding the origin of some features will inform and assist future calculations of pentlandite's electronic structure.

These findings have implications for the interpretation of core-level photoelectron spectra and for the reactions that take place on pentlandite's surface. Previous literature regarding pentlandite photoelectron spectra has argued that core level spectra should be fitted with Doniach-Sunjic tails to account for the metallic nature of pentlandite. This is assumed due to the short bond length between neighbouring tetrahedral cations. The previous chapter offered a counter argument; that the broad high binding energy tail of the S 2*p* spectrum was due to a ligand to metal charge-transfer state in the valence band, causing a number of final states that affect the core-level photoelectron spectrum. The evidence presented by resonant photoemission spectroscopy has shown that the charge-transfer state exists between the Fe and S atoms; specifically likely to be the tetrahedral Fe bonded to 4-coordinate 'linking' sulfur atoms. It is this charge-transfer final state which is contributing to the broad high binding energy tail in the S 2*p* photoelectron spectrum. Additionally, the Ni states were seen to be weakly localised such that they show some true resonance in the resonant photoemission spectra. This is reflected in the pentlandite Ni 2*p* spectra which show more discrete multiplet structure rather than Doniach-Sunjic tails expected from a many electron final state.

The implications of these valence band studies also extend to the reactions that occur on the surface of pentlandite. Since some of the samples of varied stoichiometry showed evidence of some oxidation, an insight into the initial stages of oxidation could be found. By observing core-level spectra, iron is seen to oxidise more readily than nickel. The effect of this is seen in the valence band spectrum as an increase in the Fe 3*d* state at 2 eV. The nature of this state cannot be told without a clearer understanding of the species bonded to iron, although based on Fe 3*p* core-level spectra, they are likely Fe^{III} species. Since the Fe sulfate species appear in the lower valence band, specifically at 3 eV and 10 eV, the feature at 2 eV is likely to be Fe^{III} oxide or oxyhydroxide. Further studies specifically regarding the oxidation of pentlandite are required to further understand these reactions.

7.5 References

[1] Q. Hu, G. Li, X. Liu, B. Zhu, G. Li, L. Fan, X. Chai, Q. Zhang, J. Liu, C. He, Coupling pentlandite nanoparticles and dual-doped carbon networks to yield efficient and stable electrocatalysts for acid water oxidation, *Journal of Materials Chemistry A*, 7 (2019) 461-468.

- [2] Y. Tang, H. Yang, J. Sun, M. Xia, W. Guo, L. Yu, J. Yan, J. Zheng, L. Chang, F. Gao, Phase-pure pentlandite $\text{Ni}_{4.3}\text{Co}_{4.7}\text{S}_8$ binary sulfide as an efficient bifunctional electrocatalyst for oxygen evolution and hydrogen evolution, *Nanoscale*, 10 (2018) 10459-10466.
- [3] J. Ma, L. Xu, C. Shen, C. Hu, W. Liu, Y. Wen, Fe-N-Graphene Wrapped Al_2O_3 /Pentlandite from Microalgae: High Fenton Catalytic Efficiency from Enhanced Fe^{3+} Reduction, *Environmental Science & Technology*, 52 (2018) 3608-3614.
- [4] I. Zegkinoglou, A. Zendegani, I. Sinev, S. Kunze, H. Mistry, H.S. Jeon, J. Zhao, M.Y. Hu, E.E. Alp, S. Piontek, M. Smialkowski, U.-P. Apfel, F. Körmann, J. Neugebauer, T. Hickel, B. Roldan Cuenya, Operando Phonon Studies of the Protonation Mechanism in Highly Active Hydrogen Evolution Reaction Pentlandite Catalysts, *Journal of the American Chemical Society*, 139 (2017) 14360-14363.
- [5] B. Konkena, K.J. Puring, I. Sinev, S. Piontek, O. Khavryuchenko, J.P. Dürholt, R. Schmid, H. Tüysüz, M. Muhler, W. Schuhmann, U.-P. Apfel, Pentlandite rocks as sustainable and stable efficient electrocatalysts for hydrogen generation, *Nature Communications*, 7 (2016) 12269.
- [6] J.K. Burdett, G.J. Miller, Polyhedral clusters in solids. The electronic structure of pentlandite, *Journal of the American Chemical Society*, 109 (1987) 4081-4091.
- [7] G.G. Hoffman, J.K. Bashkin, M. Karplus, Electronic structure of icosahedral cobalt-sulfur clusters, *Journal of the American Chemical Society*, 112 (1990) 8705-8714.
- [8] H.R. Chauke, D. Nguyen-Manh, P.E. Ngoepe, D.G. Pettifor, S.G. Fries, Electronic structure and stability of the pentlandites Co_9S_8 and $(\text{Fe},\text{Ni})_9\text{S}_8$, *Physical Review B*, 66 (2002) 155105.
- [9] P.P. Mkhonto, H.R. Chauke, P.E. Ngoepe, Ab initio Studies of O_2 Adsorption on (110) Nickel-Rich Pentlandite ($\text{Fe}_4\text{Ni}_5\text{S}_8$) Mineral Surface, *Minerals*, 5 (2015) 665-678.
- [10] C.N. Waterson, J.O. Sindt, J. Cheng, P.A. Tasker, C.A. Morrison, First-principles study on ligand binding and positional disorder in pentlandite, *The Journal of Physical Chemistry C*, 119 (2015) 25457-25468.
- [11] Z.E. Pettifer, J.S. Quinton, W.M. Skinner, S.L. Harmer, New interpretation and approach to curve fitting synchrotron X-ray photoelectron spectra of $(\text{Fe},\text{Ni})_9\text{S}_8$ fracture surfaces, *Applied Surface Science*, 504 (2020) 144458.
- [12] L.C. Davis, L.A. Feldkamp, Resonant photoemission involving super-Coster-Kronig transitions, *Physical Review B*, 23 (1981) 6239-6253.
- [13] V. Formoso, G. Chiarello, R.G. Agostino, L. Papagno, E. Colavita, L. Floreano, R. Gotter, A. Morgante, A. Santaniello, A. Verdini, Resonant valence-band photoemission spectroscopy on the $\text{Fe}_{62}\text{Ni}_{20}\text{Cr}_{18}$ alloy, *European Physical Journal B*, 43 (2005) 463-470.
- [14] C. Guillot, Y. Ballu, J. Paigné, J. Lecante, K.P. Jain, P. Thiry, R. Pinchaux, Y. Pétrouff, L.M. Falicov, Resonant Photoemission in Nickel Metal, *Physical Review Letters*, 39 (1977) 1632-1635.
- [15] L.H. Tjeng, C.T. Chen, J. Ghijsen, P. Rudolf, F. Sette, Giant Cu 2p resonances in CuO valence-band photoemission, *Physical Review Letters*, 67 (1991) 501-504.
- [16] A. Tanaka, T. Jo, Resonant 3d, 3p and 3s Photoemission in Transition Metal Oxides Predicted at 2p Threshold, *Journal of the Physical Society of Japan*, 63 (1994) 2788-2807.
- [17] N. Mårtensson, O. Karis, A. Nilsson, Resonant processes in the soft X-ray regime, *Journal of Electron Spectroscopy and Related Phenomena*, 100 (1999) 379-393.
- [18] U. Fano, Effects of Configuration Interaction on Intensities and Phase Shifts, *Physical Review*, 124 (1961) 1866-1878.
- [19] Z.E. Pettifer, A Study of the Dissolution of Iron and Nickel Sulfides and the Effect of Mixed Mineral Systems [Honours thesis], Flinders University, *Some of the data of this sample was presented in a previous honours thesis, however the analysis is original to the present PhD thesis*, 2014.
- [20] L. Soriano, M. Abbate, F.M.F. de Groot, D. Alders, J.C. Fuggle, S. Hofmann, H. Petersen, W. Braun, Chemical analysis of passivated and oxidized layers on FeCr and FeTi alloys by soft x-ray absorption spectroscopy, 20 (1993) 21-26.
- [21] S.W. Goh, A.N. Buckley, R.N. Lamb, L.-J. Fan, L.-Y. Jang, Y.-w. Yang, Pentlandite sulfur core electron binding energies, *Phys Chem Minerals*, 33 (2006) 445-456.

- [22] D. Briggs, M.P. Seah, Practical Surface Analysis, Auger and X-ray Photoelectron Spectroscopy, 2nd ed. ed., Wiley & Sons, Chichester, England, 1990.
- [23] R.G. Acres, S.L. Harmer, D.A. Beattie, Synchrotron PEEM and ToF-SIMS study of oxidized heterogeneous pentlandite, pyrrhotite and chalcopyrite, Journal of Synchrotron Radiation, 17 (2010) 606-615.
- [24] P.A. van Aken, B. Liebscher, V.J. Styrsa, Quantitative determination of iron oxidation states in minerals using Fe $L_{2,3}$ -edge electron energy-loss near-edge structure spectroscopy, Phys Chem Minerals, 25 (1998) 323-327.
- [25] F. Zheng, V. Pérez-Dieste, J.L. McChesney, Y.-Y. Luk, N.L. Abbott, F.J. Himpsel, Detection and switching of the oxidation state of Fe in a self-assembled monolayer, Surface Science, 587 (2005) L191-L196.
- [26] S.W. Goh, A.N. Buckley, R.N. Lamb, W.M. Skinner, A. Pring, H. Wang, L.-J. Fan, L.-Y. Jang, L.-J. Lai, Y.-w. Yang, Sulfur electronic environments in α -NiS and β -NiS: examination of the relationship between coordination number and core electron binding energies, Phys Chem Minerals, 33 (2006) 98-105.
- [27] G. van der Laan, J. Zaanen, G. Sawatzky, R. Karnatak, J.-M. Esteve, Comparison of x-ray absorption with x-ray photoemission of nickel dihalides and NiO, Physical Review B, 33 (1986) 4253-4263.
- [28] D. Li, G.M. Bancroft, M. Kasrai, M.E. Fleet, B.X. Yang, X.H. Feng, K. Tan, M. Peng, Sulfur K- and L-edge X-ray absorption spectroscopy of sphalerite, chalcopyrite and stannite, Phys Chem Minerals, 20 (1994) 489-499.
- [29] M. Fronzi, S.A. Tawfik, C. Stampfl, M.J. Ford, Magnetic properties of stoichiometric and defective Co_9S_8 , Physical Chemistry Chemical Physics, 20 (2018) 2356-2362.
- [30] M. Ohno, Transition from the radiationless resonant Raman scattering to the normal Auger decay in a charge transfer system, Journal of Electron Spectroscopy and Related Phenomena, 154 (2006) 1-8.
- [31] A. Kay, E. Arenholz, S. Mun, F.J. García de Abajo, C.S. Fadley, R. Denecke, Z. Hussain, M.A. Van Hove, Multi-Atom Resonant Photoemission: A Method for Determining Near-Neighbor Atomic Identities and Bonding, Science, 281 (1998) 679.
- [32] N. Mårtensson, M. Weinelt, O. Karis, M. Magnuson, N. Wassdahl, A. Nilsson, J. Stöhr, M. Samant, Coherent and incoherent processes in resonant photoemission, Applied Physics A, 65 (1997) 159-167.
- [33] S. Hall, J. Stewart, The crystal structure of argentian pentlandite $(\text{Fe}, \text{Ni})_8\text{AgS}_8$, compared with the refined structure of pentlandite $(\text{Fe}, \text{Ni})_9\text{S}_8$, The Canadian Mineralogist, 12 (1973) 169-177.
- [34] B. Etschmann, A. Pring, A. Putnis, B.A. Grguric, A. Studer, A kinetic study of the exsolution of pentlandite $(\text{Ni}, \text{Fe})_9\text{S}_8$ from the monosulfide solid solution $(\text{Fe}, \text{Ni})\text{S}$, American Mineralogist, 89 (2004) 39-50.
- [35] O. Knop, C.-H. Huang, F.W.D. Woodhams, Chalcogenides of the transition elements. VII. A mössbauer study of pentlandite, American Mineralogist, 55 (1970) 1115-1130.
- [36] D.J. Vaughan, M.S. Ridout, Mössbauer studies of some sulphide minerals, Journal of Inorganic and Nuclear Chemistry, 33 (1971) 741-746.
- [37] V. Rajamani, C. Prewitt, Thermal Expansion of the Pentlandite Structure, American Mineralogist, 60 (1975) 39-48.
- [38] C. Tenailleau, B. Etschmann, R.M. Ibberson, A. Pring, A neutron powder diffraction study of Fe and Ni distributions in synthetic pentlandite and violarite using ^{60}Ni isotope, American Mineralogist, 91 (2006) 1442-1447.
- [39] A. Fujimori, K. Mamiya, T. Mizokawa, T. Miyadai, T. Sekiguchi, H. Takahashi, N. Mori, S. Suga, Resonant photoemission study of pyrite-type NiS_2 , CoS_2 and FeS_2 , Physical Review B, 54 (1996) 16329.
- [40] J.J. Yeh, I. Lindau, Atomic subshell photoionization cross sections and asymmetry parameters: $1 \leq Z \leq 103$, Atomic Data and Nuclear Data Tables, 32 (1985) 1-155.

- [41] L.A.J. Garvie, P. Rez, J.R. Alvarez, P.R. Buseck, Interband transitions of crystalline and amorphous SiO₂: An electron energy-loss spectroscopy (EELS) study of the low-loss region, *Solid State Communications*, 106 (1998) 303-307.
- [42] S. Mattila, J.A. Leiro, M. Heinonen, XPS study of the oxidized pyrite surface, *Surface Science*, 566-568 (2004) 1097-1101.
- [43] T. Yamashita, P. Hayes, Analysis of XPS spectra of Fe²⁺ and Fe³⁺ ions in oxide materials, *Applied Surface Science*, 254 (2008) 2441-2449.
- [44] C. Ruby, B. Humbert, J. Fusy, Surface and interface properties of epitaxial iron oxide thin films deposited on MgO(001) studied by XPS and Raman spectroscopy, *Surface and Interface Analysis*, 29 (2000) 377-380.
- [45] A.N. Mansour, Characterization of NiO by XPS, *Surface Science Spectra*, 3 (1994) 231-238.
- [46] A.N. Mansour, Characterization of β-Ni(OH)₂ by XPS, *Surface Science Spectra*, 3 (1994) 239-246.
- [47] S. Tougaard, Improved XPS analysis by visual inspection of the survey spectrum, *Surface and Interface Analysis*, 50 (2018) 657-666.
- [48] A.A. Audi, P.M.A. Sherwood, X-ray photoelectron spectroscopic studies of sulfates and bisulfates interpreted by X_α and band structure calculations, *Surface and Interface Analysis*, 29 (2000) 265-275.

8 PENTLANDITE SURFACES EXPOSED TO ENVIRONMENTAL CONDITIONS

The previous two chapters of this thesis were concerned with fracture surfaces of pentlandite, and the electronic structure of relatively pristine pentlandite, respectively. As discussed in these preceding chapters, characterising the surface structure and electronic structure of pentlandite is crucial in its application as a catalyst, or its manipulation in minerals processing procedures. However, in a practical sense, the relatively pristine samples that were presented in the previous two chapter are unlikely to be frequently encountered. The examples of pentlandite samples or pentlandite surfaces which are more likely to be encountered will be those which are somewhat altered or oxidised to some extent. Therefore, this chapter turns its focus to pentlandite surfaces which are altered in ways which may be encountered in more practical scenarios, to determine the pathway by which these surfaces oxidise, and how the samples will typically be altered. Experimental studies of oxidised pentlandite samples are limited and somewhat dated, and therefore generally lack the resolution of modern experiments [1-5]. The aim of this chapter is therefore to present experimental documentation of oxidised surfaces using modern synchrotron photoelectron spectroscopy to reveal the surfaces expected under various conditions. Following the characterisation of pristine, or near pristine surfaces of the previous chapters, this chapter characterises the surface and bulk electronic structure of a pentlandite sample which has undergone controlled oxidation by water vapour, followed by an analysis of the surface of polished pentlandite surfaces, and finally, surfaces of pentlandite which have been exposed to sulfuric acid solution after polishing.

8.1 Controlled oxidation of a stoichiometric pentlandite surface – 420 Langmuir H₂O vapour

Pristine and near-pristine surfaces of pentlandite are of great interest for understanding their catalytic activity, physical properties, and the reactions that may occur on their surfaces. However, such systems are notoriously difficult to study. As seen in the previous two chapters of this thesis, pristine surfaces which are unoxidized and free of other mineral phases are difficult to produce, and therefore difficult to study experimentally. This is perhaps the motivation for the theoretical calculations regarding the pentlandite electronic structure. There has been numerous density functional theory (DFT) calculations regarding various pentlandite structures recently, which investigate various aspects of pentlandite's physical properties [6], and electronic structure [7]. Many pentlandite studies are highly interested in the potential for the use of pentlandite as a catalyst in the production of hydrogen [8-10]. More recently, calculations have endeavoured to study the reaction of pentlandite's surface with various ligands such as O₂ [11, 12], and water and xanthate [13]. Unfortunately, there are currently no published studies of the initial stages of oxidation of a pentlandite surface. While

there are a few theoretical calculations currently published, it is crucial to compare such results with experimental evidence. This section uses the stoichiometric sample from section 7.3 in a controlled dosing experiment, to study the initial reaction of the samples surface with water vapour.

8.1.1 Methods

The pentlandite sample used in this section is the same synthetic pentlandite sample with a stoichiometry of $\text{Fe}_{4.2}\text{Ni}_{4.4}\text{S}_{8.3}$. As described in sections 3.1.3 and 7.3.2, this sample was cleaved in a nitrogen filled glove bad that was attached to the introduction chamber of the synchrotron endstation at the Canadian Light Source. After fracture, the sample was moved into the introduction chamber which was promptly evacuated to a high vacuum. The sample was analysed; the results of which are shown in section 7.3. The sample was then transferred to the preparation chamber which was maintained at a vacuum of at least 1×10^{-8} Torr. Demineralised water was held in a glass test tube which was attached to the preparation chamber by a valved inlet. The demineralised water was frozen using liquid N_2 and the air remaining in the test tube evacuated prior to the controlled dosing. The sample was dosed with H_2O vapour by gradually opening the valved inlet containing the frozen demineralised water, while the pressure in the preparation chamber was maintained at 1×10^{-6} Torr for 420 seconds (7 minutes), before the inlet valve was closed and the vacuum in the preparation chamber allowed to recover. This pressure \times time corresponds to 420 Langmuir exposure of H_2O vapour to the pentlandite surface. The sample was then transferred back into the analysis chamber and the following spectra shown in this section were collected.

The binding energy scale of the spectra were calibrated for each photon energy such that the top of the valence band aligns with 0 eV in the binding energy scale. The Fe/Ni $3p$ core-level spectra were normalised to the Fe $3p$ peak for comparison, while each valence band spectrum was normalised to the photon flux. A Shirley background [14] was applied to the S $2p$ spectrum before fitting, and also subtracted from both Fe/Ni $3p$ spectra for ease of comparison between the spectra. The spectra which are presented in this section which are not collected from the dosed sample, have each been shown previously in section 7.3, therefore a detailed description of these spectra is omitted here.

Similar to the results of section 7.3, this section observed photoelectron spectra in the valence band region for the dosed sample. Different photon energies are used to probe the various states contributing to the valence band, and the results are analysed considering the photoionization cross sections of atomic orbitals calculated by Yeh and Lindau [15], shown in Figure 8.1.

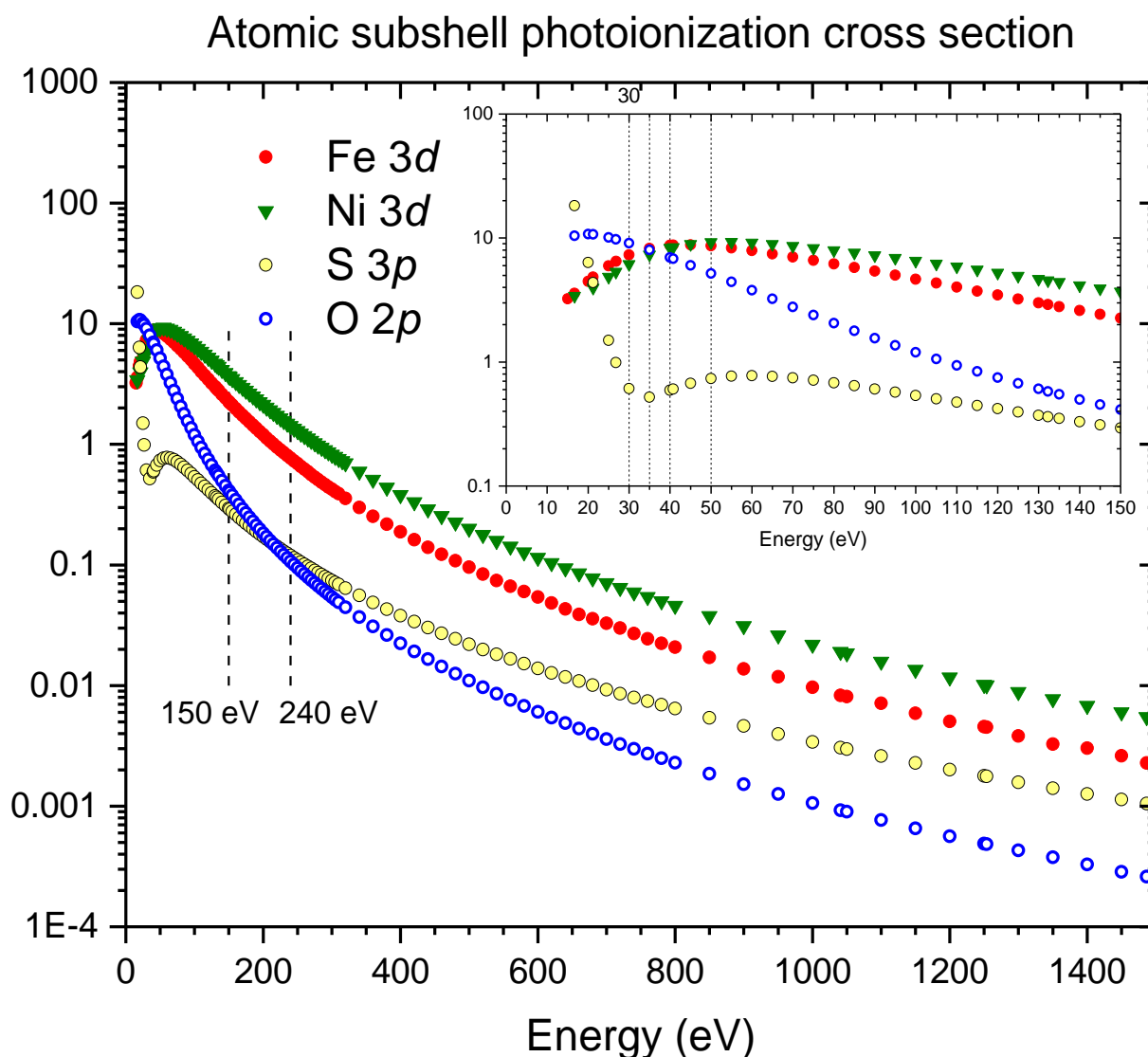


Figure 8.1: Photoionization cross sections of valence level atomic subshells [15].

8.1.2 Survey spectrum for pentlandite dosed with H₂O vapour

The survey spectrum for dosed pentlandite is shown in Figure 8.2 with the survey spectrum from Fe_{4.2}Ni_{4.4}S_{8.3} repeated from section 7.3. The key features of the survey spectrum include a strong peak around 160 eV due to S 2*p*, a broad asymmetric peak around 90 eV due to sulfur LMM Auger electrons, and the valence band between 20 – 0 eV which has contributions from S 3*s*, 3*p*, Fe and Ni 3*d*, and O 2*p*. The peaks around 70 eV and 55 eV are attributed to Ni and Fe 3*p* respectively; the shapes of which have changed from fresh to the dosed pentlandite sample. Both samples have a narrow peak just above 100 eV attributed to Si electrons from SiO₂ contamination, although this peak is relatively less intense in the dosed pentlandite sample. The other key difference between the fresh and dosed pentlandite samples is the strength of the contribution to the spectrum around 25 eV. In the fresh pentlandite sample, a small broad peak is observed and was attributed to O 2*s* from SiO₂ contamination [16]. In the dosed pentlandite sample, the contributions from the Si 2*s* electrons due to

SiO₂ contamination are expected to be less, as the Si peak at 100 eV is also less, so the increase in the O 2s peak at 25 eV can be attributed to adsorption or reaction of H₂O on the pentlandite surface as a result of the controlled dosing.

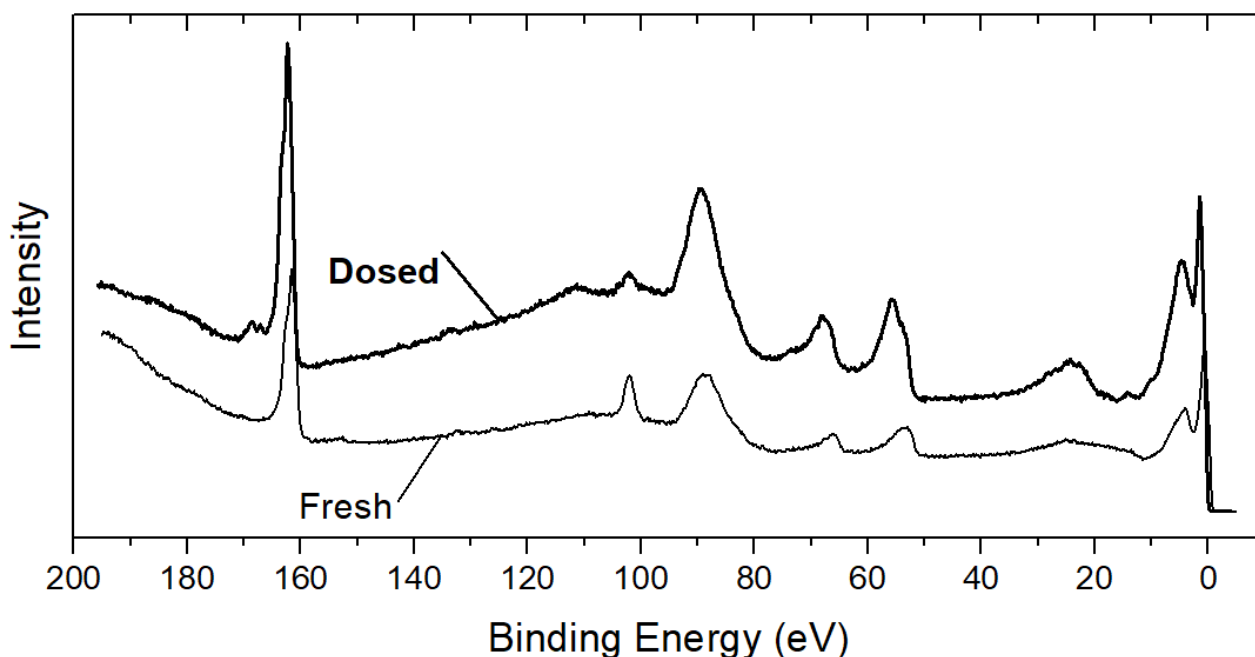


Figure 8.2: Survey spectrum for synthetic stoichiometric pentlandite after fracture in nitrogen filled glove bag (fresh) and after 420 Langmuir controlled dosing with H₂O vapour (dosed). $h\nu = 240$ eV.

8.1.3 Fe and Ni core-level spectra

The Fe and Ni 3p spectra for dosed pentlandite are shown in Figure 8.3b with the same spectra for Fe_{4.2}Ni_{4.4}S_{8.3} repeated from section 7.3 included in Figure 8.3a for comparison. Like most sulfides, the transition metal 3p peaks for pentlandite are not well studied and reliable reference spectra for transition metal 3p peaks for sulfides is generally unavailable. The spectra presented here are therefore more broadly compared to the oxides, which have some references for the metal 3p peaks, and may give an indication of the valency of the metal sites. The Fe 3p peak for both $h\nu = 150$ eV and 240 eV spectra is at 55.5 eV, with a clear shoulder on the low binding energy side around 53.5 eV. The binding energy of the peak is consistent with the Fe 3p binding energy of Fe^{III}-O in magnetite (Fe₃O₄) [17, 18] and similar to the high binding energy shoulder observed in the samples from section 7.3 that showed some Fe oxidation. The binding energy of the shoulder at 53.5 eV is consistent with Fe^{II}-O in hematite (Fe₂O₃) observed at 53.7 eV [17] and is a little higher than Fe^{II}-S in unoxidized pyrite at 53 eV [19]. Therefore, the dominant peak observed at 55.5 eV in the dosed pentlandite sample is attributed to Fe^{III} species while the shoulder on the low binding energy side is attributed to Fe^{II} species, such as is expected in the bulk pentlandite structure. The shape of the Fe 3p spectrum changes significantly between the $h\nu = 240$ eV spectrum and the more surface sensitive $h\nu = 150$ eV

Chapter 8: Pentlandite surfaces exposed to environmental conditions

spectrum, with the low binding energy shoulder more prominent in the bulk sensitive spectrum, while the peak attributed to oxidised Fe^{III} is relatively stronger in the more surface sensitive spectrum. These results show that at the surface of the dosed pentlandite sample, the iron species are oxidised from Fe^{II} to Fe^{III} species.

The Ni 3*p* peak is a broad peak centred around 67.5 eV. There is no clear structure in the Ni 3*p* peak in the $h\nu = 150$ eV spectrum, but in the $h\nu = 240$ eV spectrum there appears to be two components of similar intensity contributing to the peak at 67 eV and 68 eV respectively. The binding energy of the Ni 3*p* features observed for dosed pentlandite is slightly higher than the peak observed for Fe_{4.2}Ni_{4.4}S_{8.3} at 66 eV, with a shoulder at 68 eV, shown in Figure 8.3a. The shift to a higher binding energy and increase in peak width may indicate some alteration of the Ni species as a result of dosing with H₂O vapour, however the difference between the $h\nu = 150$ eV and 240 eV spectra is not clear, which may indicate that this alteration extends to more than just a monolayer at the surface.

The relative intensities of the Fe and Ni 3*p* peaks is seen to change between the $h\nu = 150$ eV and 240 eV spectra, showing that the Fe peaks are relatively more intense in the $h\nu = 150$ eV spectrum, which has a greater proportion of the signal from the surface monolayer. This indicates that the Fe species are more prominent at the surface than in the bulk. This is consistent with previous literature observing the surfaces of pentlandite oxidised in a wide range of conditions, all of which observe preferential oxidation of Fe sites over Ni sites [2-4, 12]. A similar observation was made for the samples presented in section 7.3, and has previously been reported for roasted pentlandite, where the core of the sample was observed to be a nickel rich sulfide, surrounded by an outer layer of Fe and O species [12]. It is proposed that this effect is attributable to the migration of Fe species to the surface due to oxidation, similar to that seen for pyrrhotite [3, 20], however this migration is not observed for the Ni species in the sample.

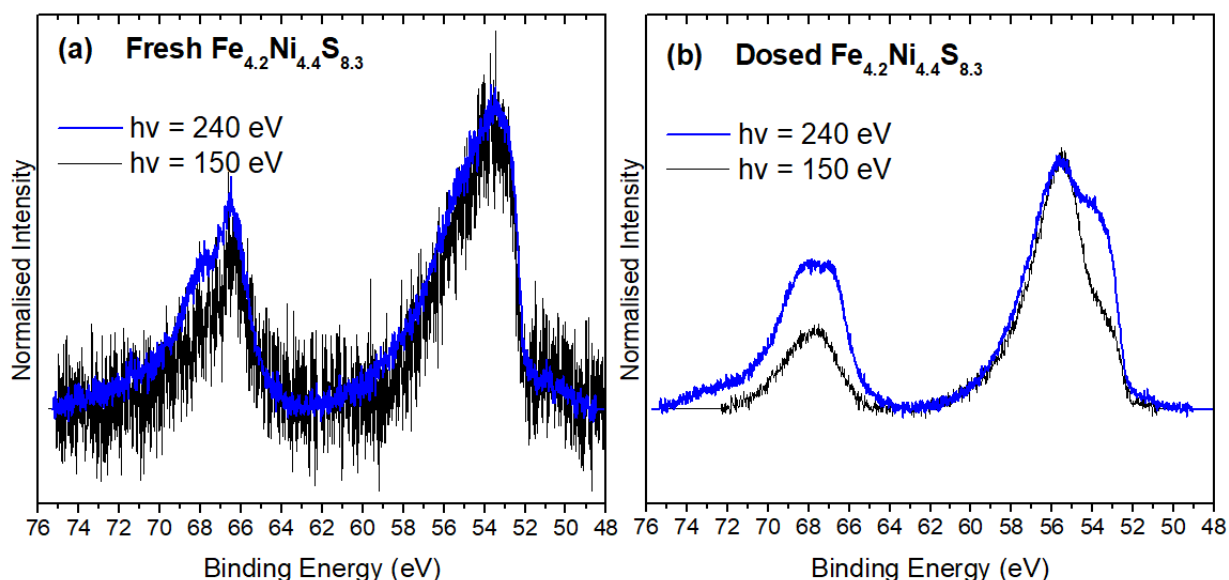


Figure 8.3: Fe/Ni 3*p* spectra with background removed for $h\nu = 150$ eV (black) and $h\nu = 240$ eV (blue) from (a) fresh pentlandite ($\text{Fe}_{4.2}\text{Ni}_{4.4}\text{S}_{8.3}$) (reproduced from Chapter 7) and (b) dosed pentlandite, showing a significant difference in both Fe and Ni structure at the surface in comparison to the bulk species.

8.1.4 S 2*p* core-level spectrum

The S 2*p* spectrum for dosed pentlandite is shown in Figure 8.4 and has been fitted with three doublets at 161.2 eV, 161.7 eV and 162.2 eV. These binding energies are consistent with the peaks fitted to the S 2*p* spectra of previous pentlandite samples shown in Chapters 6 and 7, and the peaks are attributed to surface 3-coordinate species, surface and bulk 4-coordinate species, and bulk 5-coordinate monosulfide species respectively [21]. In addition to the monosulfide species, two doublets were required at 167.1 eV and 169.7 eV to fit the additional structure in the spectrum. These peaks are attributed to sulfite (SO_3^{2-}) and sulfate (SO_4^{2-}) species respectively. The result is a good fit across the spectrum, except for the region around 164 eV. There are a number of possible explanations for the poor fit around 164 eV. Firstly, this region is the binding energy at which elemental sulfur is sometimes observed [22], however in high vacuum the elemental sulfur should be volatile and is therefore not easily detected. The second explanation is that the Shirley background could be an inaccurate simulation of the true background signal contributing to the spectrum, and that the background could be distorted from this modelled shape due to the inelastic scattering events occurring during the transport of photoelectrons from their excitation point to the surface. This phenomenon is discussed in literature [23], and its effect on some of the results presented in this thesis has been considered in Chapter 5. Since the fit shown in Figure 8.4 is reasonable ($\chi^2 = 0.043$), no further background analysis was performed for this spectrum.

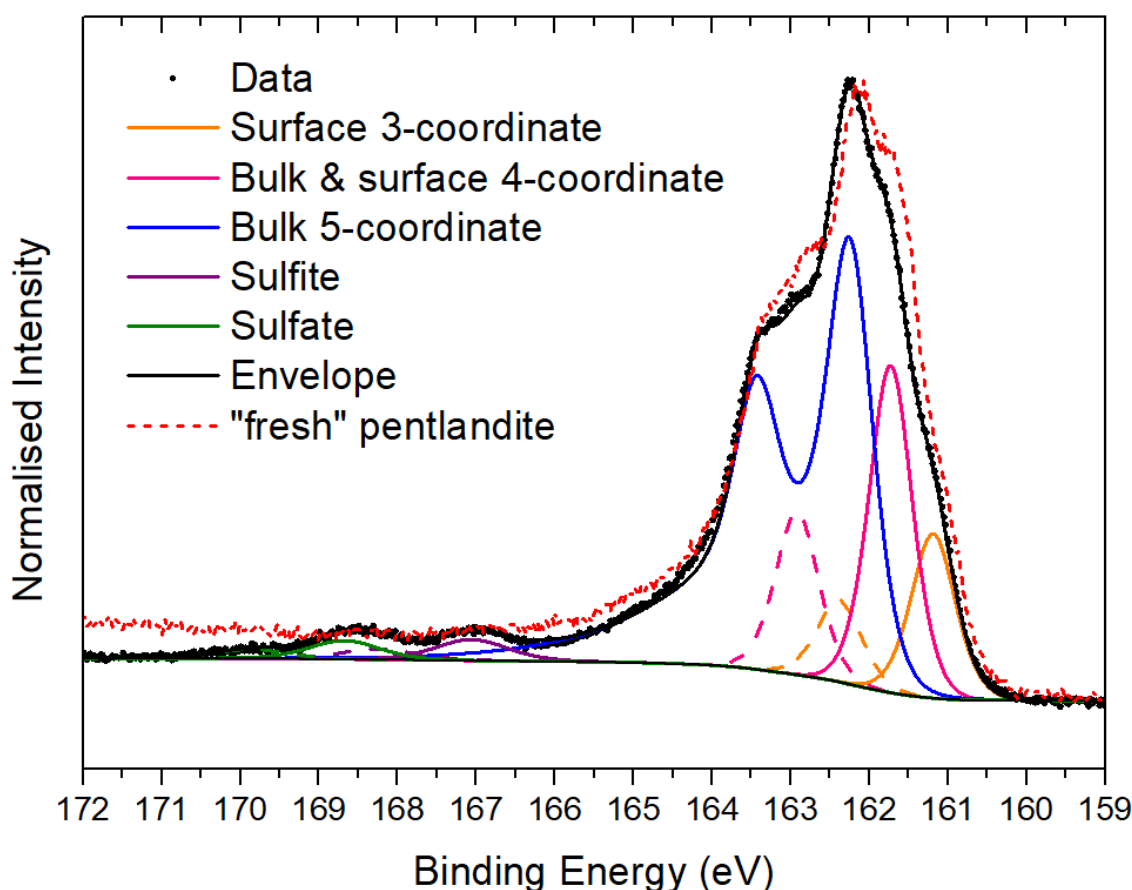


Figure 8.4: S $2p$ photoelectron spectrum for pentlandite dosed with 420 Langmuir of H_2O vapour. $h\nu = 240$ eV. “Fresh” pentlandite refers to the $\text{Fe}_{4.2}\text{Ni}_{4.4}\text{S}_{8.3}$ sample prior to dosing, repeated from Chapter 7.

Also shown in Figure 8.4 is the spectrum for fresh $\text{Fe}_{4.2}\text{Ni}_{4.4}\text{S}_{8.3}$, reproduced from Chapter 7 for comparison. By comparing these two spectra it can be seen that the general shape of the $S\ 2p$ spectra for the two samples is remarkably similar. However, although the differences between the spectra are small, their effects are noticeable. Firstly, the binding energy of the bulk peak is seen to shift to a higher binding energy in the dosed sample. This binding energy shift is not represented in the binding energies of the fitted features, as the binding energy shift is less than 0.1 eV and therefore within the uncertainty of the binding energy of the fitted features. Yet, the binding energy shift between the spectra is observable when directly comparing the spectra as in Figure 8.4. A shift in the binding energy of the bulk peak could be due to the emergence of disulfide or polysulfide species on the high binding energy side, however the contribution from these species is small enough to be estimated within the peak fitted for the bulk component.

The second observed difference is that the background in the high binding energy region of the spectrum for the fresh sample is stronger than the background for the dosed sample. The strength and shape of the background in the $S\ 2p$ spectrum for pyrrhotite was considered in Chapter 5, and it was concluded that the background was evidence of an overlayer of oxidised species. However, in the

fresh pentlandite sample, relatively little oxidised species could be expected to form, and therefore the background is unlikely to arise due to an oxidised overlayer. It is important to understand that the background itself is not sufficient evidence for a chemically distinct overlayer, but instead is a result of increased scattering length and an increase of inelastic scattering events for the photoelectrons escaping the sample. This can be caused by more scenarios than just an overlayer of distinct species. For example, the difference in backgrounds in the two spectra could be evidence of different surface roughness, and although it is the same sample before and after dosing, the area of analysis is small (approximately $500 \mu\text{m}^2$), and it is likely that distinctly different areas with different surface roughness were analysed before and after dosing. Nevertheless, it is possible that the true shape of the background differs from that which is modelled by the Shirley background in each sample, and such errors can propagate into the fitted peaks.

The third observation is that small disulfide and polysulfide components were required for the fresh pentlandite sample, to produce a good fit, whereas for dosed pentlandite, no disulfide or polysulfide components were used. The possible errors in the modelling of the background may contribute to this effect, as small changes to the shape for the background are likely to affect the intensity of peaks fitted in the higher binding energy regions such as in the polysulfide region. For example, if the contribution from the background in this binding energy region is overestimated, then less polysulfide components are required to achieve an acceptable fit to the spectrum. In the case of the dosed sample, no polysulfide is required, yet there is evidence to suggest a small polysulfide component may be contributing to the spectrum. The residual after fitting the peaks is shown below the spectrum in Figure 8.4, and shows small deviations from a perfect fit, particularly in the binding energy region where a polysulfide component could be contributing. The polysulfide component was not fitted in this case, because the residual did not have the splitting and intensity ratio expected for a S $2p$ component, and to create a good fit which included a polysulfide component resulted in the contribution from the polysulfide component being insignificantly small. It is concluded from this that any components which are contributing to the spectrum in the region around 163 – 165 eV are so small that their intensity is less than the intensity variation from the background.

The quantification of sulfur species fitted to the S $2p$ spectrum is shown in Table 8.1. Also shown for comparison is the quantification of sulfur species for this sample before it was dosed with H_2O vapour. The comparison shows that while the 3-coordinate and 5-coordinate species have similar values of % contribution to each spectrum, the 4-coordinate contribution is considerably less in the spectrum for the dosed pentlandite sample than for the fresh sample. In addition, as previously discussed, no disulfide or polysulfide components were fitted to the dosed pentlandite sample, as was

fitted for the fresh sample, but the dosed sample required contributions at higher binding energies attributed to sulfite and sulfate species. These species contribution 2.8% and 2.4% of the total sulfur components respectively. These values are similar to the contribution from polymerised sulfur in the fresh sample.

Table 8.1: Quantification of sulfur species fitted to S 2p spectrum in Figure 8.4, including the quantification of sulfur species for Fe_{4.2}Ni_{4.4}S_{8.3} before dosing. ”%” represents the contribution to the fit.

Species	Binding Energy (FWHM)	%	Fresh pentlandite (from Table 7.4) %
Surface 3-coordinate	161.2 (0.66)	13.4	10.8
Surface & bulk 4-coordinate	161.7 (0.65)	26.1	33.5
Bulk 5-coordidnate	162.2 (0.67)	55.3	51.7
Disulfide	(NA)	0.0	1.8
Polysulfide	(NA)	0.0	2.2
Sulfite	167.1 (1.0)	2.8	0.0
Sulfate	168.7 (1.0)	2.4	0.0

To show more clearly the differences between the fresh and dosed pentlandite S 2p spectra, a difference spectrum was calculated by subtracting the dosed S 2p spectrum from that of the fresh Fe_{4.2}Ni_{4.4}S_{8.3} sample. Both spectra were normalised to the bulk peak at 162.2 eV, and therefore the resulting features in the difference spectrum shown in Figure 8.5 represent the change in features relative to the bulk peak.

The difference spectrum shows negative peaks at 160.9 eV and 161.5 eV, which correspond to the peaks attributed to 3-coordinate and 4-coordinate sulfur species, indicating a relative decrease in these species in the dosed sample. The positive peak at 162.4 eV can be attributed to the shift to a higher binding energy of the main peak in the spectrum for the dosed sample, and may be due to the development of polymerised sulfur species, especially disulfide species which would be expected around that binding energy [22]. However, there is no clear doublet attributable to disulfide or polysulfide species, separate from the binding energy shifted bulk peak, confirming that these species are sufficiently small to be absorbed within the error of the fitted bulk peak. Furthermore, the height of the peak at 162.4 eV in the difference spectrum is 0.1 (normalised intensity), which is approximately 10% of the total signal, and therefore relatively small.

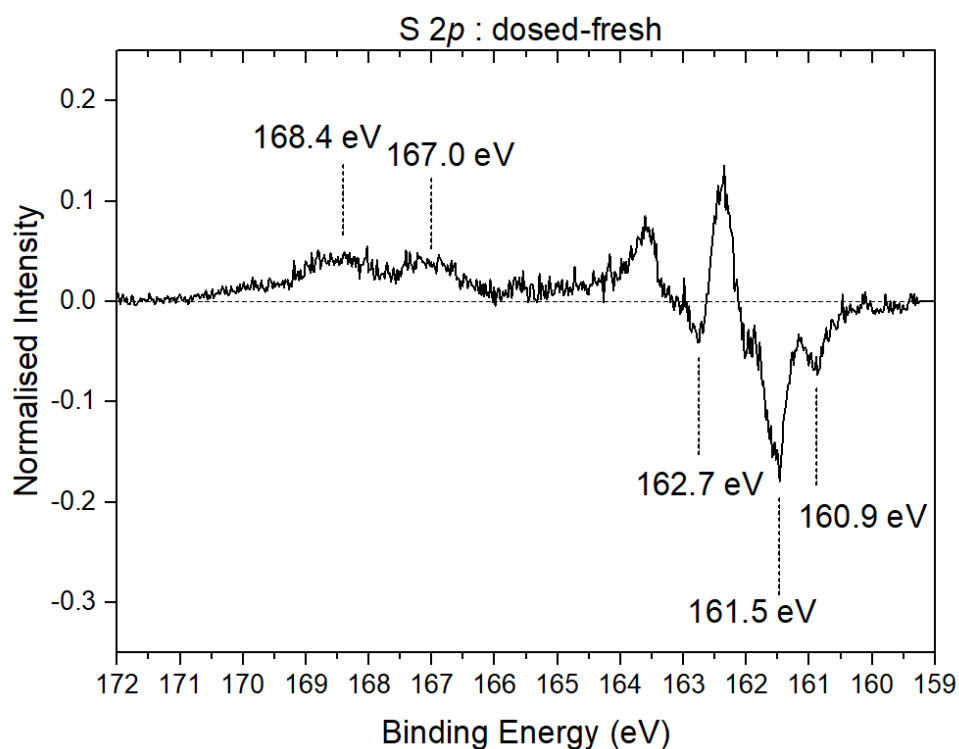


Figure 8.5: Difference spectrum calculated by subtracting the S 2p spectrum of the fresh pentlandite sample from the S 2p spectrum collected for the dosed sample. The negative peaks indicate a decrease in 4-coordinate monosulfide species, while the positive peaks show an increase in sulfur-oxy species.

8.1.5 Valence band photoelectron spectra

The valence band spectra collected with $h\nu = 150$ eV and 240 eV are shown for dosed pentlandite in comparison with those for fresh $\text{Fe}_{4.2}\text{Ni}_{4.4}\text{S}_{8.3}$ and $\text{Fe}_{4.0}\text{Ni}_{4.9}\text{S}_{8.1}$, shown in Figure 8.6. The valence band spectra for $\text{Fe}_{4.0}\text{Ni}_{4.9}\text{S}_{8.1}$ from section 7.3 are included for comparison because the $\text{Fe}_{4.0}\text{Ni}_{4.9}\text{S}_{8.1}$ pentlandite showed the greatest oxidation of all the sample presented in the previous chapter. The shape of the dosed pentlandite $h\nu = 240$ eV valence band spectrum is similar to the $h\nu = 150$ eV and 240 eV spectra of the other two samples shown here. The valence band spectrum is characterised by a strong peak in the upper valence band, and a less intense, broad peak in the lower valence band, separated by a local minimum. In comparison to previously discussed pentlandite valence band spectra, the dosed pentlandite $h\nu = 240$ eV spectrum has a few minor differences. Firstly, the peak in the upper valence band is slightly shifted to a higher binding energy. While this peak in pentlandite samples shown in previous chapters has been consistently observed at 1.1 eV, in the dosed pentlandite sample the binding energy of this peak is at 1.3 eV. Secondly, the local minimum separating the upper and lower valence band regions is not as low and distinct as is seen in previously presented valence band spectra. Additionally, upon closer inspection there is an emerging feature at 3 eV which is not observable in the valence band spectra for other samples. While the lower valence band has slightly more intensity than that observed for other samples, there is no apparent structure seen at higher binding energies.

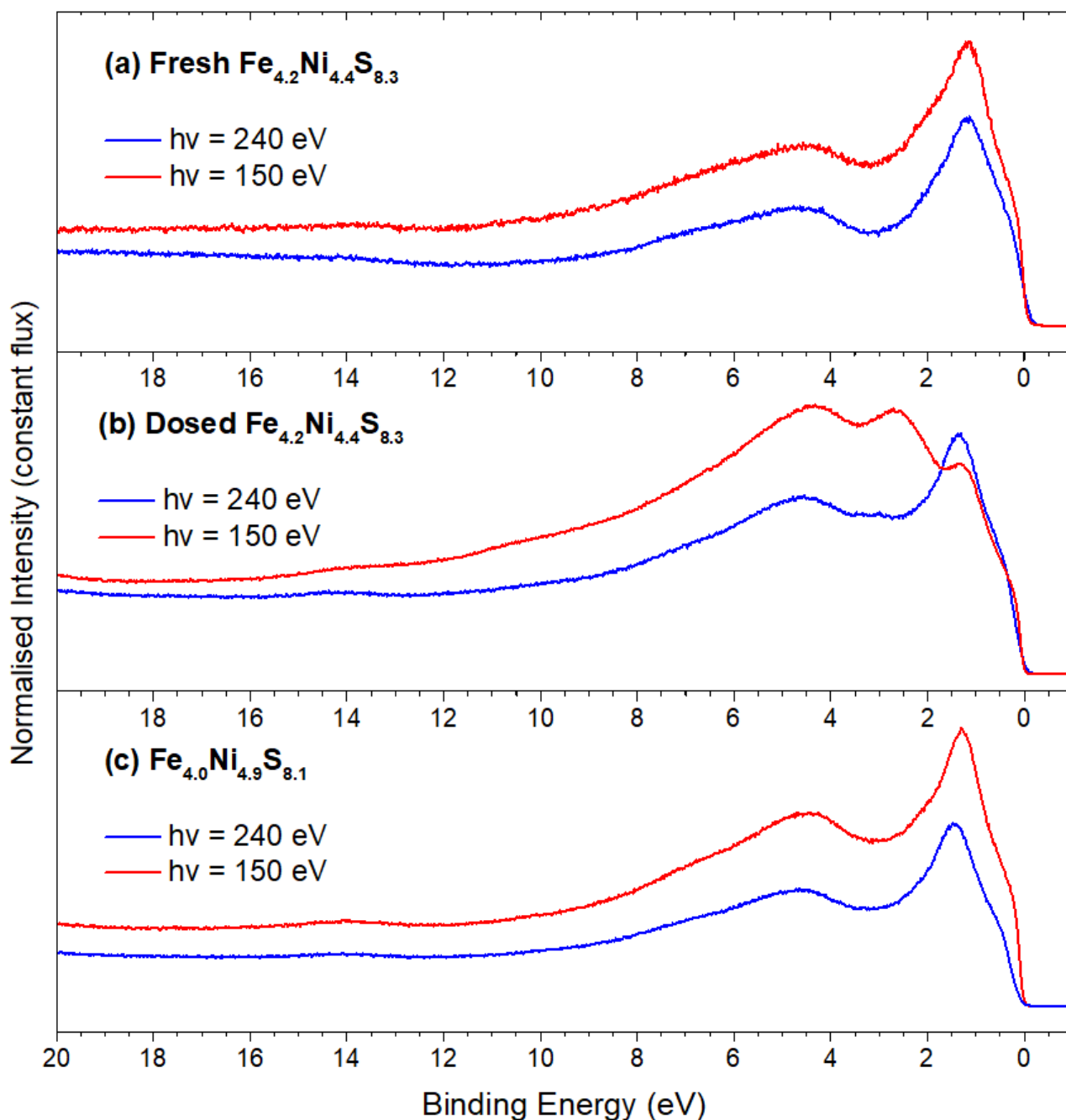


Figure 8.6: Photoelectron spectra in the valence band region for (a) $\text{Fe}_{4.2}\text{Ni}_{4.4}\text{S}_{8.3}$ fractured in a nitrogen glove bag, (b) the same sample after 420 Langmuir H_2O vapour dosing, and (c) $\text{Fe}_{4.8}\text{Ni}_{3.9}\text{S}_{8.3}$. The $\text{Fe}_{4.2}\text{Ni}_{4.4}\text{S}_{8.3}$ and $\text{Fe}_{4.8}\text{Ni}_{3.9}\text{S}_{8.3}$ samples were discussed in the previous chapter and are included here for comparison. $h\nu = 240$ eV (blue) and 150 eV (red).

The $h\nu = 150$ eV valence band spectrum for the dosed pentlandite sample shows significant deviation in shape from those of other samples. In this spectrum, the peak in the upper valence band (also at 1.3 eV) is almost overshadowed by a peak at 2.6 eV which has not been observed in previous samples. This is followed by the lower valence band peak, which appears at the same binding energy as seen in previous samples, but a much greater intensity. It is expected that the increase in intensity of this lower valence band peak is greatly contributed to by the emergence of the new peak at 2.6 eV. Since

this peak at 2.6 eV is significantly strong and was not observed in any valence band spectra presented in Chapter 7, this must be attributable to a species that was not present in other samples.

The Fe and Ni $3p$ spectra in Figure 8.3 offer some insight into the species contributing to the $h\nu = 150$ eV valence band at 2.6 eV. While there was no clear evidence of oxidation of the Ni sites in the pentlandite samples shown previously in Chapter 7, there is clear evidence of changes to the electronic structure of Ni species at the surface of the dosed pentlandite sample, shown in Figure 8.3. Therefore, the peak at 2.6 eV in the $h\nu = 150$ eV valence band spectrum is attributed to oxidised Ni surface species. This feature is similar to the shoulder observed at 2 eV in the upper valence band spectrum for some of the more oxidised samples from section 7.3. This feature was only observable in the $h\nu = 150$ eV spectrum and was attributed to oxidised Fe species. A similar explanation can be offered for the feature at 2.6 eV in the $h\nu = 150$ eV valence band spectrum in Figure 8.6. Based on calculations for atomic valence orbitals [15], the relative photoionization cross section of O $2p$ electrons is expected to be relatively higher than Fe, Ni, and S valence electrons at $h\nu = 150$ eV in comparison to $h\nu = 240$ eV. Hence, the feature at 2.6 eV, which is overlapping with the previously determined Fe-oxide peak at 2 eV, can be attributed to Ni-oxide species.

The assignment of the peak at 2.6 eV to Ni-oxide species is consistent with reports in literature of oxidised nickel metal. Literature has shown the photoelectron peak near the Fermi level for nickel metal to shift to higher binding energies of around 2 eV with an oxygen exposure of more than 30 L [24]. In the data presented here, the valence band photoelectron peak for Ni-oxide species after 420 L H₂O dosing appears at 2.6 eV.

Low photon energy ($h\nu \leq 50$ eV) valence band spectra are shown in Figure 8.7 for dosed pentlandite fresh Fe_{4.2}Ni_{4.4}S_{8.3}, and Fe_{4.0}Ni_{4.9}S_{8.1}; the latter two of which have been reproduced from section 7.3 for comparison. The general shape of the low photon energy valence band spectra deviates significantly from the $h\nu = 150$ eV and 240 eV valence band spectra, as the upper valence band peak is significantly diminished and the broad peak around 5 eV is relatively enhanced. The shape of the spectra for the dosed pentlandite sample more closely resembles the Fe_{4.0}Ni_{4.9}S_{8.1} spectra, rather than the spectra for Fe_{4.2}Ni_{4.4}S_{8.3}, since the dosed pentlandite sample shows strong shoulder at 10 eV and 3 eV, especially in the $h\nu = 50$ eV spectrum. In section 7.3 this structure was attributed to sulfite and sulfate species which were observed only in the Fe_{4.0}Ni_{4.9}S_{8.1} sample. Since these species are also observed in the S $2p$ spectrum for the dosed sample, this reinforces the proposition that the structure at 10 eV and 3 eV binding energy is owing to the sulfite and sulfate species.

There is a lack of distinct differences between the low photon energy valence band spectra for $\text{Fe}_{4.0}\text{Ni}_{4.9}\text{S}_{8.1}$ and dosed pentlandite sample, despite the dosed sample showing evidence of oxidation of the Ni sites, which was not distinctly observed for $\text{Fe}_{4.0}\text{Ni}_{4.9}\text{S}_{8.1}$. The implication of this observation is that the sulfite and sulfate species can be largely attributed to Fe-sulfite and Fe-sulfate species, and that the nickel species are oxidised by formation of NiO or Ni(OH)₂ species.

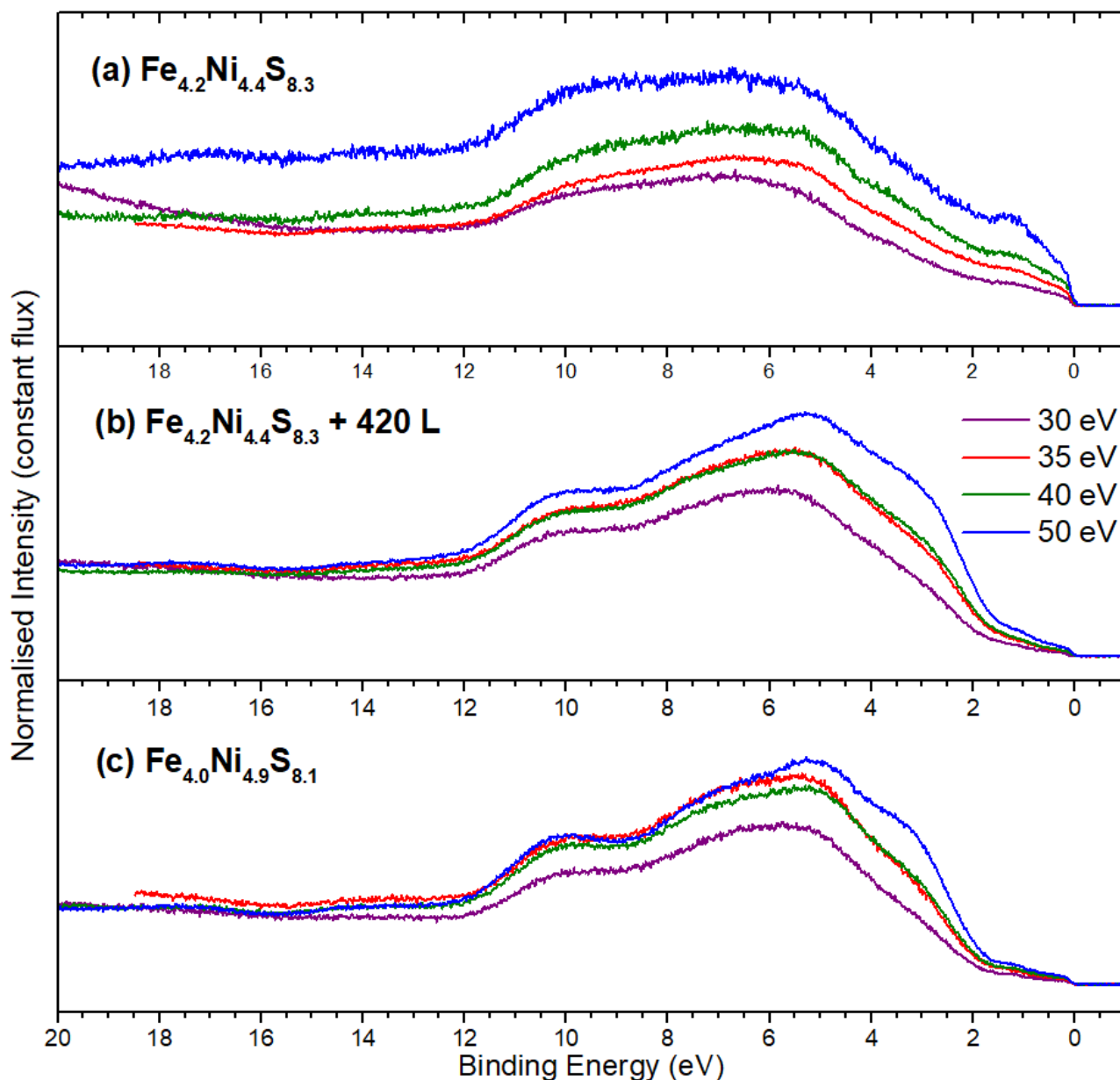


Figure 8.7: Photoelectron spectra in the valence band region collected with $h\nu = 30 - 50$ eV for (a) Stoichiometric pentlandite ($\text{Fe}_{4.2}\text{Ni}_{4.4}\text{S}_{8.3}$) fractured in a nitrogen glove bag, (b) the same sample after 420 Langmuir H_2O vapour dosing, and (c) $\text{Fe}_{4.0}\text{Ni}_{4.9}\text{S}_{8.1}$. The $\text{Fe}_{4.2}\text{Ni}_{4.4}\text{S}_{8.3}$ and $\text{Fe}_{4.0}\text{Ni}_{4.9}\text{S}_{8.1}$ samples were discussed in section 7.3 and are included here for comparison.

8.1.6 Discussion

The results presented in this section show that a stoichiometric pentlandite surface which has been exposed to 420 L H₂O vapour has significant changes to the surface physical and electronic structure. While the survey spectrum shows that the contribution due to oxygen has increased as a result of dosing, the Fe and Ni 3*p*, and S 2*p* spectra show that the reaction of the water vapour with the surface has made changes to each of the surface sites. The metal 3*p* spectra show that the Fe sites are oxidised preferentially over the Ni sites, as has been seen in previous pentlandite samples in this thesis, and numerous times published in literature. The valence band spectrum ($h\nu = 150$ eV) shows a new feature at 3 eV, which is attributed to a combination of oxidised Fe and Ni species. A shoulder in the valence band spectra of some other pentlandites has been observed in section 7.3 at 2.6 eV, and is attributed to oxidised Fe species. With the increase in oxidised Fe species, evident in the Fe 3*p* spectrum, and the emergence of oxidised Ni species, this shoulder on the upper valence band spectrum developed into a clearly defined peak at 3 eV in the dosed pentlandite sample.

The S 2*p* spectrum showed the emergence of sulfite (SO₃²⁻) and sulfate (SO₄²⁻) species, which occurs with the decrease in surface 3-coordinate and 4-coordinate monosulfide species. No significant changes were detected which were attributable to polymerised sulfur species, showing that the oxidation of sulfur sites occurs largely at the surface monosulfide sites, and oxidises these species to sulfite and sulfate species. The low photon energy ($h\nu \leq 50$ eV) valence band spectra show distinct shoulders on the lower valence band around 3 eV and 10 eV, which are attributed to sulfite and sulfate species. The comparison of the valence band spectra between the dosed pentlandite sample and pentlandite samples presented in section 7.3 indicates that the sulfite and sulfate species are likely attributed mainly to the Fe sites, and that the oxidised Ni sites are most likely NiO or Ni(OH) species.

The presence of NiO or Ni(OH) species, and sulfite and sulfate species, shows that the water molecule is dissociating at the surface to react with the pentlandite surface species. Some of the 3-coordinate and 4-coordinate sulfur species are reacting and forming sulfite and sulfate species. These are then seen to bind mainly to the Fe sites, which is unsurprising, as the Fe species are seen to oxidise preferentially over Ni, which literature indicates is due to both the energetic preference for Fe to oxidise over Ni [11, 13], and the migration of Fe species to the surface [12]. After 420 L dosing with H₂O vapour, the Ni sites are also seen to oxidise somewhat, although the results presented here indicate that the sulfite and sulfate species are not binding significantly with the Ni, and it is therefore possible that the Ni species are largely NiO or Ni(OH)₂ species.

8.2 Polished pentlandite surfaces

This sample was cut from the same synthetic pentlandite as the samples presented in Chapter 6 and has a stoichiometry of $\text{Fe}_{4.4}\text{Ni}_{4.6}\text{S}_{8.0}$ measured by microprobe analysis as described in section 3.1.2. The sample was prepared in the same way as the polished pyrrhotite sample in section 5.2.1. The sample was first shaped and polished with increasing grit silicon carbide sandpaper and cleaned in an ultrasonic bath with ultra-pure water between each polishing step. The sample was then polished on a polishing pat with 1 μm , then $\frac{1}{4}$ μm diamond paste to achieve a fine polished surface. After polishing, the sample was cleaned in the ultrasonic bath once more to remove any residual polishing material. The sample was then inserted into the vacuum chamber of the endstation at the Australian Synchrotron where the following spectra were collected [25].

The binding energy scale of the $h\nu = 1487$ eV spectra were calibrated to the Fermi level at 0 eV. The strong leading edge of the S $2p$ $h\nu = 260$ eV spectrum was calibrated to match the leading edge of the S $2p$ $h\nu = 1487$ eV spectrum, assuming that the species present in the 260 eV spectrum are the same as in the 1487 eV spectrum, but with differing intensities. The S $2p$ spectra were normalised to the bulk peak to allow for comparison between the two samples.

8.2.1 Survey spectrum for polished pentlandite

The survey spectrum for the polished pentlandite sample is shown in Figure 8.8 (solid, blue line) and shows peaks arising from Fe, Ni, S, C and O species, with the quantification of these species shown in Table 8.2. The survey spectrum shows almost 40% contribution from carbon species, and just over 30% from oxygen species. The carbon species are expected to arise from a combination of adventitious carbon and introduced species from the polishing materials. The ratio of metal (Fe+Ni) to sulfur recorded in Table 8.2 shows less sulfur than is expected from the bulk ratio. Further observations can also be made from the binding energies of the Fe and Ni $2p$ peaks in the survey spectrum. The Ni $2p$ peak appears as a sharp peak at 853 eV, consistent with that observed for vacuum fractured pentlandite surfaces in Chapter 6. There is also a shoulder on the high binding energy side of the Ni $2p$ peak around 855 eV, which is likely due to either NiO species [26], or $\text{Ni}(\text{OH})_2$ species [4]. The Fe $2p$ peak appears around 711 eV, which is significantly higher binding energy than that for $\text{Fe}^{\text{II}}\text{-S}$ in pentlandite, observed at 707 eV in Chapter 6. FeOOH species are observed at binding energies around 711 eV [27], indicating that the iron species are significantly oxidised at the surface of the polished pentlandite sample.

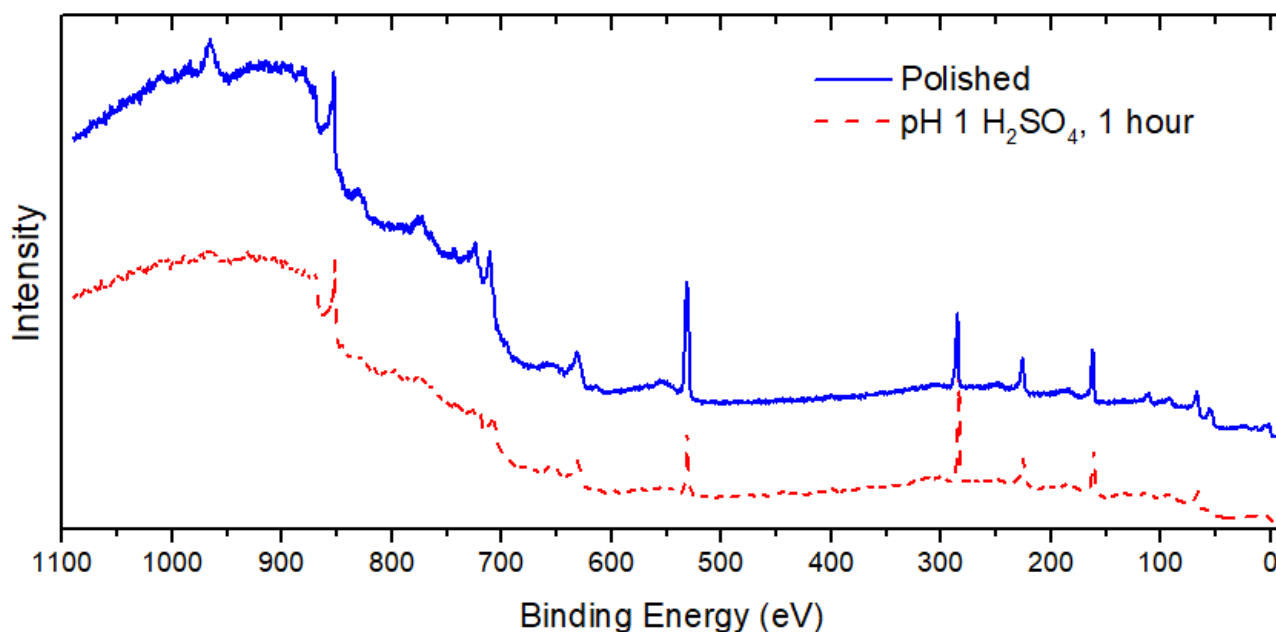
Figure 8.8: Survey spectrum for synthetic pentlandite surfaces, $h\nu = 1487$ eV.

Table 8.2: Quantification of species observed in the survey spectrum for the polished synthetic pentlandite surface shown in Figure 8.8.

Species	At%
Fe $3p$	9.1
Ni $3p$	8.5
S $2p$	11.8
O $1s$	30.8
C $1s$	39.8

8.2.2 S $2p$ photoelectron spectrum for polished pentlandite

Figure 8.9a shows the S $2p$ photoelectron spectrum for the polished pentlandite sample collected with $h\nu = 1487$ eV. A peak has been fitted at 161.4 eV, which is consistent with spectra presented in literature [3, 5]. Due to the similar binding energy with violarite peaks in literature [1, 2], this peak has tentatively been given the label “violarite”, but is most likely due to a violarite-like oxidation product, rather than the mineral phase. Additional features were fitted at 163.6 eV, due to polysulfide species, and at 166.8 eV, due to sulfite species.

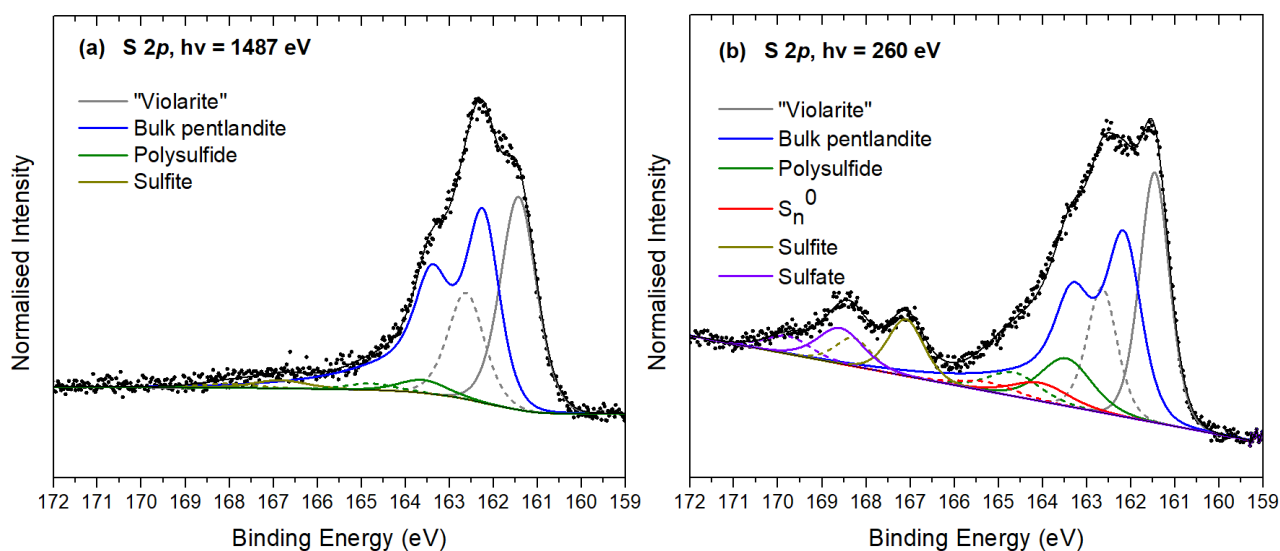


Figure 8.9: S 2p photoelectron spectra collected from polished pentlandite sample, with $h\nu =$ (a) 1487 eV, and (b) 260 eV.

The S 2p spectrum collected with $h\nu = 260$ eV is shown in Figure 8.9b and has a significantly different spectra shape to the bulk sensitive spectrum. Firstly, a linear background has been used in this spectrum to account for the relatively large secondary electron background and is fitted to the region below and above the S 2p spectrum. As discussed in Chapter 5, the intensity of the background is due to the increase in inelastic scattering events of the escaped photoelectrons, which is a result of the presence of an elementally distinct overlayer on the surface. This is considered evidence of an overlayer which likely consists of the oxyhydroxide species observed in the survey spectrum. The prominent peak in this surface sensitive spectrum is the violarite-like peak fitted at 161.5 eV. Also present is a significant contribution from polysulfide species at 163.5 eV, and sulfite and sulfate species fitted at 167.1 eV and 168.6 eV respectively. This spectrum also required an additional doublet fitted at a binding energy of 164.0 eV, which contributes to less than 5% of the fit, as seen in Table 8.3. This feature is in the binding energy region which can be attributed to elemental sulfur [22], and its presence on the sample is expected to be due to its entrapment within the near-surface layer, as was seen for the polished sample in Chapter 5.

Table 8.3: Binding energy, peak width, and % contribution from each species fitted to the $h\nu = 1487$ eV and 260 eV S $2p$ spectra shown in Figure 8.9. Binding energy and peak width (FWHM) are reported in units of eV.

$h\nu = 1487$ eV			$h\nu = 260$ eV		
Species	BE (FWHM)	%	Species	BE (FWHM)	%
“Violarite”	161.4 (0.97)	44.2	“Violarite”	161.5 (0.79)	32.0
Bulk pentlandite	162.2 (0.83)	49.8	Bulk pentlandite	162.2 (0.88)	37.3
Polysulfide	163.6 (1.3)	13.5	Polysulfide	163.5 (1.4)	10.5
Sulfite	166.8 (1.4)	2.5	Elemental sulfur	164.0 (1.5)	4.5
			Sulfite	167.1 (0.95)	8.7
			Sulfate	168.6 (1.2)	7.0

There are notable similarities between the polished pyrrhotite and polished pentlandite samples. Firstly, the quantification of species from the pentlandite survey spectrum reflect those for the polished pyrrhotite sample. The values for carbon and oxygen (39.8% and 30.8% respectively) are similar to those seen in the polished pyrrhotite sample (42.0% and 30.1% respectively). The S $2p$ spectra also share similarities, with the rise of polysulfide species, and specifically the entrapment of elemental sulfur, which is likely due to amorphous sulfur structure in the near surface layers. These similarities between the two samples indicates that the oxidation products and structure of the surface of these two oxidised minerals are similar.

8.3 Surfaces of pentlandite exposed to pH 1 H₂SO₄ for 1 hour

The following sample was cut from the same pentlandite sample used for the polished pentlandite results. This sample was polished using the method previously described. After polishing the sample and cleaning to remove residual polishing materials, the sample was placed in a beaker with pH 1 H₂SO₄ solution for 1 hour at ambient temperature. After the sample was removed from the acidic solution, it was carefully dried with a lint-free laboratory tissue, ensuring the analysis surface was not contaminated, and mounted to a sample holder, which was then inserted into the Australian Synchrotron soft X-ray beamline endstation [25].

The NEXAFS spectra in Figure 8.13 and images in Figure 8.14 were collected at the PEEM beamline (BL05B2) at the NSRRC as described in section 3.5 [25]. The Fe and Ni L edge spectra were both calibrated by comparison to spectra from the same mineral prepared using the same methods, and

measured at the Australian Synchrotron soft x-ray beamline. The PEEM images were collected with a 450 μm field of view. Images were taken with photon energies below the Fe and Ni absorption peaks, showing primarily topography of the sample surface. These images were used to remove the topography from the images collected with photon energies at key features in the NEXAFS spectra, such that only the distribution of chemical states remains in the resulting images. This background removal was done using the method described in section 3.5.1 using Eq. (5). The resulting images are shown in Figure 8.14.

8.3.1 Survey spectrum for pentlandite in pH 1 H_2SO_4

The survey spectrum for pentlandite in pH 1 H_2SO_4 is shown in Figure 8.10, with the survey spectrum for the polished sample included for comparison. The survey spectrum from the sample reacted in acid shows peaks from the same elements as was seen in the polished sample. Notably, the contribution from carbon species appears relatively greater, while the contribution from oxygen species appears relatively less in the pH 1 pentlandite sample, when compared to the polished sample. This is reflected in the quantification of elements, shown in Table 8.4. This shows that overall, the carbon species remains around 57% for both the polished and the pH 1 samples, while the oxygen species contributes approximately 30% to the polished sample, and only approximately 15% in the pH 1 pentlandite sample, indicating that some oxygen species have been removed by the exposure to sulfuric acid solution. The quantification in Table 8.4 also shows a decrease in Fe species due to exposure to sulfuric acid solution, where the overall contribution has decreased, and the ratio of Fe to Ni species has also decreased relative to the polished pentlandite sample. Furthermore, the ratio of metal to sulfur species in the sample of pentlandite exposed to acidic solution is much closer to the ratio expected from the bulk, whereas in the polished sample, the ratio of metal to sulfur was notably higher than expected from the bulk. This may indicate a removal of Fe species simultaneous with the removal of oxygen species.

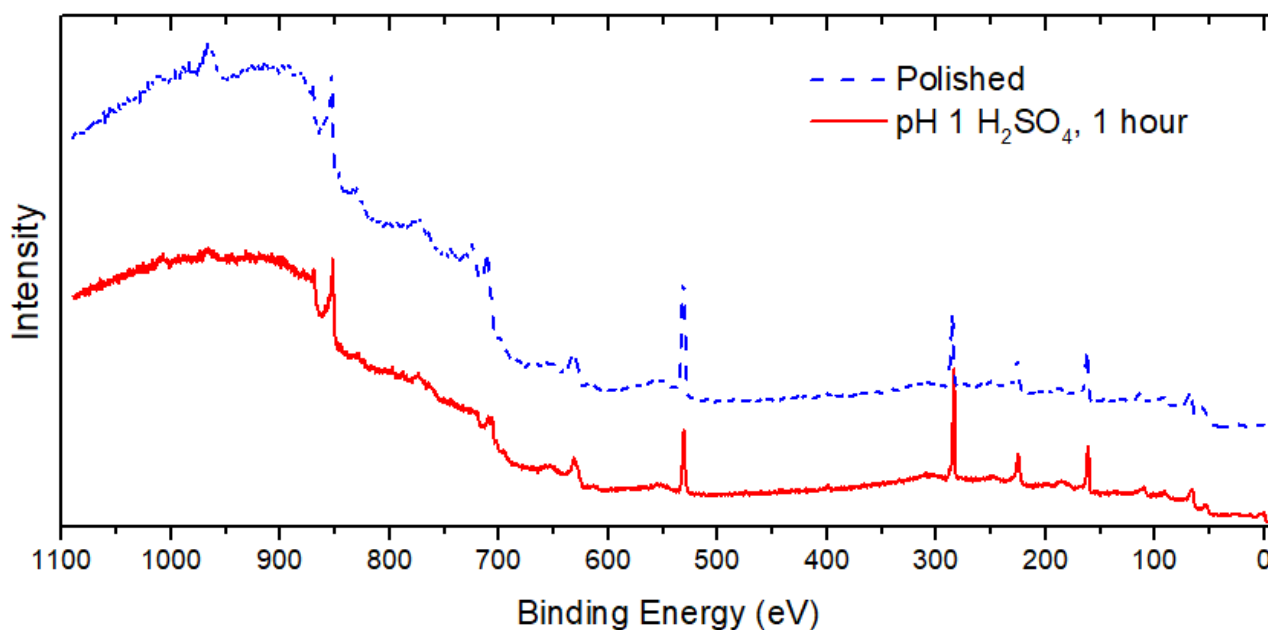


Figure 8.10: Survey spectrum for synthetic pentlandite surfaces, $h\nu = 1487$ eV.

Table 8.4: Quantification of species observed in survey spectrum for the surface of synthetic pentlandite in pH 1 H_2SO_4 shown in Figure 8.10. The quantification from the polished sample is included for comparison. These values are taken from Table 8.2.

Species	At%	(polished)
Fe 3 <i>p</i>	6.0	9.1
Ni 3 <i>p</i>	7.7	8.5
S 2 <i>p</i>	13.3	11.8
O 1 <i>s</i>	15.3	30.8
C 1 <i>s</i>	57.7	57.2

8.3.2 S 2*p* photoelectron spectrum for pentlandite exposed to pH 1 H_2SO_4 for 1 hour

The S 2*p* photoelectron spectrum for pentlandite in pH 1 H_2SO_4 shown in Figure 8.11a has a similar shape to pentlandite core-level sulfur spectra previously presented in Chapter 6. The main peak is at 162.2 eV and has been fitted with three symmetric peaks devised in Chapter 6 to model the high binding energy tail. The low binding energy side of the main peak has a broad slope. This broad slope was best fitted with two features at 161.1 eV and 161.6 eV, attributed to surface 3-coordinate sulfur, and surface and bulk 4-coordinate sulfur, respectively, as determined previously in this thesis. An attempt was made to fit the low binding energy slope with a single feature, as was done for the polished pentlandite sample, however the result was a poor fit, and an unreasonably large peak width was required to achieve a somewhat reasonable fit. The % contributions from 3-coordinate, 4-coordinate and bulk 5-coordinate sulfur are similar to those seen in vacuum fractured pentlandite

shown in Chapter 6, with a slight decrease in the 3- and 4-coordinate components. This is accompanied with the emergence of polysulfide, sulfite and sulfate species. It is not simple in this case to make the conclusion that the undercoordinated surface monosulfide species are reacting to form polysulfide, sulfite and sulfate species, since the sample is expected to have taken the form of the polished pentlandite sample previously shown. The surface structure of the polished pentlandite sample showed significant deviation from that of vacuum fractured pentlandite, with a single component at 161.4 eV replacing the two undercoordinated monosulfide species fitted to vacuum fractured pentlandite, and to the spectrum shown in Figure 8.11a. Furthermore, the peaks fitted to these surface monosulfide species are broader than those fitted to the vacuum fractured pentlandite samples shown in Chapter 6. A more likely pathway is that during exposure to acidic solution, the surface layers of the polished pentlandite sample are either dissolved somewhat, to reveal a more pristine pentlandite surface, or they are restructured to reproduce monosulfide species with similar electron density around the sulfur atom as in the 3-coordinate and 4-coordinate surface monosulfide species seen in the vacuum fractured pentlandite samples.

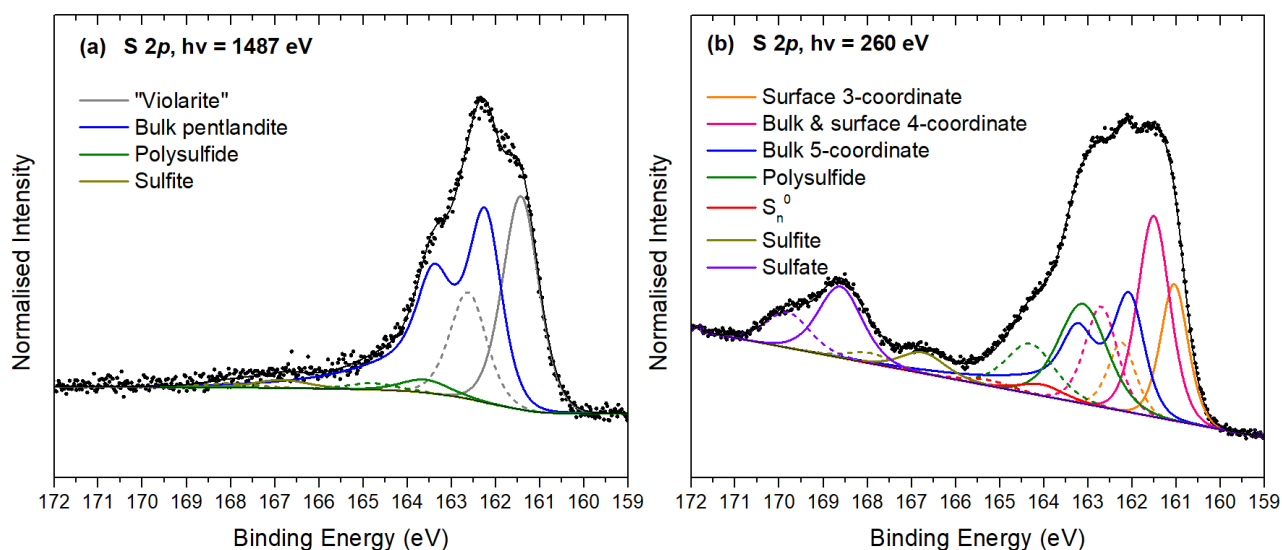


Figure 8.11: S 2p photoelectron spectra collected from the sample of pentlandite in pH 1 H₂SO₄ for 1 hour, with $h\nu =$ (a) 1487 eV, and (b) 260 eV.

The surface sensitive $h\nu = 260$ eV spectrum in Figure 8.11b has also been fitted with the surface 3-coordinate, surface and bulk 4-coordinate, and bulk 5-coordinate peaks at binding energies of 161.1 eV, 161.6 eV, and 162.2 eV respectively. The relative intensity of these peaks shows that the 3-coordinate and 4-coordinate peaks have large contributions from surface components, whereas the bulk 5-coordinate component contributes only 20% of the total fit to the spectrum, shown in Table 8.5. The $h\nu = 260$ eV spectrum required peaks to account for the polysulfide, sulfite and sulfate species, in agreement with the $h\nu = 1487$ eV spectrum. Additional to these, another component was

required to achieve a good fit to the spectrum and was fitted at 164.1 eV; consistent with the elemental sulfur fitted to the polished pentlandite surface sensitive spectrum. Although this feature only contributes 2% to the total fit, it was not possible to obtain a good fit to the spectrum without this feature, which is subsequently attributed to elemental sulfur. The presence of elemental sulfur in the S 2*p* spectrum for polished pentlandite, and polished pyrrhotite in Chapter 5 was attributed to the elemental sulfur being physically trapped by the sulfur-rich near surface layer. This feature was not seen in the pyrrhotite sample exposed to acidic solution, as the sulfur-rich surface layer forms a more crystalline structure after exposure to acidic solution and it loses its ability to trap the volatile elemental sulfur species. The presence of elemental sulfur in this pentlandite sample exposed to acidic solution indicates that this volatile species is still physically trapped within the surface layers.

Table 8.5: Binding energy, peak width, and % contribution from each species fitted to the $h\nu = 1487$ eV and 260 eV S 2*p* spectra shown in Figure 8.11. Binding energy and peak width (FWHM) are reported in units of eV.

$h\nu = 1487$ eV			$h\nu = 260$ eV		
Species	BE (FWHM)	%	Species	BE (FWHM)	%
Surface 3-coordinate	161.1 (0.73)	10.9	Surface 3-coordinate	161.1 (0.72)	15.1
Surface & bulk 4-coordinate	161.6 (0.77)	24.3	Surface & bulk 4-coordinate	161.6 (0.86)	26.2
Bulk pentlandite	162.2 (0.75)	56.6	Bulk pentlandite	162.2 (0.77)	20.7
Polysulfide	163.3 (1.2)	3.5	Polysulfide	163.2 (1.3)	19.7
Sulfite	166.8 (1.2)	2.2	Elemental sulfur	164.1 (1.2)	2.0
Sulfate	168.9 (1.6)	2.5	Sulfite	166.8 (1.2)	3.7
			Sulfate	168.7 (1.2)	12.6

8.3.3 Fe and Ni core-level spectra

The Fe 2*p* spectrum for pentlandite exposed to pH 1 H₂SO₄ solution for 1 hour is shown in Figure 8.12 with the Fe 2*p* spectra for Pn1 and Pn2 vacuum fractured samples, repeated from Chapter 6. The main 2*p*_{3/2} peak for the pentlandite sample in acidic solution is at 707 eV, which is consistent with the peak in the spectra for Pn1 and Pn2. In comparison to the vacuum fractured spectra, there is an increase in intensity in the spectrum around 710 eV, which shows the development of Fe^{III}-O species as a result of polishing and subsequent exposure to acidic solution [27]. The main 2*p*_{3/2} also appears to be less intense than in the vacuum fractured sample, which is owing to the stronger background in the spectrum for this sample. This may be due to the heterogeneity of the iron species throughout the

pentlandite sample [28], as the oxidised Fe species are expected only at the surface or in the near surface region, whereas the bulk is expected to consist of Fe-S. Although the shape of the Fe 2*p* spectrum for pentlandite exposed to acidic solution is similar to those of the vacuum fractured samples, the peak binding energy is significantly shifted from that of the polished pentlandite sample, showing that the exposure to acidic solution has a notable effect in removing the FeOOH species observed in the survey spectrum of polished pentlandite, revealing a surface which largely consists of Fe-S species, with a small contribution from Fe^{III}-O species.

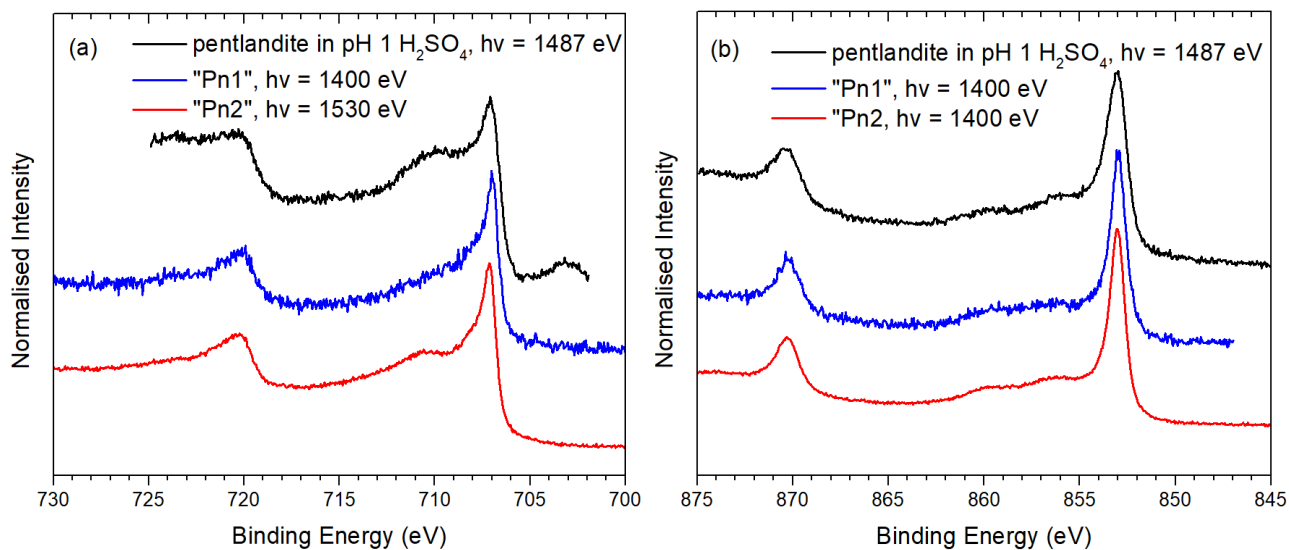


Figure 8.12: (a) Fe 2*p* spectrum and (b) Ni 2*p* spectrum for pentlandite exposed to pH 1 H₂SO₄ for 1 hour, compared to "Pn1" and "Pn2" from Chapter 6.

The Ni 2*p*_{3/2} peak for pentlandite exposed to acidic solution has a peak at 853.0 eV, consistent with the 2*p*_{3/2} peaks for the vacuum fractured pentlandite samples, also shown in Figure 8.12b. The shape of the 2*p* spectra for the three samples shown are almost identical, and the spectrum for pentlandite exposed to acidic solution differs only in a slight broadening of the main peak, which may indicate increasing disorder in the sulfur ligands binding to the nickel, rather than a significant change to the bonding or oxidation state of the Ni sites. Legrand, Bancroft and Nesbitt [4] observed the Ni 2*p* spectrum for pentlandite exposed to pH 9.3 solution after 60 minutes to have a decreased peak at 853 eV, with an increased intensity near 856 eV, owing to Ni(OH)₂ species. After 90 minutes in pH 9.3 solution, the peak at 856 eV had increased further, and additional intensity was seen at 857 eV, attributed to NiSO₄ species [4]. The survey spectrum for polished pentlandite showed a shoulder on the high binding energy side of the Ni 2*p* peak, around 855 eV, which may indicate the presence of NiO or Ni(OH)₂ species for a pentlandite sample polished in air. There is no clear evidence for oxidised Ni species for the pentlandite sample exposed to acid. Therefore, as was seen for the Fe species, the oxidised species that were observed for the polished pentlandite sample have been

removed by exposure to sulfuric acid solution, revealing a surface in which the metal sites resemble the metal sites of bulk pentlandite. In the case of the Ni sites, there is no clear evidence of oxidation of the Ni sites, whereas the Fe sites show some oxidation species, once again reinforcing the proposition that the Fe sites oxidise preferentially over the Ni sites.

This idea is once again reinforced by the Fe and Ni NEXAFS spectra for pentlandite exposed to acidic solution, shown in Figure 8.13a and b, respectively [25]. The shape of the Fe $L_{2,3}$ spectrum, shown in Figure 8.13a, deviates from the spectrum for Pn2, shown in Figure 6.13 in Chapter 6. Both spectra show the main peak around 707 eV, however unlike the Pn2 Fe $L_{2,3}$ spectrum, the acid exposed Fe L edge spectrum has a strong shoulder to the main peak, around 708 eV. A similar shoulder was observed for the Fe L edge spectrum for the pentlandite sample used for the pentlandite resonant valence band in section 7.2, for which the shoulder at 708 eV was attributed to Fe^{III} oxidised species (Figure 7.5). As was seen for this previous pentlandite sample, the L edge NEXAFS spectrum was much more sensitive to the presence of Fe^{III} species than the photoelectron spectrum due to the overlap of the Fe^{III} peak in the photoelectron spectrum with the Fe^{II} multiplet structure. This is also observed for the current sample exposed to acidic solution, which has minor evidence in the photoelectron spectrum of oxidised Fe species, but the strong shoulder in the L edge spectrum gives clear evidence of oxidised Fe species in the sample. In contrast, the shape of the Ni $L_{2,3}$ NEXAFS spectrum shown in Figure 8.13b has no observable difference to the Ni L edge spectra of the pentlandite samples shown in Figure 6.13b or in Figure 7.6.

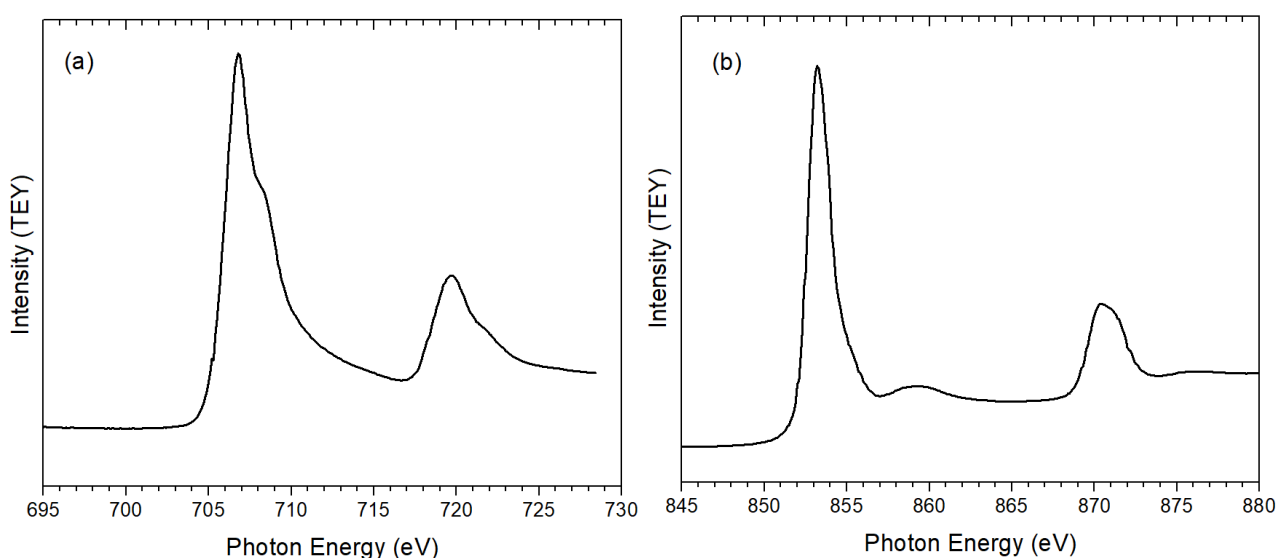


Figure 8.13: (a) Fe $L_{2,3}$ absorption spectrum, (b) Ni $L_{2,3}$ absorption spectrum for pentlandite in pH 1 H_2SO_4 solution for 1 hour.

Chapter 8: Pentlandite surfaces exposed to environmental conditions

PEEM images of the sample were taken at key energies from the NEXAFS spectra in Figure 8.13 [25], and have had a background image, taken from below the absorption edge, removed to reveal the distribution of chemical species, rather than the surface topography, with bright regions representing stronger intensity of that species, and darker regions showing less intensity. The images shown in Figure 8.14a, b and c are collected with photon energies corresponding to the Fe peak, the Fe shoulder, and the Ni peak, respectively. The distribution of Fe^{II} (peak at 707 eV) and Fe^{III} (shoulder at 708 eV) species is seen to be remarkably similar across the sample, showing that these species largely occupy the same space. The bright regions in the Ni image in Figure 8.14c occupy the alternate regions to the Fe species; however, Ni species can be seen across the whole field of view of the sample. The alternating Fe and Ni regions may be due to the orientation of the pentlandite grains, which could possibly reveal more Fe or more Ni species at the surface. However, this is not considered to be likely, as Xiong, Lu, Li, Cheng, Xu and Li [12] showed that pentlandite exposed to molecular oxygen caused the Fe atoms in pentlandite to migrate to the surface of the mineral to form a thin layer of Fe₂O₃, leaving a Ni-rich core. Considering this, it is more likely that the alternating patches of Fe and Ni on the surface of the sample shown in Figure 8.14 show regions which are more or less oxidised, where the bright Fe regions show where more Fe species have migrated to the surface to form oxidised Fe species, while the brighter Ni regions show where the sample is less oxidised and retains a more even stoichiometry. This patchy oxidation may subsequently be a result of the orientation of the crystal structure in the pentlandite sample, as different crystal orientations have been seen to affect the oxidation rate of other sulfide minerals [29]. Although these results do not definitely describe why the oxidation of the surface varies, they do show that the oxidation is not homogeneous, even for a sample which is polished to a smooth surface.

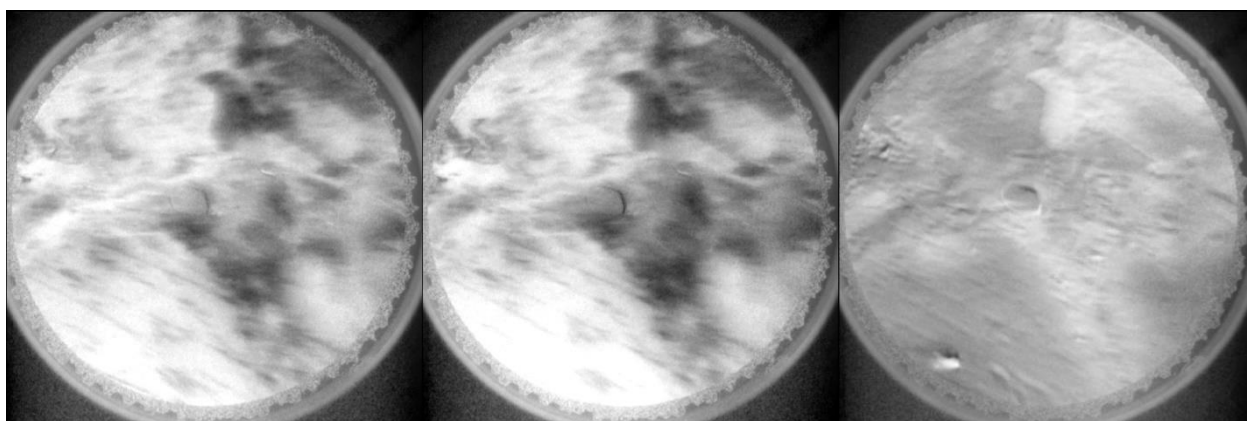


Figure 8.14: PEEM images collected at photon energies corresponding to (a) Fe L₃ peak (706.8 eV), (b) Fe L₃ shoulder (708.2 eV) (c) Ni L₃ peak (853.2 eV).

8.4 Discussion and comparison of oxidised pentlandite samples

The three samples shown in this chapter represent pentlandite samples at various stages of oxidation and show the products on the surface that result from oxidation under those conditions. The first sample was cleaved in an inert nitrogen atmosphere and dosed with 420 L of H₂O vapour under a controlled environment. Compared to the other two samples in this chapter, and many examples of pentlandite in literature, this represents a relatively small exposure to water vapour, and negligible exposure to other external oxidants. Therefore, this dosed sample gives an indication of the initial stages of oxidation of a pentlandite surface exposed to H₂O. The results showed that the Fe sites oxidise preferentially over the Ni sites, as previously observed [2-5, 12, 21]. However, evidence of alteration of the Ni sites was also observed as a slight shift in the peak in the more surface sensitive spectrum, but this peak was at significantly lower binding energy than previously recorded peaks for NiO species. The sulfur spectrum showed that the surface monosulfide species reacted with the H₂O vapour to form small amounts of sulfite and sulfate species, which were seen to bond to the Fe sites. The reconstruction of the surface due to exposure to H₂O vapour did not result in the formation of any disulfide or polysulfide species, but instead showed that the reaction of H₂O vapour with the fractured surface converted the surface monosulfide species to sulfur-oxy species, which attached to the Fe sites, but not the Ni sites.

The polished sample is the most remarkably different of the three samples provided in this chapter. The violarite-like component in the sulfur 2*p* spectrum and development of disulfide and polysulfides is a strong indication of significant restructuring of the surface, as is the notable shift to higher binding energies of both the Fe and Ni 2*p* core level shifts, showing strong contributions from FeOOH species, and NiO or Ni(OH)₂ species, respectively. In comparison, the pentlandite sample exposed to acidic solution after polishing shows relatively little variance from the fractured pentlandite surfaces shown in previous chapters. The Fe 2*p* photoelectron spectrum showed little evidence of oxidation, aside from a slight increase in intensity at 710 eV, compared to the vacuum fractured samples. The Fe L edge NEXAFS spectrum was more revealing of Fe^{III} species, with a clear shoulder to the main Fe^{II} L₃ peak, due to Fe^{III} species. In contrast, the Ni 2*p* photoelectron spectrum showed no clear evidence of alteration of Ni species from vacuum fractured samples, and this result was mirrored in the Ni L edge NEXAFS spectrum. The S 2*p* spectrum for the pentlandite sample exposed to acidic solution is the most revealing of its variance from pristine surfaces. While the S 2*p* spectrum once again shows peaks attributable to 3-coordinate and 4-coordinate monosulfide species, there are also significant contributions to the spectrum from polysulfide species, sulfite and sulfate species, and a small contribution from elemental sulfur, revealing the changes that have occurred to the surface of pentlandite during polishing and subsequent exposure to acidic solution.

The changes to the pentlandite surface due to polishing and then subsequent exposure to acidic solution follow a similar pattern to those of pyrrhotite under similar conditions, discussed in Chapter 5. It is well established in literature that Fe sites oxidise preferentially over Ni sites in the pentlandite lattice, and this result is replicated in the data presented in the current chapter. The sample dosed with H₂O vapour also showed evidence of alteration of the Ni sites. Although the survey spectrum of the polished pentlandite sample had strong evidence of significant oxidation of both the Fe and Ni sites, after exposure to acidic solution, only oxidation of the Fe sites could be detected. These results indicate that exposure of the sample to acidic solution effectively removes the oxidised Fe and Ni species from the previously air oxidised pentlandite surface to reveal metal species which largely resemble bulk pentlandite. The exception to this is the small oxidised Fe species which remain and were detected in the Fe L edge NEXAFS for pentlandite exposed to acidic solution. This small contribution from Fe^{III} species is therefore either due to exposure to acidic solution, or may have formed in the short time between removing the sample from solution and placing it in vacuum in the beamline endstation. The formation of oxidised Fe, but not Ni species, is explained by the propensity for Fe species to migrate to the surface of the sample and oxidise preferentially over the Ni species. The removal of oxidised metal species drives the equilibrium, to which the sample responds by oxidising more Fe species in preference over Ni species.

The oxidation of metal species at pentlandite surfaces is likely affected by structure of the sulfur species at the surface. The pentlandite sample dosed with H₂O vapour showed remarkably little deviation in sulfur species from the more pristine pentlandite sample analysed in section 6.3, where the biggest observed change was the conversion of 3-coordinate and 4-coordinate surface monosulfide species to sulfite and sulfate species. In comparison, the S 2*p* spectrum for the polished pentlandite sample showed significant restructuring of the lattice, to create a violarite-like 4-coordinate monosulfide peak in replacement of the surface 3-coordinate and 4-coordinate monosulfide components of more pristine pentlandite surfaces. The polished pentlandite sample also had significant contributions from disulfide and polysulfide species, with some evidence of elemental sulfur, likely trapped by the extensive polysulfide layer, as was seen for the polished pyrrhotite sample. The pentlandite sample which was exposed to acidic solution showed the restoration of low binding energy peaks attributable to 3-coordinate and 4-coordinate surface monosulfide species, indicating a return to a surface structure which more closely resembles a pristine pentlandite surface. However, this surface still showed strong peaks due to a polysulfide layer, in addition to sulfite and sulfate peaks.

Chapter 8: Pentlandite surfaces exposed to environmental conditions

The polysulfide layer on the pentlandite sample exposed to acidic solution may be hindering the oxidation of metal states which would replace those removed from the surface during the acidic exposure. The understanding that polysulfide layers cause passivation of a sulfide mineral's surface was reasonably ubiquitous [30-32]. However, in more recent years this idea has been challenged, and it has been suggested that rather than true passivation, polysulfide layers cause pseudo-passivation, observed as a decrease in dissolution rate [33]. Thomas, Jones, Skinner and Smart [34] observed a change in dissolution rate of pyrrhotite as a result of the composition of the outermost surface species. The initial dissolution of the outermost FeOOH layer is quick, but as that layer is removed and the remaining outermost layer is a metal deficient polysulfide, the dissolution is inhibited [34]. As the oxidised Fe and Ni species, observed on the polished pentlandite sample, are removed by exposure to acidic solution, the replacement of these species with more oxidised metal species is inhibited by the extensive polysulfide layer, which is removed from the surface at a much slower rate. It is subsequently possible that the Fe species oxidise preferentially over the Ni species due to their mobility within the lattice, as observed by Xiong, Lu, Li, Cheng, Xu and Li [12]. This explanation also accounts for why the Ni species in the pentlandite sample dosed with H₂O vapour shows some evidence of alteration of Ni sites, despite the relatively low dose. The S 2*p* spectrum for this sample showed no strong evidence of a polysulfide layer, therefore there is no polysulfide layer to inhibit the oxidation of metal species. Furthermore, since there is less alteration of the surface of the dosed pentlandite surface, there is less opportunity for the Fe species to diffuse to the surface, resulting in some minor changes to the Ni sites.

A key outcome of this study is the observation of the extent of the alteration of pentlandite surfaces due to polishing and subsequent exposure to acidic solution, in particular. The results in this chapter have shown that the polished sample has the most altered surface in comparison to vacuum fractured pentlandite, and that the sample exposed to acidic solution is comparatively similar to pristine pentlandite surfaces, with some key differences, as discussed. Yet, the S 2*p* spectrum for the polished pentlandite sample in this chapter was the most similar to pentlandite S 2*p* spectra shown in literature [2, 3, 5]. The violarite-like S 2*p* peak fitted at 161.4 eV was observed in work by Goh, Buckley, Lamb, Fan, Jang and Yang [5] to increase with subsequent oxidation, and is shown here to be a product of significant oxidation in air due to polishing, but is not observed in the sample dosed with H₂O vapour, or the sample exposed to acidic solution. This shows that previous studies which investigate pentlandite surfaces have likely not fully appreciated the changes which occur to surfaces as a result of sample preparation. This stems from the early studies on pentlandite, which use abrasion to create reproducible surfaces, in the absence of natural fracture or cleavage planes. Without the sample preparation techniques required to achieve pristine surfaces, and high resolution spectroscopy,

the features of pristine pentlandite surfaces have not been observed, and the features which have been remarked on in literature have been a subject of discussion [3-5, 35]. The results presented in this chapter, and their comparison to the pristine pentlandite surfaces presented elsewhere in this thesis, are crucially important to show the extent of surface oxidation which occurs when pentlandite samples are exposed to air and to acidic solution.

8.5 Conclusion

This chapter has presented pentlandite samples oxidised in three different ways; fractured in an inert nitrogen atmosphere the oxidised using a controlled dose of 420 L ($420 \text{ seconds} \times 10^{-6} \text{ Torr}$) H_2O vapour, polished in air using up to $\frac{1}{4} \mu\text{m}$ diamond paste, and polished then exposed to pH 1 H_2SO_4 solution for 1 hour at ambient temperature. The results from the dosed sample showed that even in the initial stages of oxidation, the Fe species oxidise more rapidly than the Ni sites. Polishing the pentlandite sample caused the most alteration to the surface, which included a violarite-like sulfur product in addition to an extensive polysulfide layer which accompanied oxidised Ni and especially Fe species. Exposure to acidic solution effected the removal of the oxidised metal species and the violarite-like sulfur species, returning the monosulfide species to something more closely resembling pristine pentlandite, yet the polysulfide species remain.

Although it is well established in literature, this chapter has further shown the propensity for Fe species to oxidise preferentially over Ni species due to their ability to diffuse through the pentlandite lattice. The possibility of this diffusion being hindered by an extensive polysulfide layer has been discussed, and is a likely cause of the oxidation of Fe species, but not Ni species, in the sample exposed to acidic solution, after the FeOOH and Ni(OH)_2 species were removed from the polished sample. The absence of polysulfide species on the dosed sample is likely linked to the alteration of Ni sites, as the minimal restructuring of the surface prevents the diffusion of metal ions through the lattice.

This chapter has characterised the surfaces of pentlandite polished in air and subsequently exposed to acidic solution, and by doing so in comparison to pristine and near pristine pentlandite surfaces, has shown the extent of surface alteration experienced by samples prepared in such ways. Although the polished sample showed the greatest alteration from pristine and near pristine surfaces, the S $2p$ spectrum was the most similar to those seen in previous literature. The understanding provided by the results in this chapter of the changes which occur to pentlandite surfaces is a significant contribution to scientific knowledge and will inform future studies of how sample preparation affects the surfaces of pentlandite samples and similar materials.

8.6 References

- [1] S. Richardson, D.J. Vaughan, Surface alteration of pentlandite and spectroscopic evidence for secondary violarite formation, *Mineralogical magazine*, 53 (1989) 213-222.
- [2] A.N. Buckley, R. Woods, Surface composition of pentlandite under flotation-related conditions, *Surface and Interface Analysis*, 17 (1991) 675-680.
- [3] D.L. Legrand, G.M. Bancroft, H.W. Nesbitt, Surface characterization of pentlandite, $(\text{Fe,Ni})_9\text{S}_8$, by X-ray photoelectron spectroscopy, *International Journal of Mineral Processing*, 51 (1997) 217-228.
- [4] D. Legrand, G. Bancroft, H. Nesbitt, Oxidation/alteration of pentlandite and pyrrhotite surfaces at pH 9.3: Part 1. Assignment of XPS spectra and chemical trends, *American Mineralogist*, 90 (2005) 1042-1054.
- [5] S.W. Goh, A.N. Buckley, R.N. Lamb, L.-J. Fan, L.-Y. Jang, Y.-w. Yang, Pentlandite sulfur core electron binding energies, *Phys Chem Minerals*, 33 (2006) 445-456.
- [6] M. Fronzi, S.A. Tawfik, C. Stampfl, M.J. Ford, Magnetic properties of stoichiometric and defective Co_9S_8 , *Physical Chemistry Chemical Physics*, 20 (2018) 2356-2362.
- [7] H.R. Chauke, D. Nguyen-Manh, P.E. Ngoepe, D.G. Pettifor, S.G. Fries, Electronic structure and stability of the pentlandites Co_9S_8 and $(\text{Fe,Ni})_9\text{S}_8$, *Physical Review B*, 66 (2002) 155105.
- [8] Q. Hu, G. Li, X. Liu, B. Zhu, G. Li, L. Fan, X. Chai, Q. Zhang, J. Liu, C. He, Coupling pentlandite nanoparticles and dual-doped carbon networks to yield efficient and stable electrocatalysts for acid water oxidation, *Journal of Materials Chemistry A*, 7 (2019) 461-468.
- [9] Y. Tang, H. Yang, J. Sun, M. Xia, W. Guo, L. Yu, J. Yan, J. Zheng, L. Chang, F. Gao, Phase-pure pentlandite $\text{Ni}_{4.3}\text{Co}_{4.7}\text{S}_8$ binary sulfide as an efficient bifunctional electrocatalyst for oxygen evolution and hydrogen evolution, *Nanoscale*, 10 (2018) 10459-10466.
- [10] I. Zegkinoglou, A. Zendegani, I. Sinev, S. Kunze, H. Mistry, H.S. Jeon, J. Zhao, M.Y. Hu, E.E. Alp, S. Piontek, M. Smialkowski, U.-P. Apfel, F. Körmann, J. Neugebauer, T. Hickel, B. Roldan Cuenya, Operando Phonon Studies of the Protonation Mechanism in Highly Active Hydrogen Evolution Reaction Pentlandite Catalysts, *Journal of the American Chemical Society*, 139 (2017) 14360-14363.
- [11] P.P. Mkhonto, H.R. Chauke, P.E. Ngoepe, Ab initio Studies of O_2 Adsorption on (110) Nickel-Rich Pentlandite ($\text{Fe}_4\text{Ni}_5\text{S}_8$) Mineral Surface, *Minerals*, 5 (2015) 665-678.
- [12] X. Xiong, X. Lu, G. Li, H. Cheng, Q. Xu, S. Li, Energy dispersive spectrometry and first principles studies on the oxidation of pentlandite, *Physical Chemistry Chemical Physics*, 20 (2018) 12791-12798.
- [13] C.N. Waterson, J.O. Sindt, J. Cheng, P.A. Tasker, C.A. Morrison, First-principles study on ligand binding and positional disorder in pentlandite, *The Journal of Physical Chemistry C*, 119 (2015) 25457-25468.
- [14] D.A. Shirley, High-Resolution X-Ray Photoemission Spectrum of the Valence Bands of Gold, *Physical Review B*, 5 (1972) 4709-4714.
- [15] J.J. Yeh, I. Lindau, Atomic subshell photoionization cross sections and asymmetry parameters: $1 \leq Z \leq 103$, *Atomic Data and Nuclear Data Tables*, 32 (1985) 1-155.
- [16] V.P. Zakaznova-Herzog, H.W. Nesbitt, G.M. Bancroft, J.S. Tse, X. Gao, W. Skinner, High-resolution valence-band XPS spectra of the nonconductors quartz and olivine, *Physical Review B*, 72 (2005) 205113.
- [17] T. Yamashita, P. Hayes, Analysis of XPS spectra of Fe^{2+} and Fe^{3+} ions in oxide materials, *Applied Surface Science*, 254 (2008) 2441-2449.
- [18] C. Ruby, B. Humbert, J. Fussy, Surface and interface properties of epitaxial iron oxide thin films deposited on $\text{MgO}(001)$ studied by XPS and Raman spectroscopy, *Surface and Interface Analysis*, 29 (2000) 377-380.
- [19] S. Mattila, J.A. Leiro, M. Heinonen, XPS study of the oxidized pyrite surface, *Surface Science*, 566-568 (2004) 1097-1101.

- [20] Y. Mikhlin, Y. Tomashevich, Pristine and reacted surfaces of pyrrhotite and arsenopyrite as studied by X-ray absorption near-edge structure spectroscopy, *Phys Chem Minerals*, 32 (2005) 19-27.
- [21] Z.E. Pettifer, J.S. Quinton, W.M. Skinner, S.L. Harmer, New interpretation and approach to curve fitting synchrotron X-ray photoelectron spectra of (Fe,Ni)₉S₈ fracture surfaces, *Applied Surface Science*, 504 (2020) 144458.
- [22] R.S.C. Smart, W.M. Skinner, A.R. Gerson, XPS of sulphide mineral surfaces: metal-deficient, polysulphides, defects and elemental sulphur, *Surface and Interface Analysis*, 28 (1999) 101-105.
- [23] S. Tougaard, P. Sigmund, Influence of elastic and inelastic scattering on energy spectra of electrons emitted from solids, *Physical Review B*, 25 (1982) 4452-4466.
- [24] P.R. Norton, R.L. Tapping, Photoelectron spectroscopic study of the interaction of nickel and oxygen, *Faraday Discussions of the Chemical Society*, 60 (1975) 71-80.
- [25] Z.E. Pettifer, A Study of the Dissolution of Iron and Nickel Sulfides and the Effect of Mixed Mineral Systems [Honours thesis], Flinders University, *Some of the data of this sample was presented in a previous honours thesis, however the analysis is original to the present PhD thesis*, 2014.
- [26] M.C. Biesinger, B.P. Payne, A.P. Grosvenor, L.W.M. Lau, A.R. Gerson, R.S.C. Smart, Resolving surface chemical states in XPS analysis of first row transition metals, oxides and hydroxides: Cr, Mn, Fe, Co and Ni, *Applied Surface Science*, 257 (2011) 2717-2730.
- [27] S. Suzuki, K. Yanagihara, K. Hirokawa, XPS study of oxides formed on the surface of high-purity iron exposed to air, *Surface and Interface Analysis*, 30 (2000) 372-376.
- [28] S. Tougaard, Improved XPS analysis by visual inspection of the survey spectrum, *Surface and Interface Analysis*, 50 (2018) 657-666.
- [29] J.M. Guevremont, A.R. Elsetinow, D.R. Strongin, J. Bebie, M.A.A. Schoonen, LETTERS. Structure sensitivity of pyrite oxidation: Comparison of the (100) and (111) planes, *American Mineralogist*, 83 (1998) 1353.
- [30] B.K.L. So, R.W.M. Kwok, G. Jin, G.Y. Cao, G.K.C. Hui, L. Huang, W.M. Lau, S.P. Wong, Reordering at the gas-phase polysulfide passivated GaAs(110) surface, *Journal of Vacuum Science & Technology A*, 14 (1996) 935-940.
- [31] Y. Liu, Z. Dang, P. Wu, J. Lu, X. Shu, L. Zheng, Influence of ferric iron on the electrochemical behavior of pyrite, *Ionics*, 17 (2011) 169-176.
- [32] R.P. Hackl, D.B. Dreisinger, E. Peters, J.A. King, Passivation of chalcopyrite during oxidative leaching in sulfate media, *Hydrometallurgy*, 39 (1995) 25-48.
- [33] P.R. Holmes, F.K. Crundwell, Polysulfides do not cause passivation: Results from the dissolution of pyrite and implications for other sulfide minerals, *Hydrometallurgy*, 139 (2013) 101-110.
- [34] J.E. Thomas, C.F. Jones, W.M. Skinner, R.S.C. Smart, The role of surface sulfur species in the inhibition of pyrrhotite dissolution in acid conditions, *Geochimica et Cosmochimica Acta*, 62 (1998) 1555-1565.
- [35] S.W. Goh, A.N. Buckley, R.N. Lamb, W.M. Skinner, A. Pring, H. Wang, L.-J. Fan, L.-Y. Jang, L.-J. Lai, Y.-w. Yang, Sulfur electronic environments in α -NiS and β -NiS: examination of the relationship between coordination number and core electron binding energies, *Phys Chem Minerals*, 33 (2006) 98-105.

9 STXM – A NEW METHOD OF MINERALS ANALYSIS

This focus of this thesis has been the analysis of photoelectron spectra for the sulfide minerals pyrrhotite and pentlandite under both pristine and oxidative conditions. As demonstrated in previous chapters, the implications of accurate and detailed analysis of spectra are profound for many fields of research. The most pertinent for the sulfide minerals pentlandite and pyrrhotite are for separation of minerals phases by froth flotation for minerals processing, the catalytic activity of the surfaces of these minerals, and the effect of their leaching on acid mine drainage. For each of these fields of research, the *surfaces* of these minerals and their interactions with the environment play a key role in their reactions. Hence why so much focus has been given to the surface electronic structure in previous chapters.

While the application of the knowledge explored in this thesis so far may have profound effects on other fields of research, the direct application of these minerals is not the ultimate motivation behind this work. One of the aims of this thesis is to impress upon the reader the level of detail which can be obtained from spectra, and that a little more than an initial observation of data may reveal a deeper understanding of the samples that are being analysed. This has been a driving motivation of the previous chapters; using materials of possible interest to investigate ways to form a deeper understanding of the materials using existing techniques to their greater potential.

A deeper understanding of materials may be gained from microscopy techniques in addition to spectroscopy techniques, and even more so, techniques which combine both aspects simultaneously. For many fields of research, the location and distribution of chemical species across a surface is profoundly important for the activity of that surface and its application in industry or devices. For example, the distribution of surface species on a catalyst may explain the activity, inhibition, or stability of that catalyst [1]. Similarly, the distribution of oxidation species on a mineral particle may affect the flotability [2]. Other microscopy techniques have been applied to sulfide minerals and similar systems with success, some of which also provide chemical information, such as scanning electron microscopy (SEM) when coupled with energy dispersive X-ray spectroscopy, Auger electron spectroscopy (AES), and scanning tunnelling microscopy (STM), to name a few (see [3] and references therein).

A relatively new advancement in microscopy techniques is Scanning Transmission X-ray Microscopy, which combines microscopy and spectroscopy with spatial resolution of up to 10 nm [4]. STXM uses photons in the soft X-ray regime, which includes the K shell absorption edge of light

elements such as carbon, nitrogen and oxygen, and the L shell absorption edges of many heavier elements, including the first row transition metals. Therefore, soft X-ray techniques are sensitive to many elements commonly found in biological or mineral samples and are useful for a wide range research fields.

The low radiation dose (compared to higher energy imaging or spectroscopy techniques) makes STXM more appropriate for soft matter samples. Additionally, the soft X-rays of STXM fall within the “water window”, where water is transparent to X-rays between the C K edge (around 280 eV) to the O K edge (around 530 eV). These properties make this technique highly favourable for analysis of a wide range of samples, such as biological samples [5], and organic matter found in marine sediments [6]. The sensitivity of the soft X-ray regime to the carbon K edge makes it particularly powerful for analysis of carbon based materials, such as for mapping soil components [7], mapping components of DNA, RNA and proteins in mammalian cells [8-10], mapping carbohydrates, polysaccharides and lipids in biofilms [11], and investigating the structure of rubrene hydrocarbon semiconductors [12]. Some of these studies have showed that such an analysis has potential for quantitative or semi-quantitative mapping of such species [7, 9-11, 13, 14].

There have been a few examples of applying STXM to mineral systems. For example, STXM has been used to study microbial induced calcification, by studying the C, N and O K edges, and Ca L edge of mineral deposits [15]. Al-containing mineral nanoparticles have been characterised and mapped in aqueous solutions containing microbes, and the interactions between the microbes and the Al-containing mineral particles investigated [16]. The semi-quantitative aspect of STXM has also been used to study the $\text{Fe}^{2+}/\text{Fe}^{3+}$ ratios of silicates collected from different geological sites to show the spatial distribution of these ratios on the sub-micrometer scale [17]. However, despite the potential offered by this technique, the chemical sensitivity to first row transition metals, and the possibility to investigate hydrated samples, STXM has not been used extensively for studying mineral systems, and has not yet been applied to sulfide minerals.

This technique offers a new opportunity to analyse sulfide mineral samples in a more natural environment. Many of the techniques currently used for spectroscopic or microscopic analysis of mineral samples, require the sample to be in vacuum, or highly processed. The real benefit of STXM which sets it apart from other techniques is the ability to analyse samples in more natural environments, such as in air, or sealed within solution. Unlike other similar X-ray spectroscopy techniques, the X-rays only have to pass through a small distance between exiting the beamline and passing through to the detector. This allows samples to be analysed at atmospheric pressure, either in

air or in an evacuated chamber backfilled with helium, which is transparent in the soft X-ray region. This allows for the effects of subjecting a sample to vacuum environments to be eliminated, and hydrated samples to be investigated [18], with a particular interest in biofilms [14, 19-21]. The challenges of adapting a relatively new technique to a different set of samples are not trivial, and the few examples in literature of STXM used for mineral samples examine mineral nanoparticles [15, 16], or samples which have been thinned using a focussed ion beam [17]. Therefore, the aim of this chapter is to explore the viability of using STXM for sulfide minerals research; to identify the advantages and challenges of this technique in simple sulfide mineral systems, and the effect of analysing samples in a dry environment vs a hydrated environment is explored. This chapter also identifies the possibility of identifying minority species in samples, and contributes to a discussion in the literature about the origin of a pre-edge peak in the Cu L₃ absorption spectrum for the copper sulfide mineral chalcocite (Cu₂S). Finally, this chapter will highlight the possibility of extending the research capability to in situ analysis of electrochemical systems, thereby encouraging the use of this technique to extend the possibilities for minerals research.

9.1 Methods

The data presented in this chapter was collected at either the Soft X-ray Spectromicroscopy (SM) beamline (10ID-1) at the Canadian Light Source (CLS) in Saskatoon, Canada, or the PoLux beamline at the Swiss Light Source (SLS) in Villigen, Switzerland. Both beamlines are described in section 3.6.1 and the beamline which the analysis of each sample was carried out is noted for individual samples. Samples were prepared on 100 nm thick silicon nitride membrane windows from Norcada (www.norcada.com). The electrochemical membranes had printed Au electrodes, designed by an International consortium [22] for use in an early design of a flow through electrochemical cell, and were manufactured by Norcada.

All analysis of spectra, images and stacks was performed using the Axis2000 software (analysis of X-ray Images and Spectra) [23]. The photon energy at the CLS beamline did not require correction, however this was checked by comparing a Cu L edge spectrum from chalcocite to that previously published [24]. The photon energy of the SLS beamline required a correction at the Cu L edge of -3.5 eV, which was applied to each spectrum and stack.

Since sample thickness is a concern for STXM, the samples presented in this chapter were prepared by grinding the chalcocite to a fine powder using a mortar and pestle, to reduce the particle size, then mixing with solution before either drop casing the sample onto a sample holder and allowing it to dry (dry samples), or sealing the particle and solution between two windows using epoxy adhesive around

the edges of the window (hydrated samples). The pH of each solution was adjusted with H₂SO₄ or KOH in ultrapure water before the ground mineral was added. Some solutions include a small quantity of sodium ethyl xanthate (CH₃CH₂OCS₂Na, referred to in this thesis as NaEX), with a concentration of up to 10⁻⁴ M. This was part of an attempt to observe the interaction of the ethyl xanthate ligand with the chalcocite surface. In general, the xanthate solution was found to be too dilute to observe a carbon signal, and this detail is therefore not a focus of this chapter. However, it is noted for each sample, and the effects of the xanthate solution are contemplated in section 9.3.2.

9.2 Advantages and challenges of using STXM for minerals

The reasons driving the analysis of mineral samples using STXM include the technique's chemical sensitivity, spatial resolution, but most importantly, the ability to analyse samples in more natural environments such as in solutions relating to flotation, mineral leaching, or oxidative solutions, such as those analysed in Chapters 5 and 8.

Since STXM gathers soft X-ray NEXAFS spectra, this technique is highly sensitive to changes in the sample. The Cu L₃ absorption edge is particularly sensitive to copper oxidation state. The L edge spectrum for divalent copper has a distinctive sharp peak around 931 eV attributed to the excitation of 2*p* electrons to the 3*d* valence band, whereas monovalent copper has a less intense, broader structure around 935 – 940 eV, due to the excitation of 2*p* electrons to 4*s* states [25]. In the ground state, divalent copper has mostly 3*d*⁹ character, hence the final state is mostly 2p3d¹⁰, however in covalent compounds, there is a mixture of 3*d*⁹ and 3*d*¹⁰L ground states, approximately 60% and 40% respectively for CuO, which corresponds to 2p3d¹⁰ and 2p3dL final states [26-28]. The energy of the sharp divalent absorption peak is lower than the broad monovalent structure due to the Coulomb interaction between the filled 3*d* band and the 2*p* core hole in the final state, which causes a localisation of the 3*d* states, thereby reducing the energy of this final state [27, 28]. For monovalent copper compounds, the ground state is predominantly 3*d*¹⁰ character, and therefore electrons cannot be excited to the 3*d* band, hence the structure is due to the 2p4s and 2p4s²L final states, which are significantly mixed with the sulfur ligand 3*p* states [25, 27, 28].

The spatial resolution offered by this technique is also potentially advantageous for various fields of mineral research. Froth flotation in particular relies on the hydrophobicity of individual particles to separate mineral phases. The distribution of hydrophobic and hydrophilic species across a particle may have a profound effect on the overall flotability of a particle, but is a difficult subject to study. By using techniques which map the spatial distribution of chemical species across the mineral, a deeper understanding of these effects can be gained [29-31].

The aim of this section is to showcase the potential for STXM to be used to investigate the chemical species on a sulfide mineral sample, and how these change across different sample environments. This section highlights the ability of STXM to identify distribution of species across a sample, and analyse samples in either dry or hydrated environments. A discussion of these advantages and the challenges associated is included, with proposed methods to counteract these challenges.

9.2.1 Simple analysis reveals spatial distribution of species

STXM can acquire three types of data; spectra, 2 dimensional images, and 3 dimensional stacks, which incorporate images and spectra, and from which spectra can be acquired from each pixel. The following sample is a particle of chalcocite (Cu_2S) which has been prepared in a pH 4 xanthate solution and dropped onto a single silicon nitride window and allowed to dry. This sample is used to show that a simple measurement of a sample with a combination of spectra and images can provide a reasonable and quick analysis of a sample. The data for the following sample was gathered at the SLS PolLux beamline.

The image in Figure 9.1a is a 2D image collected at a photon energy immediately below the Cu L absorption edge, shown in transmission mode, where bright regions show high photon transmission, and darker regions represent areas of thicker sample or greater absorption due to Cu species. The image is converted to optical density, using Eq. (8), and is shown in Figure 9.1b. The blue line in Figure 9.1b indicates a line from which a line scan was collected. The line scan generates a transmission spectrum at each pixel, which can be converted to an absorption spectrum using an appropriate I_0 signal. For this sample, an external I_0 signal was chosen, and is shown in the inset to Figure 9.1c, since the spectrum from the region outside of the particle showed some structure due to Cu^{II} species. The averaged spectrum over the particles is shown in Figure 9.1c.

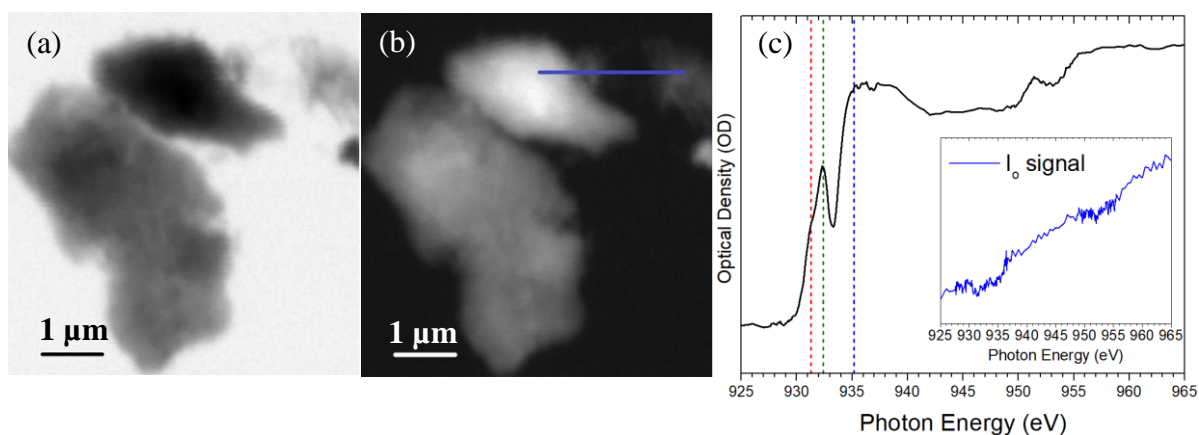


Figure 9.1: (a) Transmission image of chalcocite particle collected at 926.5 eV, just below the Cu L₃ absorption edge. (b) Optical density image of chalcocite particle. (c) Cu L_{2,3} absorption spectrum averaged over the blue line indicated in (b); inset spectrum is the external I₀ signal used to convert the spectrum to OD.

The averaged spectrum shows a broad peak around 935 eV, with a smaller peak at 932.4 eV, and a shoulder at 931.2 eV. Since the intensities of these three spectral features were observed to differ relative to one another in the spectra averaged over smaller areas in the line scan, they are temporarily assumed to be due to different chemical species. Images collected at these distinct photon energies can show the distribution of these chemical states, as shown in Figure 9.2. The images in Figure 9.2a-c are taken at the photon energies of interest indicated in the spectrum in Figure 9.1c, as shown by their respective colours.

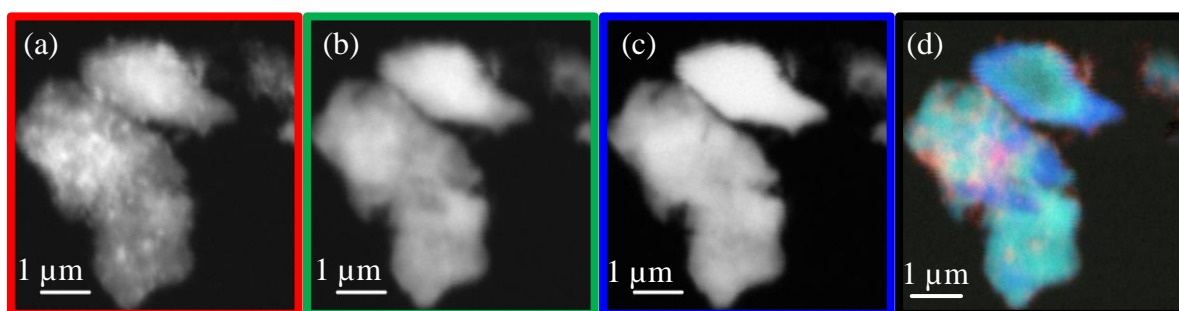


Figure 9.2: Image of chalcocite particles converted to optical density, collected with a photon energy of (a) 931.3 eV, (b) 932.4 eV, (c) 935.2 eV, and (d) RGB overlay of (a), (b), and (c) respectively. Scale = 1 μm.

Figure 9.2 shows that the species represented at 931.3 eV (which is the region for Cu^{II} species [27, 28, 32, 33]) are arranged somewhat in clusters on the sample, whereas the species represented at 932.4 eV and 935.2 eV are distributed across the whole chalcocite sample, but with differing intensities. This is most clearly visible in the red-green-blue (RGB) overlay image in Figure 9.2d, where the sample appears a mixture of green/blue, representing the images in Figure 9.2b & c

respectively, while the species in Figure 9.2a are shown in red, scattered in clustered regions across the sample.

9.2.2 Hydrated samples allow a degree of spatial freedom: the particles float

Hydrated samples are prepared by immersing the sample in solution, then depositing the solution onto a window. A second window is placed on top, as shown in Figure 9.3, encapsulating the liquid between the two windows. To achieve the correct thickness of solution, to ensure the sample is wet, but is not too thick in general for a good analysis, the amount of solution between the windows is adjusted by either adding more solution with a micropipette at the edges of the windows, or wicking away some of the solution with a lint-free wipe at the edges of the windows. The correct amount of solution can be observed under an optical microscope, by observing Newton's rings, caused by the interference of reflected light between the two windows, which indicates that the liquid between the windows is thin enough to allow a good transmission signal. The optimum thickness of a sample is determined by the incident photon energy and the elements present in the sample. Generally, a thickness which achieves a transmission signal of 1 – 2 optical densities is considered best, as it achieves a strong signal, whereas much thicker will result in distortion of the signal at higher photon energies [34]. At the copper edge, this amounts to sample thicknesses of 1 – 2 μm . Once the correct amount of solution is achieved, the windows are sealed together with epoxy adhesive around the edges to seal in the solution. This technique is of potential advantage for minerals research, as the analysis of hydrated samples may reveal previously unknown truths about the distribution of chemical species across a sample and also in solution, and may reveal that these species, which form in solutions, differ after dehydrating and analysis, often in high vacuum environments. Indeed, many of the chalcocite samples presented in this chapter are prepared in a dilute solution of sodium ethyl xanthate, as the intention was to discover what, if any, xanthate components adsorbed to the chalcocite surface and under what conditions. The attempt to study these conditions only revealed that dilute solutions of 10^{-2} M sodium ethyl xanthate did not result in adsorption on the surface in concentrations large enough to detect.

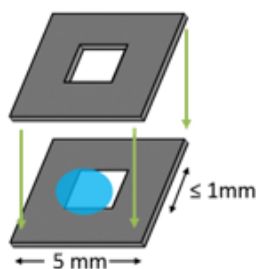


Figure 9.3: Schematic of sample holder for hydrated samples.

There are a number of challenges that arise with hydrated samples, one of which is the mobility of the particle. The sample in Figure 9.4 is a chalcocite particle in a dilute xanthate solution. The images were extracted from a stack, which contains a series of images taken at photon energies over the Cu L₃ absorption edge. There are a few features to note in these images; the first is that in the first image, the edge of the particle can be seen reasonably well, and outside of that edge, the absorption intensity has a bowed shape, as the intensity decreases at increasing distance from the particle. This is typical for a hydrated sample. The second observation is the change in the distribution of signal intensity across the sample as the photon energy changes in subsequent images; this is due to the change in absorption coefficient, μ , at each photon energy, and indicates different distributions of Cu species. The third observation, and most pertinent for this section, is that the particle appears to float somewhat out of the field of view over the time the images were collected. The data for the following sample is from the PolLux beamline at the SLS.

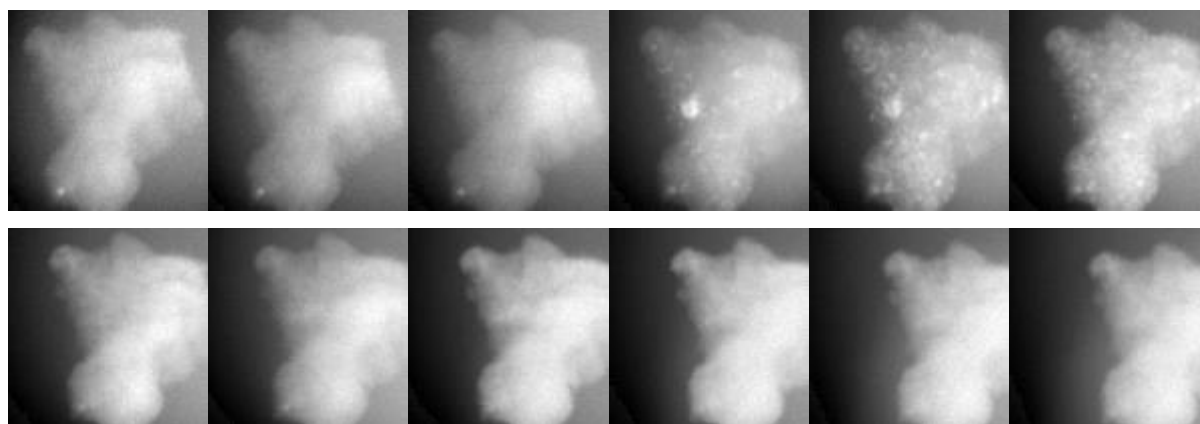


Figure 9.4: OD images of chalcocite particle in solution, in temporal order, showing the particle floating off the field of view.

The drift observed for the particle in Figure 9.4 is particularly large compared to other mineral samples observed during the experiments presented in this chapter. In general, if the sample is well sealed, there should be minimal movement of the sample between the two windows, especially for larger particles. However, this is an important factor to consider, especially when designing experiments which include more motile elements, such as live bacteria, for example. Included in the Axis2000 program are options for aligning the images in a stack, which can either be done by manually aligning each individual image, or by running an auto-alignment program, which relies on distinguishing features, such as the edge of a particle, to align subsequent images. A careful alignment of the stack is crucial for accurate analysis of the sample.

9.3 Effect of sample environment

Both the samples in this section (dry and hydrated) were analysed at the SM beamline at the CLS.

9.3.1 Dry sample

The following sample is a chalcocite particle which has been exposed to pH 4 H_2SO_4 solution and drop cast onto a single silicon nitride window, and allowed to dry before analysing. A brief analysis of the spectra from various regions of the sample indicate that much of the centre of this particle is too thick for a good analysis, as seen in the previous sample, as the spectra show signs of saturation in Figure 9.5c. Because of this, model spectra have been collected from regions around the edge of the particle where the thickness has less impact on the spectra, and a saturated spectrum is also collected, to use for mapping these components across the sample.

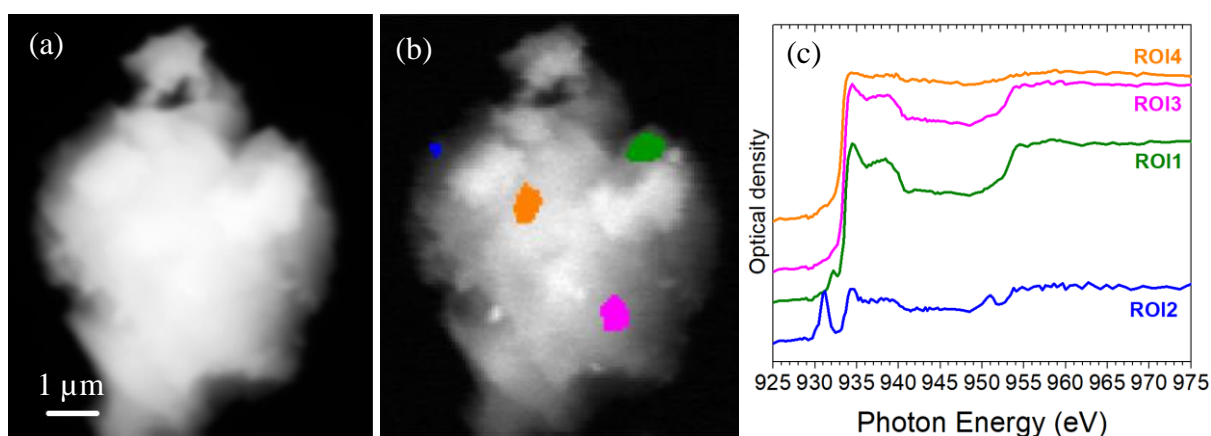


Figure 9.5: (a) Average stack image of chalcocite particle exposed to H_2SO_4 . (b) regions from which spectra are collected. (c) Cu L edge spectra collected from the regions of interest in (b).

ROI1 & ROI3 are similar spectra, but the region above 940 eV is slightly higher intensity in ROI3, which may be due to saturation effects. Due to this, ROI1 was chosen for mapping, while ROI3 was not. ROI2 has a Cu^{II} peak at 931.1 eV, in addition to the main Cu^{I} chalcocite peak at 934.6 eV. Since Cu^{II} is not generally expected in chalcocite, the Cu^{II} peak is thought to be a product of exposure to pH 4 solution. Using those three spectra, without any alteration, we obtain the following maps:

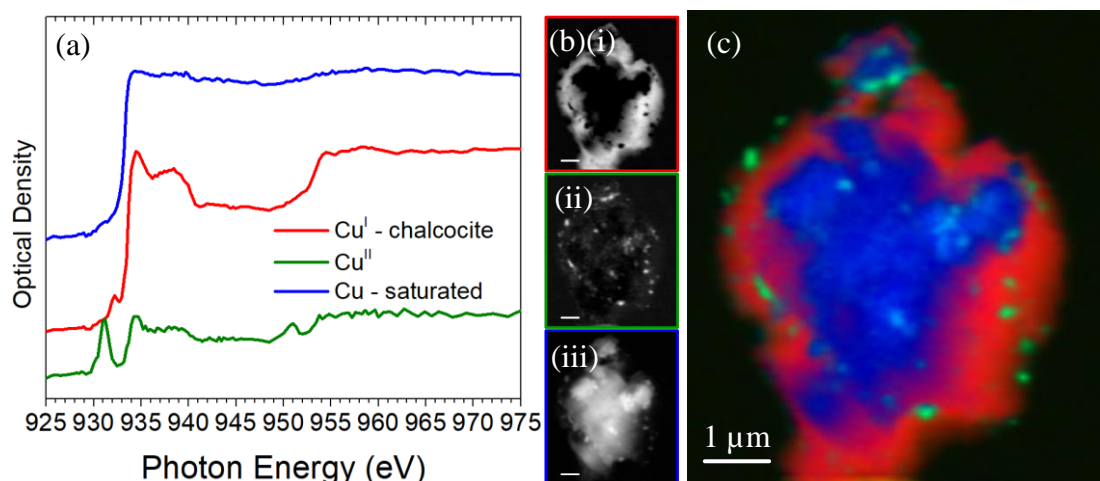


Figure 9.6: (a): internal spectra mapped to the stack, (b) mapped regions of (i) Cu^{I} – chalcocite species (ii) Cu^{II} species (iii) saturated region, (c) overlaid RGB image of the mapped regions in (b).

The mapped regions shown in Figure 9.6 did a reasonable job of fitting the stack, both spatially and spectrally. The residual stack showed two energies which were poorly fitted; the first was around the Cu^{II} peak, and the spatial regions were much aligned with the spatial map of the Cu^{II} species shown in Figure 9.6b. The spectral signal around this energy in the residual stack showed that the poor fit in these areas is due to differences in the peak width, which may be as much due to noise in the spectra, as possible changes in chemistry. The second energy which had a poor fit, was around 932.2 eV; near the pre-edge peak seen in the Cu^{I} – chalcocite spectrum. This was reflected in the images in the residual stack at this energy, which showed significant spatial resolution, as shown in Figure 9.7a. Figure 9.7b shows a region of interest mask, which was created by masking out the lower intensity regions in Figure 9.7a, and only allowing the regions of the highest intensity. This mask is then applied to the stack to generate the spectral signal from those regions, shown in Figure 9.7c, to investigate the average spectral signal in the original stack, which occurs within the identified regions of high residual signal.

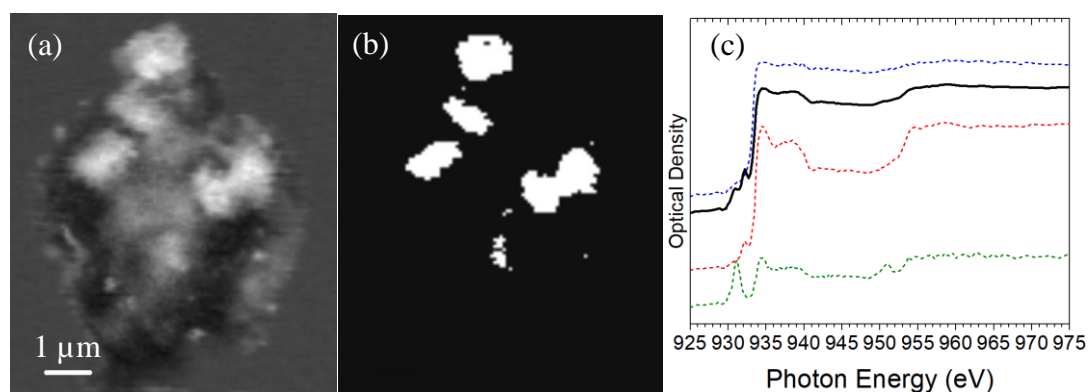


Figure 9.7: (a) image from residual stack showing intensity of poorly fit region near 932.2 eV, (b) mask generated from image in (a), used to isolate the average spectrum from those regions in the stack, (c) spectrum generated from the regions indicated in the mask in (b), plotted against the spectra from Figure 9.6.

The spectrum shown in Figure 9.7c which was collected from the masked regions shown in Figure 9.7b, appears to be a combination of the Cu^{I} and Cu-saturated spectra, with a small contribution from Cu^{II} species. However, if this was strictly true, these regions should be well fit by a linear combination of these three spectra. The poorly fitted energy was observed at 932.2 eV, which aligns with the pre-edge peak. This pre-edge peak in the new spectrum shown in Figure 9.7c appears to be a stronger intensity than the pre-edge peak in the Cu^{I} spectrum mapped to the stack.

It would be possible to manipulate the spectra which are extracted from the stack, to isolate each of the peaks which are changing in relative intensity. However, since it is not known what the pre-edge peak in particular is attributable to, separating each of the peaks into different spectra is not expected to yield a result which has a real interpretation. Instead, the assumption is made that the poor fit to the stack is due mostly to the change in height of the pre-edge peak relative to the main absorption edge. This is a reasonable assumption, since the residual stack showed the energy around the pre-edge as that which produced the greatest intensity in the residual stack. Therefore, those regions identified as a poor fit have been mapped in an overlaid RGB image, shown in Figure 9.8, where the red and green mapped regions show the Cu^{I} – chalcocite and Cu^{II} species, respectively, while the blue mapped regions show those which were poorly mapped due to the change in pre-edge peak height relative to the main Cu^{I} absorption peak.

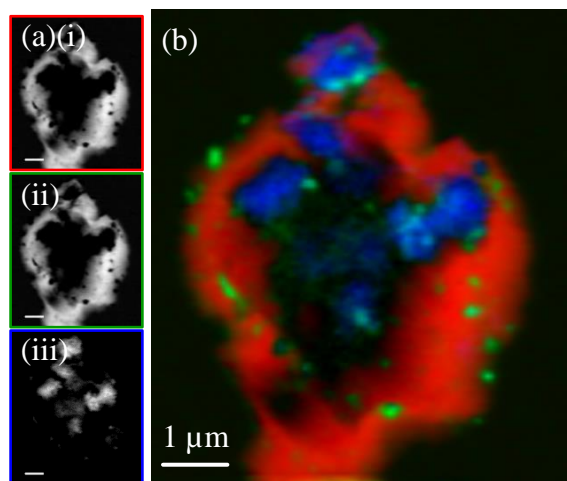


Figure 9.8: (a) Mapped regions of (i) Cu^{I} – chalcocite, (ii) Cu^{II} , and (iii) regions poorly fit due to changes in pre-edge peak height. (b) RGB overlaid image of the three regions shown in (a).

The overlay map in Figure 9.8 shows that for a chalcocite particle which has been exposed to pH 4 H_2SO_4 solution, and allowed to dry, the NEXAFS spectrum across the particle is seen to be a large proportion of characteristic chalcocite, with small spots (diameter of 0.2 – 0.3 μm) of Cu^{II} signal.

There are also larger regions (diameter of $\sim 1 \mu\text{m}$) where the pre-edge peak of the Cu^{I} chalcocite absorption spectrum differs, relative to the main absorption peak. van der Laan, Patrick, Charnock and Grguric [35] proposed that the pre-edge peak in nonstoichiometric Cu_5FeS_4 is due to the $2p^5 d^{10} Ls^2$ ligand hole final state; the intensity of which increases with decreasing electrons in the valence band. The energy of the ligand hole final state in nonstoichiometric Cu_5FeS_4 is similar to the pre-edge peak observed for the current sample, therefore this peak likely represents a defect site in the chalcocite structure, which, as shown in Figure 9.8, is observed in spatially isolated regions of the sample.

9.3.2 Hydrated sample

The following sample is a hydrated cell containing chalcocite in a pH 8 xanthate solution. It was prepared on an electrochemical cell, which has printed inert electrodes which can be seen in the images of the particle; however these electrodes were not electrically connected and played no part in the results which follow.

Firstly, a broad scan image of the chalcocite particle was taken, shown in Figure 9.9. This image is collected just above the carbon K edge absorption spectrum, at 320 eV. Both line scans have been normalised to external I_0 signals, collected from a single window. The carbon K edge spectrum has had a linear background removed to highlight the weak signal, over the strong background. The location of the spectra can be found by fitting the linescan using the “line_fit” function. This fits the linescan with a linear combination of chosen spectra and reports the intensity and location of these spectral features across the line. In these examples I used internal spectra, but in theory external reference spectra could also be used.

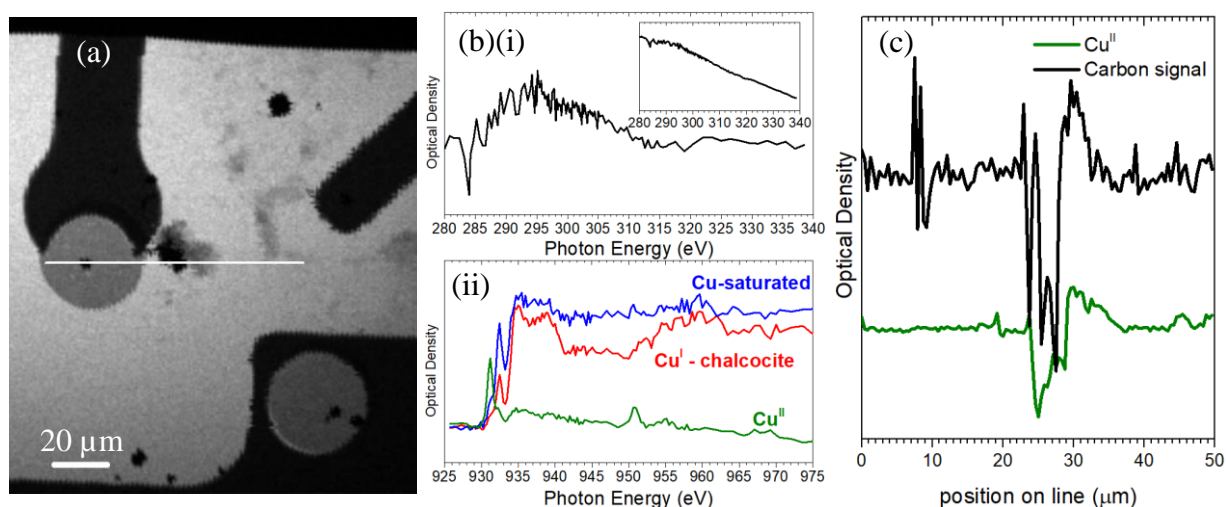


Figure 9.9: (a) broad scan image of chalcocite particle in solution, (b) C K edge and Cu L edge spectra collected from the line indicated in (a), (c) location of the spectra along the line scans.

The line scans over the C K edge and Cu L edge were both collected over the same line shown in Figure 9.9a, while Figure 9.9b shows the key spectra identified in these lines scans. The carbon signal, which is shown in the inset to Figure 9.9bi, has a very low signal to noise ratio, with a strong linear background. To enhance the signal, the linear background was removed, and the resulting spectrum is shown. This spectrum was fitted to the C K edge line scan, with the fitted intensity plotted against the position on the line, as was done for each of the Cu spectra shown in Figure 9.9bii. The location of the carbon spectrum aligned closest with the location of the Cu^{II} spectrum, shown in Figure 9.9c. If the carbon signal detected originates from the xanthate in solution, the results here indicate that under these conditions the xanthate is forming a cupric (Cu^{II}) xanthate complex, rather than a cuprous (Cu^I) xanthate complex. If the carbon signal was somewhat stronger, this would be a good place to look for the relationship between chalcocite and xanthate solution. This was indeed the aim at the time of taking the data, however only a copper stack was collected before the sample failed, and a good carbon analysis was unfortunately not achieved.

An average image from the stack taken over the copper L edge is shown in Figure 9.10a and shows the chalcocite particle in solution to the right of the inert electrode. Since the centre of the particle is quite thick and the blue spectrum in Figure 9.10b consequently appears distorted on the high energy side, the method used in the previous sample is employed here. The saturated Cu^I component is mapped in addition to the Cu^I – chalcocite and Cu^{II} components. These spectra are shown in Figure 9.10b, which have been collected from regions of the stack, and have been chosen as the spectra to be used for fitting.

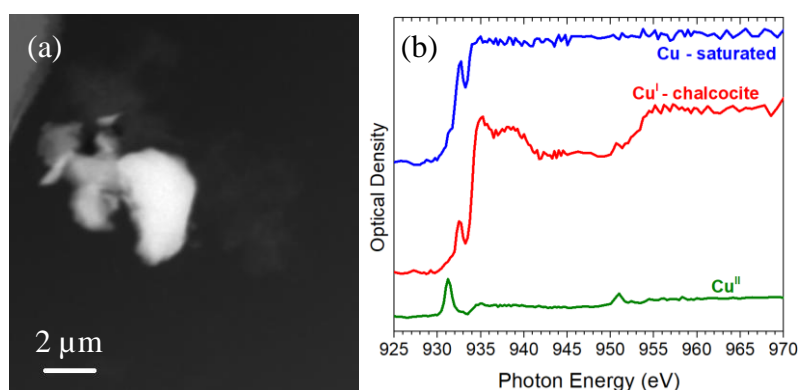


Figure 9.10: (a) average image from Cu L edge stack, (b) internal spectra used for fitting. Blue spectrum show saturated signal due to sample thickness.

Unlike in previous samples, the method chosen to fit the spectra for this stack included a constant in addition to the three spectra shown in Figure 9.10b. The constant signal accounts for thickness in the sample which does not arise from Cu species, and this was found to result in a smaller overall residual

signal, which largely arose due to the Au electrode in the top left corner of the stack. Since the constant did not have a noticeable effect on the fitting of the sample, it has not been included in the images shown here. Figure 9.11a shows the mapped regions of the Cu^{I} – chalcocite, Cu^{II} and Cu – saturated signals, respectively, while Figure 9.11b shows these three images overlaid in red, green and blue, respectively. The blue region in the middle of the particle shows where the particle is too thick for a meaningful analysis. The red region maps the chalcocite signal, while the green region shows the location of oxidised Cu^{II} species. The Cu^{II} species are observed to form small bright regions around the edge of the particle, as was observed for the previous, dry sample, although there appears to be somewhat fewer Cu^{II} patches on the hydrated sample. In addition to the intense patches of Cu^{II} , there is significant dispersion of Cu^{II} species seen outside of the particle, in solution, which forms a cloud-like dispersion of Cu^{II} species.

This is a significant observation to make with this technique, as other commonly used techniques are not able to observe the distribution of oxidised species within a solution with chemical sensitivity. This region within the solution near the particle was where the undefined carbon signal was observed. If further fine analysis of the carbon species of this sample had been possible, this technique would have been able to see the relationship between the Cu^{II} species and the carbon species, and would have shown how that relationship changes for the cloud-like Cu^{II} in solution and the particle-like Cu^{II} on the edge of the chalcocite particle.

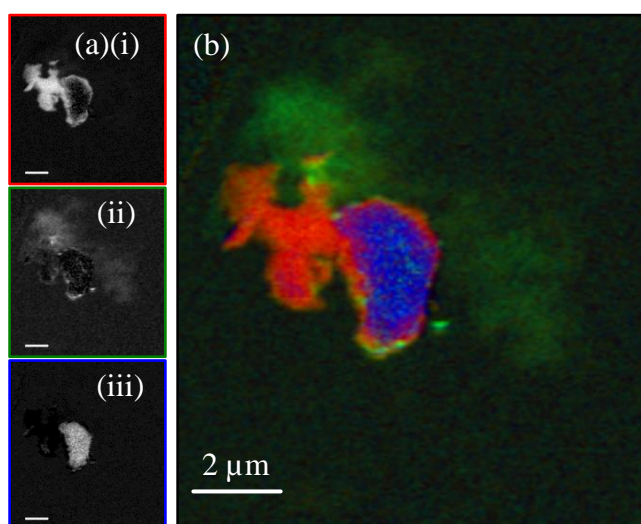


Figure 9.11: (a) mapped regions of (i) Cu^{I} - chalcocite, (ii) Cu^{II} , (iii) saturated Cu species, (b) RGB overlaid image of the mapped regions shown in (a).

The presence of Cu^{II} in the solution surrounding the particle is an important observation for this hydrated sample, as it is not an observation that can be easily made for dry samples. Many of the dry

samples which were analysed showed very small Cu^{II} structure on the windows around the particle, hence why an external I₀ signal was used. However, that structure is indicative of Cu^{II} leaching into solution. Unfortunately, once the sample is dry, although the Cu^{II} can be faintly detected, it is difficult to analyse with any certainty since there is no means to determine if it was widely dispersed in solution, or leaching from the nearby particle.

The hydrated sample showed here gives a clue about the nature of the Cu^{II} signal, since a small carbon signal was also detected in the same region as the Cu^{II} in the broad scan. A high resolution stack over the carbon K edge of this sample would potentially provide more detail about the interaction of the Cu^{II} with the carbon species, and what those carbon species are. Since this sample was prepared in a xanthate solution, the initial assumption is that the Cu^{II} is bonding to a xanthate ion or derivative. However, without high resolution spectra with reasonable signal to noise ratio and appropriate reference spectra, such a conclusion could not be made. Yet, the indication provided by the little carbon data obtained for this sample, is that the interaction between the carbon and Cu^{II} species is within the solution, and not necessarily on the chalcocite particle. This is a fine example of the importance of being able to analyse hydrated samples in addition to dry samples, or samples in vacuum, which would not be able to show that interaction at all.

9.4 Identification of minority species

The advantages of having both high spectral and spatial resolution, extends beyond the ability to see the distribution of surface species; it provides the ability to detect minority species in a sample. These species may be distinguished from the bulk, or majority species, by the difference in their spatial distribution, where in other techniques they would be otherwise undetected or not conspicuous in spectra which are averaged over large areas. This feature of microspectroscopy has already been hinted at in this chapter, specifically in the sample in Figure 9.8, where the poorly fitted regions showed a variation in the Cu L₃ pre-edge peak height in somewhat isolated spatial regions. Such a result indicates that the pre-edge peak represents a distinct species, rather than a feature of saturation due to sample thickness, and this variation in peak height was tentatively attributed to the presence of defect sites within the chalcocite lattice. The aim of this section is to further explore the minority species observed in a chalcocite sample exposed to acidic conditions, but unlike the sample in Figure 9.8, conducting this analysis on a smaller particle which showed less saturation effects.

The sample presented in this section was analysed at the PoLux beamline at the SLS. This sample was prepared in a pH 4 H₂SO₄ solution and sealed between two windows to produce a hydrated cell. To determine if the sample is actually hydrated, a number of large scale low resolution images were

collected of this sample at the Cu L edge. These images are overlaid in the combined image in Figure 9.12. Each of the overlaid images show bright regions where a transmission signal of approximately 4×10^4 photons was detected, dark patches indicating fine chalcocite particles, and intermediate grey areas. In addition to the grey areas around the chalcocite particles in the images in the middle and on the right, there is a thin grey region around the bottom left corner of the image on the left. This grey region is at the edge of the window and has a natural curved shape which may be indicative of receding solution. The transmission signal through this grey region is approximately 2×10^4 photons; approximately half that of the bright regions. This is evidence that the solution in the sample is likely receding due to the windows not being adequately sealed. The grey regions around the particles in the middle image have a transmission signal similar to the grey area around the edge of the window in the image on the left of Figure 9.12. For this reason, it was thought that the particles in the middle image may be in solution, and a small region within this image was chosen for a high resolution analysis.

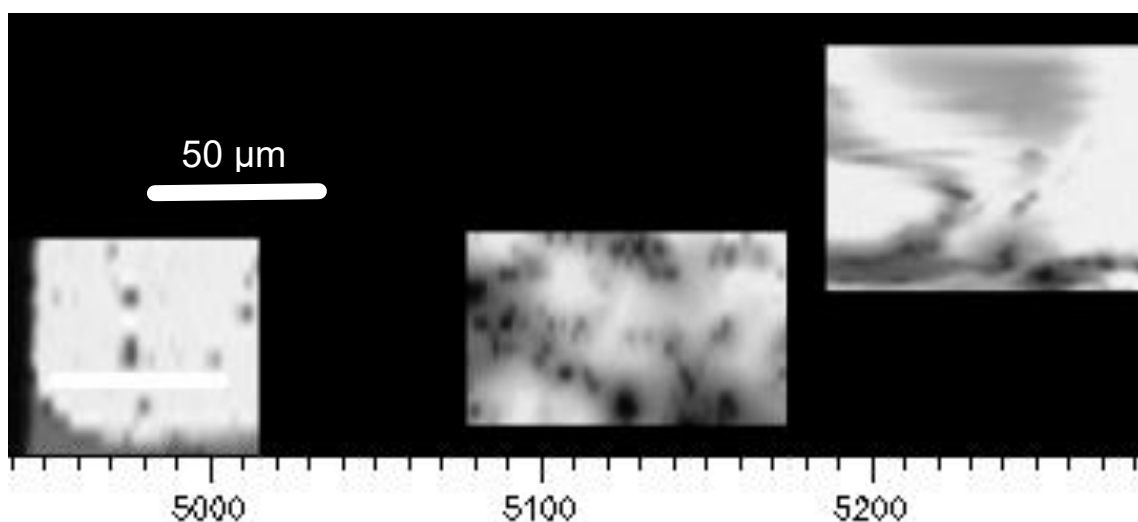


Figure 9.12: Large scale low resolution images in transmission mode of a liquid cell. Grey regions indicate greater absorption associated with the likely presence of solution.

The particle used for the analysis is shown in Figure 9.13a, with the average spectrum over the field of view shown in Figure 9.13b. The transmission signal in the bright region around the particles is approximately 4×10^4 photons, indicating that by the time the stack was collected, the region was no longer hydrated, as the hydrated regions in Figure 9.12 have a much lower transmission signal of approximately 2×10^4 photons. Although this sample was prepared as a hydrated sample, it is likely that the solution has wicked to the edges and the sample remains outside of the solution.

The average spectrum over the region has a double peak pre-edge structure, with features at 931.4 eV and 932.3 eV, consistent with the photon energy of the pre-edge peaks observed in the more surface

sensitive spectrum of chalcocite presented by Goh, Buckley, Lamb, Rosenberg and Moran [24]. These peaks are tentatively attributed to the $2p3d^{10}$ final state of Cu^{II} , and the $2p3d^{10}s$ final state of Cu^{I} species, respectively [27]. Above 935 eV the broad structure of the main absorption is observed, which is at an energy consistent with that of chalcocite absorption structure previously shown in this chapter, and those published in literature [24, 26, 27]. However, considering the relative height of the pre-edge peaks, the overall shape of the spectrum also shows resemblance to the absorption spectra of other Cu minerals, specifically bornite [35] and digenite [27]. The attribution of the pre-edge peak at 932.3 eV was a subject of concern in the work by Goh, Buckley, Lamb, Rosenberg and Moran [24], as they argued, like others in the literature ([27]) that this peak is an integral part of the Cu^{I} chalcocite spectrum, whereas others have attributed it to impurities of covellite (CuS), a Cu^{II} sulfide, in the sample [36]. Since STXM has both spatial and spectral resolution, the distribution of these species can be investigated for the sample in Figure 9.13, thus investigating the claims of the origin of the aforementioned peaks.

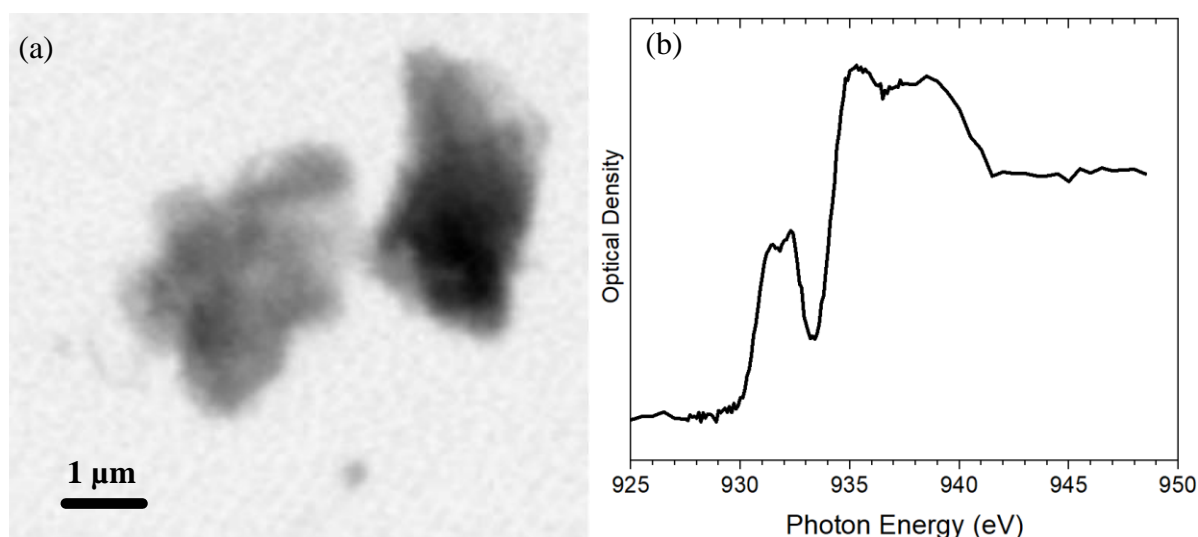


Figure 9.13: (a) Transmission image of particles used for the analysis, (b) average spectrum over the stack.

Three spectra were selected from the stack, shown in Figure 9.14a, and were mapped to the stack. The Cu^{II} spectrum (green) shows only a strong peak at 931.4 eV, similar to the tenorite (CuO) spectrum presented in literature [25], and is attributed to a pure Cu^{II} phase in this sample. The Cu^{I} spectrum (red) has a similar shape to the chalcocite spectra shown previously, but with a pre-edge peak of slightly higher relative intensity. The Cu-mixed spectrum (blue) has a strong pre-edge peak at 931.2 eV, with a shoulder in the energy region of the pre-edge peak of the Cu^{I} spectrum, below the broad absorption structure attributed to Cu^{I} . The strong low energy peak in the Cu-mixed spectrum is in the energy region attributed to Cu^{II} , and is therefore tentatively attributed to a Cu^{II} containing phase, but with the higher energy shoulder and the broad absorption structure around 935 eV, this is

expected to be a superposition of Cu^{II} and Cu^{I} species, or a separate phase which contains both Cu valences. It is notable that the energy of the Cu^{II} peaks in the Cu^{II} spectrum and the Cu-mixed spectrum differs by 0.2 eV. Since the spectra were collected simultaneously, this small energy shift is significant, and not an error in the data processing. The mapped regions of the Cu^{II} and Cu-mixed signals, shown in Figure 9.14b-c, are distinctly different, indicating that these species occupy different regions across the sample.

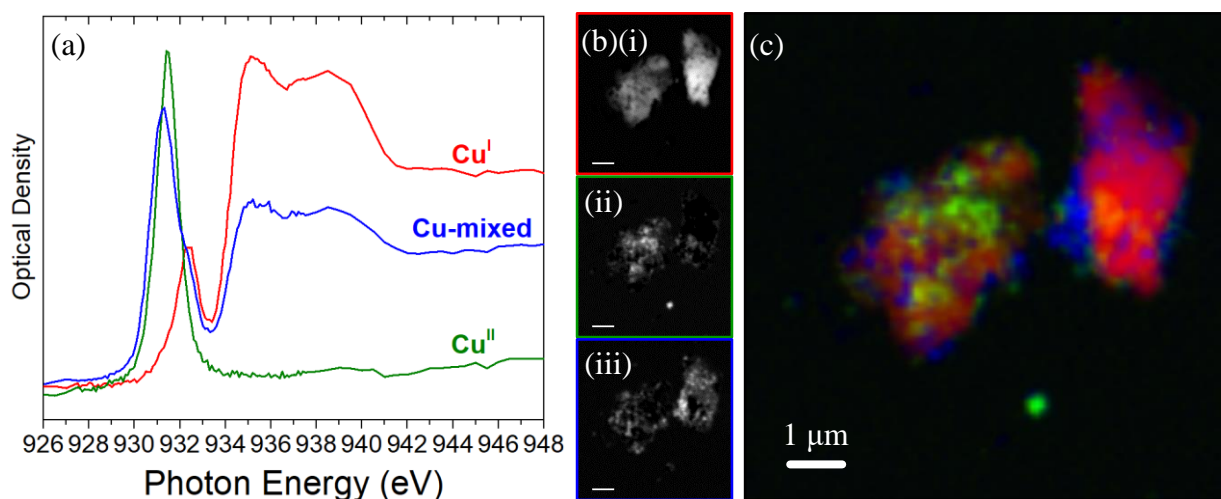


Figure 9.14: (a) Cu L edge spectra mapped to the stack, (b) mapped regions of (i) Cu^{I} similar to chalcocite, (ii) Cu^{II} , (iii) mixed Cu^{I} and Cu^{II} signal, (c) RGB overlay of the images from (b).

The spectrum from the region of high residual after the previous map is shown in Figure 9.15, and indicates that the residual largely arises from the difference in relative height of the pre-edge peak and the main Cu^{I} absorption signal. The residual signal (solid, black spectrum) has a similar shape to the Cu^{I} spectrum (dotted, red spectrum), but with a shoulder beginning to appear below the pre-edge energy at an energy consistent with the Cu^{II} signal in the Cu-mixed spectrum. While it is possible that the increase in the pre-edge peak relative intensity is due to the superposition of the Cu^{II} feature on the Cu^{I} spectrum, this is not likely. If this residual spectrum could be modelled by a linear combination of the spectra shown in Figure 9.14a, then it would have been mapped in the analysis shown in Figure 9.14b-c. This indicates that the relative intensity of the pre-edge peak varies slightly across the sample.

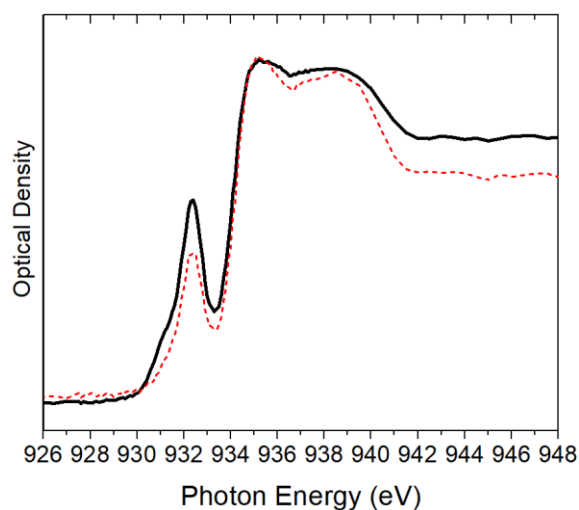


Figure 9.15: Spectrum of high residual region (solid, black), plotted against the Cu^I signal (dotted, red), showing difference in relative peak heights.

9.4.1 Discussion of minority species

The STXM data from this sample shows that there are two key elements of the Cu L₃ absorption spectrum which are observed to change across the sample; the relative intensity of the pre-edge peak at 932.3 eV, and the energy of the Cu^{II} peak.

The presence of the pre-edge peak in chalcocite at 932.3 eV has been observed and noted in previous presentations of chalcocite Cu L₃ absorption spectra in literature, but the origin of this feature is not fully understood [24, 26, 27, 37]. van der Laan, Patrick, Charnock and Grguric [35] observed the spectra of nonstoichiometric Cu₅FeS₄ samples to have a strong peak at 932.6 eV, followed by a broad absorption in the region 933 – 940 eV, which qualitatively has a similar shape to that observed in Figure 9.15. The relative intensity of this peak was seen to increase with a decrease in electron density, as the pre-edge peak is attributed to the transition from the $d^{10}\underline{L}s$ ground state with a hole in the ligand valence band to the $2pd^{10}\underline{L}s^2$ final state, whereas the main absorption structure is attributed to the transition from the d^{10} ground state to the $2pd^{10}s$ final state [35].

The Cu L edge spectrum for digenite (Cu₉S₅) shown by van der Laan, Patrick, Henderson and Vaughan [27] has a similar shape to the Cu₂S spectrum, but with an increased pre-edge peak. Arce and González [38] showed that the electrochemical oxidation of chalcocite produces djurleite (Cu_{1.96}S), and further oxidation proceeds to form digenite (Cu_{1.6}S). As the chalcocite sample is progressively oxidised, Cu ions and electrons are progressively lost until covellite (CuS) is formed [38]. It is proposed, based on the spectra seen in literature [35, 39], and their similarity to the oxidation products observed in the current sample, that the increasing relative intensity of the pre-edge peak is related to the oxidation of chalcocite due to its exposure to acidic solution, resulting in Cu ions and

electrons leaching from the sample and producing Cu_xS structures with increasing vacancies in the remaining Cu *d* band.

The energy shift observed in the Cu^{II} peak, while it is only 0.2 eV, is a notable difference in the spectra gained from the stack. The lower energy Cu^{II} peak at 931.2 eV is associated with the Cu-mixed signal, while the pure Cu^{II} signal is observed at a higher energy of 931.4 eV. This observation rejects the possibility that the observed shift may be attributed to a superposition of the Cu^{I} pre-edge feature with the Cu^{II} peak, and reinforces the assertion that these peaks, which are separated by only 0.2 eV, are due to distinct species. Due to the similarity of the pure Cu^{II} spectrum with the spectrum of tenorite (CuO), it is proposed that the higher energy peak at 931.4 eV is due to a Cu-O species, although it does not necessarily have the same structure as tenorite. Concurrently, it is proposed that the lower energy feature at 931.2 eV, which is always associated with Cu^{I} features, is due to a divalent Cu-S component, which likely arises due to more extensive oxidation of the chalcocite sample.

While more experiments would be required to support these propositions, it is important to consider that these observations are not possible without the combination of spatial and spectral resolution. The energy difference observed between the two Cu^{II} peaks is only 0.2 eV, which is close to the spectral resolution of the technique, and without such resolution, these peaks would not be distinguishable. Similarly, if the spectra obtained were averaged over larger spot sizes, the distinct Cu^{II} peaks, and the change in relative height of the pre-edge peak, would not be observable, as these features are seen to be isolated to regions of less than 1 μm in size.

9.5 In situ capabilities

This section of the thesis presents an example of how the sample holder design for STXM can be modified to allow for analysis of electrochemical processes. This technique has previously been used to observe and analyse the deposition and stripping of copper onto the gold electrode under different electrochemical conditions [40]. This technique has also more recently been developed to include *in situ* studies of both static and continuous flow electrochemical cells, showing the cyclic electrodeposition and electrostripping of copper in a similar system [41]. Electrochemistry is a common tool used for sulfide mineral flotation, as the surface species present on minerals may be controlled by electrochemistry methods [38]. Therefore, STXM has great potential to offer insight into the surface changes affected by changes to electrochemical conditions, and how these changes are affecting the flotation response of mineral phases. The aim of this section is to show the capability of this technique to analyse mineral samples under simple electrochemical conditions, thereby encouraging future studies to embrace this technique.

The following analysis was performed at the SM beamline at the CLS. The sample shown in this section was prepared in a dilute (10^{-4} M) xanthate solution at pH 4. The chalcocite particle chosen for analysis was located above the counter electrode, as shown in Figure 9.16a and has an approximate size of $4\ \mu\text{m}$ diameter. The two distinct spectra collected from within the stack are shown in Figure 9.16b, and show a typical Cu^{I} signal from chalcocite, and a small but distinct Cu^{II} signal, in addition to a saturated chalcocite signal. These three spectra have been mapped to the stack, as for previous samples, and the overlaid mapped images shown in Figure 9.16c. The centre of the larger particle shows the saturated signal, while the outside edges of this particle, and the other particles show the clear chalcocite signal. Only small regions of Cu^{II} signal can be seen within the solution near the edges of the particles.

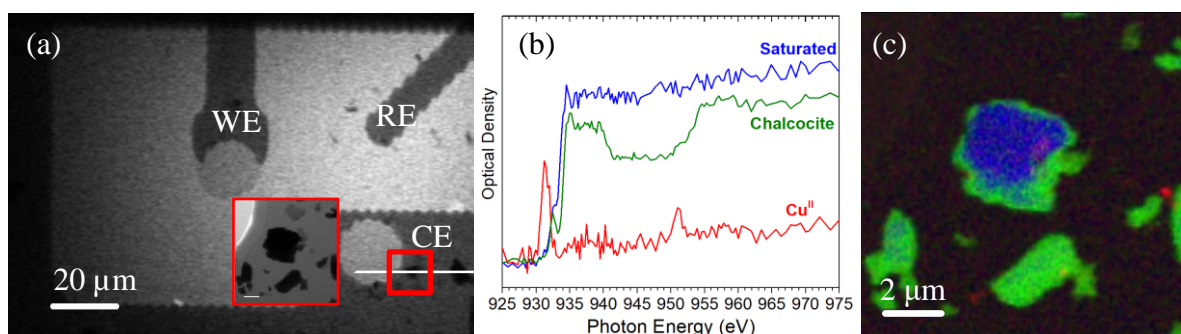


Figure 9.16: (a) WE = working electrode, RE = reference electrode, CE = counter electrode, (b) internal signals collected from the stack, (c) RGB overlay of mapped internal signals.

A voltage of $-400\ \text{mV}$ was passed through the sample, and a subsequent stack of the same region was collected. Three distinct spectra were observed within the stack, shown in Figure 9.17a, and represent a chalcocite signal, Cu^{II} , and a spectrum which shows three broad peaks, characteristic of Cu^0 [26]. When these spectra are mapped to the stack, the Cu^{I} signal is seen to dominate over the field of view, whereas the Cu^{I} signal appears in isolated regions, mostly at the bottom right of the field of view, and only a few small localised regions of Cu^{II} can be detected, seen in Figure 9.17c. This shows that by passing $-400\ \text{mV}$ through the sample, the chalcocite particle is mostly reduced to elemental copper.

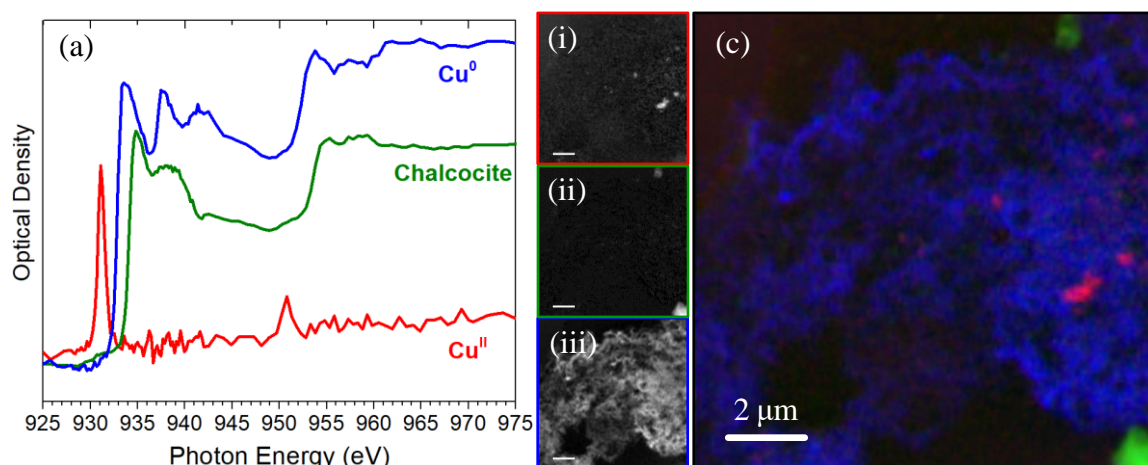


Figure 9.17: (a) three spectra collected from the stack representing Cu^{II} , Cu^{I} chalcocite, and Cu^0 , (b) mapped regions of (i) Cu^{I} , (ii) Cu^{II} , and (iii) Cu^0 , (c) RGB overlay of three mapped signals.

9.5.1 Quantification of mapped species

The intensity of the spectra mapped to each stack up to this point have been plotted on an arbitrary scale, and while the intensity of the mapped regions broadly represents the concentration or thickness of that species, the results have not been discussed quantitatively. Additionally, the scale on the coloured overlay images have automatically altered to achieve the best contrast and any quantitative information that may have been present in the mapped images is lost. This is a necessary outcome when mapping spectra which have not been normalised in some meaningful way, as the coefficient of that spectrum mapped to a particular point depends not only on the thickness of the species at that point, but also on the thickness of the species at the point from which the reference spectrum was collected. Fortunately, it is possible to normalise spectra in a meaningful way and subsequently achieve a quantitative mapping of species to a sample. Examples of this is seen in the literature, where carbon reference spectra are mapped to samples to quantify the carbon components of microbial biofilms [11], organic components of soil [7], or DNA, RNA and proteins in cells [10]. Metal L edge reference spectra have also been used to quantify metal species (namely, Fe, Ni and Mn) in biofilms [14], and to map ratios of ferrous and ferric components in silicates [17].

In principle, quantitative mapping should be possible for all elements which have core levels which lie within the photon energy range of the instrument. Reference spectra, ideally collected from well characterised reference materials, are normalised to X-ray absorption spectra, which are calculated using Eq. (14) to find the photon energy dependent absorption coefficient, calculated with the volume density of the reference material (n_v) and the absorption cross section ($\sigma_x(h\nu)$, [42]), based on the chemical formula of the reference material.

$$\mu_x(h\nu) = n_v \sigma_x(h\nu) \quad \text{Eq. (14)}$$

These are then “OD1” spectra, since their pre- and post-edge intensity matches that for 1 nm of the reference material and can therefore be used to quantify the thickness of each material in the sample being analysed, by fitting a linear combination of selected OD1 reference spectra to the spectral intensity at each point. Since the second stack of the previous sample, after -400 mV had been applied, showed no signs of saturation effects, it is a good opportunity to show the possibility of quantitative mapping. Previous samples in this chapter are not worth attempting quantitative mapping, since the saturation causes a non-linear response.

The Cu^{II} signal appears similar to the spectrum for tenorite (Cu^{II}O) [25, 28, 37], thus the Cu^{II} spectrum is normalised to the OD1 intensity calculated for tenorite, with a density of 6.5 g/cm³. The Cu^I chalcocite X-ray absorption coefficient was calculated using a density of 5.65 g/cm³, and the Cu⁰ signal was normalised to the X-ray absorption coefficient for copper metal, with a density of 8.92 g/cm³.

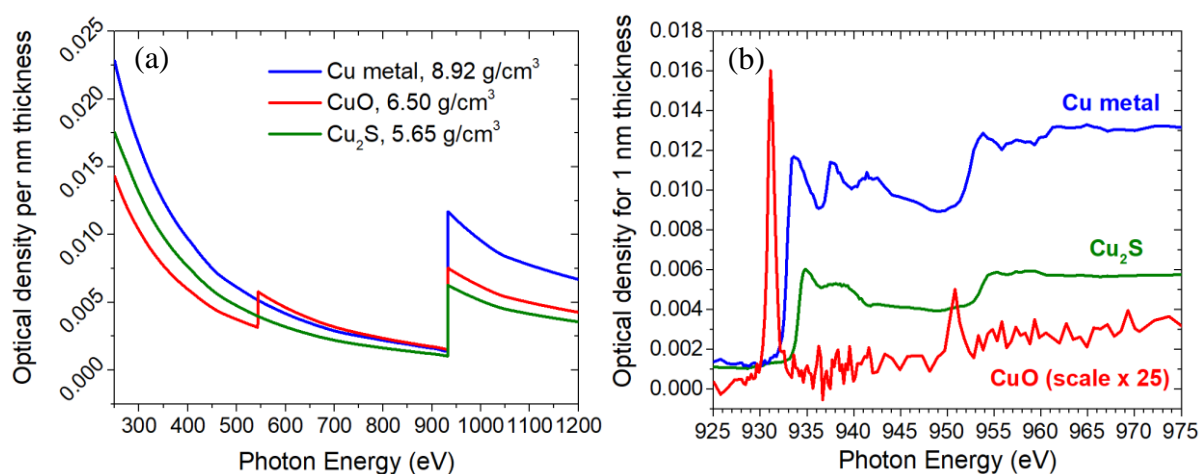


Figure 9.18: (a) calculated X-ray parameters for Cu metal, CuO, and Cu₂S, with the volume densities assumed for each material. (b) OD1 spectra normalised to the calculated intensity for 1 nm material.

When the spectra shown in Figure 9.18b are mapped to the stack, the intensity of each signal fitted to each pixel is representative of the thickness of that material present in each region. The results of mapping the quantitative OD1 spectra are visually similar to the results shown in Figure 9.17, as is expected. However, the scale on the individual mapped images is not representative of the thickness of each material. The RGB image of the quantitative mapped regions is shown in Figure 9.19, with approximate averaged values of certain areas, marked on the image. The Cu₂S particle at the bottom of the field of view (green) has an average thickness of 230 nm. The Cu^{II} signal in the middle of the

image (red), assuming it is tenorite (CuO), or is a similar material with a similar volume density, has an average thickness of 1 nm, with an uppermost thickness of approximately 1.5 nm. The thickness of the extensive Cu metal signal across the field of view varies from less than 20 nm to above 100 nm, and the averaged intensity of selected regions are indicated on the image, where the region shown on the left of the image has an average thickness of approximately 40 nm, and the region indicated on the right of the image with an average thickness of 60 nm. However, it can be seen from the variation in intensity of the Cu metal signal within these regions, there is significant variation in intensity within these regions.

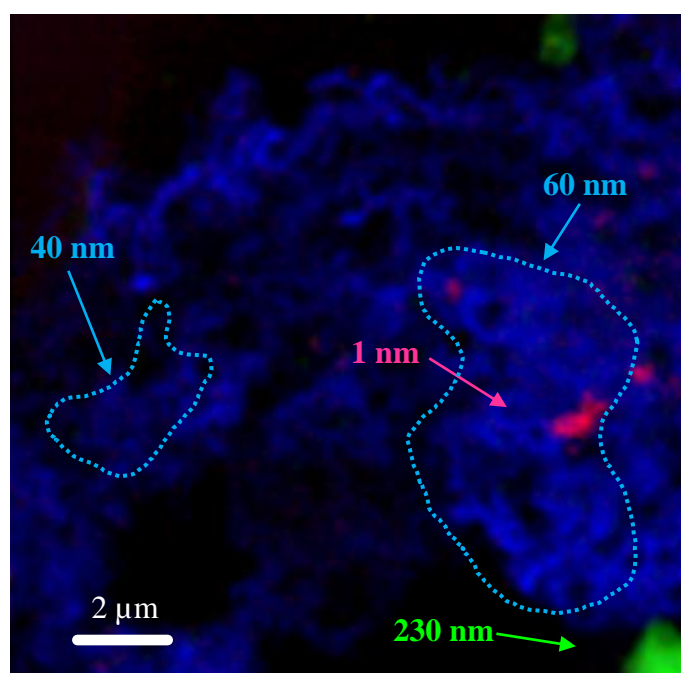


Figure 9.19: RGB overlaid image of quantitative mapped CuO, Cu₂S, and Cu metal species, showing approximate thicknesses of the areas indicated.

9.6 Conclusion

This chapter has shown the potential for using STXM for sulfide minerals research. The advantages of this technique are that samples can be analysed in more natural environments than high vacuum, such as in atmosphere, or atmospheric pressure helium, or in hydrated environments. This chapter investigated the difference between dry samples and hydrated samples, and showed that analysing samples in a hydrated environment was paramount for identifying the relationship between species in solution. It was shown that for a sample of chalcocite prepared in xanthate solution, that the Cu^{II} species spatially coincided with the carbon signal in solution. In a dry sample, the Cu^{II} signal is detectable, but it is difficult to determine the origin of the Cu^{II} signal with any certainty. The benefit of analysing hydrated samples is that species in nearby solution can be included in the analysis, and a deeper understanding of the sample in solution can be gained.

Section 9.4 showed that by combining spectral and spatial resolution, two distinct Cu^{II} species could be identified, which differed in energy by 0.2 eV. The lower energy Cu^{II} species at 931.2 eV was attributed to a divalent Cu-S species, which were associated with monovalent Cu-S species. The higher energy Cu^{II} peak at 931.4 eV was attributed to a Cu-O species and is spatially and spectrally distinct from the divalent Cu-S species. Additionally, the relative height of the pre-edge peak to the monovalent Cu spectrum was seen to vary among the sample. This pre-edge peak was proposed to be associated with the oxidation of chalcocite and the subsequent increasing electron vacancies in the Cu 3d valence band. The subtle differences in the Cu L₃ edge spectrum would not have been distinguishable without the combination of spectral and spatial sensitivity provided by STXM.

Finally, the possibility of in-situ electrochemistry was exemplified for chalcocite in solution. A modified sample holder was used with printed gold electrodes, which were connected to an external control. The sample was analysed before and after passing -400 mV through the sample. Prior to the current passing through, the sample was a typical chalcocite particle in solution. After the current, the sample showed three phases; a chalcocite phase, a small component attributable to divalent copper, and the majority of the sample dominated by elemental copper. This showed that under the acidic conditions and with a current of -400 mV, the chalcocite particle was mostly reduced to elemental copper. An example was made of this sample, to show the capabilities of STXM for a quantitative analysis of a sample. It was shown using a quantitative analysis that the remaining chalcocite particle was approximately 230 nm thick, the divalent copper species was estimated to be approximately 1 nm thick, while the thickness of the elemental copper varied around tens of nanometers in thickness. This shows the possibility for a semi-quantitative analysis of electrochemical oxidation products, showing not only the distribution of species, but regions of relative thickness across a sample.

While there are still some apparent challenges with using STXM to analyse sulfide minerals, namely the saturation of the signal which arises from overly thick particles, this chapter has shown that there are methods of analysis which can ameliorate these effects. The resulting analysis has great potential to provide a modern understanding of sulfide mineral systems in many fields of research.

9.7 References

- [1] K.J.J. Mayrhofer, S.J. Ashton, J.C. Meier, G.K.H. Wiberg, M. Hanzlik, M. Arenz, Non-destructive transmission electron microscopy study of catalyst degradation under electrochemical treatment, *Journal of Power Sources*, 185 (2008) 734-739.
- [2] S.C. Tsai, Effects of surface chemistry and particle size and density on froth flotation of fine coal, *Colloids and Surfaces*, 16 (1985) 323-336.

- [3] G. Qian, Y. Li, A.R. Gerson, Applications of surface analytical techniques in Earth Sciences, *Surface Science Reports*, 70 (2015) 86-133.
- [4] W. Chao, P. Fischer, T. Tyliczszak, S. Reka, E. Anderson, P. Naulleau, Real space soft x-ray imaging at 10 nm spatial resolution, *Opt. Express*, 20 (2012) 9777-9783.
- [5] Maser, Osanna, Wang, Jacobsen, Kirz, Spector, Winn, Tennant, Soft X-ray microscopy with a cryo scanning transmission X-ray microscope: I. Instrumentation, imaging and spectroscopy, *Journal of Microscopy*, 197 (2000) 68-79.
- [6] J.A. Brandes, C. Lee, S. Wakeham, M. Peterson, C. Jacobsen, S. Wirick, G. Cody, Examining marine particulate organic matter at sub-micron scales using scanning transmission X-ray microscopy and carbon X-ray absorption near edge structure spectroscopy, *Marine Chemistry*, 92 (2004) 107-121.
- [7] M. Schumacher, I. Christl, A.C. Scheinost, C. Jacobsen, R. Kretzschmar, Chemical Heterogeneity of Organic Soil Colloids Investigated by Scanning Transmission X-ray Microscopy and C-1s NEXAFS Microspectroscopy, *Environmental Science & Technology*, 39 (2005) 9094-9100.
- [8] K. Shinohara, A. Ito, T. Ohigashi, M. Kado, S. Toné, Discrimination of DNA and RNA distribution in a mammalian cell by scanning transmission soft X-ray microscopy, *Journal of X-Ray Science and Technology*, 26 (2018) 877-884.
- [9] K. Shinohara, T. Ohigashi, S. Toné, M. Kado, A. Ito, Quantitative analysis of mammalian chromosome by scanning transmission soft X-ray microscopy, *Ultramicroscopy*, 194 (2018) 1-6.
- [10] K. Shinohara, S. Toné, T. Ejima, T. Ohigashi, A. Ito, Quantitative Distribution of DNA, RNA, Histone and Proteins Other than Histone in Mammalian Cells, Nuclei and a Chromosome at High Resolution Observed by Scanning Transmission Soft X-Ray Microscopy (STXM), *Cells*, 8 (2019) 164.
- [11] J.R. Lawrence, G.D.W. Swerhone, G.G. Leppard, T. Araki, X. Zhang, M.M. West, A.P. Hitchcock, Scanning Transmission X-Ray, Laser Scanning, and Transmission Electron Microscopy Mapping of the Exopolymeric Matrix of Microbial Biofilms, *Applied and Environmental Microbiology*, 69 (2003) 5543-5554.
- [12] A.L. Foggatto, Y. Takeichi, K. Ono, H. Suga, Y. Takahashi, M.A. Fusella, J.T. Dull, B.P. Rand, K. Kutsukake, T. Sakurai, Study of local structure at crystalline rubrene grain boundaries via scanning transmission X-ray microscopy, *Organic Electronics*, 74 (2019) 315-320.
- [13] F.M. de Groot, E. de Smit, M.M. van Schooneveld, L.R. Aramburo, B.M. Weckhuysen, In-situ Scanning Transmission X-Ray Microscopy of Catalytic Solids and Related Nanomaterials, *ChemPhysChem*, 11 (2010) 951-962.
- [14] J.J. Dynes, T. Tyliczszak, T. Araki, J.R. Lawrence, G.D.W. Swerhone, G.G. Leppard, A.P. Hitchcock, Speciation and Quantitative Mapping of Metal Species in Microbial Biofilms Using Scanning Transmission X-ray Microscopy, *Environmental Science & Technology*, 40 (2006) 1556-1565.
- [15] K. Benzerara, T.H. Yoon, T. Tyliczszak, B. Constantz, A.M. Spormann, G.E. Brown, Scanning transmission X-ray microscopy study of microbial calcification, 2 (2004) 249-259.
- [16] T.H. Yoon, S.B. Johnson, K. Benzerara, C.S. Doyle, T. Tyliczszak, D.K. Shuh, G.E. Brown, In Situ Characterization of Aluminum-Containing Mineral-Microorganism Aqueous Suspensions Using Scanning Transmission X-ray Microscopy, *Langmuir*, 20 (2004) 10361-10366.
- [17] F. Bourdelle, K. Benzerara, O. Beyssac, J. Cosmidis, D.R. Neuville, G.E. Brown, E. Paineau, Quantification of the ferric/ferrous iron ratio in silicates by scanning transmission X-ray microscopy at the Fe L_{2,3} edges, *Contributions to Mineralogy*, 166 (2013) 423-434.
- [18] M. Obst, A. Hitchcock, T. Ayers, C. Schietinger, C. Karunakaran, A novel wet cell for in situ 2D and 3D STXM studies, *Canadian Light Source activity report*, (2008) 142-143.
- [19] M. Obst, P. Ingino, A. Hitchcock, V. Prabu, A. Picard, Redox-Chemistry of Environmental Biofilms Probed on the Submicron Scale by in-situ Electrochemistry Scanning Transmission (soft) X-ray Microscopy, *Microscopy and Microanalysis*, 24 (2018) 502-505.

- [20] R.C. Hunter, A.P. Hitchcock, J.J. Dynes, M. Obst, T.J. Beveridge, Mapping the Speciation of Iron in *Pseudomonas aeruginosa* Biofilms Using Scanning Transmission X-ray Microscopy, *Environmental Science & Technology*, 42 (2008) 8766-8772.
- [21] A.P. Hitchcock, J.J. Dynes, J.R. Lawrence, M. Obst, G.D.W. Swerhone, D.R. Korber, G.G. Leppard, Soft X-ray spectromicroscopy of nickel sorption in a natural river biofilm, *Geobiology*, 7 (2009) 432-453.
- [22] Flow Through Electrochemical cell for STXM Collaborative Project (2015):, A. Hitchcock, M. Obst, S.L. Harmer, H. Hooman, International consortium flow through electrochemical cell.
- [23] A.P. Hitchcock, aXis2000 - Analysis of X-ray Images and Spectra, <http://unicorn.mcmaster.ca/aXis2000.html>.
- [24] S.W. Goh, A.N. Buckley, R.N. Lamb, R.A. Rosenberg, D. Moran, The oxidation states of copper and iron in mineral sulfides, and the oxides formed on initial exposure of chalcopyrite and bornite to air, *Geochimica et Cosmochimica Acta*, 70 (2006) 2210-2228.
- [25] R.A.D. Patrick, J.F.W. Mosselmans, J.M. Charnock, K.E.R. England, G.R. Helz, C.D. Garner, D.J. Vaughan, The structure of amorphous copper sulfide precipitates: An X-ray absorption study, *Geochimica et Cosmochimica Acta*, 61 (1997) 2023-2036.
- [26] M. Grioni, J.B. Goedkoop, R. Schoorl, F.M.F. de Groot, J.C. Fuggle, F. Schäfers, E.E. Koch, G. Rossi, J.M. Esteva, R.C. Karnatak, Studies of copper valence states with Cu L₃ X-ray-absorption spectroscopy, *Physical Review B*, 39 (1989) 1541-1545.
- [27] G. van der Laan, R.A.D. Patrick, C.M.B. Henderson, D.J. Vaughan, Oxidation state variations in copper minerals studied with Cu 2p X-ray absorption spectroscopy, *Journal of Physics and Chemistry of Solids*, 53 (1992) 1185-1190.
- [28] R. Patrick, G. van der Laan, D. Vaughan, C. Henderson, Oxidation state and electronic configuration determination of copper in tetrahedrite group minerals by L-edge X-ray absorption spectroscopy, *Phys Chem Minerals*, 20 (1993) 395-401.
- [29] R.G. Acres, S.L. Harmer, D.A. Beattie, Synchrotron PEEM and ToF-SIMS study of oxidized heterogeneous pentlandite, pyrrhotite and chalcopyrite, *Journal of Synchrotron Radiation*, 17 (2010) 606-615.
- [30] R.G. Acres, S.L. Harmer, D.A. Beattie, Synchrotron XPS, NEXAFS, and ToF-SIMS studies of solution exposed chalcopyrite and heterogeneous chalcopyrite with pyrite, *Minerals Engineering*, 23 (2010) 928-936.
- [31] Y. Kalegowda, Y.-L. Chan, D.-H. Wei, S.L. Harmer, X-PEEM, XPS and ToF-SIMS characterisation of xanthate induced chalcopyrite flotation: Effect of pulp potential, *Surface Science*, 635 (2015) 70-77.
- [32] R.A.D. Patrick, G. van der Laan, J.M. Charnock, B.A. Grguric, Cu L₃ X-ray absorption spectroscopy and the electronic structure of minerals: Spectral variations in non-stoichiometric bornites, Cu₅FeS₄, *American Mineralogist*, 89 (2004) 541-546.
- [33] C.I. Pearce, R.A.D. Patrick, D.J. Vaughan, C.M.B. Henderson, G. van der Laan, Copper oxidation state in chalcopyrite: Mixed Cu *d*⁹ and *d*¹⁰ characteristics, *Geochimica et Cosmochimica Acta*, 70 (2006) 4635-4642.
- [34] I. Koprinarov, A.P. Hitchcock, X-ray Spectromicroscopy of Polymers: An introduction for the non-specialist, <http://unicorn.mcmaster.ca/stxm-intro/polySTXMinIntro-all.html>.
- [35] G. van der Laan, R.A.D. Patrick, J.M. Charnock, B.A. Grguric, Cu L_{2,3} x-ray absorption and the electronic structure of nonstoichiometric Cu₅FeS₄, *Physical Review B*, 66 (2002) 045104.
- [36] E. Todd, D. Sherman, J. Purton, Surface oxidation of chalcopyrite (CuFeS₂) under ambient atmospheric and aqueous (pH 2-10) conditions: Cu, Fe L-and O K-edge X-ray spectroscopy, *Geochimica et Cosmochimica Acta*, 67 (2003) 2137-2146.
- [37] E.C. Todd, D.M. Sherman, Surface oxidation of chalcocite (Cu₂S) under aqueous (pH= 2–11) and ambient atmospheric conditions: mineralogy from Cu L-and O K-edge X-ray absorption spectroscopy, *American Mineralogist*, 88 (2003) 1652-1656.

- [38] E.M. Arce, I. González, A comparative study of electrochemical behavior of chalcopyrite, chalcocite and bornite in sulfuric acid solution, *International Journal of Mineral Processing*, 67 (2002) 17-28.
- [39] G. van der Laan, M.A. Hoyland, M. Surman, C.F.J. Flipse, B.T. Thole, Surface orbital magnetic moment of ferromagnetic nickel studied by magnetic circular dichroism in Ni3*p* core level photoemission, *Physical Review Letters*, 69 (1992) 3827-3830.
- [40] A.P. Hitchcock, Z. Qin, S.M. Rosendahl, V. Lee, M. Reynolds, H. Hosseinkhannazer, Electrodeposition of Cu studied with in situ electrochemical scanning transmission x-ray microscopy, *AIP Conference Proceedings*, 1696 (2016) 020003.
- [41] V. Prabu, M. Obst, H. Hosseinkhannazer, M. Reynolds, S. Rosendahl, J. Wang, A.P. Hitchcock, Instrumentation for in situ flow electrochemical Scanning Transmission X-ray Microscopy (STXM), *Review of Scientific Instruments*, 89 (2018) 063702.
- [42] B.L. Henke, E.M. Gullikson, J.C. Davis, X-ray interactions: photoabsorption, scattering, transmission, and reflection at E=50-30000 eV, Z=1-92, *Atomic Data and Nuclear Data Tables*, 54 (1993) 181-342.

10 CONCLUSION

The original contribution to knowledge presented in this thesis is the accurate interpretation of pyrrhotite and pentlandite photoemission spectra which was resolved by identifying and separating bulk and surface contributions to spectra. An understanding of the final state effects contributing to the observed bulk line shapes was achieved by studying the electronic structure of these minerals using photoemission spectra of the valence band region of these minerals. This contribution has allowed for the identification and quantification of minority species on chemically altered surfaces of pyrrhotite and pentlandite, providing further insight into the surface species and near surface structures which form under environmental conditions. The new interpretations of photoemission spectra for these transition metal sulfides have implications for research fields which are concerned with characterisation of chemical species on sulfide minerals. Methods for identifying minority species was extended by the novel use of scanning transmission X-ray microscopy (STXM) for minerals analysis. STXM was shown not only to be applicable to mineral systems, but also was able to identify minority species through spatial resolution and provide valuable analysis of *in situ* development of chemical species under environmental conditions.

Pristine fracture surfaces of pyrrhotite and pentlandite were analysed to identify the surface species which form natively on fracture surfaces of these minerals in the absence of external oxidants. Varying the incident photon energy used to collect photoemission spectra allowed the surface features contributing to each spectrum to be distinguished from bulk features. In this way, the surface species which form on fracture surfaces were identified. The sulfur sites on the pyrrhotite surface were seen to reconstruct and form surface disulfide and polysulfide features, in addition to an undercoordinated surface monosulfide species. Using the same technique, pentlandite was shown to have two distinct undercoordinated surface monosulfide species form on its fracture surface, with very little to no disulfide or polysulfide species, depending on the individual sample. This showed that the pentlandite fracture surface undergoes relaxation rather than reconstruction to lower its surface energy. The 4-coordinate and 5-coordinate bulk sulfur species were observed to lose at least one bonding partner during fracture, resulting in 3-coordinate and 4-coordinate sulfur at the surface. The binding energy of the 4-coordinate surface monosulfide was observed to overlap with the 4-coordinate bulk monosulfide. This assignment of states to the photoelectron spectrum for pentlandite resolves the debate regarding the interpretation of the S $2p$ spectrum and clarifies the features which are expected on pristine pentlandite surfaces. This research has highlighted the 4-coordinate violarite-like feature which is observed in prior research as an oxidation species on the pentlandite fracture surface and distinguishes it from the naturally occurring 4-coordinate surface monosulfide. The ability to

Chapter 10: Conclusion

accurately fit these species in the S $2p$ spectrum and distinguish the naturally occurring surface features from surface oxidation products is significant for research concerning the application of pentlandite as a catalyst as it elucidates the correct interpretation of photoemission spectra and will aid in accurate characterisation of pentlandite surfaces using photoelectron spectroscopy.

By observing spectra with varied surface sensitivities, the core level $2p$ spectra of both pyrrhotite and pentlandite were distinguished from surface states and showed notable asymmetry in the bulk line shapes for both minerals. The asymmetry of the transition metal $2p$ lines has long been understood to be due to multiplet splitting of the spectral line, but the origin of the asymmetry in the S $2p$ line shape has not been well understood. A significant contribution to knowledge presented in this thesis is the identification of the bulk sulfide line shape, which has only been possible with the use of high resolution photoemission spectroscopy with variable photon energies. This has enabled an empirical line shape to be carefully defined for each mineral. This method has been crucial for identifying and quantifying features on the surfaces of these minerals which arise due to oxidation, as the asymmetry of the bulk peak overlaps with the binding energies of disulfide, polysulfide, and elemental sulfur species. Consequently, this thesis has highlighted the importance of using caution when fitting core level spectra and discusses the consequence of using pre-defined arbitrary peak shapes. Pre-defined peak shapes such as the Doniach-Sunjic line shape present a potential danger to the unwary spectroscopist, as they may give an illusion of being descriptive of the processes causing that line shape. In most scenarios, these line shapes are arbitrary, therefore their ability to fit an experimental line shape is often either fortuitous or by design but is not descriptive. The work presented in this thesis shows that carefully fitting the bulk line shape with an empirical set of symmetric peaks is less restrictive than pre-defined line shapes and can be a powerful tool for analysing less chemically altered surfaces.

While the empirical peaks were not considered descriptive, the asymmetry of the bulk sulfide line shapes were justified using valence band photoemission spectroscopy to study the electronic structure of these minerals. Resonant photoemission spectroscopy identified the spectral features of the valence band region which originate from cation sites in the lattice of each mineral. In both pyrrhotite and pentlandite, a close association between the sulfur and iron states was observed at 4.7 eV for pyrrhotite, and 4.4 eV for pentlandite. These results indicate S $2p \rightarrow$ Fe $3d$ ligand-to-metal charge transfer final states for both minerals. These final state effects are proposed to be the origin of the broad asymmetric line shapes observed for pyrrhotite and pentlandite bulk S $2p$ core level spectra. This explanation differs from that of previous studies which have assigned the origin of the

Chapter 10: Conclusion

asymmetry to metallic properties of the minerals, which were previously assumed due to the small radial distance between neighbouring cations in the lattice.

Photoemission spectroscopy of the valence band region of pentlandite in particular identified the features in the valence band spectrum which originate from Fe and Ni cations, which was enhanced by analysing samples of varying cation ratios. Resonant photoemission studies revealed the upper valence band to be dominated by Ni 3*d* states, whereas the lower valence band had stronger Fe 3*d* character, rather than Ni 3*d* states. Observations of the valence band region of pentlandites with differing stoichiometries was critical for assigning the origin of valence states to each cation. Low photon energies were used to exploit the difference in photoionization cross sections between the cation and the sulfur states. This revealed polymerised sulfur states in the 3 – 6 eV region of the valence band, and sulfate states in a slightly oxidised sample at 3 eV and 10 eV. These observations are significant, as valence band spectra have been difficult to calculate due to the presence of Fe and Ni atoms in both tetrahedral and octahedral cation sites, the overlapping states from the cations, and their covalency with the S atoms. These complications cause the electronic structure to be difficult to model accurately using common calculation techniques. The availability of high resolution valence band spectra and the interpretation of the origin of individual features in these spectra will inform future calculations of the electronic structure of pentlandite and provide an experimental basis on which to refine the models.

Careful analysis and description of pristine surfaces of pyrrhotite and pentlandite allowed for a detailed investigation into the oxidised surfaces of these minerals. Having well defined core level spectra such as those found in the pristine fracture surface chapters, was essential for tracking the oxidation products present on pyrrhotite and pentlandite surfaces after oxidation in air due to polishing, exposure to acid, and in the case of pentlandite, after exposure to a low dose of H₂O vapour. The comparison between the spectra from pristine surfaces and those of oxidised surfaces revealed an extensive overlayer of FeOOH species on both pyrrhotite and pentlandite which had been oxidised in air by polishing. The sulfur spectra revealed elemental sulfur in the near surface layers of both minerals, which was asserted to be trapped by a combination of amorphous sulfur-rich structure, and an overlayer of FeOOH species. The samples exposed to acidic solution had much less contribution from FeOOH species, and the elemental sulfur component in pyrrhotite had been removed by reaction of the surface with H₂SO₄, but a small contribution in the pentlandite sample remained. Previous studies had indicated that the disappearance of elemental sulfur in the pyrrhotite sample exposed to acidic solution is due to the near-surface forming a more crystalline structure, as opposed to the amorphous structure of the air oxidised pyrrhotite. Due to analysis of photoemission electron

Chapter 10: Conclusion

microscopy (PEEM) images and Fe 2*p* spectra, this current work proposes that exposure to acidic solution removes much of the extensive FeOOH layer which forms during polishing, while only isolated patches of this oxidised overlayer remain, resulting in the liberation of the volatile elemental sulfur species. In contrast, the pentlandite sample exposed to acidic solution still showed some contribution from elemental sulfur which was proposed to be trapped by the extensive polysulfide created by the migration of Fe species to the upper surface layer, causing a metal deficient near surface layer.

The observation of oxidised pentlandite surfaces reinforced the preferential oxidation of Fe species over Ni species, as this was mirrored in all oxidised pentlandite samples. By comparing the initial oxidation by water vapour with the extensive oxidation by polishing and exposure to acidic solution, it was concluded that the propensity for Fe states to oxidise over Ni states is likely due to the increased mobility of Fe ions through the lattice, which is enhanced by the restructuring of the near surface layers. Consequently, for the sample which was oxidised only by water vapour, relatively little reconstruction of the surface occurred, therefore the Ni ions experienced a similar level of oxidation as the Fe ions due to their inability to migrate away from the surface with such little surface reconstruction under those conditions.

A key understanding developed by the analysis of oxidised mineral surfaces in this thesis is the extent to which a surface restructures due to different preparation techniques. The samples which differed the most from the pristine fracture surfaces were the polished mineral samples, whereas the samples subsequently exposed to acidic solution had a remarkably similar surface structure to the pristine surfaces. This highlights the importance of understanding how sample preparation methods affect the surfaces of the mineral and that it is the activity of these *altered* surfaces which must be considered when designing catalysts from these minerals. This idea, and the understanding of the surface changes which occur due to oxidation, is increasingly significant as there is a building interest in uses of naturally occurring small band gap semiconductors such as sulfide minerals for catalysts.

The final chapter of this thesis presented a significant contribution to the application of a new microspectroscopy technique for sulfide minerals research. Scanning transmission X-ray microscopy was shown to be a viable and powerful tool for minerals research, despite the challenge of sample thickness which was encountered. The analysis of these thicker samples using a saturated signal presented a method to avoid regions which are too thick and proceed with a meaningful analysis of the samples. STXM analysis of the copper sulfide chalcocite showed that the combination of spatial and spectral resolution in this spectromicroscopy technique can reveal critical information about the

Chapter 10: Conclusion

origin of features in the spectra. It can detect and distinguish minority species which are otherwise overshadowed by majority species in spectra averaged over large areas. This chapter also highlighted the importance of being able to analyse samples in different environments, such as hydrated samples in solution, rather than changing the environmental conditions to analyse in ultra-high vacuum, as is necessary for techniques such as X-ray photoelectron and absorption spectroscopies. The ability to analyse hydrated samples opens up the possibilities for this technique to be extended to more diverse analysis. An example of this was shown for a chalcocite particle in an electrochemical cell, where the particle was observed to be reduced to elemental copper as a result of a voltage passed through the cell. The samples shown in this final chapter are significant for mineral research and froth flotation in particular, where the spatial distribution of chemical species across a particle, and the interaction of the mineral's surface with its surrounding environment is critical for the efficient separation of that mineral.

10.1 Future work

There is increasing access to photoemission techniques and higher resolution instruments; this is reflected in the continual use of photoemission spectroscopy for analysis of sulfide structures applied as catalysts for hydrogen and oxygen evolution reactions in particular. It is important to dedicate research towards interpreting spectra and developing simple methods of analysis for sulfide structures. It is unreasonable for research which is focussed on applications to do the heavy lifting in spectral interpretation, consequently dedicated interpretation studies such as these presented in the current work are critical for accurate spectral interpretation and subsequent detection of reacted surface species. Further work is required to understand the effect of cation occupancy on the surface electronic structure of pentlandite.

The surface structure and reactivity of cobalt pentlandite (Co_9S_8) in particular should be of interest due to the invariability of its stoichiometry. Questions arising from this current work involve how the surface structure and reactivity of pentlandite is affected and importantly, how the interpretation of cation and S $2p$ spectra should change due to differences in cation occupancy. Is a Co_9S_8 structure more or less stable without the preferential oxidation of Fe species observed for $(\text{Fe},\text{Ni})_9\text{S}_8$? Future work should focus on characterising fracture surfaces and oxidised surfaces of synthetic samples of Co_9S_8 and $(\text{Fe},\text{Ni},\text{Co})_9\text{S}_8$ with varied ratios of Fe, Ni, and Co. Comparisons of the core level bulk line shapes may uncover some differences in final state effects caused by changing the ratios of cations in the lattice. This is an important question particularly for Co_9S_8 , since a charge transfer final state was detected for the Fe sites, but not the Ni sites; it is unknown what final state effects contribute to the spectra for cobalt pentlandite. While some studies have observed high resolution core level spectra

Chapter 10: Conclusion

for Co_9S_8 , there are none which are focussed on careful interpretation of these spectra. Comparing the photoemission spectra of the valence band region for a series of pentlandite structures would reveal changes to the band structure caused by altered stoichiometry in the pentlandite structure and would aid in the accurate interpretation of core level spectra.

The future work arising from the analysis of sulfide minerals using STXM is far-reaching and only limited by the interpretation of spectra which is guided by the understanding of the electronic structure of the sample. This technique will enhance current minerals research by enabling analysis within environmental conditions. STXM provides a tool for investigating the interaction of sulfide minerals with the reagents used for separation of mineral phases by froth flotation. Such research would assist in the design of flotation reagents for efficient mineral separation and metal extraction. This technique could also have significant impacts on the understanding of the degradation of sulfide catalysts during the hydrogen or oxygen evolution reactions. This is the advantage of modified sample holders such as the electrochemical cell presented in this work. This opens up the opportunities to analyse samples in more natural conditions and observe the chemical changes *in situ*.